UNIVERSIDAD COMPLUTENSE DE MADRID
FACULTAD DE CIENCIAS FÍSICAS
DEPARTAMENTO DE FÍSICA ATÓMICA, MOLECULAR Y NUCLEAR

TESIS DOCTORAL

Diagnostics and modeling of cold plasmas with high hydrogen content

Diagnóstico y modelado de plasmas fríos con alto contenido en hidrógeno

MEMORIA PARA OPTAR AL GRADO DE DOCTOR

PRESENTADA POR

Miguel Jiménez Redondo

DIRECTORA

Isabel Tanarro Onrubia

Madrid, 2017

UNIVERSIDAD COMPLUTENSE DE MADRID

FACULTAD DE CIENCIAS FÍSICAS

DEPARTAMENTO DE FÍSICA ATÓMICA, MOLECULAR Y NUCLEAR

Diagnostics and modeling of cold plasmas with high hydrogen content

Diagnóstico y modelado de plasmas fríos con alto contenido en hidrógeno

Memoria presentada para optar al grado de Doctor en Física por:

Miguel Jiménez Redondo

Directora:

Dra. Isabel Tanarro Onrubia

Madrid, 2016

A mis padres y a Patricia

Agradecimientos

Quiero aprovechar estas líneas para agradecer a aquellas personas que, de una forma u otra, en mayor o menor medida, han ayudado a que este trabajo haya salido adelante. Quisiera agradecer especialmente a Isabel Tanarro, directora de esta tesis, y a Víctor Herrero, su inestimable esfuerzo, dedicación y ayuda día tras día desde que empecé a colaborar con el grupo. Gracias a los dos por introducirme en la investigación y el mundo de los plasmas, y por todo el conocimiento y experiencia que habéis compartido conmigo.

A Esther Carrasco, por toda la ayuda y consejos prestados al comienzo de la realización de la tesis, y por las tardes compartidas en el laboratorio. A las demás personas del grupo, en especial a Belén Maté, Miguel Ángel Moreno y Rafa Escribano, por la oportunidad de colaborar con vosotros y la paciencia para resolver las dudas sobre los experimentos en la cámara de hielos. A mis compañeros de despacho a lo largo de todos estos años: David, Maite, Delia, Paco, Elena y Germán, por todos los buenos momentos compartidos. Finalmente, tengo que agradecer al resto de gente del Departamento de Física Molecular el ambiente de trabajo tan bueno que mantienen. Ha sido un placer trabajar todo este tiempo con vosotros.

A Jesús, por la cantidad innumerable de horas compartidas, primero durante la licenciatura y después a la hora de comer en el Consejo, y a Amelia, por poder seguir compartiendo penas y alegrías a pesar de vivir a 2000 km de distancia.

A mi familia por todo su apoyo y su ayuda, y a mis padres, sin vuestro cariño y motivación esta tesis no hubiera sido posible.

Por último, a Patricia, gracias por estar siempre a mi lado.

Table of Contents

Resumen

El estudio de los plasmas fríos con alto contenido en hidrógeno tiene interés en una gran variedad de campos. La caracterización de las especies en estos plasmas y su interacción con las superficies tiene aplicaciones tecnológicas, como el crecimiento de láminas delgadas y el procesado de materiales. Los iones que se pueden observar en este tipo de plasmas tienen un papel importante en la formación de moléculas en el medio interestelar.

En este trabajo se presenta un estudio de las especies neutras e iónicas presentes en los plasmas de H_2 + Ar, H_2 + N_2, y H_2 + O_2 generados en descargas de cátodo hueco, basado en el diagnóstico experimental y el modelado cinético, con el objetivo de determinar los principales procesos físico-químicos de cada una de las mezclas.

El reactor de cátodo hueco empleado en los experimentos consiste en un cilindro de acero inoxidable conectado a tierra, con un ánodo central sometido a una tensión de cientos de voltios, donde se genera una corriente de décimas de amperio. Para generar el plasma se emplean mezclas de H_2 + Ar, H_2 + N_2, y H_2 + O_2 en diferentes proporciones, a baja presión (∼ Pa), en flujo continuo de gas. Las especies neutras del plasma se analizan mediante un espectrómetro de masas cuadrupolar, mientras que los iones positivos se muestrean mediante un monitor de plasmas que permite analizar sus distribuciones de energía. La temperatura y densidad electrónica del plasma se determinan usando una sonda de Langmuir doble. Las temperaturas vibracional y rotacional se obtienen mediante espectroscopía visible de emisión.

Con el objetivo de reproducir las abundancias de las diferentes especies determinadas experimentalmente en cada tipo de mezcla y determinar los mecanismos que gobiernan la cinética del plasma, se emplea un modelo cinético que tiene en cuenta los principales procesos físicoquímicos que tienen lugar en la descarga. Entre ellos, los más relevantes son las reacciones de ionización y disociación por impacto electrónico y las reacciones ion-molécula, que tienen lugar en fase gas, y los procesos heterogéneos que ocurren en las paredes de la cámara.

El plasma de H_2 + Ar se estudió a 1.5 y 8 Pa para todo el rango de proporciones de mezcla entre Ar puro y H_2 puro. Este plasma presenta una química neutra simple, dado que no se forman nuevas moléculas en la descarga. Respecto a los iones positivos, las distribuciones están dominadas por Ar^+, ArH^+ y H_3^+, cuyas concentraciones dependen fuertemente de la presión y la proporción de la mezcla. La región donde predomina el ArH^+ cambia drásticamente con la presión, dado que a 1.5 Pa dicho ion es mayoritario para una amplia variedad de mezclas intermedias, mientras que a 8 Pa se reduce a una pequeña región de mezclas con una cantidad muy reducida de H_2. Hay dos factores que determinan fundamentalmente la química del plasma: la temperatura electrónica, que depende de la presión, y el equilibrio de la reacción $H_3^+ + Ar \rightleftarrows ArH^+ + H_2$, que afecta decisivamente a la relación entre las concentraciones de ArH^+ y H_3^+. La reacción directa es endotérmica, por lo que el coeficiente de velocidad de la misma depende grandemente de la excitación interna de los reactivos. Los experimentos y simulaciones sugieren que, en los plasmas estudiados, a 1.5 Pa la excitación interna del H_3^+ es suficiente para superar la barrera de potencial, pero a 8 Pa este ion es desexcitado colisionalmente y predomina la reacción inversa.

Las descargas de H_2 + N_2 se estudiaron a cinco presiones diferentes entre 0.8 y 8 Pa, con mezclas de H_2 + ~ 10 % N_2. Se detectó amoniaco en cantidades significativas en todas las descargas, alcanzando concentraciones comparables a las del N_2 para las presiones más bajas. Este NH_3 se forma en las paredes del reactor en una serie de reacciones heterogéneas incluyendo procesos Langmuir-Hinshelwood y Eley-Rideal. Las distribuciones de iones positivos están determinadas fundamentalmente por la temperatura electrónica de la descarga, que controla el balance entre las reacciones de ionización directa y las de tipo ion-molécula. A las presiones más bajas, donde la temperatura electrónica es más alta, ambos tipos de procesos tienen una importancia similar y la distribución de iones es equilibrada. Sin embargo, a las presiones mayores predominan las reacciones ion-molécula, y la carga positiva se concentra en el NH_4^+, debido a su formación en reacciones de otros iones protonados con NH_3, y a la ausencia de reacciones de destrucción en fase gas de dicho ion.

Los plasmas de H_2 + O_2 se estudiaron a una presión de 8 Pa con proporciones de mezcla entre H_2 puro y O_2 puro. Se detectó agua en concentraciones importantes, comparables a las del precursor minoritario en la mezcla. Este H_2O se produce en una serie de reacciones heterogéneas de tipo Eley-Rideal en las paredes del reactor. En las distribuciones de iones positivos predomina el H_3O^+, formado en reacciones entre H_3^+ y H_2O, en un amplio rango de mezclas intermedias, mientras que para plasmas con alto contenido en hidrógeno el H_3^+ es el ion mayoritario, y en las mezclas con más oxígeno predomina el O_2^+ formado por ionización directa de las moléculas de O_2. Los iones H_2O^+, OH^+ y HO_2^+ presentan concentraciones con escasas variaciones para la mayoría de

proporciones de mezcla intermedias. Las concentraciones de iones negativos se simularon con el modelo cinético, observando que acumulan hasta un 25 % de la carga negativa, pero presentan un impacto limitado en la química de la descarga.

Se realizó también un estudio experimental de descargas de $H_2 + N_2 + O_2$, utilizando para ello mezclas de H_2 con pequeñas cantidades de aire a 8 Pa. Las concentraciones de NH_3 y H_2O medidas resultaron ser comparables, a pesar de la diferencia en abundancia de los respectivos precursores, debido a que la formación del agua en la pared necesita menos etapas. Los iones protonados dominan la distribución de iones, siendo el NH_4^+ el ion mayoritario seguido por el H_3O^+. En estos plasmas, con temperaturas electrónicas relativamente bajas, se encontró una fuerte correlación entre la afinidad protónica de las especies y su abundancia en la descarga.

Abstract

The study of cold plasmas with high hydrogen content is relevant in a wide variety of fields. The characterization of the different species in these plasmas and their interaction with surfaces has technological applications, such as thin film growth and materials processing. The ions present in this type of plasmas play an important role in molecule formation in the interstellar medium.

In this work, a study of the neutral and ionic species present in plasmas of H_2 + Ar, H_2 + N_2, and H_2 + O_2 generated in hollow cathode discharges is presented. Experimental diagnostics in combination with kinetic modeling have been employed in order to determine the main processes behind the physics and chemistry of each of the different mixtures.

The hollow cathode reactor used in the experiments consists of a grounded stainless steel cylinder with a central anode. A voltage of hundreds of volts is applied to the anode, generating a current of tenths of an ampere. A steady flow of mixtures of H_2 + Ar, H_2 + N_2, and H_2 + O_2 with different mixture ratios at low pressures (~ Pa) is employed as precursor. The neutral species in the plasma are analyzed with a quadrupole mass spectrometer, while positive ions are sampled using a plasma monitor that allows the measurement of their energy distributions. The electron temperature and density of the plasma are determined using a double Langmuir probe. Vibrational and rotational gas temperatures are obtained by optical emission spectroscopy.

A kinetic model accounting for the main physico-chemical processes occurring in the discharge is employed in order to simulate the abundances of the different species. The comparison with the experimental results allows the determination of the fundamental mechanisms behind the chemistry of the different mixtures. The main processes considered are electron impact dissociation and ionization, ion-molecule reactions, and heterogeneous reactions occurring at the reactor walls.

H_2 + Ar plasmas were studied at 1.5 and 8 Pa for the whole range of mixture ratios. The neutral chemistry in these discharges is simple, since no new molecules are formed in

the plasma. The positive ion distributions are dominated by Ar^+, ArH^+ and H_3^+, with concentrations depending strongly on the pressure and mixture ratio. The ArH^+ dominance region greatly varies with pressure, from a wide range of mixture ratios at 1.5 Pa to a narrow window close to the pure Ar plasma in the 8 Pa discharge. Two key factors drive the observed ion chemistry: the electron temperature, which depends on the pressure, and the equilibrium of the process $H_3^+ + Ar \rightleftarrows ArH^+ + H_2$, which ultimately determines the ArH^+/H_3^+ ratio. The forward reaction is endothermic for ground state reactants, so the rate coefficient greatly depends on the internal excitation of the reactants. The experimental data and simulations suggest that at 1.5 Pa the internal excitation of H_3^+ in the plasmas studied is sufficient to overcome the energetic barrier at the lower pressure, but is efficiently quenched at 8 Pa and the inverse reaction prevails.

The chemistry in $H_2 + N_2$ plasmas was studied at five different pressures, from 0.8 to 8 Pa, using mixtures of $H_2 + \sim 10$ % N_2. Ammonia was found in significant amounts in all the discharges, reaching concentrations comparable to those of N_2 for the lowest pressures. This NH_3 is formed at the reactor walls in a series of heterogeneous reactions involving both Langmuir-Hinshelwood and Eley-Rideal mechanisms. Ion distributions are mainly determined by the electron temperature of the discharge, which controls the balance between direct ionization and ion-molecule reactions. At the lower pressures, with higher electron temperatures, both kinds of processes have a similar relevance, leading to a balanced positive ion distribution in which several ions are found in high concentrations. Conversely, when the pressure is higher, ion-molecule reactions prevail, and the positive charge is concentrated in the NH_4^+ ion formed in reactions of NH_3 with other protonated ions, due to the lack of gas phase destruction reactions involving said ion.

The plasmas of $H_2 + O_2$ were studied at 8 Pa for the whole range of mixture ratios. Water was detected in substantial concentrations, comparable to those of the minor precursor in the mixture. This H_2O is primarily produced in a series of heterogeneous Eley-Rideal reactions in the surfaces of the reactor. Experimental positive ion concentrations were found to be dominated by H_3O^+ for a wide variety of intermediate mixtures, due to the proton transfer between H_3^+ and H_2O, while H_3^+ is the major ion in the discharge for H-rich mixtures. For O-rich plasmas, O_2^+, formed by the direct ionization of O_2 molecules, is the dominant ion. The mixed ions H_2O^+, OH^+, and HO_2^+ maintain a roughly stable concentration for intermediate H_2/O_2 ratios. Negative ion concentrations were simulated with the kinetic model, showing that these species concentrate up to 25 % of the total negative charge in the plasma, but have a very limited effect in the global chemistry of the discharge.

Experimental measurements were also performed in $H_2 + N_2 + O_2$ discharges. In particular, mixtures of H_2 with small concentrations of air were employed as precursors,

with a total pressure of 8 Pa. Ammonia and water were detected in comparable concentrations, despite the differences in the abundance of the precursors N_2 and O_2, due to the lower number of reactions required for the formation of H_2O. Protonated ions were found to be the major species in the positive ion distributions, with NH_4^+ prevailing in the discharge followed by H_3O^+. In these relatively low electron temperature plasmas, a strong correlation was found between the proton affinity of the species and their abundance in the discharge.

List of Symbols

A	Electrode of the Langmuir probe
a	Natural isotopic abundance
A_R	Reactor area
C^{PPM}	PPM signal
D	Diffusivity
e	Electron charge
E_A	Activation energy
E_d	Activation energy for surface diffusion
f	Bayard-Alpert correction coefficient
f_X	Fraction of species X in the mixture
I	Electric current
k	Rate coefficient
k_B	Boltzmann constant
M	Average mass
m	Mass
N^-	Negative ion density
N_c	Charge density
N_e	Electron density
N_i	Positive ion density
P	Pressure
Q	Production/destruction term in the differential equation
R	Distance between molecular nuclei
S	Area of electrode
S_T	Surface saturation concentration
T	Transmission

T_e	Electron temperature
T_g	Gas temperature
T_w	Wall temperature
V	Voltage
v	Velocity
V_R	Reactor volume
α	Molecular polarizability
γ	Reaction probability
θ	Net production/destruction of charge
Λ	Characteristic dimension of the reactor
λ_D	Debye length
μ	Reduced mass
ν	Surface diffusional jump frequency
σ	Cross section
τ	Characteristic time
τ_R	Residence time
Φ	Total flow
ϕ	Flow term in the differential equation

Chapter 1.

Introduction

Plasmas, often referred to as the fourth state of matter, are the subject of intense scientific research in various fields of physics and chemistry. Even though 99 % of the known matter in the universe is considered to be in this state, the study of plasmas is relatively recent in historical terms. The first studies of plasmas possibly date from the end of the 18th century, when four Dutch chemists applied an electrical arc discharge to ethylene [1]. Plasmas were identified in Crookes tubes by Sir William Crookes in the last half of the 19th century. Crookes called them "radiant matter" and introduced the concept of classifying plasma as the fourth state of matter [2]. However, it was not until the 1920s that the American physicist Irving Langmuir and his coworkers established a solid theoretical ground for the study of plasmas. Langmuir also coined the term "plasma" in 1928, using it to "describe this region containing balanced charges of ions and electrons" in a mercury vapor arc discharge [3].

Plasmas present an interest in a wide variety of scientific fields, as systems in the state of plasma can be found in very different environments in nature, from flames and lightning to ionospheres and stars. There are also numerous technological applications of plasmas. They are employed in controlled fusion, where great efforts have been made in the last decades to confine these media with very high temperatures ($\sim 10^8$ K) and charge densities ($\sim 10^{14}$ cm^{-3}) in order to obtain a viable energy source [4,5]. In aerospace engineering, plasmas are used for spacecraft propulsion through the use of ion thrusters, which create thrust by accelerating ions with electromagnetic forces [6]. Plasmas are routinely used for industrial applications, including laser ablation, plasma etching, notably in the semiconductor industry, or coatings using plasma enhanced chemical vapor deposition (PECVD). Plasmas are found in devices commonly used in daily life, such as plasma displays, fluorescent lamps, or neon signs.

A plasma can be defined as a quasi-neutral medium of charged and neutral particles characterized by a collective behavior [7]. According to the kinetic theory of ideal gases, in a neutral gas, no forces act between the molecules of the gas (disregarding gravitational forces), so the particles travel in straight lines with a varying distribution of velocities, and their motion is controlled by collisions between themselves and with the walls of the container.

By contrast, in a plasma, the motion of the particles causes local concentrations of positive and negative electric charges, which in turn create electric fields that affect the motion of distant charged particles, inducing the characteristic collective behavior. Local concentrations of charge are confined to volumes of size given by the Debye length, λ_D, which is a characteristic dimension of the plasma. If an electric field is created in the plasma, the charged particles, and especially the electrons due to their higher mobility, will respond to reduce the electric field. The Debye length is a measure of the attenuation caused by this shielding effect. Outside of these small volumes, the charge density of ions is equal to the density of electrons, and as a result the plasma is considered a quasi-neutral gas. For a plasma to be stable, the dimensions of the system must be much greater than the Debye length.

A plasma is usually obtained when sufficient energy, higher than the ionization threshold, is added to the atoms or molecules of a gas, causing ionization and production of ions and electrons, and the corresponding recombination to form atoms or molecules. A plasma can also be obtained when sufficient energy is provided to a liquid or a solid, causing their vaporization and ionization, which is commonly achieved by means of a laser. In a gas, a plasma is usually generated and sustained by providing electromagnetic energy in some form, such as direct current (dc), radio frequency (rf), or microwave. Plasmas are often referred to as gas discharges because the most common way to produce plasma is by passing an electrical discharge through a gas.

Media with very different characteristics fall inside the definition of plasma, from star cores and fusion plasmas, to flames and glow discharges. In order to classify the different types of plasmas, two parameters are considered: the mean energy of the free electrons, usually conveyed through the electron temperature, T_e, and the electron density, N_e. The ionization ratio, the ratio of the positive ion density to the total number density, is sometimes used in place of the latter.

Glow dc discharges are produced by applying a high dc voltage between an anode and a cathode inserted into a gas at low pressure (typically ~ 1–100 Pa). The neutral gas is an electrical isolator. Once the plasma is ignited, the medium becomes a good electric conductor. Electrons originating from the cathode by secondary emission, mainly due to ion impact, are accelerated by a large electric field, which quickly decreases as the distance

from the cathode increases, and also cause ionizations. The neutralization of positive ions in collisions with electrons and the subsequent decay of their excitation energy produce luminosity in this region, known as the cathode glow. Most of the voltage drop occurs in the Crookes dark space, which is a positive space charge plasma sheath, where there is no emission due to the lack of electrons. There is a sharp transition from this dark space to the following region, the negative glow. Here, the field reaches a minimum value, the potential hardly increases and the light emitted by the negative glow originates from spontaneous emission after excitation by electrons. In the glow, the discharge is practically quasi-neutral, albeit with a large positive and negative charge. Ionizations in this region compensate for the loss of charge carriers to the wall. After the negative glow, a dark space (Faraday dark space) can be observed, as the electrons have so little energy that neither ionizations nor excitations take place. A positive column will appear after the Faraday dark space if the discharge is long enough, where a quasi-neutral plasma with a reasonably small, constant field strength prevails. The anode glow, which is slightly brighter than the positive column, marks the border of the anode dark space. This sheath, which appears just in front of the anode, is a small region with negative net space charge and increasing potential through which electrons are further accelerated [8]. The various regions are shown in Figure 1.1.

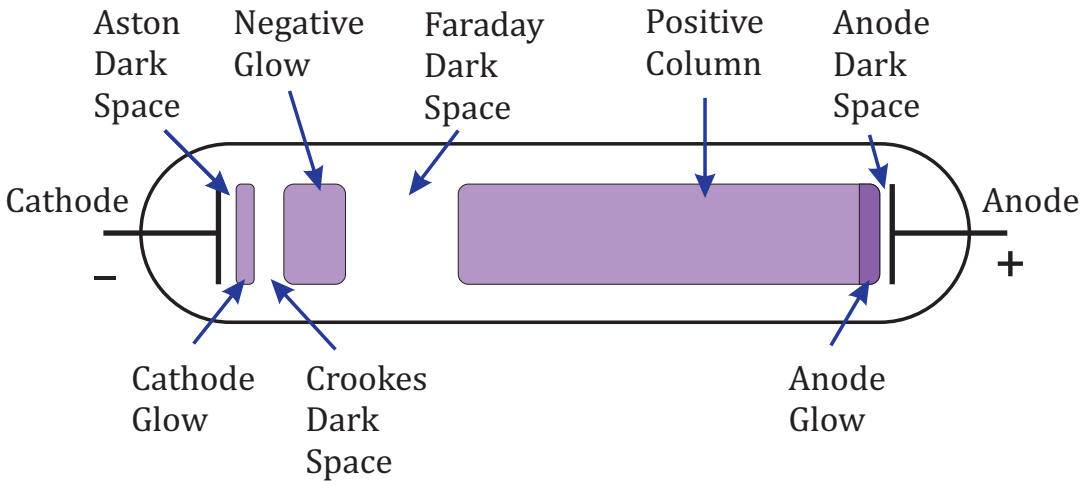

Figure 1.1. The different regions of a dc glow discharge.

Glow discharges are non-thermal plasmas, i.e., they are characterized by a lack of thermal equilibrium. The gas temperature, T_g, is usually close to the room temperature, whereas the electron temperature, T_e, is orders of magnitude higher, typically in the 1–10 eV range (~ 10^4–10^5 K). The fraction of energy transferred from electrons to heavy particles (neutrals and ions) in elastic collisions is very low (~ 10^{-4}) due to the difference

in mass and, given the relatively low electron densities, the gas temperature does not increase substantially. Electrons are energetic enough to break molecular bonds and cause the ionization of atoms and molecules, leading to reactions that would not otherwise occur at such low gas temperatures. This feature makes glow discharges useful for a variety of applications. Typical electron densities for glow discharges are $N_e \sim 10^9$–10^{10} cm^{-3}, which implies low ionization ratios $\sim 10^{-4}$–10^{-6}. Due to the relatively low gas temperature compared with the electron temperature, these types of discharges are considered cold plasmas.

Low pressure discharges are relevant in a variety of scientific and technological fields. PECVD has been used for thin film deposition and surface treatment since the early 1960's [9-11]. This technique has been widely used for semiconductor manufacturing [12] and in the development of efficient solar cells [13,14], and is also employed for the functionalization of surfaces with different applications [15,16]. The production and processing of nanoscale objects can be more efficient when using plasmas of different types, including low pressure discharges [17,18]. The conditions of the edges of fusion plasmas resemble those of glow discharges [19] so the latter can be used for laboratory studies in fusion research [20,21]. Low pressure plasmas are also of interest in the investigation of catalytic processes, such as the reaction between hydrogen and nitrogen to produce ammonia [22-24]. These types of discharges can also be used to conduct spectroscopic studies of ions and radicals [25,26], that is, very reactive transient species that are efficiently generated in cold plasmas and cannot be easily found under different conditions. Since low pressure discharges are cold plasmas, they can be used in applications involving thermally sensitive materials. Hydrogen is present in most of the gas mixtures employed in the applications mentioned in this paragraph.

Multiple types of geometry can be used to produce a dc glow discharge. The classic example is the planar electrode geometry, in which the anode and cathode are placed facing each other inside the vacuum vessel. This geometry allows for the easy identification of the different luminous and dark zones of the discharge described above. The interest of this thesis, however, lies in the hollow cathode configuration. In this type of discharge, the negative glow, where the majority of energetic electrons can be found, fills most of the volume, and the plasma is confined inside the cathode, which is usually cylindrical. The positive column is reduced to a small region close to the anode. There are multiple advantages to this configuration, such as a better confinement and homogeneity of the plasma, which in turn results in an easier diagnostic of the discharge. Hollow cathode discharges also present the lowest gas temperature of the different types of low pressure discharges, improving the spectral resolution, and the absence of electric field in the negative glow prevents Stark broadening. For that reason, hollow cathode discharges are commercially used as spectroscopic sources (hollow cathode lamps). They can be used

to obtain emission lines of different materials that are not easily vaporized, as they can be sputtered by the ions of the discharge if they are used as a coating for the cathode or directly as the cathode material [27]. This type of lamps can also be used to control the wavelength tuning of light sources, usually lasers, to a specific atomic transition by making use of the optogalvanic effect [28,29].

There are various advantages to using hollow cathode glow discharges for kinetic studies of mixtures of gases. Since the negative glow fills most of the volume of the reactor, energetic electrons are present in considerable amounts, and, subsequently, gas phase reactions occur in great numbers. These gas phase processes are limited to two body reactions, as the densities are too low for three body reactions to take place due to the low pressure. Furthermore, because of the low temperature of the heavy species, reactions with an energetic barrier are essentially absent from the discharge. This implies that neutral-neutral reactions are not likely to occur, barring specific cases usually involving metastable species. Due to all this, reactions between neutral species are fundamentally limited to heterogeneous processes occurring at the surfaces of the reactor. The chemistry in hollow cathode discharges is thus simplified, with electron driven processes (ionization, dissociation and excitation) taking place in the gas phase, along with ion-molecule reactions, and neutral chemistry being limited to the reactor walls. A disadvantage of this kind of setup, and low pressure glow discharges in general, is that the electron energy distribution might deviate from the maxwellian shape, as the high energy tail may either be depleted, since those electrons are responsible for most of the reactions in the plasma, or grow as a result of other processes such as secondary emission from the cathode. This uncertainty in the shape of the electron energy distribution function can introduce some complications in the kinetic modeling of the discharge.

The study of hollow cathode glow discharges with hydrogen content can be useful for the characterization of other types of media, provided they share some fundamental characteristics, as in the already mentioned edges of fusion plasmas. This is also the case of some extraterrestrial environments, such as the interstellar medium and planetary ionospheres. Molecular clouds, the regions where star formation occurs, are mainly composed by molecular hydrogen. In these environments, the degree of ionization is low, and only binary collisions take place due to the low pressure. As a result, ion-molecule reactions play an important role in the chemistry of the molecular cloud, and molecules are formed in heterogeneous reactions in the surface of dust grains [30,31]. These characteristics are shared with hollow cathode discharges, while the ionization mechanism, through cosmic rays, and the neutralization of ions, in collisions with electrons, are different. The interaction of hydrogenic ions with the different molecules present in the medium is of great importance in the chemistry of molecular clouds [32]. A somewhat similar situation is found in planetary atmospheres, where the chemistry of

hydrogenic ions is relevant in photoionization regions where hydrogen is present, such as the uppermost portions of giant planet atmospheres [33,34].

The aim of this work is to analyze the complex chemistry found in discharges of hydrogen with other simple gases, identify the main processes responsible for the observed concentrations of the different species, and establish, on the one hand, the role of heterogeneous processes in the production of secondary stable molecules, and, on the other hand, the role of protonated ions in the positive ion chemistry of the discharges, evaluating the effect of the proton affinity of their parent molecules. To fulfill these objectives, plasmas of H_2 + Ar, H_2 + N_2, H_2 + O_2, and H_2 + N_2 + O_2 and have been produced in a low pressure hollow cathode reactor, at pressures between 0.8 and 8 Pa and with different mixture ratios. Concentrations for the neutral stable species and positive ions have been obtained by quadrupole mass spectrometry. A double Langmuir probe has been employed to obtain the electron temperature and density of the plasmas. Complementary to the experimental characterization of the discharges, zero order kinetic models have been developed in order to identify the main processes behind the chemistry of the different mixtures. The comparison between experimental and theoretical data allows the analysis of the various physico-chemical processes occurring in the plasma, characterizing their relevance and variation when the conditions of the discharge are changed.

The work has been divided into the following chapters:

- In Chapter 2, the experimental setup employed in this work is presented, with a detailed description of the different diagnostic techniques.

- In Chapter 3, the theoretical modeling of the plasma is described, illustrating the types of processes considered and including the reactions tables used for the different mixtures.

- In Chapters 4, 5 and 6, the results obtained for the H_2 + Ar, H_2 + N_2, and H_2 + O_2 (including H_2 + N_2 + O_2) mixtures are respectively shown. A description of the state of the art is given at the beginning of the chapter for each of the different mixtures.

- In Chapter 7, an overview of the results of the different studies and general conclusions are given, and future perspectives are commented on. Chapter 8 contains the appendices, including the different programs used in this work.

Chapter 2.

Experimental setup

The plasmas studied in this work have been generated in an electric discharge reactor in hollow cathode configuration built in the laboratory. In this setup, with the reactor walls acting as the cathode and the anode located inside, the negative column is uniform and stable, and it fills the whole volume of the vessel with the exception of the sheath region close to the walls. A diagram of the experimental setup used in this work can be found in Figure 2.1, and a photograph is shown in Figure 2.2. The reactor consists of a grounded cylindrical stainless steel vessel (10 cm diameter, 34 cm length) that acts as the cathode, set with its axis in a vertical position. The chamber possesses a total of eight DN 40 KF flanges on its sides, which are used to connect the gas inlet, pressure gauges, observation windows, Langmuir probes, electron gun and the anode of the discharge. The anode consists of a stainless steel cylinder (1 cm diameter, 7 cm length) and is placed roughly in the middle of the chamber. A glass tube surrounding the anode in the narrow zone of its connecting flange prevents the establishment of a secondary glow in this region. The exact placement of the anode does not have an effect in the homogeneity of the plasma glow, as can be seen in the spatially resolved measurements of the electron density performed in [35] in the same setup.

The lower end of the vessel is connected to a vacuum system through a gate valve. This vacuum system consists of a turbomolecular pump (Leybold Turbovac TMP 361, 300 l s^{-1}) in series with a dry pump (Leybold Ecodry M15, 15 m^3 h^{-1}) that provides the fore-vacuum. This allows obtaining a background pressure of $\sim 10^{-4}$ Pa (10^{-6} mbar) in the reactor. In the upper end of the reactor a differentially pumped chamber is connected through a $\sim$ 100 μm diameter diaphragm. The two quadrupole mass spectrometers used (Balzers Prisma QMS 200, and Balzers PPM 421) are installed in this chamber, which is pumped by means of a vacuum system comprised of a turbomolecular pump (Pfeiffer

Vacuum D-35614 Asslar TMU 261P with a TC 600 electronic drive unit, 150 l s^{-1}) backed by a dry pump (Pfeiffer Vacuum XtraDry 150-2, 7.5 m^3 h^{-1}). The background pressure obtained for this chamber is in the 10^{-5} Pa range.

Different pressure gauges are used to monitor the pressure in various parts of the experimental setup. The pressure inside the reactor during plasma operation and diagnostics is determined with a capacitance manometer (Leybold Capacitron CTR90), calibrated for absolute pressures between 10^{-2} and 100 Pa. Auxiliary pressure gauges are used to control the pressure in the whole range of pressures available. These are a Pirani (Pfeiffer Vacuum TPR 010) and a Penning manometer (Pfeiffer Vacuum IKR 050). For the differentially pumped chamber in which the mass spectrometers are located, a combination of Pirani (10^5–10^{-1} Pa) and Bayard-Alpert (10^{-1}– 10^{-6} Pa) gauges in a single head (Leybold Ionivac ITR90) is employed.

The gas inlet is connected to one of the 40 KF flanges on the side of the reactor chamber. The different gases have their own lines with a manometer, two ball valves and a needle valve that allow the regulation of the gas flow. In order to be able to adjust the discharge pressure in the desired range and to prevent damage to the turbomolecular pump by working above its advisable upper pressure limit (~ 1 Pa), the gate valve before the reactor pumping system is throttled and its position is kept fixed during the experiments, using the aforementioned needle valves to balance the gas flow and obtain the desired pressure in the discharge chamber.

Residence times for each gas inside the reactor were measured by abruptly closing the gas inlet with the ball valve and monitoring the time evolution of the pressure through the capacitance manometer by means of a digital oscilloscope. Values between 0.5 and 1 s are typically obtained, corresponding to 2–40 sccm flows for the pressures considered.

In order to maintain the discharge, a direct current (DC) high voltage power supply built in the laboratory (JR81) is employed. This voltage source is adjustable and provides up to 0.2 A and 2000 V. A 100 Ω ballast resistor is connected between the power supply and the anode, and the system is grounded through the cathode. Discharge currents of 150 mA were maintained during the experiments, with supplied voltages depending on the precursor gasses, pressure, and mixture ratio. For H_2 + Ar mixtures, they were in the 300–400 V range, 300–450 V for mixtures with N_2, and 500–550 V for H_2 + O_2 mixtures.

At the low plasma pressures studied in this work (~ 1–10 Pa), the discharge cannot be ignited by using only the power supply, due to the breakdown voltage being higher than the supplied voltage, as predicted by Paschen's Law [7]. To overcome this, an electron gun built in the laboratory (JR121) is used. It consists of a small spiral formed by a tungsten filament with 0.13 mm diameter and 1–2 cm length connected to a floating

current source of up to 3 A, which in turn is connected to a negative high voltage of up to –2000 V. When the filament is heated by Joule effect with a current slightly higher than 2 A, it becomes incandescent (with an intense white-yellowish emission) and thermionic emission of electrons occurs. These electrons are repelled by the negative voltage and flow into the plasma, beginning the ionization processes necessary for the plasma ignition. Once the discharge has been ignited, the power supply is enough to maintain it and the electron gun is no longer needed, so it is turned off.

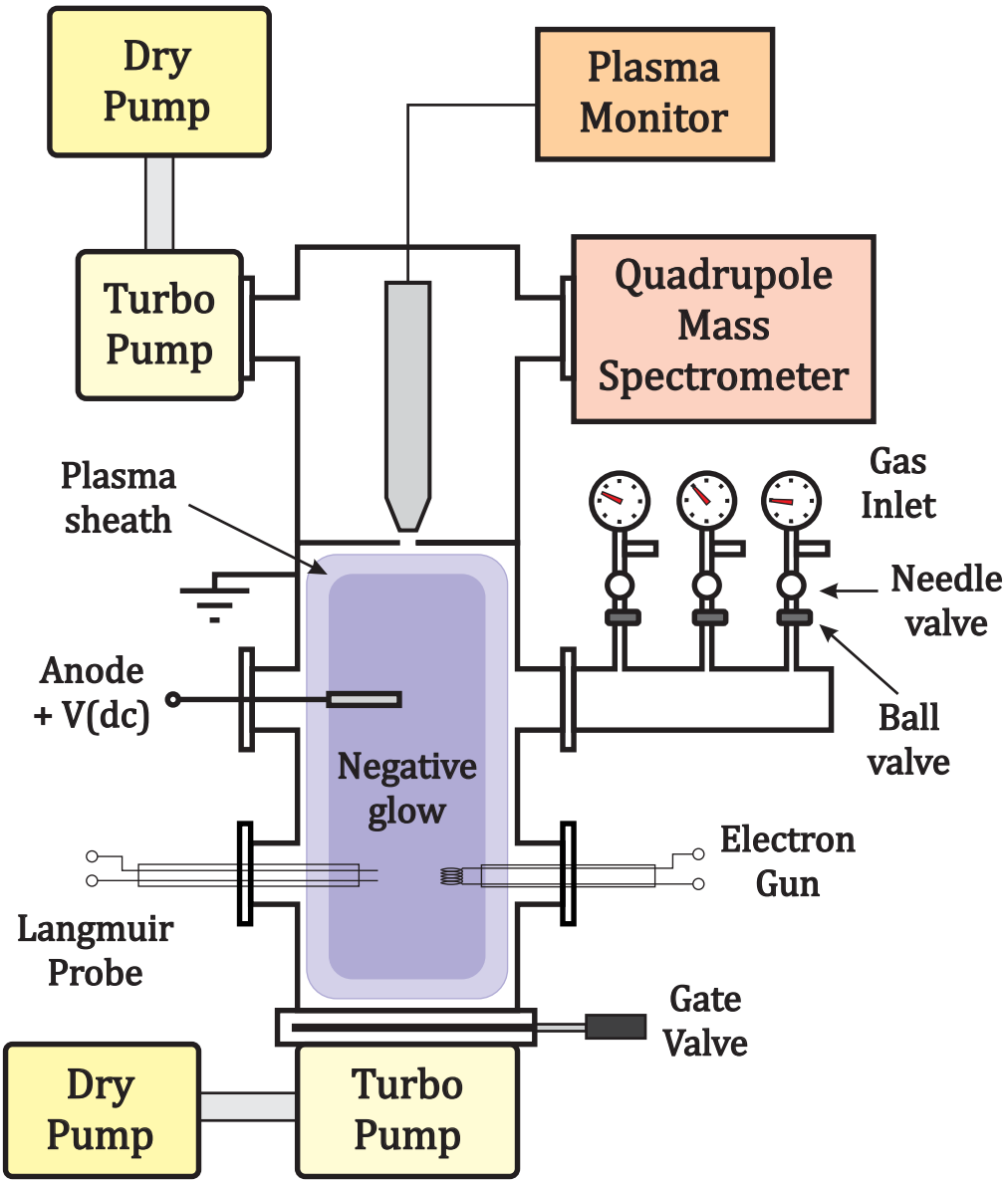

Figure 2.1. Diagram of the experimental setup.

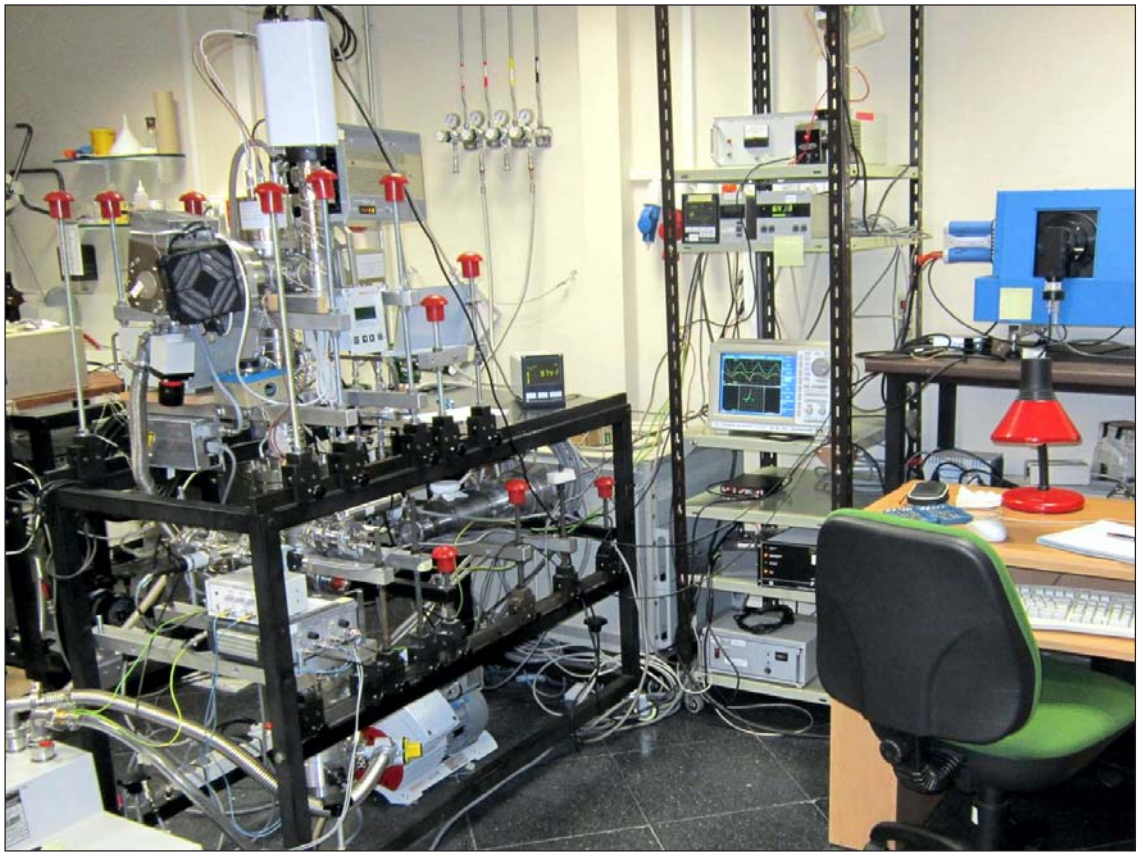

Figure 2.2. Photograph of the experimental setup employed in this work.

2.1 Diagnostics

Characterization of the plasma properties is done by means of different experimental techniques. A double Langmuir probe is used to determine the electron temperature and the charge density, the concentrations of the neutral and ionic species are measured by quadrupole mass spectrometry and the vibrational and rotational temperatures of the gas are determined using optical spectroscopy. A detailed description of the techniques employed is given below.

2.1.1 Double Langmuir probe

A Langmuir probe is a device which is used to determine plasma parameters like electron temperatures, charge densities and plasma potentials. It consists of a small metallic electrode, which is immersed into the plasma and connected to a potential source. Generally the source is connected to a reference electrode, which in many cases serves

simultaneously as the cathode or the anode of the discharge. In a Langmuir probe experiment a so-called I-V characteristic is measured, i.e. the current density flowing to the surface of the probe within the plasma as a function of the voltage drop between the electrode and the reference. The measured currents and potentials in this system allow the determination of the physical properties of the plasma mentioned above. There are different types of Langmuir probes. In this work, the double probe configuration has been employed.

The double probe system consists of two parallel electrodes of similar shape and size, which are connected to a floating variable potential source reversible in polarity. If the two electrodes have the same dimensions, the measurement yields a symmetric characteristic [36]. The double probe configuration does not need connection to a reference electrode; instead, the potential difference between the two probes is used to obtain the I-V curve. A diagram of the double Langmuir probe is presented in Figure 2.3.

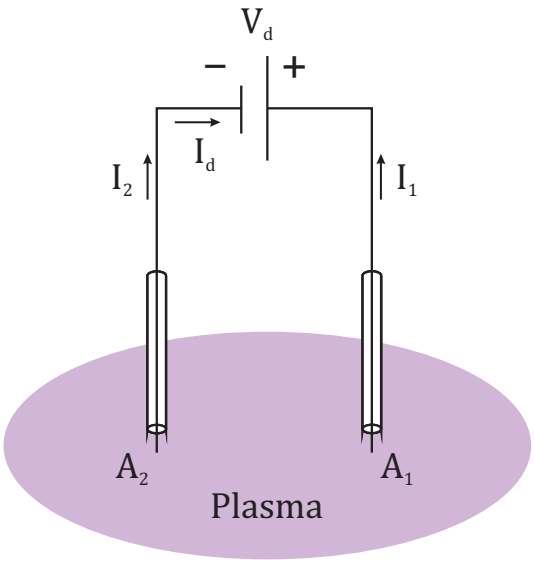

Figure 2.3. Schematic of the double Langmuir probe.

The double Langmuir probe used in the experiments was designed and built in the laboratory, including the electronic circuits. The two electrodes are tungsten filaments of 0.13 mm diameter, and are inserted in glass capillaries so that only a small length, between 5 and 8 mm depending on the probe used, is exposed to the plasma. The separation between the filaments is about 5 mm. The probe is placed such that the electrodes are close to the center of the reactor. The floating electrodes are connected to a dual ramp generator (JR101), which applies a sawtooth voltage between ~ –100 and +100 V, with a period of 3 s. The current and voltage signals pass through an optically isolated

double amplifier (JR163) and are displayed in a digital oscilloscope (Yokogawa DL708E) working in X-Y mode, where several cycles can be averaged if necessary to increase the signal/noise ratio.

An extensive description of the fundamentals of double Langmuir probe measurements can be found in [8,36,37], and will be briefly described here. The typical characteristic curve obtained in the discharges studied is shown in Figure 2.4.

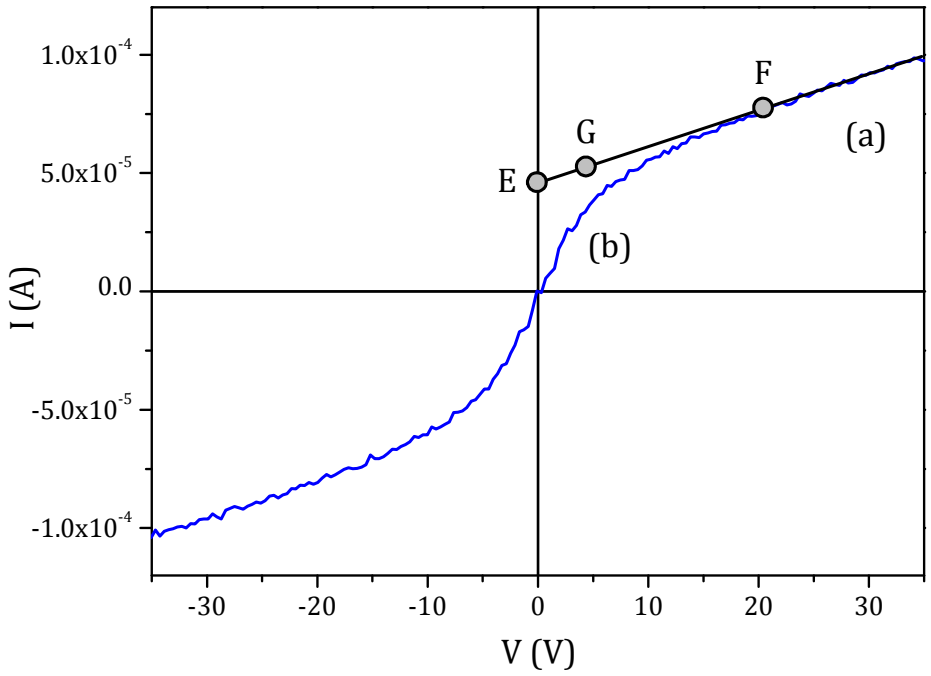

Figure 2.4. Typical double Langmuir probe characteristic.

There are two different regions in the curve. Region (a) is the ion saturation region, in which the potential of one of the electrodes (A_2) is very negative with respect to the other (A_1), so mainly positive ions flow to the former. In order to balance this current, an equal electron current flows to A_1. Taking a pair of I-V values in this region (the saturation voltage, V_{sat}, and the saturation current, I_{sat}), the charge density of the plasma $N_c \approx N_e \approx N_i$ can be obtained from:

$$N_c(\mathrm{cm}^{-3}) = 1.81\times10^{13}\,\frac{\sqrt{M^+(\mathrm{amu})}}{S(\mathrm{cm}^2)}\,\frac{I_{sat}(\mathrm{A})}{\sqrt{V_{sat}(\mathrm{V})}} \qquad (2.1)$$

Where M^+ is the ionic mass and S is the total surface of the probe. In the plasmas studied, more than one ionic species is present, so the value for M^+ is calculated from the

average of the ion masses weighted by their relative abundancies, which are obtained from the mass spectrum.

In region (b), the difference in voltage between the two electrodes is lower, and electrons contribute to the current of electrode A_2. Given that the probe is floating, the current equilibrium dictates that [8]:

$$I_d = I_{i_1} - I_{e_1} = I_{e_2} - I_{i_2} \tag{2.2}$$

Where I_d is the current in the closed circuit of the probe, I_i are the ion currents and I_e are the electron currents. Assuming a Maxwellian distribution for the energy of the electrons, the electron current flowing to each electrode is given by:

$$I_{e_i} = \frac{1}{4} S_i e N_e \sqrt{\frac{2k_B T_e}{2\pi m_e}} \exp\left(\frac{eV_i}{k_B T_e}\right) \tag{2.3}$$

Where S_i is the area of each electrode in m^2, e is the electron charge in coulombs, k_B is the Boltzmann constant, T_e is the electron temperature in K, m_e is the electron mass in kg, and V_i is the potential of each electrode in volts.

Using the expressions for I_{e1} and I_{e2} from Eqs. (2.2) and (2.3), assuming $S_1 = S_2$ and dividing I_{e1} by I_{e2} :

$$\frac{I_{e_1}}{I_{e_2}} = \frac{I_{i_1} - I_d}{I_{i_2} + I_d} = \exp\left(\frac{eV_d}{k_B T_e}\right) \tag{2.4}$$

With $V_d = V_1 - V_2$. Differentiating this expression with respect to V_d and taking into account that close to $V_d = 0$ ion currents do not change much compared to electron currents, the following analytical expression can be obtained for the electron temperature [36]:

$$T_e = -\frac{e}{k_B}\left[\frac{I_{e_1} I_{e_2}}{I_{i_1} + I_{i_2}} \frac{dV_d}{dI_d}\right]_{V_d=0} \tag{2.5}$$

A better approximation to the value of T_e (in eV, with 1 eV = 11605 K) can be obtained using the expression deduced by Johnson and Malter [38]:

$$T_e(\text{eV}) = \frac{I_G(\text{A})}{2}\left[\frac{dV_d(\text{V})}{dI_d(\text{A})}\right]_{V_d=0} \tag{2.6}$$

Where $[dV_d / dI_d]_{V_d=0}$ is the so-called equivalent resistance and I_G is the value of the current at point G in the graph. This point is found using the linear extrapolation of the ion

saturation region (E–F), where E is the intersection with the vertical axis and F is the point of separation from the characteristic. Point G is defined such that the ratio between the distances EG and GF is 1:4.

The presence of negative ions in the discharge can modify the shape of the Langmuir probe characteristic, leading to an error in the determination of the electron temperature. However, this effect is only relevant when the negative ion density is very close (> 99 %) to the charge density of the discharge [39], which does not occur in the present experiments.

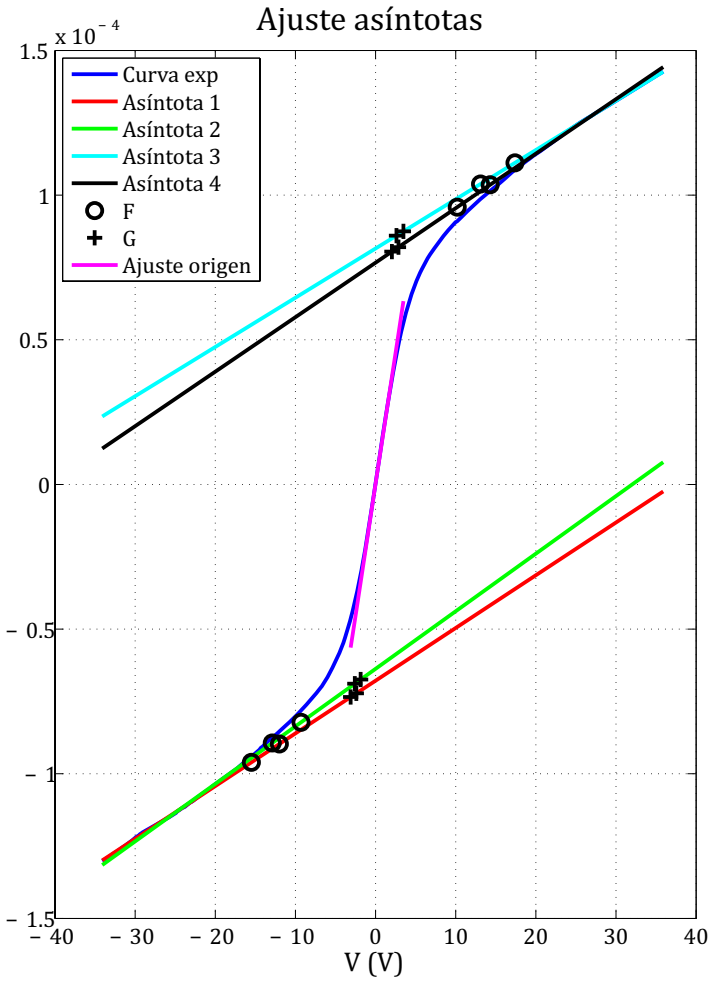

Figure 2.5. Example output of the MATLAB program used to analyze the double Langmuir probe characteristics.

A MATLAB program has been developed during the course of this thesis by its author to easily obtain the charge densities and electron temperatures from the data

acquired with the double Langmuir probe. A detailed description of the program and the full code can be found in Appendix A.1. The program averages the different (I,V) cycles obtained in a single measurement with the Langmuir probe to produce a single curve, smooths it, and obtains values for the parameters V_{sat}, I_{sat}, I_G and $[dV_d / dI_d]_{V_d=0}$, using them to calculate N_e and T_e. An example of an output graph from the program is displayed in Figure 2.5., showing two different linear fits of the ion saturation region and four different F and G points calculated for each branch of the characteristic.

2.1.2 Mass spectrometry

Mass spectrometry is one of the most used techniques in plasma diagnostics. It is based on the generation of positive ions from the neutral species of the plasma and their subsequent separation depending on their charge/mass ratio. Mass spectrometers are sensitive instruments and are able to provide absolute values of the concentration of the species with adequate calibration.

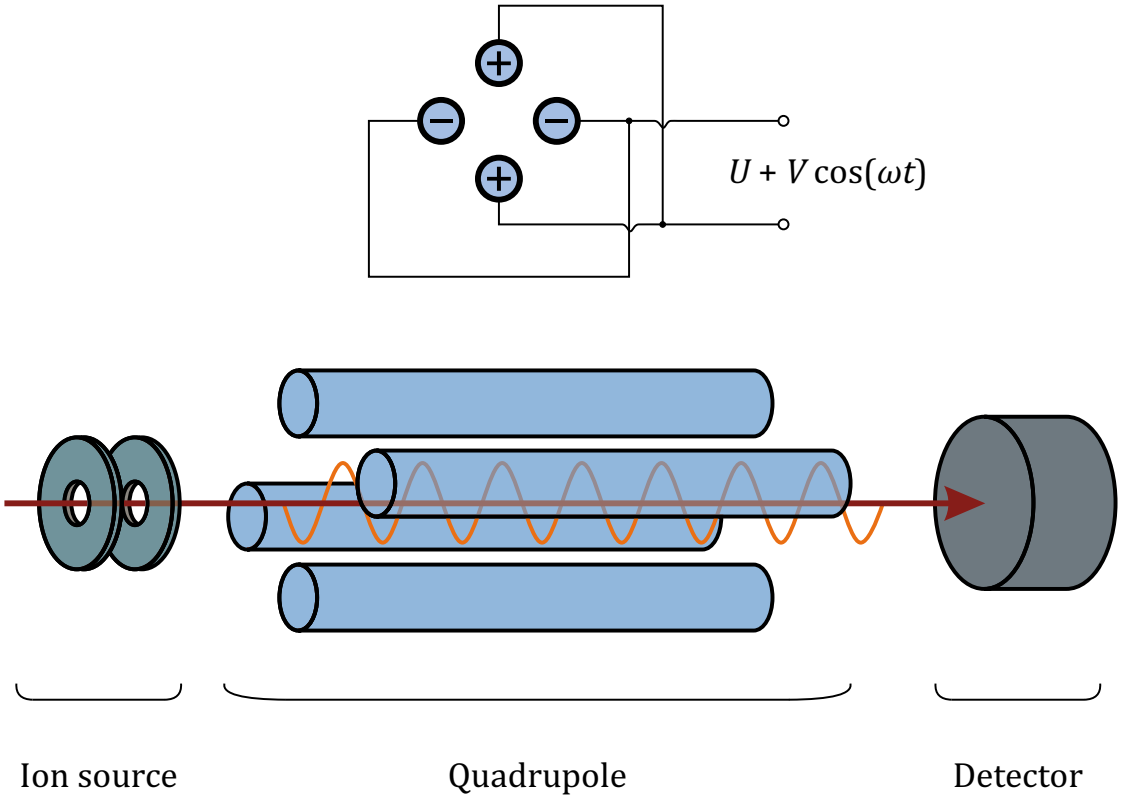

Figure 2.6. The different parts of a quadrupole mass spectrometer. The electrical diagram for the quadrupole rods is displayed above. The orange curve represents the trajectory of an ion hitting the detector.

There are different types of mass spectrometers, depending on the filtering mechanism used to separate the species. In this work, the two mass spectrometers employed use quadrupole mass filters. A diagram of a typical quadrupole mass spectrometer can be seen in Figure 2.6.

A measurement using quadrupole mass spectrometry usually consists of four basic stages. First, neutral species are ionized in the so-called ionizer. This is usually achieved by electron bombardment, using an incandescent filament to liberate the electrons that are then accelerated by a potential of several tens of volts, where the ionization efficiency of most species is high enough. Next, the ions are extracted from the ionizer and accelerated by means of a set of electrostatic lenses. These two stages comprise the ion source.

Ions then enter the quadrupole, which consists of four parallel equally spaced cylinders. A combination of constant and radiofrequency electric fields, whose amplitudes can be varied with time, is applied to these rods, causing the ions passing through them to describe different trajectories depending on their charge/mass ratio and on the applied fields, in such a way that only those ions with a given charge/mass ratio are able to reach the detector, placed in the central axis of the rods at the end of the quadrupole. Of the different types of detectors available, both spectrometers employed in this work are equipped with Faraday cups, which directly collect the ion current, and electron multipliers, where the ion current is transformed into an amplified electron current by secondary emission effect in a series of collisions with the different regions of the detector surface set to different electric potentials. Electron multipliers were the preferred detectors for the experiments described in this work.

2.1.2.1 Mass spectrometry of neutrals

A Balzers Prisma QMS 200 quadrupole mass spectrometer has been employed for the detection of neutral species. It comprises the analyzer (QMA 200) and external elements for power management and control. The analyzer is fitted to the vacuum chamber and consists of an open ion source with two tungsten filaments, the mass filter, and the two alternative detectors: a Faraday cup and a channel electron multiplier (CEM). The mass filter is formed by four stainless steel bars of 6 mm diameter and 10 cm length mounted on a stable structure. The CEM is composed of a curved glass tube coated inside with a semiconducting oxide. Electrons collide with the walls along the tube producing the secondary emission and amplifying the signal. The external elements, located outside the vacuum chamber, include the control unit (QMS 200), the mass filter electronics (QME 200) with its corresponding power source (SP 200), the DC high voltage source for the CEM (which is polarized to 900 V) and the preamplifiers for the Faraday cup (EP 200) and the electron multiplier (CP 400).

Mass/charge ratios between 1 and 100 amu can be sampled with the spectrometer, with a maximum mass resolution of 0.5 amu. The controlling software (Quadstar 422) allows operation in two different modes. The Scan mode registers the complete spectrum in a particular range of masses, with configurable resolution and sampling time. The MID (Multiple Ion Detect) mode allows to select up to 64 different masses to detect and follow their evolution, choosing the sampling time for each of them.

Calibration of the sensitivities for the different mass/charge ratios is performed in a different way depending on whether the species is a precursor gas or not. For precursor gases, the process is relatively simple. Different pressures of the studied gas are introduced in the reactor and measured with the absolute capacitance manometer, and, for each of them, the corresponding counts in the spectrometer are acquired. These pairs of values can be fitted to a straight line with a fixed intercept of zero, as shown in Figure 2.7, yielding the calibration for that species.

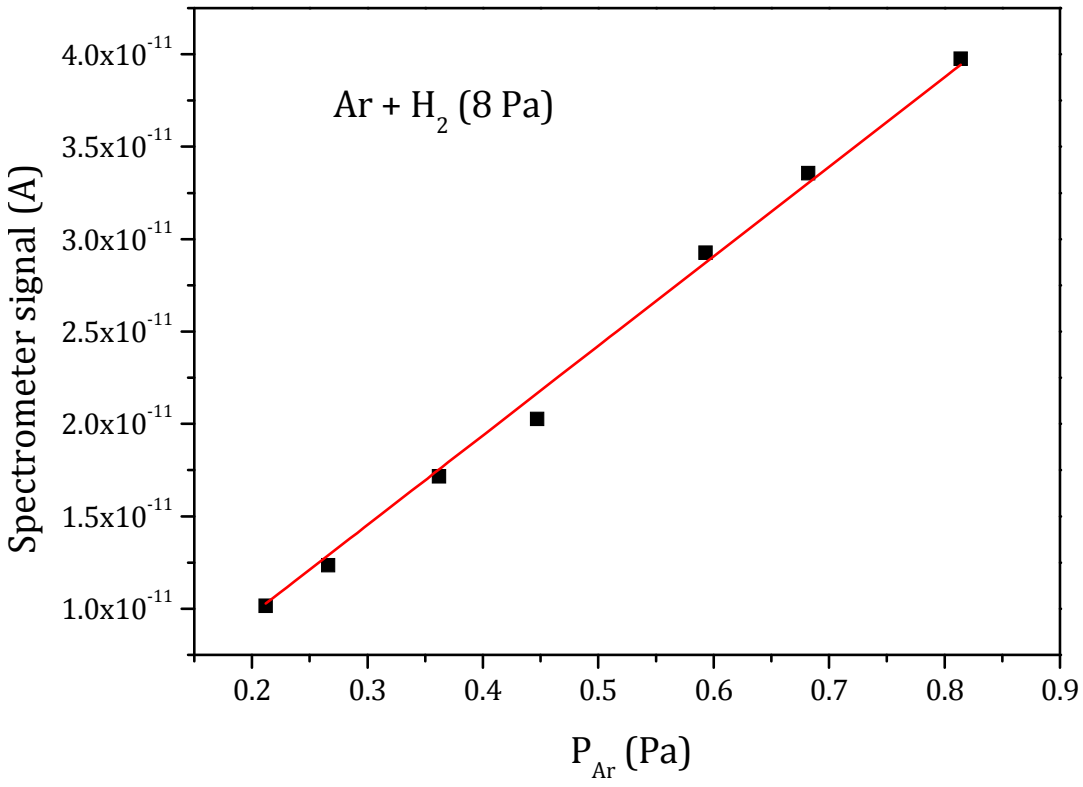

Figure 2.7. Calibration for Ar sensitivity in a mixture with 8 Pa of H_2.

It has been found empirically that the presence of significant amounts of H_2 in the reactor can alter the relative sensitivity of the quadrupole mass spectrometer to the rest of the species. It might be due to a change in the electron emission coefficient of the filament

of the ionizer due to some kind of reaction with this species. To account for that, calibrations have been carried out filling the chamber with different background pressures of H_2 and then proceeding with the steps described before, since H_2 is one of the main components in all of the gas mixtures studied in this work.

When the species is not a precursor gas, the calibration process is slightly more complex. In that case, a noble gas with a mass close to that of the studied species is chosen. In the experiments presented in this work, this type of calibration has been performed for NH_3 and H_2O, so in both cases Ne was the noble gas employed, using the signal of mass 20 (^{20}Ne). The calibration is performed for this noble gas, obtaining the proportionality constant between the spectrometer signal and the reactor pressure, β (Pa/A). Assuming that the difference in masses does not affect the sensitivity significantly, the calibration for the studied species X can be obtained from:

$$\beta_X = \beta_{Ne} \frac{\sigma_{Ne}^{ion}\, a(^{20}\mathrm{Ne})}{\sigma_X^{ion}} \tag{2.7}$$

Where σ^{ion} is the electron impact ionization cross section for the species in the subscript at the energy of the electrons in the spectrometer ionizer, which is 100 eV. The natural isotopic abundance of ^{20}Ne, $a(^{20}\mathrm{Ne}) = 0.905$, is also taken into account.

2.1.2.2 Mass spectrometry of ions

Positive ion abundances have been measured by means of a Balzers PPM 421 plasma monitor. It consists of an ion focusing lens system, ITRO (Ionic Transfer Optical System), an ion source allowing its alternative use as a neutral species detector, a cylindrical capacitor ion energy analyzer, CMA (Cylindrical Mirror Analyzer), a QMA 400 mass filter composed of 4 molybdenum bars of 8 mm diameter and 20 cm length mounted on two ceramic brackets, and two alternative detectors: a Faraday cup, and an electron multiplier (SEM 217 with 17 dynodes) which was preferred for the measurements. The spectral range for this instrument is 1–340 amu, and the resolution can be regulated by tweaking the potentials of the focusing system, obtaining values below 0.5 amu. Auxiliary units include the power source for the ion source (IS 420), the energy analyzer electronics (PA 421), the radiofrequency source QMH400-5, a preamplifier for the Faraday cup (EP 112) and the SEM (CP 400), the DC high voltage source for the SEM, which has been usually operated between 2800 and 3200 V and a control unit for the quadrupole filter QMG 421. The same Quadstar software described for the QMS 200 is used with this instrument, and provides some extra operation modes. For the measurements performed in this work, the M-MID, E-cycled option is selected. In this mode, the user can input a list of masses to sample and an energy range, and the spectrometer outputs the counts for each mass against the energy of the ion. The instrument allows measurements for energies

between 1 and 512 eV. A different mode, E-fixed, M-cycled, has also been employed. In this case, a selected range of masses is sampled for a defined ion energy.

Ionic species are sampled through the grounded ~ 100 μm diaphragm connecting the two vacuum chambers. Ions in the plasma are accelerated through the sheath towards the grounded reactor walls by a potential close to the anode-cathode voltage. The entrance of the ion focusing system is placed directly behind the diaphragm, in order to collect as many ions as possible.

Calibration of the relative sensitivity of the instrument for the different ion masses is performed using the noble gases He, Ne and Ar in the neutral detection mode (i.e. with the electron impact ionizer turned on), similarly to [40]. The signal in the plasma monitor is compared to the pressure in the PPM chamber, measured with the Bayard-Alpert manometer. This is done due to the similarity between the two instruments, as the Bayard-Alpert manometer uses a hot cathode ionizer (with an accelerating potential of 100 V) and an ion collector to measure the pressure in the chamber. The transmission T of the species i is obtained as:

$$T_i \propto \frac{f_i \, C_i^{PPM}}{P_i^{BA} \, a_i \, \sigma_i^{ion}} \tag{2.8}$$

Where C^{PPM} is the signal measured in the spectrometer, P^{BA} is the pressure read in the Bayard-Alpert manometer, f is a correction coefficient for the Bayard-Alpert measurements, a is the natural isotopic abundance of the mass studied, and σ^{ion} is the electron impact ionization cross section at 70 eV, which is the energy of the electrons in the PPM ionizer. Coefficient f is related to the ionization cross section of the gas by the electrons of the hot cathode, and can be found in tables provided by the manufacturer or calculated from the cross section values. The transmission obtained for the different noble gasses can be represented as a function of the mass, as shown in Figure 2.8. In order to extrapolate for the rest of masses, these points can be fitted to a curve of the form $T = Am^B$, where coefficient B is the relevant parameter, giving the dependence with the mass. The value of B depends on the voltage applied to the SEM. For a voltage of 3200 V, $B \sim -0.5$ is obtained.

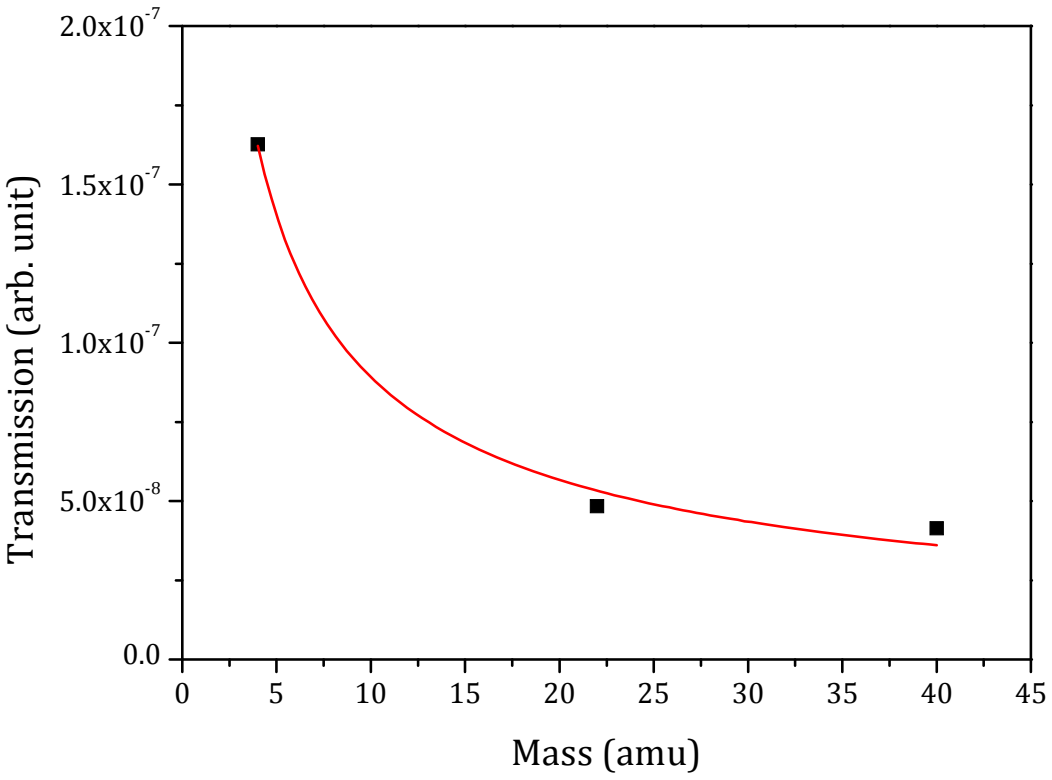

Figure 2.8. Transmission of the plasma monitor as a function of the mass.

A typical PPM measurement consists of an energy spectrum for each of the ion mass/charge ratios relevant to the experiment. These energy distributions have a narrow peak corresponding to the plasma potential, with a low energy tail that is usually negligible except in cases where collisions with molecules in the sheath have high cross sections [41]. An example of the ion energy distributions measured with the PPM can be seen in Figure 2.9.

The relative ion fluxes for each mass are determined by integrating their respective ion energy distribution. In order to obtain the relative ion densities in the plasma, and taking into account that the velocity of an ion is inversely proportional to the square root if its mass, these ion fluxes are multiplied by the square root of their mass/charge ratio and divided by their relative transmission. Absolute values for the concentrations can then be obtained by normalizing to the charge density measured with the Langmuir probe.

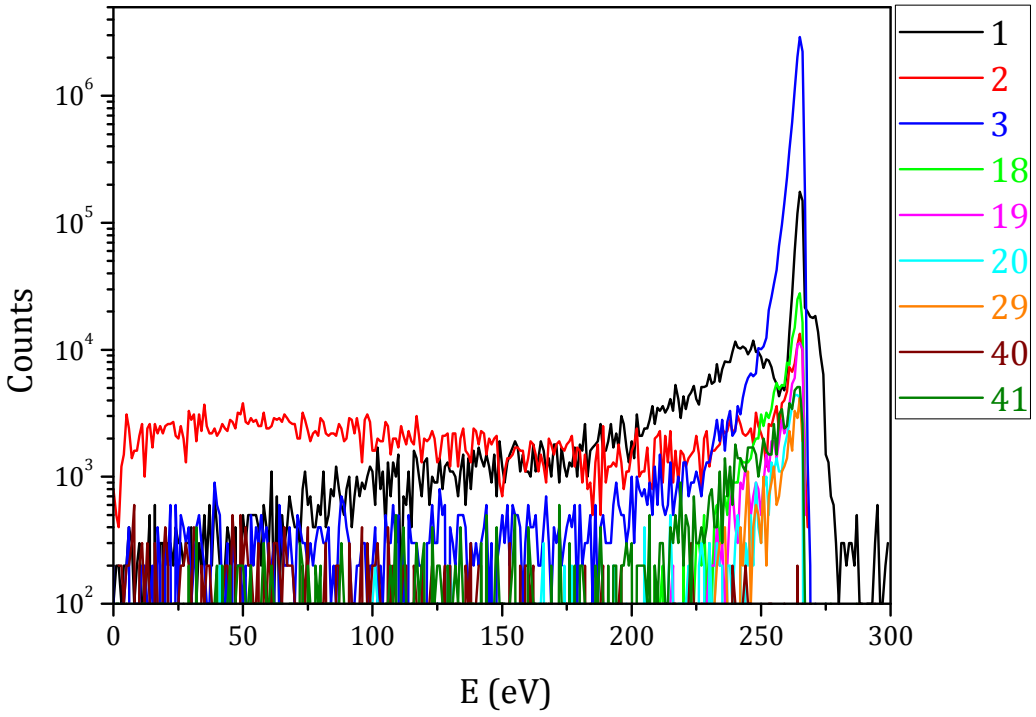

Figure 2.9. Energy distributions obtained with the plasma monitor for the different ions in a H_2 + Ar plasma at 8 Pa.

Even though the instrument allows the measurement of negative ion abundances, the sampling of these species in glow discharges presents some serious difficulties, since negative ions are confined to the glow due to the positive potential of the plasma with respect to all surfaces [42,43]. Due to this, negative ion abundances have not been experimentally determined in this work.

2.1.3 Optical spectroscopy

The rotational, translational and vibrational temperatures of the gas are important parameters that influence the chemistry of the discharge, and can be determined through the analysis of the emission lines from the plasma.

An optical fiber is placed at the observation window, and is connected to a Jobin Yvon-Horiba FHR1000 dispersive Czerny-Turner spectrometer to record the emission spectra. The focal distance of the spectrometer is 1 m, and a 1800 mm^{-1} diffraction grating is employed. Both a photomultiplier and a CCD camera (with a pixel width of 26 μm) can

be used as detectors, with the latter being preferred for this kind of measurements due to the faster acquisition times. With a slit width of 24 μm, the instrumental line width for this configuration was 0.020 nm, as determined from the measurements of the Hg line at 546.07 nm from a fluorescent tube.

The rotational temperatures of the hydrogen molecules are determined by generating a Boltzmann plot using the Q-branch line intensities for a fixed vibrational level, as described in [44]. The rotational temperature of the ground level is often assumed to coincide with the translational temperature [45], providing an estimation of the gas temperature T_g. Typical values of the gas temperature in the experimental setup used are around 400 K [46].

The vibrational temperatures of H_2 are obtained using a collisional-radiative model based on [47] (not presented in this work), generating a synthetic spectrum to fit the intensities of the Q-branch band heads. This type of experimental measurements and analysis has been employed in the same experimental setup [46] and in a different plasma reactor [48] in the laboratory.

Chapter 3.

Plasma modeling

A great variety of physical and chemical processes involving neutral and charged species occur in plasmas. Plasma modeling is a helpful tool to characterize these processes and establish their relevance in the plasma kinetics. The objective of the kinetic models elaborated in this work is the determination of the fundamental processes responsible for the chemistry of the different mixtures studied.

The main kinetic processes that take place in cold plasmas are electron impact dissociation, excitation to metastable states and ionization, collisional quenching, gas phase reactions between neutrals (usually including radicals or excited species), ion-molecule reactions, and heterogeneous processes. Only the most relevant processes are included in the kinetic models to avoid complexity, excluding the reactions that do not have a noticeable influence in the final results, due to their low rate coefficients or because they involve very minor species. For that reason, reactions between two stable molecular species are not considered, given that they only become relevant at temperatures much higher than the ones in the plasmas studied in this work. Similarly, three body reactions are not included, as the probability of their occurrence at the pressures studied is very low. Electron impact excitation to radiative levels is also ignored, since deexcitation by spontaneous emission, responsible for the characteristic brightness of glow discharges, depopulates these levels quick enough to prevent their collisional energy transfer to other particles.

To further avoid complexity, only two distinct volumes, the plasma glow and the sheath, are considered in the discharge. In each of these volumes, concentrations of the different species are assumed to be uniform (i.e. no spatial distribution). The thickness of the sheath is estimated from spatially resolved measurements of the electron density in the setup [35] and from the ion energy distributions [41]. It depends on the discharge

parameters [8], so the plasma volume changes for the different conditions simulated. Neutral species are assumed to fill the whole volume of the reactor, so their concentrations are the same in both volumes, whereas charged species (electrons and ions) are considered negligible in the sheath, and are only present in the plasma glow. The latter is due to electrons and negative ions being repelled by the negative potential of the sheath with respect to the plasma, while positive ions are accelerated towards the wall by this potential and leave the sheath quickly, thus drastically decreasing their density in this volume.

The model consists of a set of coupled differential equations describing the time evolution of the concentrations of the different species due to the various physicochemical processes occurring in the plasma from the ignition of the discharge to the attainment of the steady state. The differential equation for a given species X takes the form:

$$\frac{d[X]}{dt} = \sum_i Q_i^P - \sum_j Q_j^D \tag{3.1}$$

Where [X] is the concentration of the species X, and Q^P and Q^D are the production and destruction terms respectively. Most of these terms are weighted by the ratio of the volume in which the process takes place (usually the glow) and the volume in which species X is found (glow or reactor). The exact form of each of these terms depends on the process considered.

In this context, a chemical reaction X + Y → XY is characterized by its rate coefficient k, so the dependence with time of the concentration of species XY can be written as:

$$\frac{d[XY]}{dt} = k[X][Y] \tag{3.2}$$

Electrons are treated differently from the heavy species in the plasma, as there is no differential equation for the electron density. The electroneutrality condition is imposed, meaning that the total concentration of positively charged species must be equal to the total concentration of negatively charged species. The value of this total concentration is the charge density, N_c, which is used as an input parameter for the model and thus it does not evolve with time. When negative ions are present, the electron density is obtained from:

$$N_e = N_c - N^- \tag{3.3}$$

Where N^- is the total negative ion density. When negative ions are not present in the discharge, the situation is much simpler and the electron density is constant throughout the simulation.

The electron energy distribution functions (EEDF) in the model are assumed to be Maxwellian. However, the electron energy distribution function is not known with precision in the plasmas studied, as there are mechanisms that can significantly affect the magnitude of the high energy tail of the distribution. On one hand, the tail can be depleted by inelastic and reactive collisions [49-51]. On the other hand, a small amount of non-thermal electrons resulting from secondary electron emission by the cathode, with energies that extend to that corresponding to the cathode-anode voltage, can also be present in the discharge [52,53]. However, previous works in the same reactor at comparable pressures [35,54,55] have shown that the Maxwellian assumption for the EEDF is not a bad approximation for the global kinetics.

There are however some instances in which the Maxwellian EEDF is not sufficient to explain some of the processes observed in the plasma. This is the case of the H_2 + Ar model, where the observed concentrations of Ar^{2+} cannot be justified with ionization by electrons with a Maxwellian EEDF at the measured T_e. To account for that, a small amount of high energy electrons are included in the model (see section 3.4.1 for more details).

A variety of parameters are used as inputs for the kinetic model. To characterize the gas composition and flow, the experimental values for precursor fractions, pressure and residence time are employed. The geometry of the reactor is described through the radius, surface and volume. Values for the electron density and the electron temperature are used as input but, due to their crucial influence in the chemistry of the discharge, they are adjusted to better fit the observed concentrations of the different species and thus they often differ slightly from the ones obtained experimentally. These adjusted values are commonly within the experimental errors.

The use of these last two parameters as input results in a model that is not self-consistent. In principle, it would be possible to calculate the electron energy distribution and density by solving the Boltzmann equation, provided that the rate coefficients for all processes involving electrons (ionizations and dissociations, diffusion to the anode and walls, etc.) are known. In a less complex way, the electron density alone could be obtained by solving a differential equation including these processes, and using the T_e value as a model input. Those two methods would result in a more realistic simulation of the discharge and, in the first case, of the electron energy distribution, and it would be necessary if no experimental data were available. The approach employed in this work, where T_e and N_e measured values are used as input data, results in a simpler model, with reduced calculation times (of a few seconds), and allows for a very easy variation of the discharge parameters to observe their separate effect on the chemistry of the different mixtures, while ensuring that rate coefficients are calculated from the experimental T_e value.

The main mechanisms responsible for the variation of the concentrations of the different species in the models developed in this work are homogeneous reactions, heterogeneous reactions, and the changes induced by the precursor gas flow and the pumping of the reactor. The modeling of these types of processes is described in the following subsections.

3.1 Homogeneous reactions

Reactions in the gas phase can be fundamentally divided in two different categories: reactions with activation energy, which generally involve electrons, and reactions without activation energy. The modeling of these two types of reactions is different.

3.1.1 Reactions with activation energy

These types of reactions are dominated by repulsive forces, thus an energy barrier must be overcome to go from reactants to products. The main reactions of this type occurring in the plasma are electron impact dissociation and ionization.

The dependence of the rate coefficient k_e with the electron temperature T_e is often expressed by the empirical relationship for kinetic processes with a barrier, the Arrhenius formula [56]:

$$k_e = A\exp\left(-E_A/T_e\right) \tag{3.4}$$

Where A is a pre-exponential coefficient assumed to be independent or weakly dependent on the temperature, and E_A is the activation energy. In many cases, both of these values can be obtained from bibliographic sources.

The rate coefficient as a function of the electron temperature can also be obtained from the reaction cross section σ:

$$k_e = \left\langle \sigma_e(v)\, v \right\rangle \tag{3.5}$$

Where v is the electron velocity. If a Maxwellian electron energy distribution is assumed, eq. (3.5) becomes:

$$k_e = \int_0^\infty \sigma_e(\varepsilon)\left(\frac{8eT_e}{\pi m_e}\right)^{1/2}\frac{\varepsilon}{T_e}\exp\left(-\frac{\varepsilon}{T_e}\right)\frac{d\varepsilon}{T_e} \tag{3.6}$$

Where e is the electron charge, m_e is the electron mass, and ε is the kinetic energy of the electron. If $\sigma(\varepsilon)$ is known, k_e can be obtained from the integration. Usually, a numerical integration has to be performed, and the resulting data for $k_e(T_e)$ is then fitted to an Arrhenius-like expression:

$$k_e = A T_e^{\,B} \exp\left(-C/T_e\right) \tag{3.7}$$

The $\sigma(\varepsilon)$ distributions or the coefficients A, B and C can also be usually found in bibliographic sources.

3.1.2 Reactions without activation energy

Contrary to reactions with activation energy, barrierless reactions are not dominated by repulsion forces. Attractive forces, either strong (ion-electron and ion-ion neutralization) or weak (ion-molecule reactions), are involved.

Ion-electron neutralization processes have a weaker dependence on the electron temperature than the ionization and dissociation processes. In the discharges studied, due to the low concentrations of both species involved in the reaction, they do not balance out the charge formation by ionization reactions and are not the main neutralization mechanism for positive ions. Instead, positive ions are primarily neutralized by collisions with the walls of the reactor.

Ion-ion neutralization processes occur when there are positive and negative ions in the plasma. Similar to ion-electron neutralization, these processes are relatively unimportant in regard to positive ion neutralization due to the low relative concentration of both kinds of species, being less prominent than wall neutralization. However, negative ions are trapped in the plasma and do not diffuse to the walls, so this type of reaction is usually a relevant destruction mechanism in their chemistry.

In the case of ion-molecule reactions, and specifically a single-charged ion, the interaction potential is attractive and proportional to $(1/R^4)$, where R is the distance between the molecular nuclei, and it can be shown [57] that the corresponding cross section is given by:

$$\sigma_m(\varepsilon) = \pi\left(2e^2\alpha/\varepsilon\right)^{1/2} \tag{3.8}$$

Where α is the polarizability of the molecule. This expression is known as the Langevin form of the reaction cross section. As shown before, the rate coefficient can be obtained from:

$$k_m = \langle \sigma_m(v)\, v \rangle = \left(\frac{4\pi^2 e^2 \alpha}{\mu} \right)^{1/2} \tag{3.9}$$

Where μ is the reduced mass of the ion-molecule pair. As can be seen, in this case the rate coefficient does not depend on the temperature. The Langevin formula is usually taken as an upper bound for the value of the rate coefficient, and more precise values can be determined experimentally. Therefore, the values of the rate coefficients for this type of reactions used in this work have been obtained from bibliographic sources.

The lack of dependence on the temperature coupled with the relatively high values of the rate coefficients make ion-molecule reactions very important processes in cold plasmas, and their primary effect is the redistribution of the charge created by electron impact ionizations in new ionic species.

3.2 Heterogeneous reactions

3.2.1 Neutral species

Recombination at the reactor walls is the main source of new molecular species in the discharges presented in this work. Heterogeneous reactions can happen in one or various stages at the surface, and their characteristic times together with the diffusion time of the radicals to the wall are what determine the relevance of these processes.

The two alternative mechanisms responsible for wall recombination are Eley-Rideal (ER) and Langmuir-Hinshelwood (LH).

3.2.1.1 Eley-Rideal mechanism

In the Eley-Rideal mechanism, a radical coming from the gas phase reacts with another radical adsorbed at the surface to form a molecule and return to the gas phase. A scheme of the mechanism is shown in Figure 3.1. The process can be summarized as:

$$X + Y(s) \rightarrow XY$$

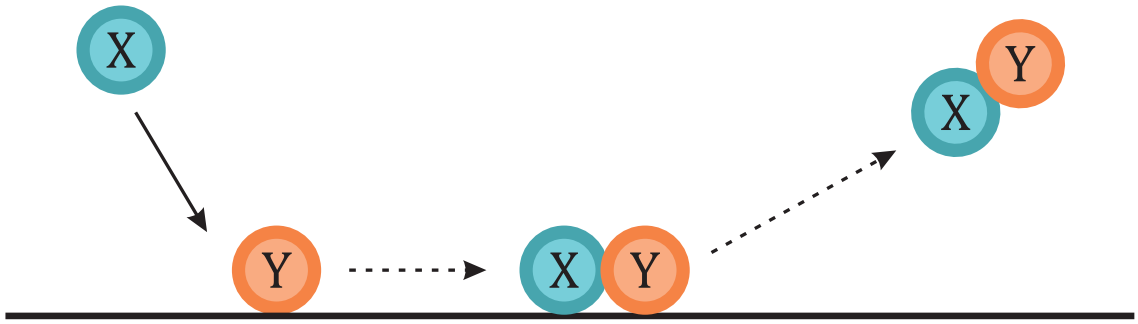

Figure 3.1. The Eley-Rideal mechanism.

The characteristic time for the process is the result of the addition of the characteristic time for the diffusion of radical X from the plasma to the wall and the characteristic time of the reaction occurring at the wall. The rate coefficient of the process is given by the inverse of the characteristic time.

As shown in [58], the characteristic time of diffusion can be calculated from:

$$\tau_{diff_X} = \frac{\Lambda^2}{D_X} \tag{3.10}$$

Where Λ is the characteristic dimension of the reactor and D_X is the diffusivity for the species X.

The characteristic time for the reaction at the wall can be expressed as [59]:

$$\tau_{ER_{XY}} = \frac{4V_R\left(1-\frac{\gamma_{ER_{XY}}}{2}\right)}{A_R\,\gamma_{ER_{XY}}\left\langle v_{t_X}\right\rangle} \tag{3.11}$$

Where V_R is the reactor volume, A_R is the reactor area, $\gamma_{ER_{XY}}$ is the recombination coefficient, and $\langle v_{t_X} \rangle$ is the mean thermal speed of the radical X. The rate coefficient is obtained as:

$$k_{ER_{XY}} = \frac{1}{S_T}\frac{1}{\tau_{diff_X}+\tau_{ER_{XY}}} \tag{3.12}$$

Where S_T is the surface saturation concentration, i.e. the total number of possible free sites per unit area. This parameter is usually estimated from the number of atoms of the surface material per area unit [60], and so a value of $S_T = 10^{15}$ cm^{-2} is assumed. The reaction rate thus depends on the partial surface coverage of species Y at the reactor walls.

Adsorptions of radicals to the wall, which are necessary for this mechanism to take place, are modeled following the same formulation. The adsorption of a radical to the surface can be expressed as:

$$X + F_s \rightarrow X(s)$$

Where F_s represents a free site in the surface. The probabilities of all radical adsorptions (sticking coefficients) are assumed to be equal to 1. In the plasmas studied in this work, the surface of the reactor is almost fully covered due to the high influx of radicals to the walls, creating a monolayer of adsorbed species.

Deexcitation of neutral species at the wall is also modeled based on these expressions.

$$X^* + \text{Wall} \rightarrow X$$

In this case, the reaction rate is independent of the concentration of species adsorbed at the wall or the number of free sites, and within this formulation it is essentially equivalent to a reaction of the excited species X^* with a species with a surface concentration of S_T.

3.2.1.2 Langmuir-Hinshelwood mechanism

The Langmuir-Hinshelwood mechanism differs from the Eley-Rideal one in the fact that both reacting species are adsorbed at the surface, which is shown schematically in Figure 3.2. The reaction can be written as:

$$X(s) + Y(s) \rightarrow XY$$

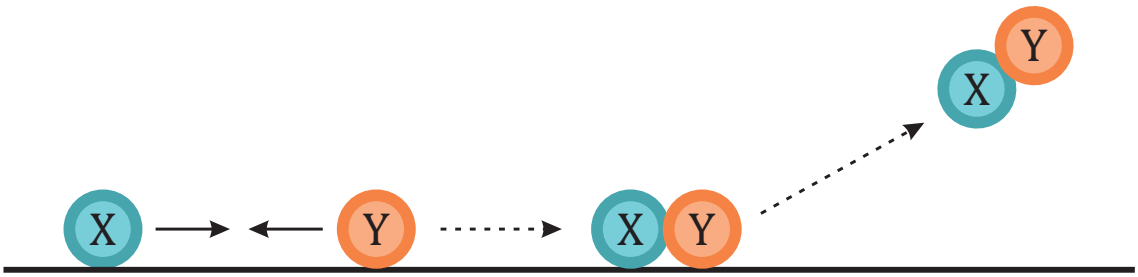

Figure 3.2. The Langmuir-Hinshelwood mechanism.

Following the formulation in [61], which considers the surface diffusion of the adsorbed species, the rate coefficient for the LH reaction is expressed as:

$$k_{LH} = \frac{A_R}{V_R}\frac{\nu}{4S_T}\exp\left(-\frac{E_d + E_A}{k_B T_w}\right) \tag{3.13}$$

Where E_d is the activation energy for diffusion, E_A is the activation energy for the chemical process, k_B is the Boltzmann constant and T_w is the temperature of the reactor walls (~ 300 K). The value of the surface diffusional jump frequency, ν, is assumed to be ~ 10^{13} s^{-1} [62].

3.2.2 Positive ions

Heterogeneous reactions are very relevant for the chemistry of the positive ions, as they are a far more efficient neutralization mechanism than gas phase reactions. In the model, wall neutralization is used as a means to preserve the quasi-neutrality of the discharge. Since the charge density of the plasma is constant, it then follows that:

$$\theta_{ion} = \theta_{neut(g)} + \theta_{neut(w)} \tag{3.14}$$

Where θ_{ion} represents the net production of charge in the plasma, and $\theta_{neut(g)}$ and $\theta_{neut(\mathrm{w})}$ represent the net destruction of charge in the gas phase and at the walls, respectively. In other words, the amount of ions generated in the plasma must be equal to the number of ions disappearing in gas phase reactions plus the ones neutralized at the walls. The quantities θ_{ion}, $\theta_{neut(g)}$ and $\theta_{neut(\mathrm{w})}$ can be written as:

$$\begin{aligned}
\theta_{ion} &= \sum_i k_i [X_i] N_e \\
\theta_{neut(g)} &= \sum_j k_j [X_j^+][Y_j^-] \\
\theta_{neut(w)} &= \sum_n k_n [X_n^+]
\end{aligned} \tag{3.15}$$

In these expressions, the index i represents the ionization reactions, with k_i being the rate coefficient and $[X_i]$ the concentration of the precursor. The same applies for index j, which represents gas phase neutralizations, with Y_j^- being either an anion or an electron. Finally, index n represents the different positive ions in the discharge, and k_n are the wall neutralization rate coefficients. The plasma sheath in the setup used in these experiments is essentially collisionless, since the mean free path for ions is much larger than the Debye length [8]. This is supported by the shape of the experimental ion energy

distributions, as shown in [41]. In these conditions, the rate with which an ion reaches the cathode is inversely proportional to the square root of its mass, so it follows that:

$$k_n = \frac{K}{\sqrt{m_n}} \tag{3.16}$$

Where K is a constant that depends on the experimental conditions (discharge current, reactor geometry, etc.), but is the same for all the different ions. From this and the expressions in (3.14) and (3.15), the rate coefficients can finally be obtained:

$$k_n = \frac{\sum_i k_i[X_i]N_e - \sum_j k_j[X_j^+][Y_j^-]}{\sqrt{m_n}\sum_p \frac{[X_p^+]}{\sqrt{m_p}}} \tag{3.17}$$

3.3 Gas flow and pumping

The flow of species entering and exiting the reactor has to be considered in the model. A term ϕ_{in} is added in the differential equations for the precursor species to account for the amount of molecules flowing into the reactor, and all neutral species have a term ϕ_{out} subtracted due to the pumping of the chamber. The flow of charged species out of the reactor is not considered since their specific destruction processes (namely wall and gas phase neutralization) are much more efficient. For a precursor species X, the expression is:

$$\frac{d[X]}{dt} = \frac{\phi_{in}(X)}{V_R} - \frac{\phi_{out}(X)}{V_R} \tag{3.18}$$

The flow of a precursor species into the reactor can be obtained from the residence time, τ_R, which is determined experimentally, and the fraction of that species in the precursor mixture, f_X, determined before the ignition of the discharge. Since the residence times measured for the different species are in the 0.5–1 s range, a mean value is taken for the mixture in order to simplify the formulation.

$$\phi_{in}(X) = f_X \Phi_{in} = \frac{f_X V_R}{\tau_R} \tag{3.19}$$

Where Φ_{in} is the total flow of molecules entering the reactor. The flow of molecules out of the reactor is considered to be proportional to the species concentration, so, for any neutral species X_i:

$$\phi_{out}(X_i) = \Phi_{out} \frac{[X_i]}{\sum_j [X_j]} \tag{3.20}$$

Where Φ_{out} is the total flow out of the reactor. The total flows in and out of the reactor are not necessarily equal, due to the slight increase or decrease in the number of particles (and thus the pressure) in the reactor caused by dissociation reactions and wall recombination respectively. Assuming that Φ_{out} is proportional to the pressure in the reactor, it can be expressed as:

$$\Phi_{out} = \Phi_{in} \frac{\sum_i [X_i]}{\sum_i [X_{i_0}]} \tag{3.21}$$

Where $[X_{i_0}]$ stands for the concentration of species X_i at the beginning of the simulation (i.e. before the ignition of the discharge).

3.4 Specific features and reaction tables

The general concepts behind the modeling of the low pressure glow discharges have been discussed in the previous part of the chapter. This section deals with the specific characteristics of the model for each of the different mixtures studied, as well as the set of reactions considered for the simulation of the plasma chemistry.

3.4.1 H_2 + Ar model

The model employed in this work is based on a previous one developed for the same mixture and experimental setup [63]. Given that the number of species formed in this kind of plasmas is not high, with H_2 being the only neutral molecule, the total number of reactions is fairly low. There is however a feature that differentiates this model from the others presented in this thesis, and that is the inclusion of a small amount of high energy electrons, with energies ~ 50–300 eV, through a special set of rate coefficients (k^B) for some of the electron impact reactions. The fraction of high energy electrons is a parameter of the model, set manually for each condition simulated.

The reason behind this decision is the observation of the Ar^{2+} ion with mass spectrometry. The threshold for the electron impact double ionization of the Ar atom, which is the main source of Ar^{2+} ions, is ~ 48 eV [64]. The threshold for the ionization of Ar^{+} is somewhat lower (~ 27 eV), but the lower abundance of Ar^{+} in the plasma compared to Ar causes it to be a less relevant mechanism. Neither of these two reactions can justify the amount of Ar^{2+} observed when only the typical Maxwellian electron temperatures for the plasmas studied (~ 2–8 eV) are taken into account, obtaining simulated concentrations orders of magnitude lower than the experimental ones. The inclusion of the high energy electron component (which, as explained in the beginning of the chapter, is known to exist in glow discharges) accounts for the observed Ar^{2+} concentration while the chemistry for the rest of the species remains largely unaffected.

The calculation of the rate coefficients for high energy electrons, k^B, is performed using certain simplifications. As seen in eq. (3.5), the rate coefficient for an electron impact reaction can be obtained from $k_e = \langle \sigma_e(v) v \rangle$. In the energy range of these electrons, however, the cross section decays with growing energy, so that the product with the electron velocity is roughly constant. With this consideration, k^B values are obtained by taking an average value of the rate coefficient over energies from 50 to 300 eV.

A list of the species included in the model can be found in Table 3.1. The set of gas phase reactions included in the model is shown in Table 3.2, along with their rate coefficients and the corresponding reference. In the case of electron impact reactions, the given rate coefficients are those obtained considering a Maxwellian electron energy distribution (k^A). Table 3.3 contains the rate coefficients for reactions involving high energy electrons (k^B).

Only one excited species is included in the model, the metastable Ar atoms in $4s^3P_2$ and $4s^3P_0$ states, represented here as Ar^*. The reason for their inclusion is their contribution to the formation of atomic hydrogen through reaction 23, and Ar^{+} ions through Penning ionization (reaction 24). Even though excited H atoms (H^*) are included in the table, particularly in reaction 9, these excited states are not metastable and thus they are assumed to decay to the ground state before any further reaction can occur. Therefore, these H^* are effectively treated in the model as H atoms in the ground state. This assumption is replicated in the models for the other two mixtures.

Table 3.1. Species considered in the H_2+ Ar model.

Neutral species	Ionic species
H_2	H^+
H	H_2^+
Ar	H_3^+
Ar^*	Ar^+
	Ar^{2+}
	ArH^+

Table 3.2. Homogeneous reactions considered in the H_2 + Ar model. Rate coefficients, k^A, are given for Maxwellian electrons at T_e (eV). Two alternative values are given for the rate coefficient of reaction ${}^{H}k_{18}$ and ${}^{L}k_{18}$. The origin of these coefficients and their influence in the model simulations is discussed in sections 4.2 and 0.

	Process	Rate coefficient, k^A ($cm^3\ s^{-1}$)	Ref.
1	$H + e \rightarrow H^+ + 2e$	$6.50 \times 10^{-9}\ T_e^{0.49} \exp(-12.89/T_e)$	[35]
2	$H_2 + e \rightarrow H^+ + H + 2e$	$3.00 \times 10^{-8}\ T_e^{0.44} \exp(-37.73/T_e)$	[35]
3	$H_2^+ + e \rightarrow H^+ + H + e$	$1.07 \times 10^{-7}\ T_e^{0.049} \exp(-9.69/T_e)$	[35]
4	$H_2^+ + e \rightarrow H^+ + H^+ + 2e$	$2.12 \times 10^{-9}\ T_e^{0.31} \exp(-23.30/T_e)$	[35]
5	$H_2^+ + H \rightarrow H_2 + H^+$	6.4×10^{-10}	[65]
6	$H_2 + H^+ \rightarrow H_2^+ + H$	1.19×10^{-22}	[35]
7	$H_2 + e \rightarrow H_2^+ + 2e$	$3.12 \times 10^{-8}\ T_e^{0.17} \exp(-20.08/T_e)$	[35]
8	$H_3^+ + e \rightarrow H_2^+ + H + e$	$4.85 \times 10^{-7}\ T_e^{-0.05} \exp(-19.17/T_e)$	[35]
9	$H_2^+ + e \rightarrow H^* + H$	$a + b \times T_e + c \times T_e^2 + d \times T_e^3 + e \times T_e^4$ (*)	[35]
10	$H_2^+ + H_2 \rightarrow H_3^+ + H$	2.0×10^{-9}	[65]
11	$H_3^+ + e \rightarrow 3H$	$0.5 \times K$ (**)	[35]
12	$H_3^+ + e \rightarrow H_2 + H$	$0.5 \times K$ (**)	[35]
13	$H_2 + e \rightarrow 2H + e$	$1.75 \times 10^{-7}\ T_e^{-1.24} \exp(-12.59/T_e)$	[35]
14	$Ar + e \rightarrow Ar^+ + 2e$	$2.53 \times 10^{-8}\ T_e^{0.5} \exp(-16.3/T_e)$	[63]
15	$Ar + e \rightarrow Ar^{2+} + 3e$	$2.58 \times 10^{-9}\ T_e^{0.5} \exp(-47/T_e)$	[63]
16	$Ar^+ + e \rightarrow Ar^{2+} + 2\ e$	$1.9 \times 10^{-8}\ T_e^{0.5} \exp(-27.7/T_e)$	[63]
17	$H_2^+ + Ar \rightarrow ArH^+ + H$	2.1×10^{-9}	[65]
18	$H_3^+ + Ar \rightarrow ArH^+ + H_2$	${}^{H}k_{18} = 3.65 \times 10^{-10}$ ${}^{L}k_{18} = 1 \times 10^{-11}$	[65] [66]
19	$Ar^+ + H_2 \rightarrow H_2^+ + Ar$	$0.02 \times 8.9 \times 10^{-10}$	[65]
20	$Ar^+ + H_2 \rightarrow ArH^+ + H$	$0.98 \times 8.9 \times 10^{-10}$	[65]
21	$ArH^+ + H_2 \rightarrow H_3^+ + Ar$	6.3×10^{-10}	[65]

	Process	Rate coefficient, k^A ($cm^3\ s^{-1}$)	Ref.
22	$Ar + e \rightarrow Ar^* + e$	$9.90 \times 10^{-10}\ T_e^{-0.08} \exp(-11.72/T_e)$	[67]
23	$Ar^* + H_2 \rightarrow 2H + Ar$	7.0×10^{-11}	[68]
24	$Ar^* + Ar^* \rightarrow Ar + Ar^+ + e$	6.4×10^{-10}	[68]

(*) $a = 7.51 \times 10^{-9}$, $b = -1.12 \times 10^{-9}$, $c = 1.03 \times 10^{-10}$, $d = -4.15 \times 10^{-12}$, $e = 5.86 \times 10^{-14}$

(**) $K = 8.39 \times 10^{-9} + 3.02 \times 10^{-9}\ T_e - 3.80 \times 10^{-10}\ T_e^2 + 1.31 \times 10^{-11}\ T_e^3 + 2.42 \times 10^{-13}\ T_e^4 - 2.30 \times 10^{-14}\ T_e^5 + 3.55 \times 10^{-16}\ T_e^6$

Table 3.3. Rate coefficients, k^B, for homogeneous reactions with high energy electrons (> 50 eV, see text).

	Process	Rate coefficient, k^B ($cm^3\ s^{-1}$)	Ref.
1	$H + e \rightarrow H^+ + 2e$	4.2×10^{-8}	[63]
2	$H_2 + e \rightarrow H^+ + H + 2e$	4.5×10^{-9}	[63]
7	$H_2 + e \rightarrow H_2^+ + 2e$	5.0×10^{-8}	[63]
13	$H_2 + e \rightarrow 2H + e$	1×10^{-8}	[63]
14	$Ar + e \rightarrow Ar^+ + 2e$	1.6×10^{-7}	[63]
15	$Ar + e \rightarrow Ar^{2+} + 3e$	1.1×10^{-8}	[63]
22	$Ar + e \rightarrow Ar^* + e$	2.4×10^{-8}	[68]

H_2 molecules in vibrationally excited states, $H_2(v)$, can be present in the discharge. Electron impact reactions with these molecules are more efficient than with ground state H_2, as the energy barrier is lowered. Practically, the rate coefficients for reactions with vibrationally excited molecules are usually obtained by considering that the energy threshold of the cross section is reduced by the value of the excitation energy [67], resulting in a higher value of the rate coefficient.

Vibrational temperatures of ~ 3000 K have been measured in H_2 discharges in the same experimental setup [35], which means that only the lower vibrational levels are significantly populated, and most of the molecules are in the ground state (12 % $H_2(v \geq 1)$). Although vibrational temperatures for each of the specific mixtures have not been measured, they are not expected to vary significantly given the similar electron temperatures and the inefficient quenching of vibrationally excited H_2 molecules in collisions with different species. The low abundance of vibrationally excited molecules neutralizes the increase in the rate coefficient, and so they are not included in the model.

Wall reactions are listed in Table 3.4. Only one molecule is formed at the surface, namely H_2, and the rest of reactions are wall neutralization of positive ions or wall deexcitation of the metastable Ar.

Table 3.4. Heterogeneous processes and reaction probabilities.

	Wall neutralization	γ		Heterogeneous reaction	γ
1	$H^+ + Wall \rightarrow H$	1	1	$H + Wall \rightarrow ½\ H_2$	0.03
2	$H_2^+ + Wall \rightarrow H_2$	1			
3	$H_3^+ + Wall \rightarrow H_2 + H$	1			
4	$Ar^+ + Wall \rightarrow Ar$	1			
5	$ArH^+ + Wall \rightarrow Ar + H$	1			
6	$Ar^{2+} + Wall \rightarrow Ar$	1			
7	$Ar^* + Wall \rightarrow Ar$	1			

A simplified model of surface reactions based on previous works [35,63], which does not take into account adsorbed species and surface coverage, has been used for this study. In this model, the Eley-Rideal surface formation of the H_2 molecule from gas phase hydrogen atoms [55] occurs in one step, and the formulation is similar to the one applied to surface deexcitations. Due to this difference, the γ coefficient for hydrogen recombination is not directly comparable to the ones used in the other models, which follow the usual formulation shown in section 3.2.1.1.

The reason for this simplification of the surface model is the lack of complexity of the heterogeneous chemistry. Only one molecular species can be formed at the walls, so the effective role of the hydrogen surface reaction is to control the dissociation degree of H_2. Adding more depth to the surface model would result in a better simulation of the time evolution of the system, but since the interest of this work lies in the analysis of the steady state, this is not a major concern.

3.4.2 $H_2 + N_2$ model

This model is significantly more complex than the one for H_2 + Ar, due to the higher number of neutral and ionic species present in H_2 + N_2 plasmas. Given that there are two molecular precursors, there are more ions and radicals in the gas phase, resulting in a significant increase in the number of reactions, as can be seen in Table 3.5. In contrast to the H_2 + Ar model, surface reactions are modeled taking into account the surface coverage, in order to obtain a good simulation of the formation of ammonia at the reactor walls.

Table 3.5. Species included in the H_2+ N_2 model.

Neutral species	Ionic species
H_2	H^+
H	H_2^+
N_2	H_3^+
N	N^+
NH	N_2^+
NH_2	NH^+
NH_3	NH_2^+
	NH_3^+
	NH_4^+
	N_2H^+

The gas phase reactions included in the model are listed in Table 3.6. As the number of chemical processes is much higher than in the H_2 + Ar model, they have been grouped by type for clearer notation.

Table 3.6. Set of gas phase reactions considered in the H_2 + N_2 model.

	Process	Rate coefficient ($cm^3\ s^{-1}$)	Ref.
	Electron impact ionization		
I_1	$N + e \rightarrow N^+ + 2e$	$1.26 \times 10^{-10}\ T_e - 1.72 \times 10^{-10}\ T_e^2 + 6.51 \times 10^{-11}\ T_e^3 - 5.75 \times 10^{-12}\ T_e^4 + 1.71 \times 10^{-13}\ T_e^5$	[69]
I_2	$N_2 + e \rightarrow N^+ + N + 2e$	$- 5.68 \times 10^{-12}\ T_e + 8.57 \times 10^{-12}\ T_e^2 - 4.11 \times 10^{-12}\ T_e^3 + 7.26 \times 10^{-13}\ T_e^4 - 3.09 \times 10^{-14}\ T_e^5$	[70]
I_3	$N_2 + e \rightarrow N_2^+ + 2e$	$1.01 \times 10^{-10}\ T_e - 1.13 \times 10^{-10}\ T_e^2 + 3.14 \times 10^{-11}\ T_e^3 - 7.52 \times 10^{-13}\ T_e^4 - 5.14 \times 10^{-14}\ T_e^5$	[70]
I_4	$H + e \rightarrow H^+ + 2e$	$6.50 \times 10^{-9}\ T_e^{0.49} \exp(-12.89/T_e)$	[35]
I_5	$H_2 + e \rightarrow H^+ + H + 2e$	$3.00 \times 10^{-8}\ T_e^{0.44} \exp(-37.72/T_e)$	[35]
I_6	$H_2 + e \rightarrow H_2^+ + 2e$	$3.12 \times 10^{-8}\ T_e^{0.17} \exp(-20.07/T_e)$	[35]
I_7	$NH + e \rightarrow NH^+ + 2e$	$1.38 \times 10^{-10}\ T_e - 1.85 \times 10^{-10}\ T_e^2 + 6.65 \times 10^{-11}\ T_e^3 - 4.36 \times 10^{-12}\ T_e^4 + 3.02 \times 10^{-14}\ T_e^5$	[71]
I_8	$NH + e \rightarrow N^+ + H + 2e$	$5.66 \times 10^{-11}\ T_e - 6.91 \times 10^{-11}\ T_e^2 + 2.33 \times 10^{-11}\ T_e^3 - 1.96 \times 10^{-12}\ T_e^4 + 4.96 \times 10^{-14}\ T_e^5$	[71]

	Process	Rate coefficient ($cm^3\ s^{-1}$)	Ref.
I_9	$NH_2 + e \rightarrow NH_2^+ + 2e$	$1.76 \times 10^{-10}\ T_e - 2.70 \times 10^{-10}\ T_e^2 + 1.17 \times 10^{-10}\ T_e^3 - 1.24 \times 10^{-11}\ T_e^4 + 4.23 \times 10^{-13}\ T_e^5$	[71]
I_{10}	$NH_2 + e \rightarrow NH^+ + H + 2e$	$1.08 \times 10^{-10}\ T_e - 1.28 \times 10^{-10}\ T_e^2 + 4.11 \times 10^{-11}\ T_e^3 - 2.91 \times 10^{-12}\ T_e^4 + 5.15 \times 10^{-14}\ T_e^5$	[71]
I_{11}	$NH_3 + e \rightarrow NH_3^+ + 2e$	$1.53 \times 10^{-10}\ T_e - 2.24 \times 10^{-10}\ T_e^2 + 9.37 \times 10^{-11}\ T_e^3 - 9.79 \times 10^{-12}\ T_e^4 + 3.33 \times 10^{-13}\ T_e^5$	[71]
I_{12}	$NH_3 + e \rightarrow NH_2^+ + H + 2e$	$1.57 \times 10^{-10}\ T_e - 2.02 \times 10^{-10}\ T_e^2 + 7.22 \times 10^{-11}\ T_e^3 - 6.69 \times 10^{-12}\ T_e^4 + 1.97 \times 10^{-13}\ T_e^5$	[71]
	Electron impact dissociation		
D_1	$H_2 + e \rightarrow 2H + e$	$1.75 \times 10^{-7}\ T_e^{-1.24} \exp(-12.59/T_e)$	[35]
D_2	$N_2 + e \rightarrow 2N + e$	$1.18 \times 10^{-8}\ T_e^{0.5} \exp(-13.3/T_e)$	[72]
D_3	$NH + e \rightarrow N + H + e$	$5.0 \times 10^{-8}\ T_e^{0.5} \exp(-8.6/T_e)$	[73]
D_4	$NH_2 + e \rightarrow N + H_2 + e$	$5.0 \times 10^{-8}\ T_e^{0.5} \exp(-7.6/T_e)$	[74]
D_5	$NH_2 + e \rightarrow NH + H + e$	$5.0 \times 10^{-8}\ T_e^{0.5} \exp(-7.6/T_e)$	[74,75]
D_6	$NH_3 + e \rightarrow NH_2 + H + e$	$5.0 \times 10^{-8}\ T_e^{0.5} \exp(-4.4/T_e)$	[76]
D_7	$NH_3 + e \rightarrow NH + H_2 + e$	$5.0 \times 10^{-8}\ T_e^{0.5} \exp(-5.5/T_e)$	[76]
	Electron impact neutralization		
N_1	$H_2^+ + e \rightarrow H^* + H$	$7.51 \times 10^{-9} - 1.12 \times 10^{-9}\ T_e + 1.03 \times 10^{-10}\ T_e^2 - 4.15 \times 10^{-12}\ T_e^3 + 5.86 \times 10^{-14}\ T_e^4$	[35]
N_2	$H_3^+ + e \rightarrow 3H$	$0.5 \times K^{(*)}$	[35]
N_3	$H_3^+ + e \rightarrow H_2 + H$	$0.5 \times K^{(*)}$	[35]
N_4	$N_2^+ + e \rightarrow N + N$	$2.8 \times 10^{-7}\ (0.026/T_e)^{0.5}$	[77]
N_5	$NH^+ + e \rightarrow N + H$	$4.30 \times 10^{-8}\ (0.026/T_e)^{0.5}$	[78]
N_6	$NH_2^+ + e \rightarrow NH + H$	$1.02 \times 10^{-7}\ (0.026/T_e)^{0.40}$	[79]
N_7	$NH_2^+ + e \rightarrow N + 2H$	$1.98 \times 10^{-7}\ (0.026/T_e)^{0.40}$	[79]
N_8	$NH_3^+ + e \rightarrow NH + 2H$	$1.55 \times 10^{-7}\ (0.026/T_e)^{0.50}$	[78]
N_9	$NH_3^+ + e \rightarrow NH_2 + H$	$1.55 \times 10^{-7}\ (0.026/T_e)^{0.50}$	[78]
N_{10}	$NH_4^+ + e \rightarrow NH_3 + H$	$8.015 \times 10^{-7}\ (0.026/T_e)^{0.605}$	[79]
N_{11}	$NH_4^+ + e \rightarrow NH_2 + 2H$	$1.226 \times 10^{-7}\ (0.026/T_e)^{0.605}$	[79]
N_{12}	$N_2H^+ + e \rightarrow N_2 + H$	$7.1 \times 10^{-7}\ (0.026/T_e)^{0.72}$	[80]
	Ion-molecule		
T_1	$H^+ + NH_3 \rightarrow NH_3^+ + H$	5.20×10^{-9}	[65]
T_2	$H_2^+ + H \rightarrow H_2 + H^+$	6.4×10^{-10}	[65]
T_3	$H_2^+ + H_2 \rightarrow H_3^+ + H$	2.00×10^{-9}	[65]
T_4	$H_2^+ + NH_3 \rightarrow NH_3^+ + H_2$	5.70×10^{-9}	[65]

	Process	Rate coefficient ($cm^3\ s^{-1}$)	Ref.
T_5	$H_2^+ + N_2 \rightarrow N_2H^+ + H$	2.00×10^{-9}	[65]
T_6	$H_3^+ + N \rightarrow NH^+ + H_2$	2.6×10^{-10}	[65]
T_7	$H_3^+ + N \rightarrow NH_2^+ + H$	3.9×10^{-10}	[65]
T_8	$H_3^+ + NH_3 \rightarrow NH_4^+ + H_2$	4.40×10^{-9}	[65]
T_9	$H_3^+ + N_2 \rightarrow N_2H^+ + H_2$	1.86×10^{-9}	[65]
T_{10}	$N^+ + H_2 \rightarrow NH^+ + H$	5.00×10^{-10}	[65]
T_{11}	$N^+ + NH_3 \rightarrow NH_2^+ + NH$	$0.20 \times 2.35 \times 10^{-9} = 4.7 \times 10^{-10}$	[65]
T_{12}	$N^+ + NH_3 \rightarrow NH_3^+ + N$	$0.71 \times 2.35 \times 10^{-9} = 1.67 \times 10^{-9}$	[65]
T_{13}	$N^+ + NH_3 \rightarrow N_2H^+ + H_2$	$0.09 \times 2.35 \times 10^{-9} = 2.12 \times 10^{-10}$	[65]
T_{14}	$NH^+ + H_2 \rightarrow H_3^+ + N$	$0.15 \times 1.23 \times 10^{-9} = 1.85 \times 10^{-10}$	[65]
T_{15}	$NH^+ + H_2 \rightarrow NH_2^+ + H$	$0.85 \times 1.23 \times 10^{-9} = 1.05 \times 10^{-9}$	[65]
T_{16}	$NH^+ + NH_3 \rightarrow NH_3^+ + NH$	$0.75 \times 2.40 \times 10^{-9} = 1.8 \times 10^{-9}$	[65]
T_{17}	$NH^+ + NH_3 \rightarrow NH_4^+ + N$	$0.25 \times 2.40 \times 10^{-9} = 6.0 \times 10^{-10}$	[65]
T_{18}	$NH^+ + N_2 \rightarrow N_2H^+ + N$	6.50×10^{-10}	[65]
T_{19}	$NH_2^+ + H_2 \rightarrow NH_3^+ + H$	1.95×10^{-10}	[65]
T_{20}	$NH_2^+ + NH_3 \rightarrow NH_3^+ + NH_2$	$0.5 \times 2.30 \times 10^{-9} = 1.15 \times 10^{-9}$	[65]
T_{21}	$NH_2^+ + NH_3 \rightarrow NH_4^+ + NH$	$0.5 \times 2.30 \times 10^{-9} = 1.15 \times 10^{-9}$	[65]
T_{22}	$NH_3^+ + NH_3 \rightarrow NH_4^+ + NH_2$	2.10×10^{-9}	[65]
T_{23}	$N_2^+ + H_2 \rightarrow N_2H^+ + H$	2.00×10^{-9}	[65]
T_{24}	$N_2^+ + NH_3 \rightarrow NH_3^+ + N_2$	1.95×10^{-9}	[65]
T_{25}	$N_2H^+ + NH_3 \rightarrow NH_4^+ + N_2$	2.30×10^{-9}	[65]

(*) $K = 8.39247 \times 10^{-9} + 3.01631 \times 10^{-9}\, T_e - 3.80439 \times 10^{-10}\, T_e^2 + 1.31108 \times 10^{-11}\, T_e^3 + 2.41631 \times 10^{-13}\, T_e^4 - 2.29832 \times 10^{-14}\, T_e^5 + 3.5472 \times 10^{-16}\, T_e^6$

The surface chemistry in this model is the most complex of the three mixtures studied. It includes both Langmuir-Hinshelwood and Eley-Rideal reactions, which are necessary to explain the formation of NH_3 at the reactor walls. The full set of surface reactions is shown in Table 3.7, with values of the γ coefficients given for E-R reactions.

Table 3.7. Heterogeneous reactions included in the $H_2 + N_2$ model.

	Wall neutralization	γ		Heterogeneous reaction	γ
K_1	$H^+ + Wall \rightarrow H$	1	W_1	$H + F_s \rightarrow H(s)$	1
K_2	$H_2^+ + Wall \rightarrow H_2$	1	W_2	$H + H(s) \rightarrow H_2 + F_s$	1.5×10^{-3}
K_3	$H_3^+ + Wall \rightarrow H_2 + H$	1	W_3	$N + F_s \rightarrow N(s)$	1
K_4	$N^+ + Wall \rightarrow N$	1	W_4	$N + N(s) \rightarrow N_2 + F_s$	6×10^{-3}
K_5	$N_2^+ + Wall \rightarrow N_2$	1	W_5	$NH + F_s \rightarrow NH\,(s)$	1
K_6	$NH^+ + Wall \rightarrow NH$	1	W_6	$NH_2 + F_s \rightarrow NH_2\,(s)$	1
K_7	$NH_2^+ + Wall \rightarrow NH_2$	1	W_7	$N + H(s) \rightarrow NH(s)$	1×10^{-2}
K_8	$NH_3^+ + Wall \rightarrow NH_3$	1	W_8	$H + N(s) \rightarrow NH(s)$	8×10^{-3}
K_9	$NH_4^+ + Wall \rightarrow NH_3 + H$	1	W_9	$H + NH(s) \rightarrow NH_2(s)$	8×10^{-3}
K_{10}	$N_2H^+ + Wall \rightarrow N_2 + H$	1	W_{10}	$NH + H(s) \rightarrow NH_2(s)$	1×10^{-2}
			W_{11}	$NH(s) + H(s) \rightarrow NH_2(s) + F_s$	–
			W_{12}	$H + NH_2(s) \rightarrow NH_3 + F_s$	8×10^{-3}
			W_{13}	$NH_2 + H(s) \rightarrow NH_3 + F_s$	1×10^{-2}
			W_{14}	$H_2 + NH(s) \rightarrow NH_3 + F_s$	8×10^{-4}
			W_{15}	$NH_2(s) + H(s) \rightarrow NH_3 + 2F_s$	–

The parameters used in the model to describe L-H reactions (W_{11} and W_{15}) are shown in Table 3.8. The values of the surface diffusional jump frequency ν and diffusional activation energy E_d are those of H(s) and are common for both reactions, as it is assumed that the lighter species is the one diffusing on the surface.

Table 3.8. Parameters for the L-H reactions in the $H_2 + N_2$ model.

Parameter	Value
ν_H	$1.0 \times 10^{13}\ s^{-1}$
E_d (H)	0.2 eV
E_A (W_{11})	0.2 eV
E_A (W_{15})	0.2 eV

3.4.3 $H_2 + O_2$ model

The model of the $H_2 + O_2$ discharge includes the most gas phase reactions of the three mixtures studied, as shown in Table 3.10. This is due to the inclusion of minor neutral species (HO_2 and O_3), metastable excited states of atoms and molecules ($O(^1D)$ and $O_2(a)$), and negative ions (H^-, OH^- and O^-). The full list of species is found in Table 3.9.

Table 3.9. Species included in the H_2+ O_2 model.

Neutral species	Ionic species
H_2	H^+
H	H_2^+
O_2	H_3^+
O	O^+
OH	O_2^+
H_2O	OH^+
HO_2	H_2O^+
O_3	H_3O^+
$O(^1D)$	HO_2^+
$O_2(a)$	H^-
	OH^-
	O^-

Table 3.10. Gas phase reactions included in the $H_2 + O_2$ model.

	Process	Rate coefficient ($cm^3\ s^{-1}$)	Ref.
	Electron impact ionization		
I_1	$e + O \rightarrow O^+ + 2e$	$1.03 \times 10^{-8}\ T_e^{0.5} \exp(-14.3/T_e)$	[69]
I_2	$e + O_2 \rightarrow O^+ + O + 2e$	$4.84 \times 10^{-9}\ T_e^{0.5} \exp(-22.5/T_e)$	[81]
I_3	$e + O_2 \rightarrow O_2^+ + 2e$	$7.07 \times 10^{-9}\ T_e^{0.5} \exp(-13.1/T_e)$	[81]
I_4	$e + H \rightarrow H^+ + 2e$	$6.50 \times 10^{-9}\ T_e^{0.49} \exp(-12.89/T_e)$	[35]
I_5	$e + H_2 \rightarrow H^+ + H + 2e$	$3.00 \times 10^{-8}\ T_e^{0.44} \exp(-37.72/T_e)$	[35]
I_6	$e + H_2 \rightarrow H_2^+ + 2e$	$3.12 \times 10^{-8}\ T_e^{0.17} \exp(-20.07/T_e)$	[35]
I_7	$e + OH \rightarrow OH^+ + 2e$	$1.48 \times 10^{-8}\ T_e^{0.5} \exp(-12.6/T_e)$	[82]
I_8	$e + H_2O \rightarrow H_2O^+ + 2e$	$9.87 \times 10^{-9}\ T_e^{0.5} \exp(-13.3/T_e)$	[83]
I_9	$e + H_2O \rightarrow OH^+ + H + 2e$	$2.88 \times 10^{-9}\ T_e^{0.5} \exp(-17.7/T_e)$	[83]
I_{10}	$e + H_2O \rightarrow H^+ + OH + 2e$	$1.77 \times 10^{-9}\ T_e^{0.5} \exp(-20.0/T_e)$	[83]
I_{11}	$e + H_2O \rightarrow O^+ + H_2 + 2e$	$3.03 \times 10^{-10}\ T_e^{0.5} \exp(-23.5/T_e)$	[83]

	Process	Rate coefficient ($cm^3\ s^{-1}$)	Ref.
I_{12}	$e + O_2(a) \rightarrow O_2^+ + 2e$	$9.0 \times 10^{-10}\ T_e^{2.0} \exp(-11.6/T_e)$	[42]
	Electron impact dissociation		
D_1	$e + H_2 \rightarrow 2H + e$	$1.75 \times 10^{-7}\ T_e^{-1.24} \exp(-12.59/T_e)$	[35]
D_2	$e + O_2 \rightarrow 2O + e$	$4.2 \times 10^{-9} \exp(-5.56/T_e)$	[84]
D_3	$e + O_2 \rightarrow O + O^1D + e$	$5.0 \times 10^{-8} \exp(-8.40/T_e)$	[84]
D_4	$e + OH \rightarrow O + H + e$	K_{D4} [a]	[85]
D_5	$e + H_2O \rightarrow OH + H + e$	K_{D5} [b]	[83]
D_6	$e + H_2O \rightarrow O^1D + H_2 + e$	$2.0 \times 10^{-9}\ T_e^{0.5} \exp(-7.0/T_e)$	[83]
D_7	$e + O_2(a) \rightarrow 2O + e$	$4.2 \times 10^{-9} \exp(-4.6/T_e)$	[42]
	Electron impact neutralization		
N_1	$H_2^+ + e \rightarrow H^* + H$	K_{N1} [c]	[35]
N_2	$H_3^+ + e \rightarrow 3H$	$0.5 \times K_{N2}$ [d]	[35]
N_3	$H_3^+ + e \rightarrow H_2 + H$	$0.5 \times K_{N2}$ [d]	[35]
N_4	$O_2^+ + e \rightarrow O + O$	$4.9 \times 10^{-8}\ (0.026/T_e)^{0.7}$	[86]
N_5	$O_2^+ + e \rightarrow O + O^1D$	$1.06 \times 10^{-7}\ (0.026/T_e)^{0.7}$	[86]
N_6	$O_2^+ + e \rightarrow O^1D + O^1D$	$7.56 \times 10^{-8}\ (0.026/T_e)^{0.7}$	[86]
N_7	$OH^+ + e \rightarrow O + H$	$3.75 \times 10^{-8}\ (0.026/T_e)^{0.5}$	[78]
N_8	$H_2O^+ + e \rightarrow OH + H$	$8.6 \times 10^{-8}\ (0.026/T_e)^{0.5}$	[87]
N_9	$H_2O^+ + e \rightarrow O + H_2$	$3.9 \times 10^{-8}\ (0.026/T_e)^{0.5}$	[87]
N_{10}	$H_2O^+ + e \rightarrow O + H + H$	$3.05 \times 10^{-7}\ (0.026/T_e)^{0.5}$	[87]
N_{11}	$H_3O^+ + e \rightarrow OH + H + H$	$2.85 \times 10^{-7}\ (0.026/T_e)^{0.5}$	[88]
N_{12}	$H_3O^+ + e \rightarrow O + H_2 + H$	$5.6 \times 10^{-9}\ (0.026/T_e)^{0.5}$	[88]
N_{13}	$H_3O^+ + e \rightarrow OH + H_2$	$6.02 \times 10^{-8}\ (0.026/T_e)^{0.5}$	[88]
N_{14}	$H_3O^+ + e \rightarrow H_2O + H$	$1.08 \times 10^{-7}\ (0.026/T_e)^{0.5}$	[88]
N_{15}	$HO_2^+ + e \rightarrow O_2 + H$	$3 \times 10^{-7}\ (0.026/T_e)^{0.5}$	[89]
	Neutral homogeneous		
G_1	$H + O_3 \rightarrow O + HO_2$	7.51×10^{-13}	[90]
G_2	$H + HO_2 \rightarrow H_2O + O$	$9.18 \times 10^{-11} \exp(-971.9/T_g)$	[91]
G_3	$H + HO_2 \rightarrow H_2O + O(^1D)$	$4.8 \times 10^{-16}\ T_g^{1.55} \exp(80.58/T_g)$	[90]
G_4	$H + HO_2 \rightarrow O_2 + H_2$	$1.1 \times 10^{-12}\ T_g^{0.56} \exp(-346/T_g)$	[91]
G_5	$H + HO_2 \rightarrow 2OH$	$2.35 \times 10^{-10} \exp(-373.7/T_g)$	[91]
G_6	$O(^1D) + HO_2 \rightarrow OH + O_2$	$2.9 \times 10^{-11} \exp(200/T_g)$	[91]
G_7	$O_2(a) + HO_2 \rightarrow OH + O + O_2$	1.66×10^{-11}	[92]
G_8	$H + O_3 \rightarrow OH + O_2$	$2.71 \times 10^{-11}\ (T_g/300)^{0.75}$	[90]
G_9	$O(^1D) + O_3 \rightarrow 2O_2$	1.2×10^{-10}	[90]
G_{10}	$O(^1D) + O_3 \rightarrow 2O + O_2$	1.2×10^{-10}	[90]
G_{11}	$O(^1D) + H_2 \rightarrow OH + H$	1.1×10^{-10}	[91]
G_{12}	$O(^1D) + O_2 \rightarrow O + O_2$	$4.8 \times 10^{-12} \exp(67/T_g)$	[77]

	Process	Rate coefficient ($cm^3\ s^{-1}$)	Ref.
G_{13}	$O(^1D) + O_2 \rightarrow O + O_2(a)$	$1.6 \times 10^{-12} \exp(67/T_g)$	[93]
G_{14}	$O(^1D) + OH \rightarrow H + O_2$	$6 \times 10^{-11}\ T_g^{-0.186} \exp(-154/T_g)$	[91]
G_{15}	$O(^1D) + H_2O \rightarrow 2OH$	$1.62 \times 10^{-10} \exp(64.95/T_g)$	[90]
G_{16}	$O(^1D) + H_2O \rightarrow O + H_2O$	1.2×10^{-11}	[94]
	Ion-molecule		
T_1	$H^+ + O \rightarrow O^+ + H$	3.75×10^{-10}	[65]
T_2	$H^+ + H_2O \rightarrow H_2O^+ + H$	8.20×10^{-9}	[65]
T_3	$H^+ + O_2 \rightarrow O_2^+ + H$	1.17×10^{-9}	[65]
T_4	$H_2^+ + H \rightarrow H_2 + H^+$	6.40×10^{-10}	[65]
T_5	$H_2^+ + H_2 \rightarrow H_3^+ + H$	2.00×10^{-9}	[65]
T_6	$H_2^+ + H_2O \rightarrow H_2O^+ + H_2$	$0.53 \times 7.30 \times 10^{-9} = 3.87 \times 10^{-9}$	[65]
T_7	$H_2^+ + H_2O \rightarrow H_3O^+ + H$	$0.47 \times 7.30 \times 10^{-9} = 3.43 \times 10^{-9}$	[65]
T_8	$H_2^+ + O_2 \rightarrow O_2^+ + H_2$	$0.29 \times 2.70 \times 10^{-9} = 7.83 \times 10^{-10}$	[65]
T_9	$H_2^+ + O_2 \rightarrow HO_2^+ + H$	$0.71 \times 2.70 \times 10^{-9} = 1.92 \times 10^{-9}$	[65]
T_{10}	$H_3^+ + O \rightarrow OH^+ + H_2$	$0.70 \times 1.20 \times 10^{-9} = 8.40 \times 10^{-10}$	[65]
T_{11}	$H_3^+ + O \rightarrow H_2O^+ + H$	$0.30 \times 1.20 \times 10^{-9} = 3.60 \times 10^{-10}$	[65]
T_{12}	$H_3^+ + H_2O \rightarrow H_3O^+ + H_2$	5.30×10^{-9}	[65]
T_{13}	$H_3^+ + O_2 \rightarrow HO_2^+ + H_2$	6.70×10^{-10}	[65]
T_{14}	$O^+ + H \rightarrow H^+ + O$	6.40×10^{-10}	[65]
T_{15}	$O^+ + H_2 \rightarrow OH^+ + H$	1.62×10^{-9}	[65]
T_{16}	$O^+ + H_2O \rightarrow H_2O^+ + O$	2.60×10^{-9}	[65]
T_{17}	$OH^+ + H_2 \rightarrow H_2O^+ + H$	9.70×10^{-10}	[65]
T_{18}	$OH^+ + H_2O \rightarrow H_2O^+ + OH$	$0.55 \times 2.89 \times 10^{-9} = 1.59 \times 10^{-9}$	[65]
T_{19}	$OH^+ + H_2O \rightarrow H_3O^+ + O$	$0.45 \times 2.89 \times 10^{-9} = 1.30 \times 10^{-9}$	[65]
T_{20}	$OH^+ + O_2 \rightarrow O_2^+ + OH$	3.80×10^{-10}	[65]
T_{21}	$H_2O^+ + H_2 \rightarrow H_3O^+ + H$	7.60×10^{-10}	[65]
T_{22}	$H_2O^+ + H_2O \rightarrow H_3O^+ + OH$	1.85×10^{-9}	[65]
T_{23}	$H_2O^+ + O_2 \rightarrow O_2^+ + H_2O$	3.30×10^{-10}	[65]
T_{24}	$O_2^+ + H_2 \rightarrow HO_2^+ + H$	4.00×10^{-11}	[65]
T_{25}	$HO_2^+ + H_2 \rightarrow H_3^+ + O_2$	3.30×10^{-10}	[65]
T_{26}	$O^- + H_2 \rightarrow OH^- + H$	3×10^{-11}	[95]
T_{27}	$O^- + H_2O \rightarrow OH^- + OH$	1.4×10^{-9}	[96]
	Electron impact attachment		
A_1	$e + O_2 \rightarrow O^- + O$	$1.07 \times 10^{-9}\ T_e^{-1.391} \exp(-6.26/T_e)$	[97]
A_2	$e + H_2O \rightarrow OH + H^-$	$3.54 \times 10^{-9}\ T_e^{-1.5} \exp(-6.66/T_e)$	[83]
A_3	$e + H_2 \rightarrow H^- + H$	$5.6 \times 10^{-13}\ T_e^{0.5} \exp(-5.5/T_e)$	[98]
A_4	$e + O_2(a) \rightarrow O + O^-$	$2.28 \times 10^{-10} \exp(-2.29/T_e)$	[42]
A_5	$e + H_2O \rightarrow H_2 + O^-$	$7.08 \times 10^{-10}\ T_e^{-1.3} \exp(-8.61/T_e)$	[83]

	Process	Rate coefficient ($cm^3\ s^{-1}$)	Ref.
A_6	$e + H_2O \rightarrow OH^- + H$	$1.24 \times 10^{-10}\ T_e^{-1.3} \exp(-7.32/T_e)$	[83]
	Detachment		
Dt_1	$e + H^- \rightarrow H + 2e$	$2.32 \times 10^{-8}\ T_e^2 \exp(-0.13/T_e)$	[99]
Dt_2	$H^- + H \rightarrow H_2 + e$	1.3×10^{-9}	[100]
Dt_3	$H^- + O \rightarrow OH + e$	1×10^{-9}	[100]
Dt_4	$H^- + O_2 \rightarrow HO_2 + e$	1.2×10^{-9}	[101]
Dt_5	$OH^- + H \rightarrow H_2O + e$	1.8×10^{-9}	[102]
Dt_6	$OH^- + O \rightarrow HO_2 + e$	2×10^{-10}	[102]
Dt_7	$e + OH^- \rightarrow OH + 2e$	$9.67 \times 10^{-6}\ T_e^{-1.9} \exp(-12.1/T_e)$	[103]
Dt_8	$O^- + O_2(a) \rightarrow O_3 + e$	1.9×10^{-10}	[104]
Dt_9	$O^- + H \rightarrow OH + e$	5×10^{-10}	[95]
Dt_{10}	$O^- + H_2 \rightarrow H_2O + e$	$6 \times 10^{-10}\ (T_g/300)^{-0.24}$	[105]
Dt_{11}	$O^- + O \rightarrow O_2 + e$	2.3×10^{-10}	[104]
	Electron impact excitation and deexcitation		
X_1	$e + O_2 \rightarrow O_2(a) + e$	$1.7 \times 10^{-9} \exp(-3.1/T_e)$	[42]
X_2	$e + O \rightarrow O(^1D) + e$	$4.5 \times 10^{-9} \exp(-2.29/T_e)$	[42]
Dx_1	$e + O_2(a) \rightarrow O_2 + e$	$5.6 \times 10^{-9} \exp(-2.2/T_e)$	[42]
	Ion-ion neutralization		
IN_1	$H^+ + H^- \rightarrow 2H$	$1.8 \times 10^{-7}\ (T_g/300)^{-0.5}$	[106]
IN_2	$H_2^+ + H^- \rightarrow H + H_2$	$2 \times 10^{-7}\ (T_g/300)^{-0.5}$	[107]
IN_3	$H_3^+ + H^- \rightarrow 2H_2$	$2 \times 10^{-7}\ (T_g/300)^{-0.5}$	[108]
IN_4	$O^+ + H^- \rightarrow H + O$	$2.3 \times 10^{-7}\ (T_g/300)^{-0.5}$	[95]
IN_5	$O_2^+ + H^- \rightarrow H + O_2$	$2 \times 10^{-7}\ (T_g/300)^{-0.5}$	[77]
IN_6	$OH^+ + H^- \rightarrow H_2O$	$2 \times 10^{-7}\ (T_g/300)^{-0.5}$	[77]
IN_7	$H_2O^+ + H^- \rightarrow H + H_2O$	$2 \times 10^{-7}\ (T_g/300)^{-0.5}$	[77]
IN_8	$H_3O^+ + H^- \rightarrow H_2 + H_2O$	$2.3 \times 10^{-7}\ (T_g/300)^{-0.5}$	[95]
IN_9	$H^+ + O^- \rightarrow H + O$	$2 \times 10^{-7}\ (T_g/300)^{-0.5}$	[77]
IN_{10}	$H_2^+ + O^- \rightarrow H_2O$	$2 \times 10^{-7}\ (T_g/300)^{-0.5}$	[77]
IN_{11}	$H_3^+ + O^- \rightarrow OH + H_2$	$2 \times 10^{-7}\ (T_g/300)^{-0.5}$	[77]
IN_{12}	$O^+ + O^- \rightarrow 2O$	$2 \times 10^{-7}\ (T_g/300)^{-1}$	[93]
IN_{13}	$O_2^+ + O^- \rightarrow O_2 + O$	$2 \times 10^{-7}\ (T_g/300)^{-0.5}$	[109]
IN_{14}	$OH^+ + O^- \rightarrow HO_2$	$2 \times 10^{-7}\ (T_g/300)^{-0.5}$	[77]
IN_{15}	$H_2O^+ + O^- \rightarrow O + H_2O$	$2 \times 10^{-7}\ (T_g/300)^{-0.5}$	[77]
IN_{16}	$H_3O^+ + O^- \rightarrow H_2O + OH$	$2 \times 10^{-7}\ (T_g/300)^{-0.5}$	[77]
IN_{17}	$H_2^+ + OH^- \rightarrow H_2O + H$	1×10^{-7}	[77]
IN_{18}	$H_3^+ + OH^- \rightarrow H_2 + H_2O$	$2 \times 10^{-7}\ (T_g/300)^{-0.5}$	[77]
IN_{19}	$O^+ + OH^- \rightarrow HO_2$	$2 \times 10^{-7}\ (T_g/300)^{-0.5}$	[77]
IN_{20}	$O_2^+ + OH^- \rightarrow OH + O_2$	$2 \times 10^{-7}\ (T_g/300)^{-0.5}$	[77]

	Process	Rate coefficient ($cm^3\ s^{-1}$)	Ref.
IN_{21}	$OH^+ + OH^- \rightarrow 2OH$	$2 \times 10^{-7}\ (T_g/300)^{-0.5}$	[77]
IN_{22}	$H_2O^+ + OH^- \rightarrow H_2O + OH$	$2 \times 10^{-7}\ (T_g/300)^{-0.5}$	[77]
IN_{23}	$H_3O^+ + OH^- \rightarrow 2H_2O$	$4 \times 10^{-7}\ (T_g/300)^{-0.5}$	[106]

T_g is given in K.

T_e is given in eV.

[a] $K_{D4} = -2.82402 \times 10^{-11}\ T_e + 3.38111 \times 10^{-11}\ T_e^2 - 7.01504 \times 10^{-12}\ T_e^3 + 6.09826 \times 10^{-13}\ T_e^4 - 1.96671 \times 10^{-14}\ T_e^5$

[b] $K_{D5} = 1.67959 \times 10^{-10}\ T_e - 1.22568 \times 10^{-11}\ T_e^2 + 2.19508 \times 10^{-11}\ T_e^3 - 3.01892 \times 10^{-12}\ T_e^4 + 1.2549 \times 10^{-13}\ T_e^5$

[c] $K_{N1} = 7.51 \times 10^{-9} - 1.12 \times 10^{-9}\ T_e + 1.03 \times 10^{-10}\ T_e^2 - 4.15 \times 10^{-12}\ T_e^3 + 5.86 \times 10^{-14}\ T_e^4$

[d] $K_{N2} = 8.39 \times 10^{-9} + 3.02 \times 10^{-9}\ T_e - 3.80 \times 10^{-10}\ T_e^2 + 1.31 \times 10^{-11}\ T_e^3 + 2.42 \times 10^{-13}\ T_e^4 - 2.30 \times 10^{-14}\ T_e^5 + 3.55 \times 10^{-16}\ T_e^6$

The neutral species HO_2 and O_3 are included in the model due to their production in detachment reactions (Dt_4, Dt_6 and Dt_8), which are important to the chemistry of negative ions. These molecules also react with other neutral species in the gas phase (reactions G_1–G_{10}) with relatively high rate coefficients.

Concerning the two excited species considered in the model, the metastable states $O(^1D)$ and $O_2(a^1\Delta_g)$ (also referred to as $O_2(a)$), the $O(^1D)$ metastable plays an important role in the neutral chemistry, as it participates in neutral homogeneous reactions in the gas phase (reactions G_6, G_9–G_{16}) with high rate coefficients. On the other hand, the $O_2(a^1\Delta_g)$ metastable is involved in the negative ion chemistry, taking part in formation (reaction A_4) and destruction (reaction Dt_8) processes, while also reacting with neutral molecules in the gas phase (reaction G_7).

The negative ions H^-, OH^- and O^- are included in the model, as the prevalence of anions in oxygen discharges is well known [110]. The modeling of these species has some particularities, which are detailed below.

Negative ions are charge carriers, and as such are subject to the electroneutrality condition. As explained at the beginning of the chapter, the charge density of the plasma is constant during the simulation, and the electron density is obtained by subtracting the total negative ion density from it. Thus, when negative ions are formed in the discharge, the electron density decreases. Since negative ions are only produced through electron impact detachment, it is ensured that chemical equilibrium will be reached and the simulation will be stable.

Opposite to positive ions, negative ions do not diffuse to the walls of the reactor, since, as mentioned in section 2.1.2.2, the plasma potential causes them to be trapped in the glow. They are only destroyed by gas phase processes, namely ion-ion neutralizations and detachment reactions.

It can be noticed that the negative ion H^- was not included in the previous models, even though it can be formed through dissociative attachment of the hydrogen molecule (reaction A_3). The reason for its absence is the low rate coefficient for this reaction. Assuming typical values for the electron temperature (3 eV) and the dissociation degree of H_2 (0.1), it can be shown that, in a pure H_2 plasma, the main production and destruction processes for H^- are reactions A_3 and Dt_2 respectively. In the steady state:

$$\frac{d[H^-]}{dt} = 0 \approx k_{A_3} N_e [H_2] - k_{Dt_2} [H^-][H] \tag{3.22}$$

Then the H^- concentration can be obtained as:

$$[H^-] \approx \frac{k_{A_3}[H_2]}{k_{Dt_2}[H]} N_e \sim 10^{-3} N_e \tag{3.23}$$

Which is a low value, making its contribution to the plasma chemistry negligible. In the H_2 + O_2 plasma, however, the main production mechanism for H^- is the dissociative attachment of H_2O (reaction A_2), which has a much higher rate coefficient than reaction A_3, so this negative ion can reach significant concentrations and thus should be included in the model. This can be seen clearly in section 6.2.3.

In contrast to the gas phase, surface chemistry is slightly simpler in this model compared to the one for H_2 + N_2 for two main reasons. First, the formation of H_2O in the reactor walls needs one less step than NH_3, reducing the number of intermediate species and reactions. Second, only E-R reactions have been included in this model, given that the high activation energies of L-H reactions render their contribution negligible. For instance, the L-H water production reactions, OH(s) + H(s), and OH(s) + OH(s), have activation energies of ~ 1.1 eV and ~ 0.65 eV respectively [111], much higher than the 0.2 eV of the equivalent reaction for NH_3 formation included in the H_2 + N_2 model. The list of surface reactions for this model is shown in Table 3.11.

Table 3.11. Wall reactions for positive ions (neutralization) and neutrals (adsorption and recombination) in the $H_2 + O_2$ model.

	Wall neutralization	γ		**Heterogeneous reaction**	γ	**Ref.**
K_1	$H^+ + Wall \rightarrow H$	1	W_1	$H + F_s \rightarrow H(s)$	1	*e*
K_2	$H_2^+ + Wall \rightarrow H_2$	1	W_2	$H(s) + H \rightarrow H_2 + F_s$	0.0035	[112]
K_3	$H_3^+ + Wall \rightarrow H_2 + H$	1	W_3	$O + F_s \rightarrow O(s)$	1	*f*
K_4	$O^+ + Wall \rightarrow O$	1	W_4	$O(s) + O \rightarrow O_2 + F_s$	0.024	*f*
K_5	$O_2^+ + Wall \rightarrow O_2$	1	W_5	$OH + F_s \rightarrow OH(s)$	1	*e*
K_6	$OH^+ + Wall \rightarrow OH$	1	W_6	$H(s) + O \rightarrow OH(s)$	0.006	*f*
K_7	$H_2O^+ + Wall \rightarrow H_2O$	1	W_7	$H + O(s) \rightarrow OH(s)$	0.002	*f*
K_8	$H_3O^+ + Wall \rightarrow H_2O + H$	1	W_8	$OH(s) + H \rightarrow H_2O + F_s$	0.004	*f*
K_9	$HO_2^+ + Wall \rightarrow O_2 + H$	1	W_9	$OH + H(s) \rightarrow H_2O + F_s$	0.005	*f*
			W_{10}	$O(s) + H_2 \rightarrow H_2O + F_s$	5×10^{-5}	*f*
			W_{11}	$O(^1D) + Wall \rightarrow O$	1	[93]
			W_{12}	$O_2(a) + Wall \rightarrow O_2$	0.007	[113]

e : Adsorption of atoms and radicals is assumed to have a probability of 1

f : Assumed in this work

Chapter 4.

H_2 + Ar plasmas

The argonium ion, ArH^+, has been recently detected in space in the course of the Herschel mission [114] through emission lines of $^{36}ArH^+$ observed in spectra from the Crab Nebula. It is the first noble gas compound observed in space. In that article, Barlow *et al.* suggested that ArH^+ is formed most likely in transition zones between fully ionized and molecular gas and that electron collisions provide the likely excitation mechanism. Shortly afterwards, Schilke *et al.* [115] assigned to $^{36}ArH^+$ a previously unidentified absorption at 617.5 GHz in the diffuse interstellar medium (ISM), present in spectral line surveys towards many galactic sources. From a careful analysis of the observations using a chemical model for diffuse molecular clouds, the authors concluded that ArH^+ should be a very good tracer of gas with very low (10^{-4}–10^{-3}) fractional abundances of H_2.

ArH^+ is usually produced in laboratory plasmas containing Ar and H_2. Due to their technical applications such as elemental analysis [116-119], sputtering [120-123], film deposition [10,11], hydrogenation [124,125], or functionalization of nanostructured materials [17,126], the properties of these type of discharges have been studied both experimentally and theoretically by a number of research groups [63,67,68,90,127-137]. In some of these works, the ion chemistry of the discharges has been specifically studied. Bogaerts and co-workers developed theoretical models for different types of glow discharges [68,90,134]. In their hybrid Monte Carlo fluid model for dc discharges [68], Bogaerts and Gijbels simulated the conditions of a typical glow discharge used for analytic mass spectrometry (Ar + 1 % H_2, 70 Pa). The model calculations yielded an ionic distribution dominated by Ar^+, with ArH^+ and H_3^+ having also a significant presence, and with very small amounts of H^+ and H_2^+. Qualitatively similar ion distributions were also obtained in the modeling of a higher pressure (850 Pa) Grimm type dc discharge [134] and of a capacitively coupled radio frequency (rf) discharge [90] at lower pressures (7–33 Pa).

These models helped identify the main processes in the discharges, but were not compared to experimental data.

Similarly, distributions of ion densities in inductively coupled rf discharges were also modeled, but not measured, in the recent works of Kimura and Kasugai [135] and Hjartarson *et al.* [67]. They used self-consistent global models to study Ar/H_2 discharges with variable mixture proportions in the pressure ranges 2.7–8 Pa and 0.13–13 Pa, respectively. In both works, they found that the major ions were also Ar^+, H_3^+ and ArH^+, with different relative concentrations depending of the pressure and mixture conditions, but in no case was ArH^+ the prevalent ion.

Sode *et al.* [136,137] performed a detailed comparison of experimental ion distributions and model calculations for Ar/H_2 inductively coupled rf plasmas for a pressure of 1 Pa. In contrast with the calculations mentioned in the previous paragraph [67,135], the measurements of Sode *et al.* indicated that ArH^+ was the dominant ion over a wide range of Ar fractions, where it accounted for roughly 60 % of the positive charge. Their model reproduced the overall trends in the evolution of the ion distributions, but underestimated the measured ArH^+ concentration and overestimated the densities of the hydrogenic ions. Sode *et al.* [137] suggested that their measurements and calculations would be in much better agreement by assuming a zero rate coefficient for the $ArH^+ + H_2 \rightarrow H_3^+ + Ar$ reaction, instead of the large literature values currently used, which are in the upper half of the 10^{-10} cm^3 s^{-1} range (see ref. [65] and references therein).

A comparison of experimental and calculated ion density distributions in Ar/H_2 plasmas was also reported in a previous study for a dc hollow cathode discharge performed in the same experimental setup as this work [63]. The experiments were carried out at pressures of 0.7 and 2 Pa for a fixed H_2 fraction of 0.85. Due to the low amount of Ar in the mixture, the discharges were dominated by hydrogenic ions (H_3^+ at 2 Pa and H_3^+ and H_2^+ for 0.7 Pa), but ArH^+ ions were second in importance. Small amounts of Ar^{2+} ions were also measured. The experimental ion distributions could be well accounted for by a kinetic model if a tiny fraction of high energy electrons (> 50 eV) was used in the calculations.

Hollow cathodes and other types of dc glow discharges were used for spectroscopic studies of the ArH^+ ion [138-144]. In order to improve detection, the concentration of the ion was empirically maximized, and it was found that the largest ArH^+ signals were obtained with a small H_2 fraction [139-143], or even with no H_2 at all [138,144] in the precursor mixture. This apparent paradox suggests that molecular hydrogen from small impurities or from the reactor walls would be adequate to produce significant amounts of ArH^+ in the plasma. In general, these discharges were run at higher pressures (> 30 Pa) than those commented on the previous paragraphs.

In the present work, the details of the ionic chemistry in Ar/H_2 plasmas and, in particular, of the processes leading to the production and destruction of ArH^+, have been studied for different plasma conditions. Hollow cathode discharges, spanning the whole range of mixture proportions for two different pressures, 1.5 and 8 Pa, have been investigated. The relative densities of the various ions have been found to vary markedly between these pressures over the range of mixture proportions sampled. The kinetic model has provided a clear picture of the chemistry underlying the observed ion distributions and has helped identify the main sources and sinks of the major plasma ions (Ar^+, ArH^+ and H_3^+). The results are discussed and whenever possible compared to previous works.

4.1 Experimental results

The chemistry of H_2 + Ar mixtures has been studied at two different pressures, 1.5 Pa and 8 Pa. For each of them, experiments have been carried out at several different mixture ratios, ranging from pure Ar plasma to pure H_2 plasma. Concentrations of the positive ions, as well as the electron temperatures and densities, have been determined for the different experimental conditions and are presented below. As there are no neutral stable species formed in this kind of discharges, no experimental results will be shown for neutrals besides initial precursor concentrations (mixture ratios).

4.1.1 Electron temperatures and densities

Values of the electron temperature and electron density have been obtained from the measurements with the double Langmuir probe for each of the pressures and mixtures studied.

The results for the lowest pressure, 1.5 Pa, are displayed in Figure 4.1, along with the values employed in the kinetic modeling. For this pressure, the electron temperature remains relatively constant (within the experimental error), whereas the electron density presents a steady decrease with growing H_2 content in the mixture.

The situation at 8 Pa is somewhat different, as can be seen in Figure 4.2. It can be noted that the measurements are concentrated in the lower H_2 concentrations. This was done to increase the number of experimental points in the narrow window in which the ArH^+ ion prevails, as will be seen in the next section.

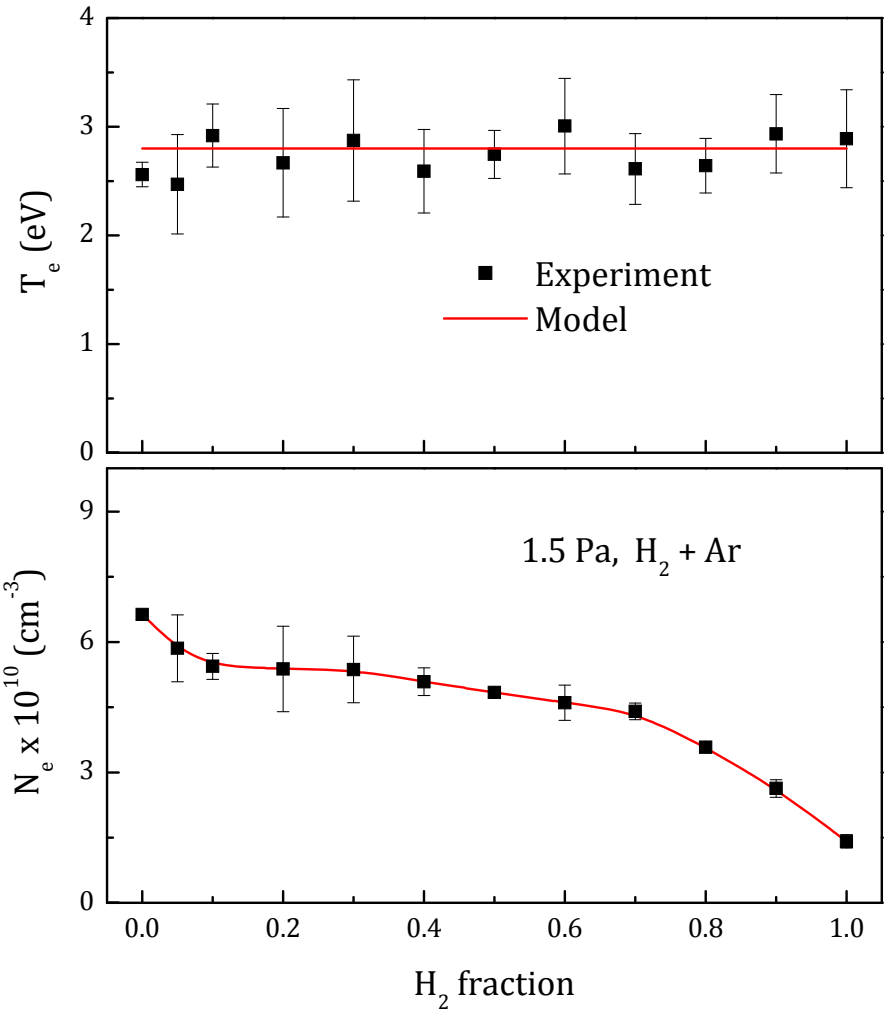

Figure 4.1. Electron temperature and electron density measured with the Langmuir probe (black squares) and values used in the model (red lines) for the H_2 + Ar plasma at 1.5 Pa.

At this higher pressure, the electron temperature increases as hydrogen is introduced in the mixture, reaching a maximum at ~ 10 % H_2, and slowly decreasing towards the higher H_2 fractions.

The electron density is globally higher than in the previous case, as could be expected, but shows a different dependence on the H_2 fraction. It decreases abruptly from the pure Ar plasma to ~ 10 % H_2 mixture, remaining moderately stable for the rest of the compositions.

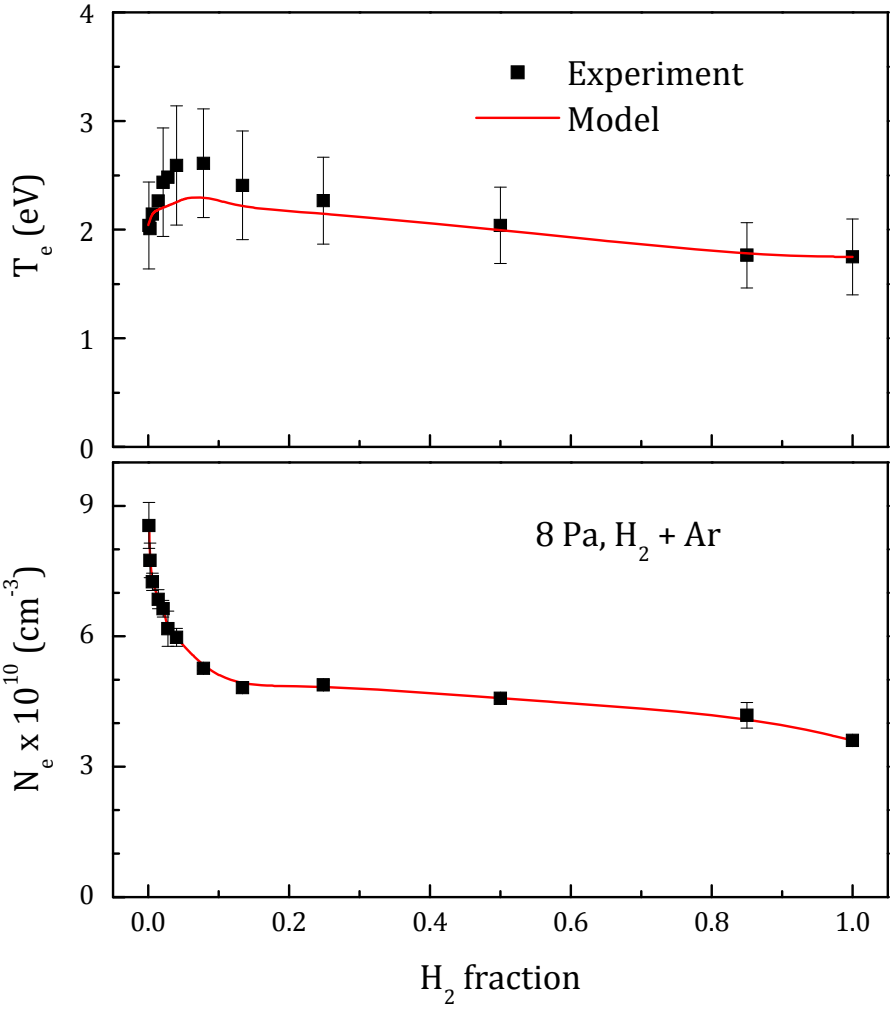

Figure 4.2. Same as Figure 4.1, but for a pressure of 8 Pa.

The observed behavior of the electron density can be associated with the ionic composition of the discharge. The plasma current is approximately proportional to the charge density and inversely proportional to the square root of the mean ion mass, since heavier ionic species leave the discharge at a lower rate than their lighter counterparts. Since in the experiments the plasma current is kept constant, the charge density will be roughly proportional to the square root of the mean ion mass. This is illustrated in Figure 4.3, where the experimental values of the electron density are compared to the square root of the mean ion mass, obtained from the PPM measurements (see next section).

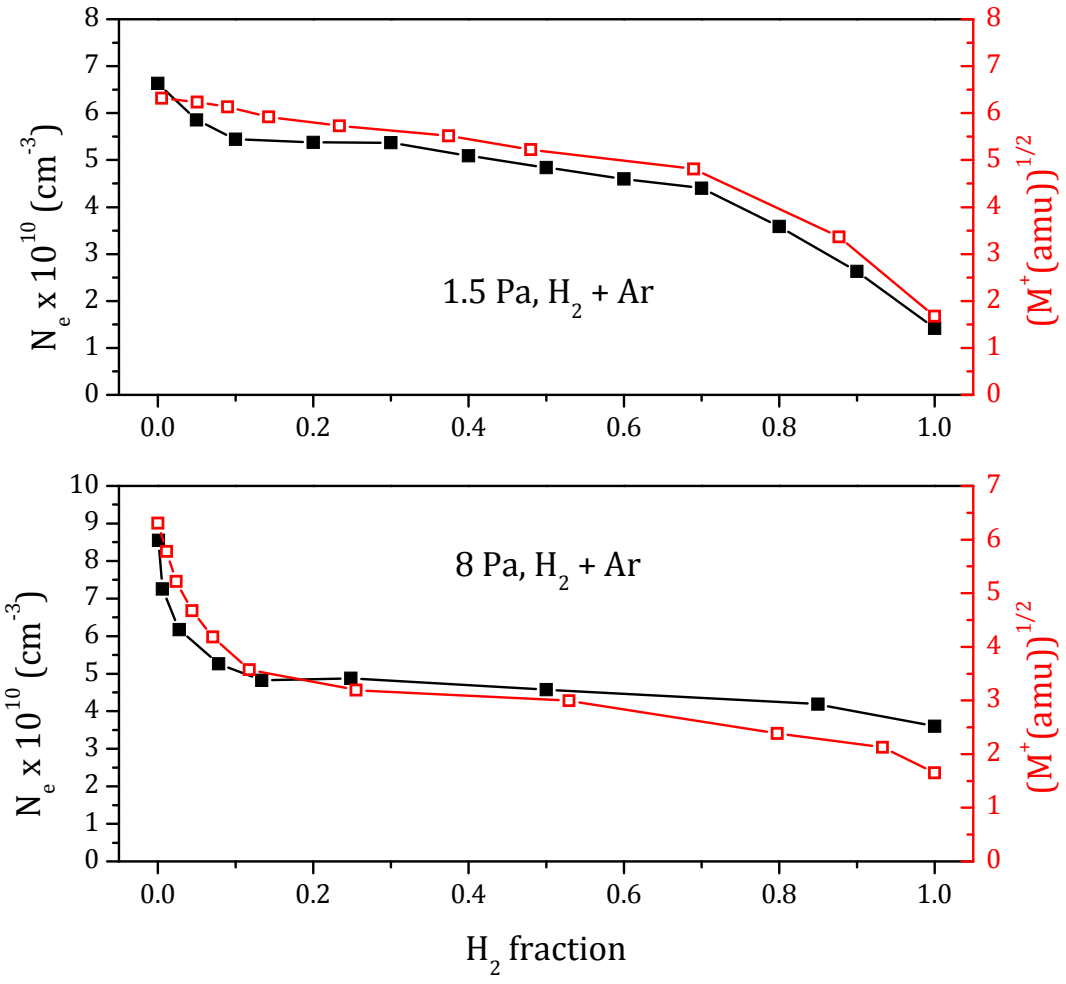

Figure 4.3. Electron density (black squares) and mean ion mass (red open squares) for the H_2 + Ar mixtures studied at 1.5 Pa (upper panel) and 8 Pa (lower panel). Some experimental points have been removed for clarity. Lines are only given as guides to the eye.

When the heavy species dominate the ion distribution, the flow of charged species to the walls is slower. The charge density in a discharge with heavy ions (in this case, Ar-rich mixtures) will be higher than in one dominated by lighter species (H_2-rich mixtures).

4.1.2 Ion concentrations

The abundances of the different positive ions in the discharge have been determined with the plasma monitor.

The relative concentrations of the ions in the discharge at 1.5 Pa can be seen in Figure 4.4.

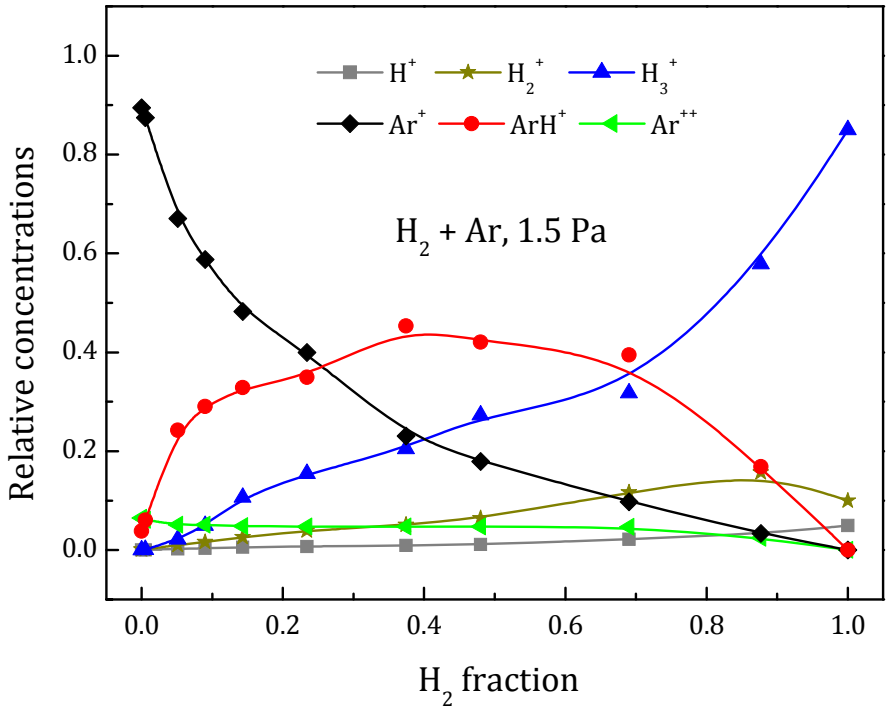

Figure 4.4. Relative concentrations of positive ions in the 1.5 Pa H_2 + Ar plasma at various mixture ratios. Lines are only a guide to the eye.

The major ions in this plasma are Ar^+, ArH^+ and H_3^+. The shape of the ion distribution is rather symmetric, with Ar^+ dominating at low H_2 fractions (~ 0–0.3), H_3^+ dominating at high H_2 fractions (~ 0.7–1), and ArH^+ being the major ion for the intermediate mixtures, reaching concentrations of ~ 40 %. The other hydrogenic ions, H^+ and H_2^+, have low abundances and are relevant for H_2 fractions close to unity, with H^+ concentrations only being noticeable (> 1 %) for mixtures with more than 50 % H_2. Ar^{2+} is present in the discharge with concentrations of ~ 5 % for the majority of the H_2/Ar ratios, only disappearing from the discharge when the H_2 fraction is close to 1.

The situation at 8 Pa is quite different, as displayed in Figure 4.5. In this case, the relevant changes in ion composition are limited to the lower H_2 fractions (< 0.2). A detailed representation of the ion composition for Ar-rich mixtures is given in the lower panel of the figure.

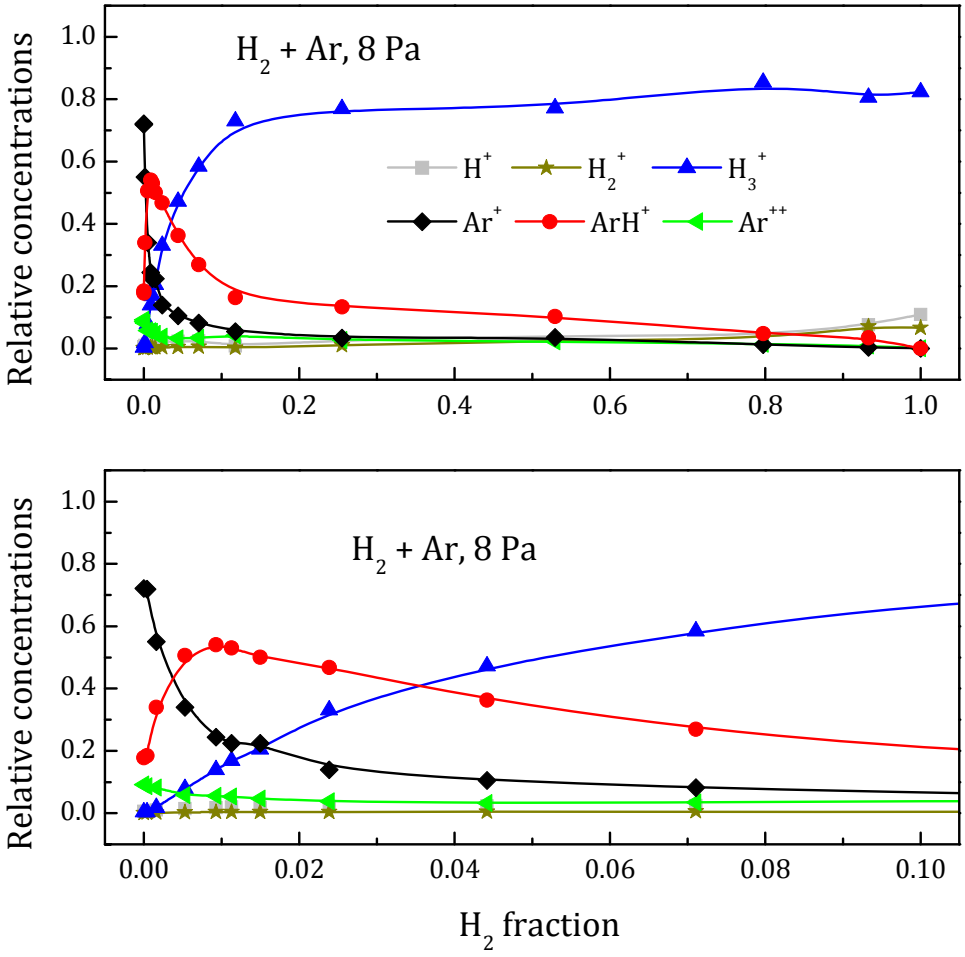

Figure 4.5. Upper panel: relative concentrations of positive ions in the 8 Pa H_2 + Ar plasma. Lower panel: detail for the lower H_2 fractions. Lines are only a guide to the eye.

Ar^+ ions are dominant only when the precursor composition is almost pure Ar. As soon as a slight amount (~ 0.5 %) of H_2 is present in the discharge, the concentration of ArH^+ grows and Ar^+ disappears. The region where ArH^+ ions are dominant is also very narrow, as H_3^+ grows steadily with the H_2 fraction, surpassing the mixed ion when the mixture is just ~ 3 % H_2. Towards higher H_2 precursor concentrations, ArH^+ decreases quickly and relatively stabilizes at ~ 20 % H_2, whereas H_3^+ quickly increases and stabilizes in the same point. Between ~ 0.2 and 0.9 H_2 fractions the situation changes very little, with H_2^+ and H^+ appearing only at the very end of the mixture spectrum. For this pressure, Ar^{2+} reaches a peak concentration of ~ 10 % for the pure Ar plasma, and constantly declines as the amount of H_2 in the discharge is increased.

4.2 Model simulations

In order to better understand the ion distributions determined experimentally, simulations with the kinetic model described in section 3.4.1 have been carried out. For each of the two pressures studied, a different set of input parameters has been used, and there is also a difference in the value of the rate coefficient for reaction 18 ($H_3^+ + Ar \rightarrow ArH^+ + H_2$) of Table 3.2.

The values for the electron temperature and density used in the model were shown in Figure 4.1. For the electron density, the experimental values have been used directly in the model, since the result of the simulation does not depend greatly on them. However, in the case of the electron temperature, adjustments have been made (mostly within the margins of error) to obtain a better fit for the concentrations of the different species, as a slight variation in the temperature can induce major changes in the chemistry of the discharge. For the lowest pressure, a constant T_e = 2.8 has been assumed for all mixtures, whereas in the 8 Pa case the electron temperature values used in the model are consistently lower than the experimental ones for the lower H_2 fractions.

The k_{18} rate coefficient may be dependent on the internal excitation of the H_3^+ ion, as is discussed in the next section. Due to this, two different values have been used in the model simulations. A higher value for this coefficient ($^H k_{18}$ = 3.65 × 10^{-10} cm^3 s^{-1}) is given in the compilation by Anicich [65] as the recommended value. A lower value ($^L k_{18}$ = 1 × 10^{-11} cm^3 s^{-1}) has been taken from the tables of Albritton [66]. Simulations at 1.5 and 8 Pa using both of these values of the rate coefficient can be seen in Figure 4.6 and Figure 4.7, together with the previously discussed experimental values.

For the lower pressure, the best agreement between model and experiment is achieved with the higher value of k_{18}. Using $^L k_{18}$, the simulated concentrations of ArH^+ are globally lower than the experimental ones, and conversely H_3^+ grows quicker than observed, crossing the Ar^+ curve at a lower H_2 fraction than in the experiment.

On the other hand, with $^H k_{18}$, the ArH^+ densities obtained are higher than in the previous case, with a maximum ArH^+ concentration of ~ 40 % in the range of 0.3–0.5 H_2 fraction, which is comparable to the experimental results. The crossing of the Ar^+ and H_3^+ curves is also well reproduced, both in the concentration of the species and in the mixture ratio in which it occurs. However, the interval of dominance for ArH^+ is narrower in the simulations, as the H_3^+ concentration grows quicker with H_2 fraction than what is observed experimentally.

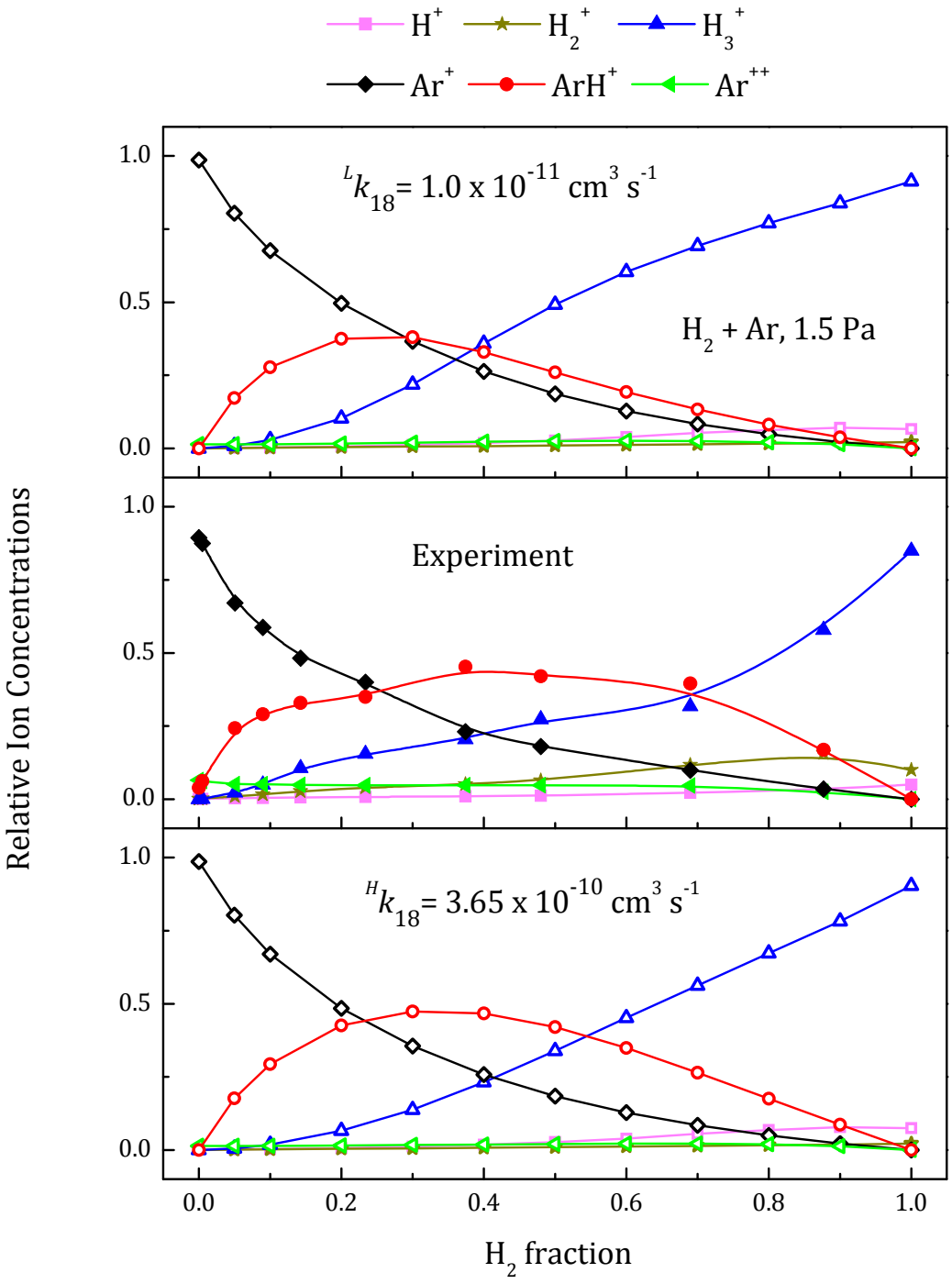

Figure 4.6. Model simulations with a low (upper panel) and high (lower panel) value of the k_{18} rate coefficient, and experimental values (middle panel) for the relative ion concentrations in the H_2 + Ar plasma at 1.5 Pa.

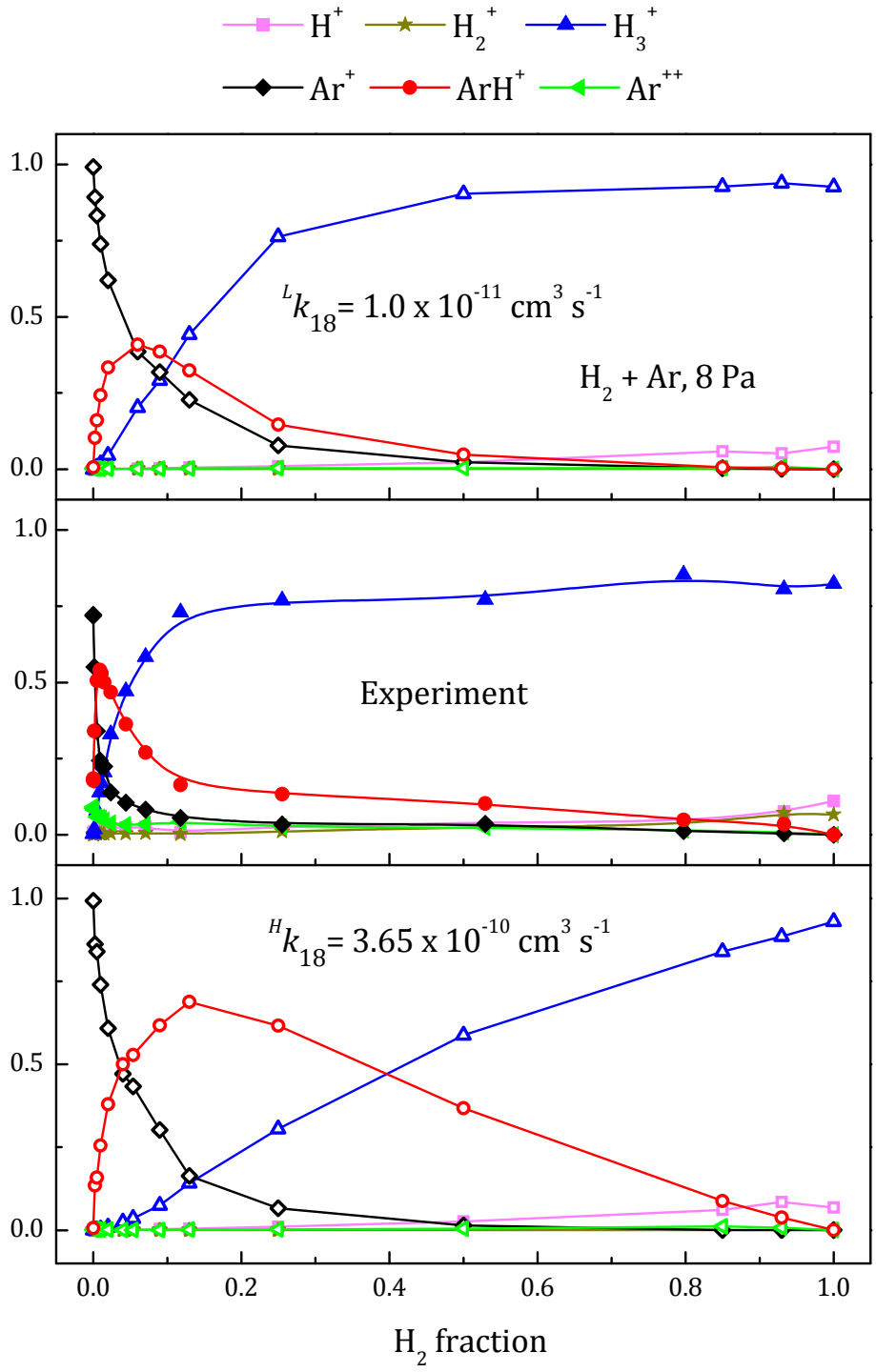

Figure 4.7. Same as Figure 4.6, but for a pressure of 8 Pa.

For the 8 Pa discharge, the simulations with ${}^{H}k_{18}$ are much less satisfactory than in the previous case. The global trends are reproduced, as the maximum for ArH^+ is displaced to lower H_2 fractions than in the 1.5 Pa plasma, and the growth of H_3^+ is faster than in the lower pressure. Quantitative agreement, however, is poor, with the peak of ArH^+ concentration occurring at a H_2 fraction of ~ 0.1, as opposed to the experimental ~ 0.01. The gradual decrease of ArH+ with growing H_2 content is smoother than observed, and, as a consequence, H_3^+ increases much more slowly than it should.

When ${}^{L}k_{18}$ is used in the model, the ion distribution obtained is closer to the experimental one. The maximum value of the ArH^+ density takes place at ~ 0.05 H_2 with a narrower peak, and the growth of H_3^+ is much more similar to the experimental trend. However, the evolution of the major ions with growing H_2 content is still too smooth, as the ion distribution should stabilize around the 0.2 fraction instead of the ~ 0.5 obtained with this simulation.

The minor ions in these distributions can be seen in detail in the logarithmic representations of Figure 4.8 and Figure 4.9, where only the simulations with the better agreement (${}^{H}k_{18}$ for 1.5 Pa and ${}^{L}k_{18}$ for 8 Pa) are used for comparison.

In the 1.5 Pa discharge, the agreement is good for most of the minor ions. The growth of H^+ and H_2^+ is accounted for and their concentrations are essentially well reproduced. In the 8 Pa discharge, H^+ behavior is very similar to the one observed experimentally, especially for H_2-rich mixtures, although H_2^+ is underestimated in the simulations by an order of magnitude The concentration of Ar^{2+} ions in the simulations is directly related to the amount of high energy electrons present in the discharge. A small fraction ($< 5 \times 10^{-4}$) of these electrons is enough to justify the experimental concentrations. Larger high energy electron fractions affect the ionization rates of Ar and H_2 noticeably, resulting in a less satisfactory reproduction of the ion concentrations, while lower fractions result in fewer Ar^{2+} ions in the plasma.

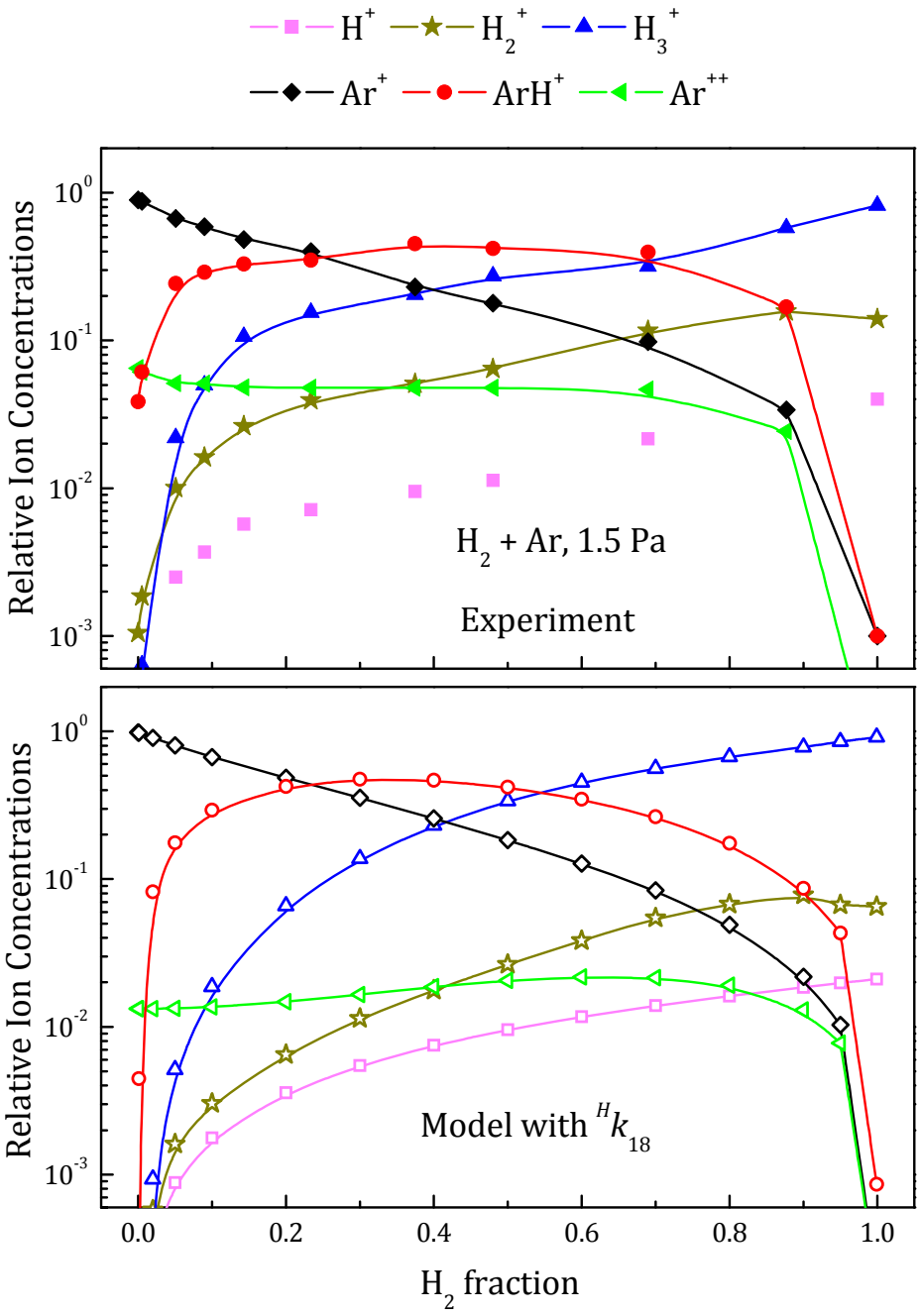

Figure 4.8. Ion distributions at 1.5 Pa in logarithmic scale. Upper panel: experiment. Lower panel: model.

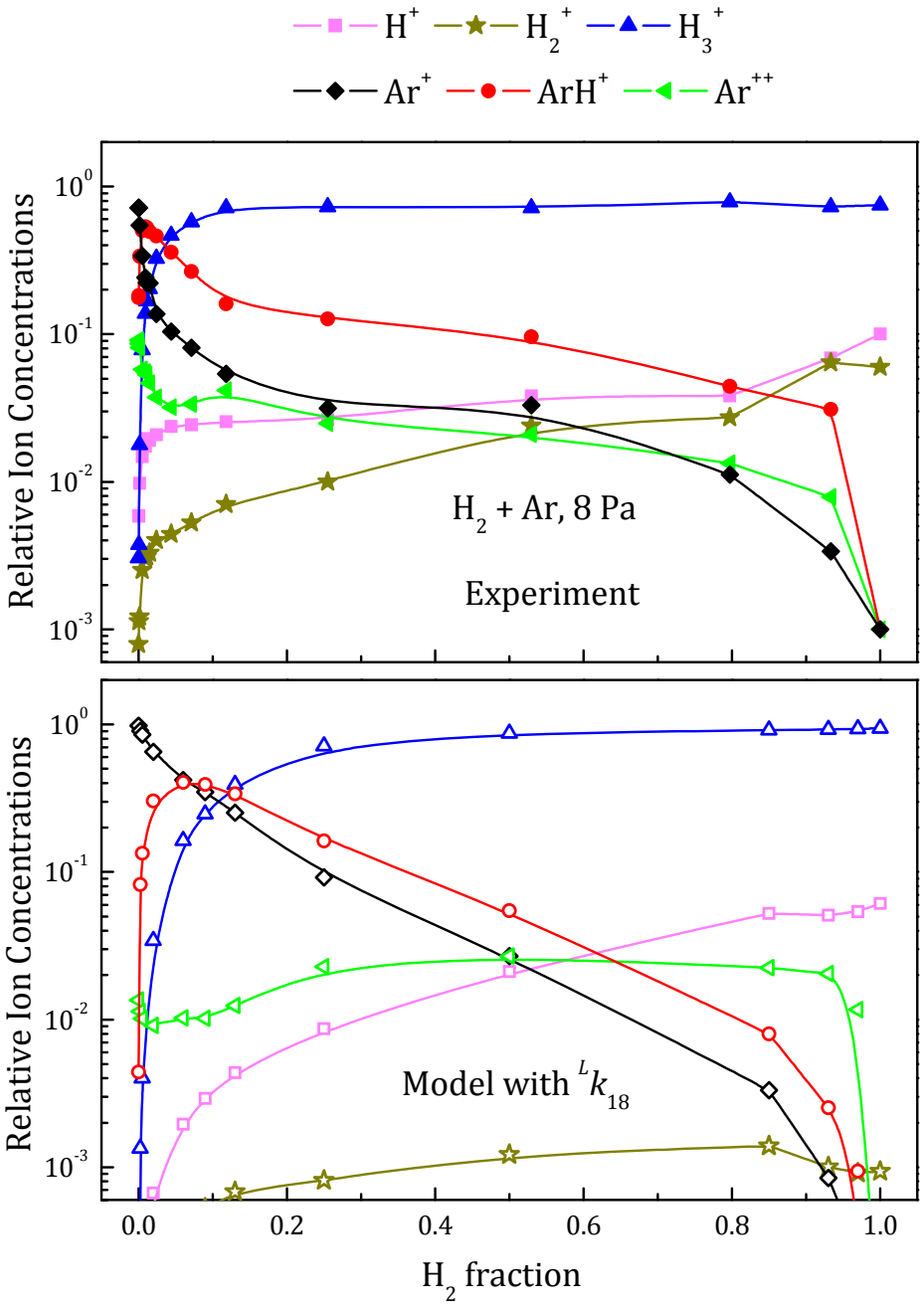

Figure 4.9. Same as Figure 4.8, but for the 8 Pa discharge.

4.3 Discussion

4.3.1 Main reaction mechanisms

The chemistry of the major ions in these plasmas is relatively simple and can be reduced to the set of reactions shown in Table 4.1, and their rate coefficients are displayed in Figure 4.10 as a function of the electron temperature. It is worth mentioning that for ionizations by electron impact (reactions 7 and 14) the rate coefficients change more than three orders of magnitude for a variation of T_e of less than 3 eV.

Table 4.1. Main processes in the chemistry of the major ionic species Ar^+, ArH^+, and H_3^+.

	Process	**Rate coefficient, k^A ($cm^3\ s^{-1}$)**
7	$H_2 + e \rightarrow H_2^+ + 2e$	$3.12 \times 10^{-8}\ T_e^{0.17} \exp(-20.08/T_e)$
10	$H_2^+ + H_2 \rightarrow H_3^+ + H$	2.0×10^{-9}
14	$Ar + e \rightarrow Ar^+ + 2e$	$2.53 \times 10^{-8}\ T_e^{0.5} \exp(-16.3/T_e)$
17	$H_2^+ + Ar \rightarrow ArH^+ + H$	2.1×10^{-9}
18	$H_3^+ + Ar \rightarrow ArH^+ + H_2$	${}^H k_{18} = 3.65 \times 10^{-10}$ ${}^L k_{18} = 1 \times 10^{-11}$
20	$Ar^+ + H_2 \rightarrow ArH^+ + H$	$0.98 \times 8.9 \times 10^{-10}$
21	$ArH^+ + H_2 \rightarrow H_3^+ + Ar$	6.3×10^{-10}

The first step for the formation of the ions is the ionization from the neutral precursors, Ar and H_2. Given that the rate coefficient for the ionization of Ar (k_{14}) is ~ 5 times higher than that of H_2 (k_7) for all the T_e interval considered, Ar^+ will be the main ion formed by electron impact ionization for the great majority of mixtures.

The rest of the major ions are then formed through ion-molecule reactions that do not depend on the electron temperature. Ar^+ reacts with H_2 to form ArH^+ (reaction 20) with a high rate coefficient. When the electron temperature is close to 2 eV, which is in the range of values measured at 8 Pa, this rate coefficient is much higher than the one for the direct ionization of Ar. Given this condition, in a mixture with sufficient H_2 content, Ar^+ will be quickly transformed into ArH^+. At ~ 3 eV (1.5 Pa), however, the values of these rate coefficients are much closer, and thus there is a smoother transition from Ar^+ to ArH^+ as the H_2 content of the discharge grows. Reaction 17 also contributes to the formation of ArH^+, in this case from Ar and H_2^+, but should not be relevant since they are not both present in the discharge in significant amounts for any mixture ratio.

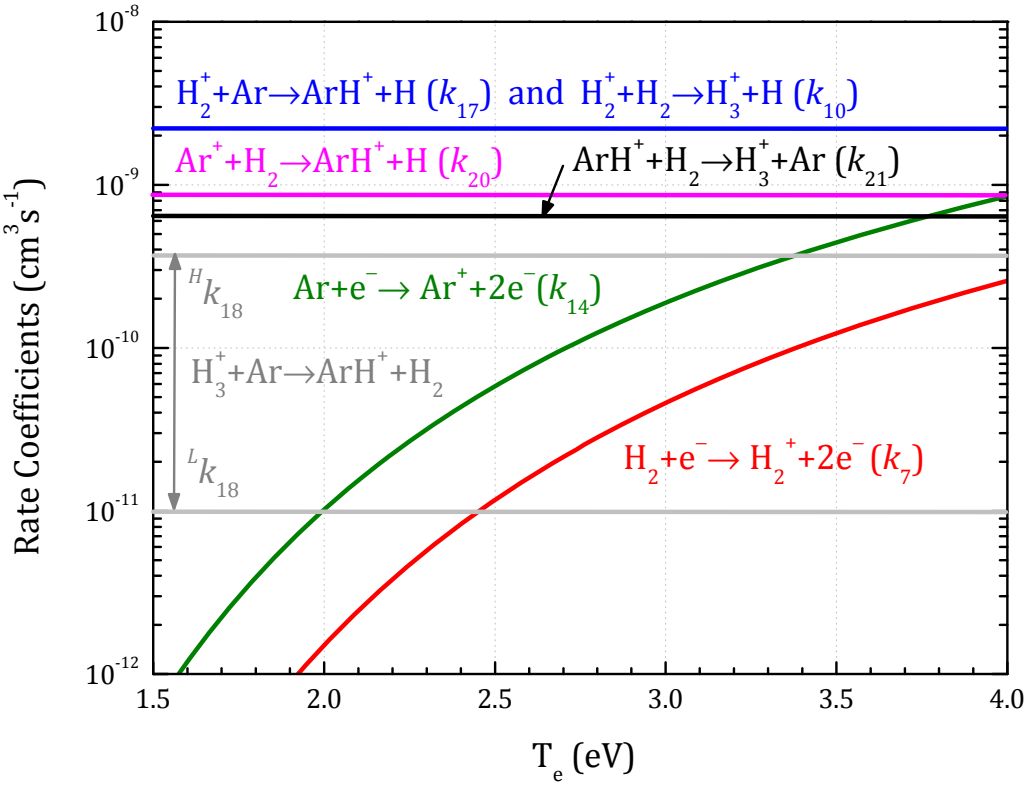

Figure 4.10. Rate coefficients as a function of the electron temperature for the most relevant reactions involving the major ions in the H_2 + Ar discharge.

The last step of this ion chemistry is the formation of H_3^+ from ArH^+ through collisions with H_2 (reaction 21). This is a reversible process, as H_3^+ can react with Ar atoms to form ArH^+ again (reaction 18). Since two different values for the k_{18} rate coefficient are considered, the equilibrium will be markedly affected by this decision. When $^H k_{18}$ is chosen, a greater amount of H_3^+ ions will react to form ArH^+, thus delaying the region of H_2 fractions where H_3^+ is dominant, as happens for 1.5 Pa. Conversely, if $^L k_{18}$ is used, H_3^+ formed in reaction 21 will be less likely to react again, and H_3^+ will be the major ion for much lower H_2 fractions, which is the case at 8 Pa. Reaction 10, which accounts for the formation of H_3^+ from H_2^+, is mainly relevant for the mixtures containing close to 100 % H_2, but less important for the other mixture ratios. In conclusion, the chemistry of the major ions depends heavily on the electron temperature, which is significantly dependent on the gas pressure and determines the relative relevance of electron impact reactions versus ion-molecule reactions, and on the value of the rate coefficient for reaction 18.

The relevance of internal energy effects in interconversion reactions 18 and 21 has been studied in previous works [145-149]. Reaction 21, forming H_3^+ from ArH^+, is

exothermic by ~ 0.55 eV [148]. This expectedly leads to a high rate coefficient (~ 5–15 × 10^{-10} cm^3 s^{-1}), as has been determined in a variety of works cited in the compilation by Anicich [65]. The value used in the model, k_{21} = 6.3 × 10^{-10} cm^3 s^{-1}, which is the recommended value from this compilation, should then be a good assumption. Since the reaction is exothermic, internal excitation of the reactants should not play a major role in the reaction rate.

The case is different for reaction 18, leading from H_3^+ to ArH^+. As the reverse reaction of the previous one, it is endothermic by 0.55 eV. The recommended value by Anicich [65] is k_{18} = 3.65 × 10^{-10} cm^3 s^{-1}, which is what has been taken as ${}^{H}k_{18}$. This value, relatively close to the one taken for k_{21}, corresponds to ion-cyclotron resonance (ICR) measurements by Bowers and Elleman [150]. Later measurements by Roche [151] in a flow reactor suggested however that the value of the rate coefficient should at least be an order of magnitude lower than that of reaction 21. Following these results, Albritton [66] gave an upper limit for the rate coefficient of k_{18} = 1 × 10^{-11} cm^3 s^{-1}, which is the value taken for ${}^{L}k_{18}$.

This large discrepancy between the two values of the rate coefficient could be due to the different experimental techniques employed by the two groups. In the experiment by Bowers and Elleman, the source of the reacting H_3^+ ions is reaction 10, between H_2^+ ions and H_2 molecules. This reaction is highly exoergic (1.72 eV) [152], and, as noted by the authors, a large part of this energy could be stored as vibrational energy of the formed H_3^+ ion. Due to the low pressure of the ICR measurements, this vibrational excitation would not be significantly deactivated by collisions, so the actual measurements would correspond to the reaction $[H_3^+]^* + Ar \rightarrow ArH^+ + H_2$. If the internal excitation of the H_3^+ ion is greater than 0.55 eV, the reaction would be exothermic and thus have a high rate coefficient, comparable to reaction 21, as is the case in these measurements. Roche *et al.* [151] used a different setup, performing their measurements in a flow reactor where collisional relaxation of the reacting H_3^+ ions is much more efficient. It could then be assumed that their measurements correspond to the actual endothermic reaction.

The high vibrational excitation of H_3^+ ions produced from collisions of H_2^+ ions with H_2 (reaction 10) can be quenched through collisions with H_2 molecules [145,146,153-155], although there is no unanimity on the actual deactivation efficiency. In H_2 + Ar plasmas, reaction 10 is only dominant when the Ar concentration is very low. For the rest of mixtures, H_3^+ main production process is reaction 21, from ArH^+. If this ArH^+ is in the ground state, then the resulting H_3^+ ion will not have enough vibrational excitation to overcome the endothermic reaction threshold and will largely remain as H_3^+. However, if the ArH^+ ion is excited, part of this excitation could be transferred to the formed H_3^+ ion, which in turn could then have enough internal energy to revert to ArH^+ through an exothermic reaction, effectively displacing the equilibrium of reactions 18 and 21 towards

ArH^+ [149]. H_3^+ ions could also be vibrationally excited through electron impact reactions [156], resulting in the same effect.

As discussed before, ArH^+ ions are mainly formed in H_2 + Ar plasmas through reaction 20 involving Ar^+ and H_2. Studies of this reaction have been performed experimentally and theoretically (see for instance [157] and [158]), but still some aspects of the state specific dynamics are not fully known, including energy partitioning between the nascent products. Trajectory calculations by Chapman [159] on a semiempirical potential energy surface indicate that a large part of the exothemicity of both reactions 17 and 20 should appear initially as vibrational excitation of the ArH^+ ion. In the presence of sufficient Ar, this vibrationally excited ArH^+ could be quenched through collisions with Ar atoms.

To summarize, although both the degree of vibrational excitation of ArH^+ and H_3^+ ions produced in reactions 20 and 21, and the relevance of the different relaxation pathways are not precisely known, collisional relaxation, in particular of the H_3^+ ion, would be expected to have a more important role in the 8 Pa discharge than in the 1.5 Pa one. As a simplification of these mechanisms the lower coefficient (${}^{L}k_{18}$) has been used for the higher pressure discharge, assuming that H_3^+ is not vibrationally excited at this pressure and the reaction taking place is endothermic. The upper and lower panels of Figure 4.7 show that the lower rate coefficient provides a better agreement to the experimental data. Even better results can be achieved if the electron temperature is lowered to 1.7 or 1.8 eV, but those values are outside the estimated uncertainty for the Langmuir probe measurements, and thus these simulations are not presented for consistency. It should however be noted that the electron temperature is determined experimentally assuming a Maxwellian energy distribution for the electrons, which is not necessarily the actual case in the plasmas studied. A selective depletion in the high energy tail of the distribution would not be noticeable in the measurements but affect the chemistry of the discharge. As such, the effective electron temperature could be lower than the one measured and better justify the observed chemistry.

The contrary happens in the 1.5 Pa discharge. In this case it is assumed that, given the low pressure, the quenching of the vibrationally excited H_3^+ is not efficient, and reaction 18 becomes effectively exothermic, with a corresponding high rate coefficient (${}^{H}k_{18}$). As before, the better results achieved with this rate coefficient could be seen in Figure 4.6.

The increase in the pressure of the discharge has, as has been shown, two major consequences for the plasma chemistry. On one hand, the electron temperature decreases as the pressure grows, drastically changing the balance between electron impact reactions and ion-molecule processes. On the other hand, the quenching of vibrationally excited H_3^+

ions is more effective, as the number of collisions is increased. These factors have an effect on the region of prevalence of ArH^+, as it is reduced to a narrower range of H_2 fractions and displaced towards Ar-rich mixtures as pressure grows. This explains the results of the spectroscopy experiments mentioned at the beginning of the chapter [138-142,144,160], where the best signals for ArH^+ are obtained in mixtures with little or no H_2. These experiments were performed in conditions either comparable to those of the 8 Pa discharge studied here, where the maximum for ArH^+ concentration is found for a mixture with ~ 1 % H_2, or mostly at higher pressures (> 30 Pa). Furthermore, mass spectrometry measurements in a different hollow cathode discharge cell [144] show that using 40 Pa of pure Ar as precursor, a tiny amount (~ 0.2 Pa) of H_2 is ejected from the cathode when the discharge is on. This small amount of H_2 provided an adequate concentration of ArH^+ for spectroscopic measurements.

4.3.2 Main formation and loss rates

Model simulations provide the rates of formation and destruction for the different species considered. In particular, the rates for the major ions can be analyzed, as is shown in Figure 4.11 and Figure 4.12 for the two different pressures, using the corresponding k_{18} value giving the best agreement with the experimental measurements.

In Figure 4.11, the rates can be seen for the lower pressure discharge. Ar^+ ions are produced through electron impact ionization, and destroyed mainly at the wall for Ar-rich mixtures, and by collisions with H_2 (reaction 20) when the H_2 fraction is high enough (> 0.2). ArH^+ is in turn produced by reaction 20 but, with high H_2 fractions, reaction 18 (H_3^+ + Ar) is comparable, while reaction 17 (H_2^+ + Ar) is comparably negligible for all mixtures. This ion is mainly destroyed by reactions with H_2 except for H_2 fractions < 0.2, in which case wall neutralization is the dominant process. Lastly, H_3^+ ions are produced through reaction 21 (ArH^+ + H_2) for almost all plasma compositions, except close to pure H_2, where reaction 10 (H_2^+ + H_2) becomes relevant. The H_3^+ ions are destroyed both at the wall and through reaction 18, with comparable rates for the whole range of mixtures.

The production and destruction rates for the 8 Pa pressure are shown in Figure 4.12, and some changes can be observed when compared to the 1.5 Pa Figure. The production of Ar^+ ions has a maximum for the mixture with ~ 20 % H_2, corresponding to the peak value of the electron temperature, and the region where wall neutralization is the dominant destruction mechanism is reduced to H_2 fractions < 0.03, while reaction 20 is the primary mechanism for the rest. ArH^+ production is simplified, as reaction 20 is the main source of these ions for all mixture ratios, and, similarly to Ar^+, wall neutralization is only dominant for very low H_2 fractions, with reaction 21 being responsible for the destruction

in the rest. Finally, H_3^+ ions have a very simple chemistry at this pressure, being formed by reaction 21 and neutralized at the wall for the whole range of mixtures.

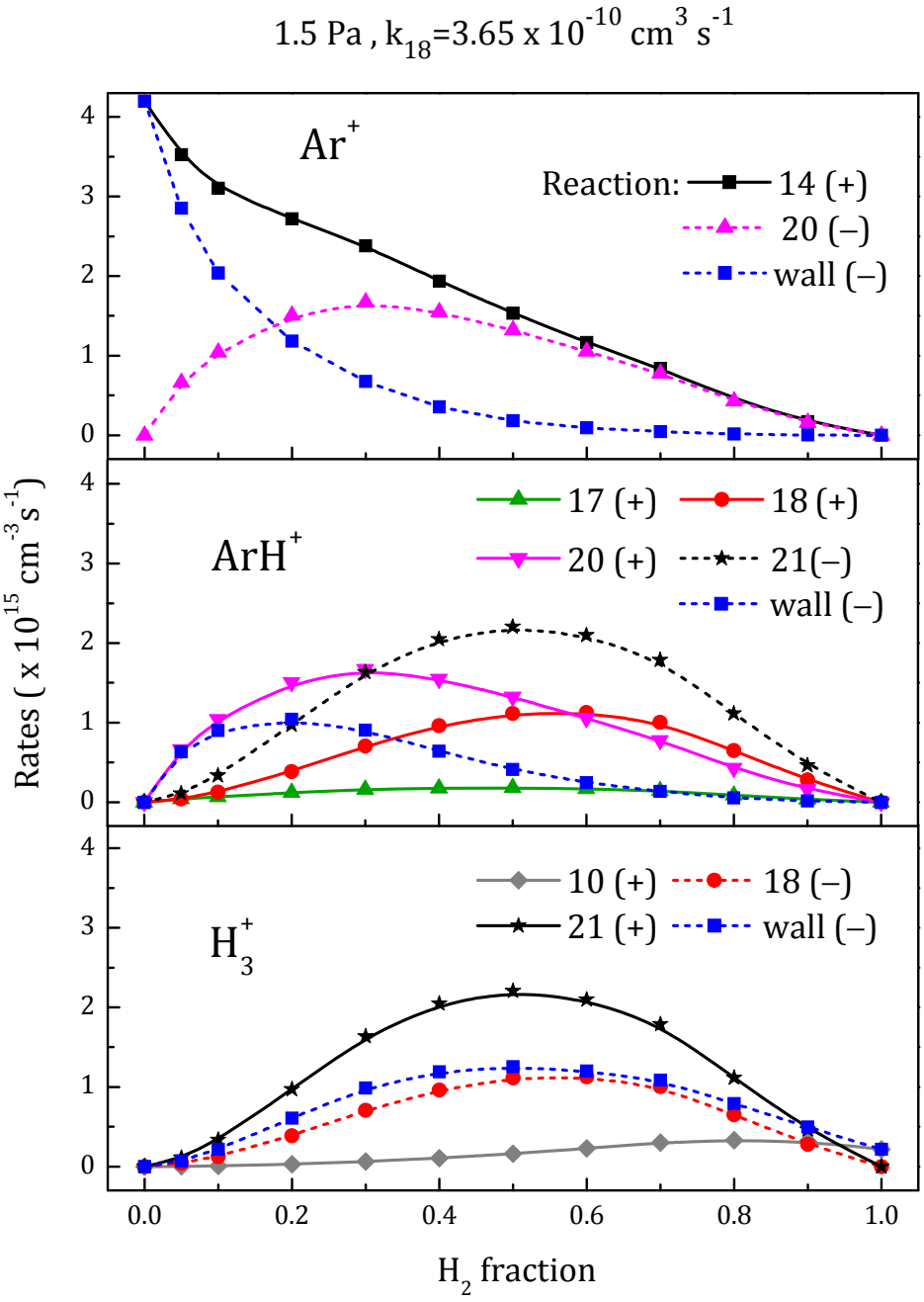

Figure 4.11. Production rates (solid lines) and destruction rates (dashed lines) for the major ions in a 1.5 Pa H_2 + Ar discharge.

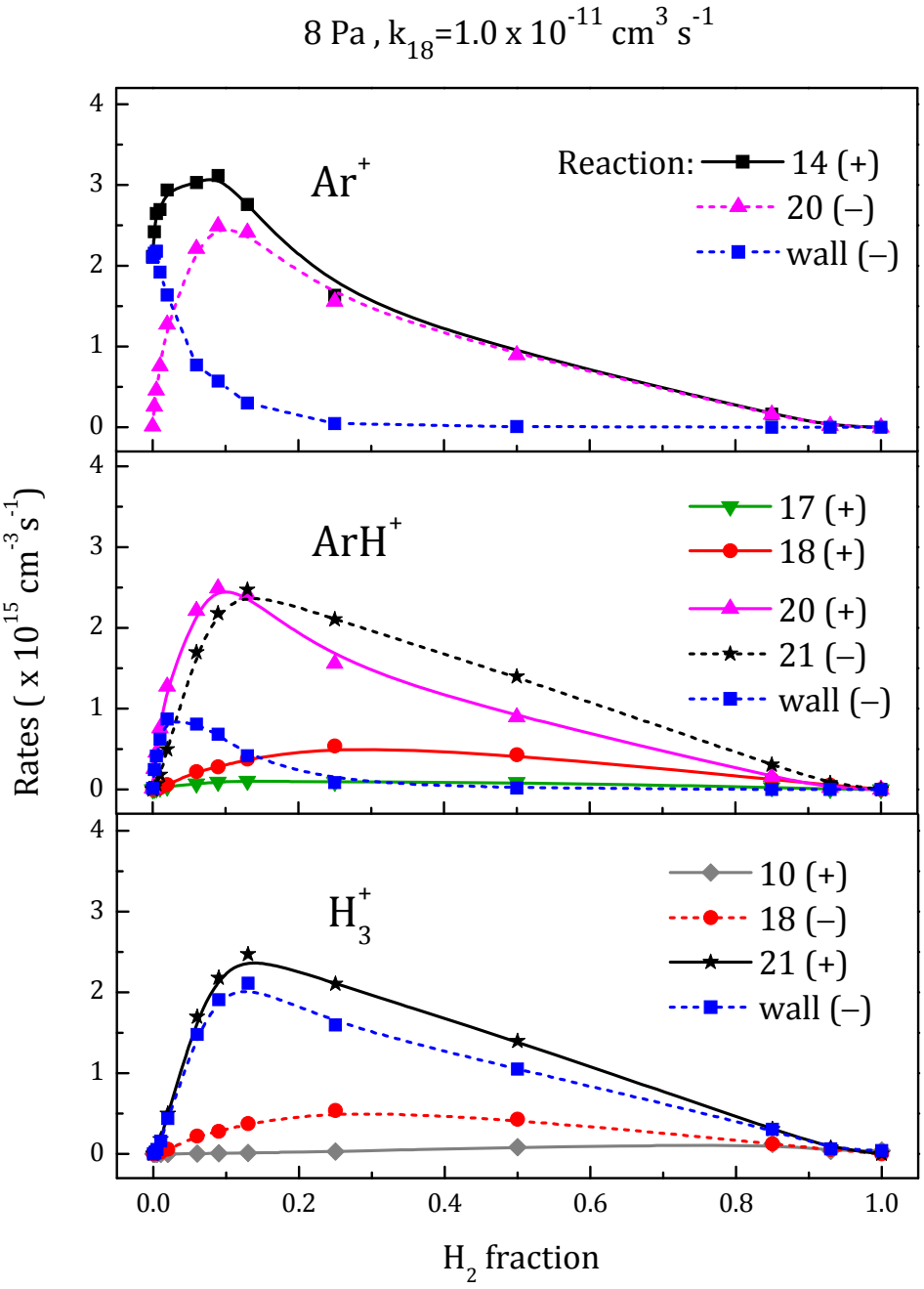

Figure 4.12. Same as Figure 4.11, but for the 8 Pa discharge.

4.3.3 Comparison with previous works

As mentioned at the beginning of this chapter, there are recent studies on the chemistry of H_2 + Ar plasmas, and in particular of the ion chemistry, in inductively coupled

rf discharges with variable mixture ratios and pressures comparable to the ones reported here [67,135,137]. As these discharges have different properties to the ones studied, a direct comparison between the results is not viable, but a qualitative analysis can be performed since the ionic chemistry is mostly determined by the electron temperature and mixture proportion.

Kimura and Kasugai [135] studied these plasmas both experimentally and with a model, but did not measure ion distributions. Their model does not include as many production mechanisms for ArH^+ as the one in this work, leaving out reactions 17 and specially 18. It also uses a value of 1.5×10^{-9} cm^3 s^{-1} for the rate coefficient of reaction 21, which destroys ArH^+ to produce H_3^+, a value twice as high as the one employed in this work. As a result, ArH^+ is never dominant in their simulations, with Ar^+ or H_3^+ being the major ion depending on the mixture and pressure (2.7 and 8 Pa). ArH^+ is the third ion in relevance in most cases and does not reach relative concentrations greater than ~ 20 %.

Hjartarson *et al.* [67] employed a global model to study these plasmas. Again in their case, the concentrations of ArH^+ obtained are too low compared with the present work. Their calculations at 1.3 Pa show a dominance of Ar^+ ions for H_2 fractions below ~ 0.7 and H_3^+ for the rest, with ArH^+ concentration being consistently less than a half than that of Ar^+ for most of the mixture ratios. Regarding the rate coefficients, these authors also employed the higher value of k_{21} that Kimura and Kasugai used, and took $k_{18} = 1 \times 10^{-11}$ cm^3 s^{-1}, which is the value used for the 8 Pa simulations ($^L k_{18}$), but found too low for the (comparable) 1.5 Pa case. Similarly to Kimura and Kasugai, they did not compare the model results to experimental data.

The study of Sode *et al.* [137] provided both experimental values for the ion concentrations and model simulations at 1.0 Pa, with electron temperatures in the range of 3–5 eV. Model simulations were performed for the whole range of mixtures, whereas experimental measurements were carried out for H_2 fractions between 0.28 and 1. Experimentally, ArH^+ was determined to be the major ion, followed by Ar^+, while H_3^+ was only dominant for the pure H_2 plasma and quickly decreased with growing Ar content, along with the rest of the hydrogenic ions. For the model, Sode *et al.* used the set of rate coefficients recommended by Anicich [65] for the relevant ArH^+ reactions. In particular, for reaction 18, they took $k_{18} = 3.65 \times 10^{-10}$ cm^3 s^{-1}, which is the same value used in this work for the 1.5 Pa simulations ($^H k_{18}$). Subsequently, their model simulations led to higher H_3^+ densities than those measured in their experiments, and correspondingly lower ArH^+ concentrations. The reasons for the disagreement are not clear. The authors noted that a rate coefficient close to zero for reaction 21 would lead to simulations in better accordance with their measurements, by drastically reducing the conversion of ArH^+ into H_3^+, and thus questioned the reliability of the recommended value [65] (6.3×10^{-10} cm^3 s^{-1}). However, this rate coefficient has been measured by several groups [65,148,161]

through different methods, and, despite some spread in the data, consistently high values have been reported. In the 1.5 Pa simulations presented here, with conditions similar to those of Sode *et al.*, the use of the recommended rate coefficients leads to a reasonably good agreement with the experimental data, as was seen in Figure 4.6. In fact, the simulations of Sode *et al.* are also in acceptable agreement with the measurements in this work, which is reasonable, given the relative similarities between the two discharges.

The chemistry of the positive ions appearing in these plasmas is also studied in the diffuse interstellar cloud model of Schilke *et al.* [115]. In this medium, ArH^+ is formed in collisions of H_2 with Ar^+ ions (reaction 20), which are in turn produced through ionization of Ar atoms by cosmic rays or X-rays. These ArH^+ ions can then be destroyed through collisions with O atoms or with H_2 molecules (reaction 21). The authors remark that the unusually low rates for photodissociation and electron impact dissociative recombination of ArH^+ increase the lifetime of the ion in the diffuse interstellar medium. When molecular hydrogen is present in sufficient concentrations ($2[H_2]/[H] > 10^{-4}$), reaction 21 is by far the most important mechanism for ArH^+ destruction, implying that this ion should not be abundant in molecular clouds. Reaction 18, converting H_3^+ into Ar^+, is also included in this model, but with a very low rate coefficient ($8 \times 10^{-10}\exp(-6400\ K/T)\ cm^3\ s^{-1}$), which seems appropriate for the vibrationally relaxed H_3^+ expected in diffuse cloud sources . In other environments like the knots and filaments of the Crab Nebula, where ArH^+ was first identified [114], internal excitation of H_3^+ by warm electrons may increase the relevance of this reaction. The reactions dominating the interstellar chemistry of ArH^+ are thus very similar to those found in the plasmas studied in this work, and in particular the disappearance of ArH^+ when H_2 is present is clearly seen in the 8 Pa discharge (Figure 4.7), where ion-molecule reactions dominate over electron impact ionization.

4.4 Summary and conclusions

The ion chemistry in cold Ar/H_2 plasmas has been investigated in hollow cathode discharges. The experiments have been carried out for total pressures of 1.5 and 8 Pa, and spanning the whole range of $[H_2]/([H_2]+[Ar])$ ratios for each of the two pressures. A simple kinetic model, which takes the measured electron temperatures and densities as input parameters, has been used to interpret the experimental data and to identify the main reaction mechanisms.

The ion distributions are dominated by three species, Ar^+, ArH^+ and H_3^+, but their relative densities markedly vary with pressure and with the Ar/H_2 mixture proportion. Special attention has been paid to the chemistry of ArH^+. This ion was prevalent in the

range 0.3 < $[H_2]/([H_2]+[Ar])$ < 0.7 in the 1.5 Pa discharge, but its predominance became restricted to $[H_2]/([H_2]+[Ar])$ < 0.05 in the 8 Pa plasma.

The kinetic model reveals two key factors for the ion chemistry in these plasmas: Electron temperature and the equilibrium of the process $H_3^+ + Ar \rightleftarrows ArH^+ + H_2$. Electron temperature, which depends on the plasma pressure, determines the rates of formation of the primary plasma ions (Ar^+ and H_2^+) that start the ion-molecule chemistry. Due to the lower ionization threshold, the rate of formation of Ar^+ is always 6–7 times larger than that of H_2^+, and Ar^+ is the dominant primary ion up to very high H_2 fractions. Electron temperature decreases roughly from 3 to 2 eV when the discharge pressure is increased from 1.5 to 8 Pa. As a result, the ionization rates of Ar and H_2 drop by a factor of ~ 30 and the ions produced through ion-molecule chemistry (ArH^+ and H_3^+) gain relevance as compared with those directly formed by electron impact. Collisions of Ar^+ with H_2 lead to an efficient production of ArH^+. This ion can then give rise to H_3^+ in subsequent collisions with H_2. The ratio between ArH^+ and H_3^+ depends strongly on the rate of the $H_3^+ + Ar \rightarrow ArH^+ + H_2$ reaction, which is endothermic and should be slow for ground state reactants, but becomes exothermic and should be much faster for an internal excitation of H_3^+ larger than 0.55 eV.

The experiments and model simulations presented here strongly suggest that H_3^+ has an appreciable degree of internal excitation in the lower pressure (1.5 Pa) plasma and that this excitation is largely quenched in the higher pressure (8 Pa) discharge. This interpretation reconciles conflicting literature values for the rate coefficient of the $H_3^+ + Ar$ reaction and leads to a reasonably good agreement between the measurements and model simulations over the whole range of conditions sampled. On the other hand, the results corroborate the comparatively large ($> 5 \times 10^{-10}$ cm^3 s^{-1}) rate coefficient for the exothermic reaction $ArH^+ + H_2 \rightarrow Ar + H_3^+$, currently accepted in the literature, but questioned in a recent work. In the absence of a mechanism that regenerates ArH^+ like the mentioned $[H_3^+]^* + Ar$ reaction, the argonium ion is efficiently removed in H_2 containing media, even if H_2 is present in very small amounts. This behavior, exemplified in the higher pressure discharge in this work, was also reported in previous spectroscopic investigations carried out in comparable discharge cells, and is also displayed by the astrochemical models applied to the recent observations of ArH^+ in the interstellar medium.

The results of this study invite further theoretical and experimental work on the detailed state-specific dynamics of the processes involved in the production, destruction, excitation and quenching of ArH^+ and H_3^+.

Chapter 5.

H_2 + N_2 plasmas

Low pressure H_2 and N_2 plasmas have been studied both experimentally [22-24,61,162-168] and theoretically [61,163,165,169,170] in the last decades. The early experimental works focused on the synthesis of ammonia [24,164,166-168]. Although no detailed mechanisms were proposed, there was a general agreement that plasma-surface interactions were responsible for NH_3 production. Different experiments demonstrated that the NH_3 concentration was dependent on the materials of the electrodes [167] or on those employed to cover the walls of the plasma reactor; platinum, stainless steel and iron being more efficient than other metals or oxides [24,162,164,166,168]. The experimental characterization of the catalysts showed that NH_x radicals were present at the surface [24,164]. The postulated mechanism involved the adsorption of excited N_2 molecules and N_2^+ ions. After their dissociation at the surface, they recombined with atomic hydrogen from the gas phase or on the surface to successively form NH_x adsorbed species. Finally, ammonia was produced and desorbed (ref. [164,166] and references therein).

From a different perspective, theoretical studies of H_2 and N_2 plasmas, mainly focused on the modeling of gas-phase volume reactions, were developed in the nineties [169,170]. However, surface processes had to be included subsequently by Gordiets *et al.* [61] in order to explain the production of ammonia and in connection with iron nitriding [165]. In their model, the authors proposed the direct adsorption of atomic N and H (instead of dissociative adsorption of N_2 and H_2 molecules) and then, the formation of NH_x species at the surface by successive hydrogenation reactions [61]. Recent experiments have supported this reaction scheme [22,163,171]. Nevertheless, the wall material did not have influence on the ammonia synthesis. This discrepancy with previous publications was explained by the high fluxes of N and H atoms reaching the surface and passivating it. Under these conditions, the formation of ammonia took place in an additional layer on top

of the passivated surface [22]. In this sense, the determination of absolute concentrations of N, H and NH_x radicals in the gas phase could help establish the mechanism of their production and their role in the reactions at the surface [22,162,163]. The interaction of these radicals with the surface of different materials was analyzed in ref. [172] and some reaction pathways could be hypothesized in spite of the complex phenomena examined.

The characterization of these radicals and atoms in H_2/N_2 containing plasmas, and their interactions with the surface, are also of high relevance for technological applications, such as thin film growth and materials processing, extended at present to the level of the nanoscale [13,18]. As an example, silicon nitride (SiN) thin films deposited by plasma-enhanced chemical vapor deposition (PECVD) are widely employed in the semiconductor industry (as a gate dielectric or passivation layer) [173] and in the photovoltaic industry [14]. Most of the deposition processes use mixtures of N_2-SiH_4 and more frequently NH_3-SiH_4, since the electron energies necessary for the dissociation of ammonia are lower than for N_2. Several groups have tried to identify the main precursors for SiN deposition with different results [12,174-176]. These works exemplify the complexity of the chemistry involved in film deposition and the necessity of getting further insight into the underlying mechanisms, since the properties of the films are correlated with the plasma composition and conditions [175] and have effects on the properties of the devices where these films are deposited [177].

In nuclear fusion research, the interest is focused on the inhibition of carbon film deposition [19]. High fluxes of hydrogen isotopes produce chemical sputtering of carbon-based materials, which leads to the formation and deposition of hydrogenated amorphous carbon (a:C-H) films in regions not directly exposed to plasma [178]. Under real operation conditions, these films would have high tritium content and pose a major problem for the handling of fusion devices [5]. Laboratory experiments with conditions similar to those present at these regions in fusion reactors have achieved the reduction of a-C:H film deposition by the introduction of N_2 in H_2/CH_4 plasmas [20]. Studies using binary and ternary mixtures of H_2, CH_4, and N_2 [179,180] or NH_3 [181], provided some insight on relevant chemical processes. However, the exact inhibition mechanism is still not well understood. Nitrogen is also employed to cool the surfaces of fusion reactors exposed to the plasma, particularly the divertor. The study of the chemistry of this species with hydrogen isotopes is relevant as it could cause issues for the correct operation of the reactor [21,182].

The importance of surface processes in plasma chemistry is not exclusively limited to plasmas produced under laboratory conditions. Gas-phase reactions alone cannot explain the abundances of gas phase H_2, NH_3, some alcohols and other complex species in interstellar clouds, and a combination of gas-phase and surface chemistry on the ice and dust particles has been invoked to account for these abundances and for the variety of

chemical species detected [31]. Research in the field is very active at the moment and theoretical efforts to improve models (see refs. [183,184] and references therein), as well as advances in experimental studies regarding surface reactions on cosmic ice and dust [185] and closely related surface processes [186], are growing fast, but a good understanding of the involved chemistry is still a pending issue.

On the other hand, ions play an important role in the synthesis of molecules in the interstellar medium and provide a partial picture of the free-electron abundance necessary to guarantee approximate electroneutrality. The electron density is relevant in astrophysics since it is believed to determine the rate of cloud collapse and star formation [187]. In addition, some ionic species can be used as tracers of interstellar neutrals. N_2, assumed to be the major reservoir of nitrogen in the interstellar medium [188], lacks a permanent dipole moment and, therefore, it has no rotational transitions to be detected by radioastronomy. Then, N_2H^+ measurements are employed to estimate the concentration of N_2 [187,189]. However, proton transfer from H_3^+ to N_2, which is considered the main route of N_2H^+ formation, is balanced by the destruction mechanism of dissociative electron recombination. The uncertainty in the concentrations of the charged particles involved, apart from the possible presence of additional sources and sinks of N_2H^+, results in errors as high as a factor of ten in the N_2 concentrations [189].

In summary, experimental plasma characterization could help to improve quantitative estimations of gas phase species in H_2 and N_2 discharges, whose presence is significant in different low pressure plasmas. On the other hand, kinetic calculations can be useful to determine the relevant surface and gas-phase chemical processes and the interrelations between ionic and neutral species. In this work, a combined diagnostics and modeling of low pressure H_2/(10 %)N_2 plasmas generated in a hollow cathode DC reactor is presented. The basic mechanisms leading to the observed neutral and ion distributions, as well as their relative importance in the studied pressure range, are identified and discussed.

5.1 Experimental results

Mixtures of H_2 (90 %) + N_2 (10 %) have been used for the experiments, at total pressures of 0.8, 1, 2, 4 and 8 Pa. Electron temperatures and densities have been determined for each of these conditions, along with the relative concentrations of the stable neutral species and positive ions.

5.1.1 Electron temperatures and densities

The values of the electron temperature and density derived from the Langmuir probe measurements are listed in Table 5.1. The table also includes the values of these magnitudes employed in the model simulations to obtain the best fits for the neutral and ion concentrations. Only three of the pressures studied are shown for brevity.

Table 5.1. Electron temperatures and densities obtained experimentally and adjusted values for the simulations.

	T_e (eV)		N_e (× 10^{10} cm^{-3})	
Pressure (Pa)	**Experiment**	**Model**	**Experiment**	**Model**
0.8	3.8 ± 0.5	4.15	2.6 ± 0.5	2.3
2	3.4 ± 0.5	3.1	3.5 ± 0.5	3.6
8	3.1 ± 0.5	2.8	2.8 ± 0.5	3.3

As expected, higher temperature values are obtained for the lower pressures. The electron density varies non-uniformingly with pressure, with the higher value of 3.5 × 10^{10} cm^{-3} corresponding to the intermediate pressure of 2 Pa. The values employed in the model are adjusted to obtain a better fit to the experimental concentrations, but are nonetheless within the limits of the experimental error.

5.1.2 Neutral concentrations

The concentrations of the stable neutrals in the plasma have been determined with mass spectrometry for each of the different pressures employed in the experiment. The results of the measurements are displayed in Figure 5.1.

Apart from the precursors, ammonia is detected in significant amounts. The distribution of neutrals is fairly stable, with no large changes in the range of pressures studied. The higher concentration of NH_3 is found at the lower pressure, and it decreases towards higher values. Conversely, precursor hydrogen is found in greater amounts at 8 Pa, while the concentration of N_2 stays mostly constant within the experimental error.

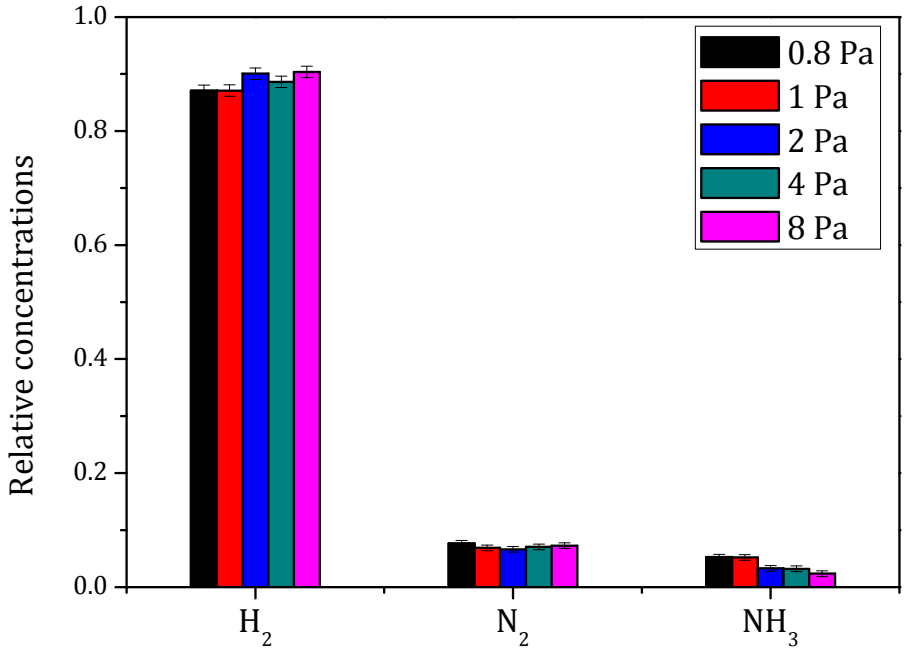

Figure 5.1. Experimental relative concentrations of the neutral species of the H_2 + N_2 discharge at the different pressures studied.

5.1.3 Ion concentrations

Relative concentrations of the positive ions present in the plasma were determined with the plasma monitor for the different conditions studied, leading to the values shown in Figure 5.2.

It is apparent that the pressure of the discharge has a strong effect in the ion distributions. For the lowest pressure, 0.8 Pa, a relatively homogeneous distribution is obtained, with no ions exceeding 20 % concentration. Five different species (H_2^+, H_3^+, NH_3^+, NH_4^+ and N_2H^+) can be found in significant amounts, with concentrations between 10 and 20 %. When the pressure is increased to 2 Pa, two of these ions, H_2^+ and NH_3^+, decrease drastically, while a large growth is observed in the NH_4^+ concentration. This trend continues with growing pressure. At 8 Pa, the concentrations of all ions decrease except that of NH_4^+, which accumulates ~ 65 % of the total positive charge.

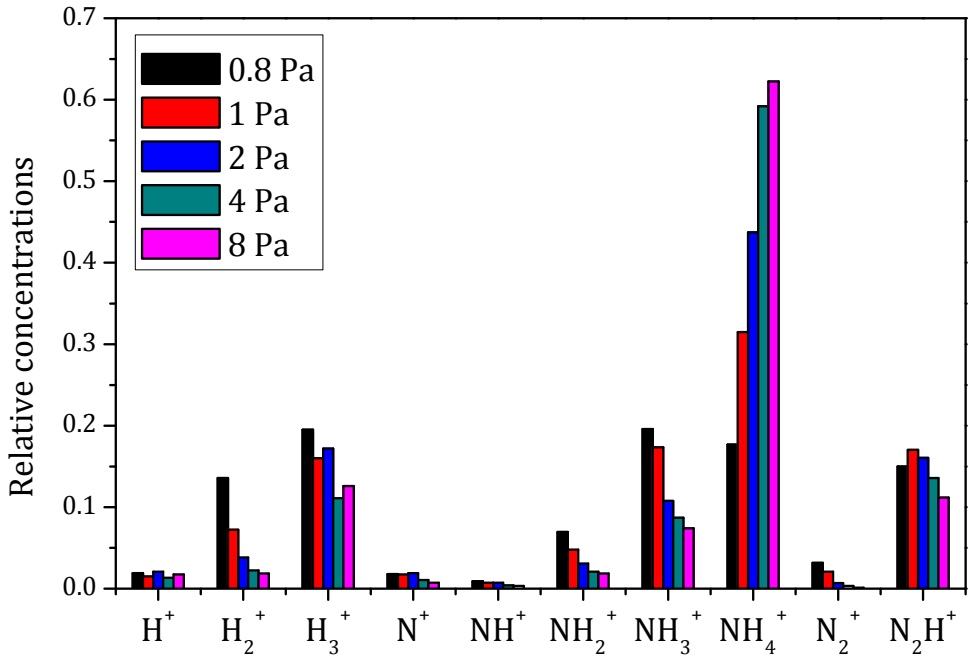

Figure 5.2. Experimental abundances of the positive ions in the H_2 + N_2 discharge at the different pressures studied.

5.2 Model simulations and relevant processes

Model simulations have been used to identify the key mechanisms behind the neutral and ionic chemistry of the H_2 + N_2 discharges. Special attention has been paid in this particular case to the surface chemistry, due to its great relevance in the formation of ammonia. The details of the model can be found in section 3.4.2. Reaction numbers given in the text refer to Table 3.6 and Table 3.7 in that section.

5.2.1 Neutral species

The relative concentrations of the stable species of the plasma have been calculated using the kinetic model, allowing for a comparison with the experimental data. Additionally, the model can be used to obtain the concentrations of radicals (H and N atoms, NH and NH_2) in the plasma. Although these species have not been experimentally detected, the relatively high atomic H concentrations are consistent with previous results from studies in the same experimental setup [35] and appreciable concentrations of the NH and NH_2 radicals have also been observed by other groups in H_2/N_2 discharges

[162,163]. In the plasmas studied in this work, gas phase dissociation of ammonia is the main source of NH and NH_2 radicals. The results are displayed in Figure 5.3. Since the measurements at 1 and 4 Pa present intermediate results, only three pressures, 0.8, 2 and 8 Pa, have been considered for simplicity.

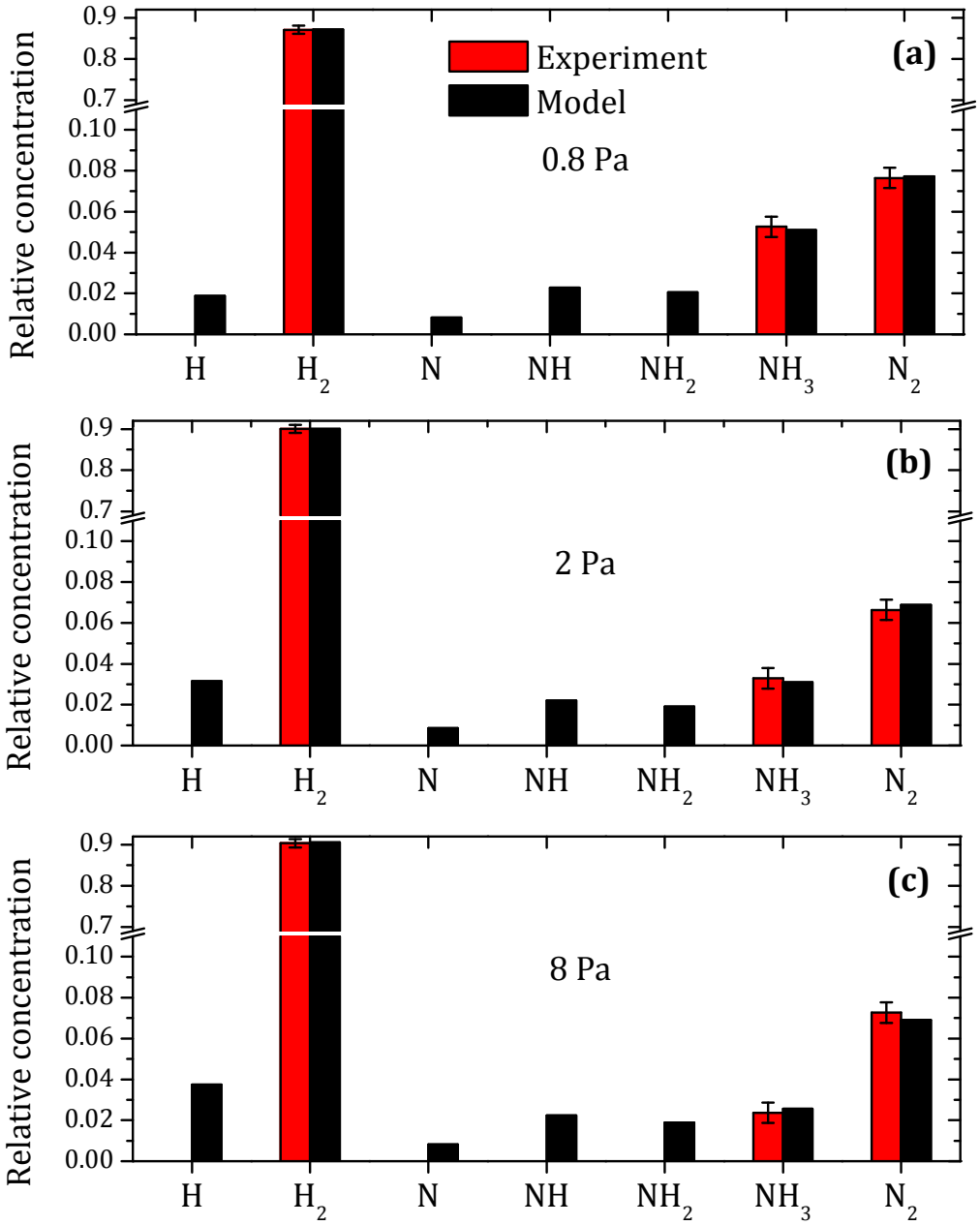

Figure 5.3. Comparison between experimental and simulated concentrations for the neutral species of the discharge. Only three different pressures, 0.8 Pa (a), 2 Pa (b) and 8 Pa (c), are considered.

The steady-state concentrations of the neutral species for each pressure are the result of a complex balance between the electron impact dissociation of the stable molecules (both of the H_2 and N_2 precursors and of ammonia) and radicals, and surface generation of the stable species, predominantly NH_3 but also H_2 and N_2 (see Table 3.7). The precursor gases are largely recycled before leaving the reactor due to the relatively long residence times (between ~ 0.45 and 0.75 s). The increase in NH_3 concentration at 8 Pa, which could be intuitively expected due to the higher residence time at this pressure, is basically compensated by a slight increase of the plasma volume (i.e., a smaller sheath width that is estimated to change from 2 to 1.5 cm with increasing pressure due to the decrease in the discharge voltage and the increase in the electron density [8,41]), which favors NH_3 dissociation. NH_3 formation is triggered by the supply of atomic H and N to the surface, which depends on an efficient dissociation of H_2 and N_2. The efficiency grows substantially with increasing electron temperature, T_e, as can be observed in Figure 5.4, where the rate coefficients for electron impact dissociation of the various neutrals present in the plasma (reactions D_1–D_7) are displayed over the range of electron temperatures of interest for the experiments (note that the rate coefficients for the two possible dissociations of NH_2, reactions D_4 and D_5, are equal).

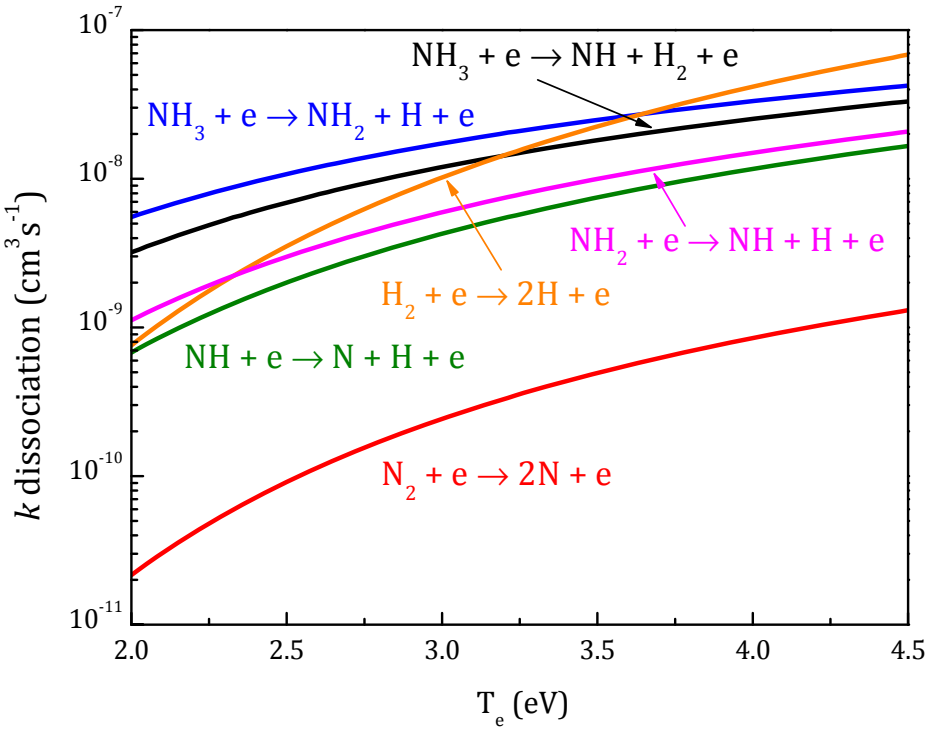

Figure 5.4. Dissociation rate coefficients of the stable molecules (H_2, N_2 and NH_3) as well as radical species (NH and NH_2) as a function of the electron temperature, T_e.

Since the dissociation rate of N_2 is the lowest of all neutral species and its proportion in the mixture is only 10 %, the adequate supply of N atoms to the reactor walls, dependent on T_e, will be an important control parameter for the production of ammonia at the surface. It is worth noting that the dissociation of the NH_x species is very efficient already at low electron temperatures but less sensitive than that of H_2 and N_2 to a change in T_e.

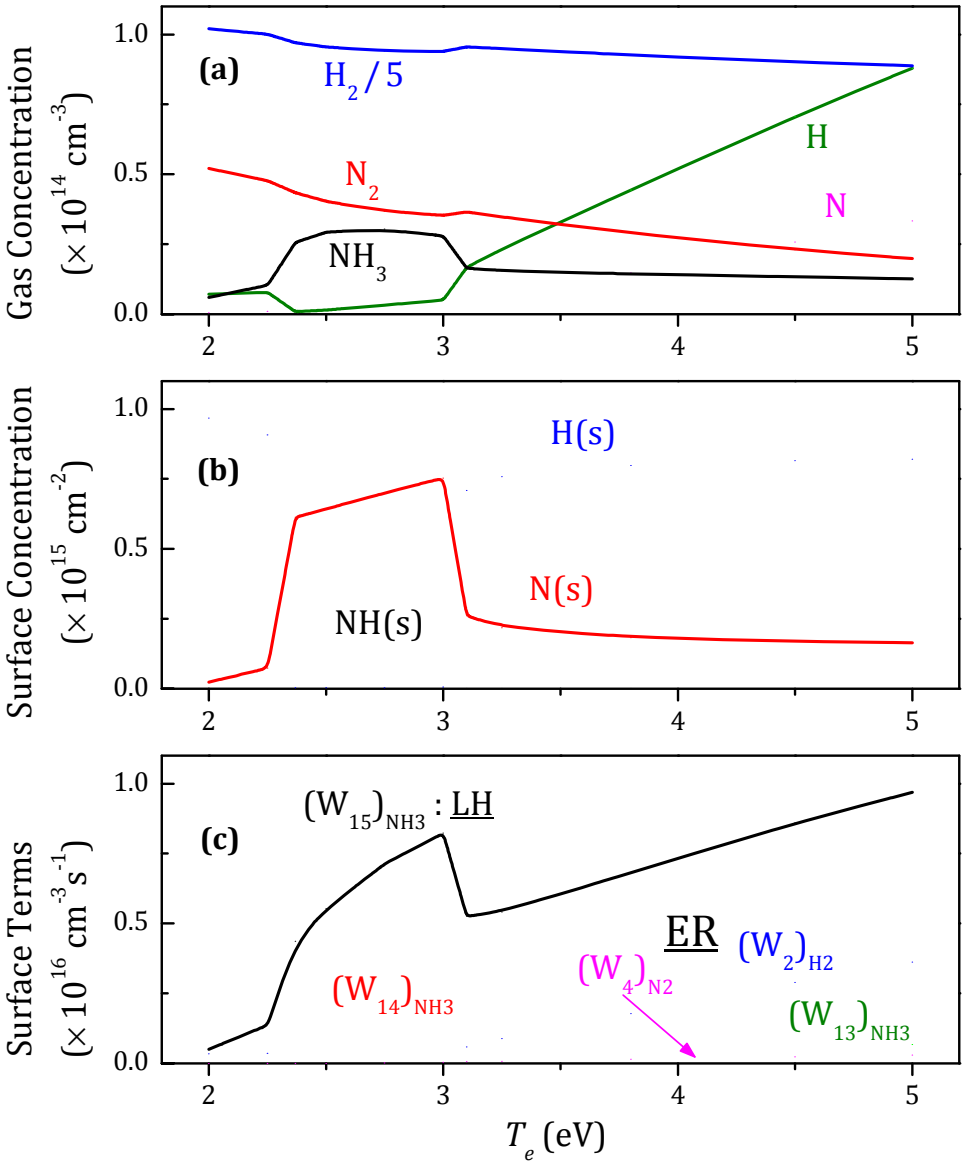

Figure 5.5. Calculated variations of the steady-state concentrations for the most significant gas phase neutrals (a), adsorbed species (b) and surface production terms (c) with electron temperature at 2 Pa.

Further insight into the interconnected gas phase and surface chemistry can be gained by analyzing the model steady-state concentrations of the most relevant neutral species as a function of electron temperature. Calculated results at 2 Pa are displayed in Figure 5.5 for gas phase molecules and atoms (a), adsorbed species (except for $NH_2(s)$, < 10^{12} cm^{-2} anywhere) (b), and the most representative surface production terms (c).

The minimum concentration of NH_3 is predicted at the lowest T_e (2 eV) due to a limited supply of atomic N; but even for this electron temperature, a significant amount of NH_3 is already produced, mainly through reactions W_{13} and W_{15}. Reaction W_{12} represents a minor contribution to ammonia formation at any pressure and is not shown in the figure. Given that H_2 constitutes 90 % of the precursor mixture and its dissociation is more efficient than the dissociation of N_2, H is the main atomic or radical species in the gas phase and at the surface. This second circumstance allows not only the formation of NH_3 but also the formation of H_2 via reaction W_2. As a consequence, part of the adsorbed H is lost for the generation of ammonia and another part is recovered as one of the precursor species. However, between 2.5 and 3 eV, the dissociation of N_2 starts to be more efficient, N adsorption is more relevant than before, reaction W_8 gains in importance and, under steady-state conditions, an enriched N(s) surface produces NH_3 mainly through reactions W_{14} and W_{15}. At the same time, the formation of H_2 via W_2 is inhibited and the production of N_2 via W_4 too, since most of the atomic N is at the surface or takes part in ammonia generation. The most favorable situation for NH_3 production corresponds to the conditions in which atomic gas-phase concentrations are drastically reduced and the surface is preferentially covered with atomic N. These conditions are not fulfilled beyond 3 eV, since gas phase dissociation is significant, leading especially to atomic H. The excess of atomic H reverts to a prevailing H(s) covered surface and the production of H_2 at the surface grows substantially. With growing T_e, the dissociation of N_2 is also favored and reaction W_4 produces also more N_2. These processes are responsible for the small upturn in both molecular concentrations near 3.1 eV. At higher T_e, the dissociation of molecular species is so efficient that their steady-state concentrations drop in spite of the more efficient surface production.

As a consequence of the complex balance between electron impact dissociation and the various surface processes, the concentration of NH_3 is predicted to be maximized in the plasma over a given T_e range that depends on pressure. Figure 5.6 shows the evolution of the relative NH_3 concentration as a function of T_e for the three pressures considered, together with the experimental measurements corresponding to the actual discharges investigated.

Only one experimental point can be measured at each pressure with the experimental set-up, with the corresponding T_e value adjusted for each pressure. The measured data are certainly consistent with the calculations, but they should not be

viewed as a rigorous proof of the predictions, which are not restricted to a single electronic temperature, but extend over a T_e range. In this respect, the figure depicts basically model results. As can be seen, the interval of maximal NH_3 concentration is narrow at the higher pressures, but becomes broad, with a gentle decline toward higher T_e, for 0.8 Pa. The experimental points for the 2 Pa and 8 Pa discharges turn out to be just beyond their respective maxima, which end in an abrupt fall. The point for the 0.8 Pa discharge is also past the maximum, but its value is not much lower, since it is placed on the gentle down-going slope. In retrospect it is not surprising that the maximum relative concentration of ammonia was measured for the lower pressure, since in this case, NH_3 production is favored over a much wider T_e range.

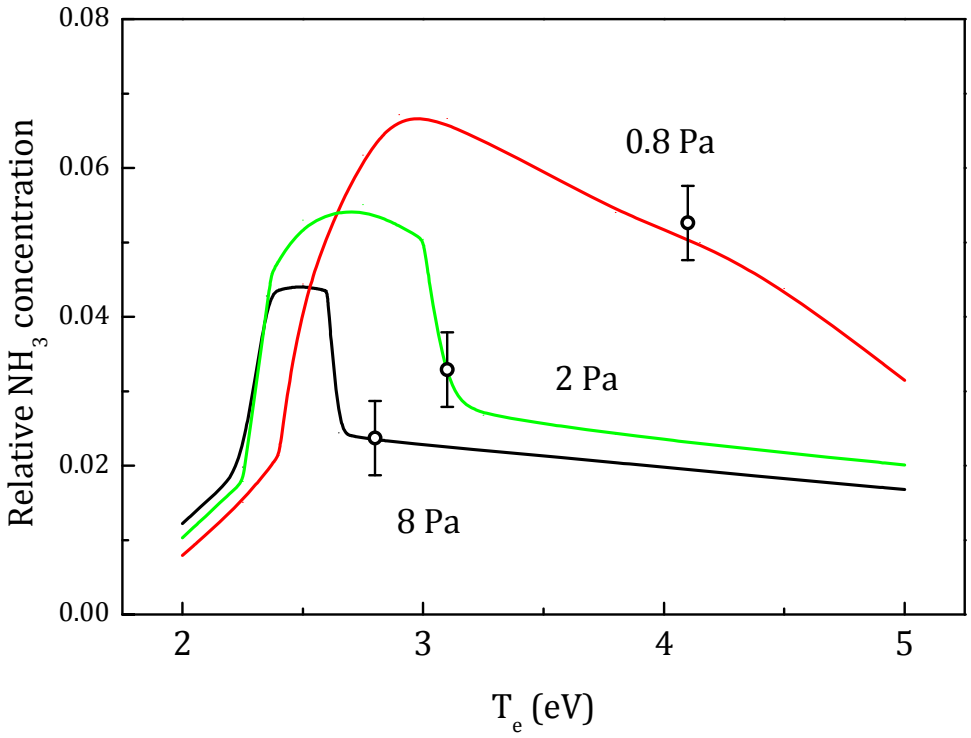

Figure 5.6. Relative NH_3 concentration as a function of T_e for 0.8, 2 and 8 Pa obtained from model simulations. The dots with error bars indicate the experimental values.

As indicated in section 3.4.2, both Langmuir-Hinshelwood and Eley-Rideal mechanisms have been considered in a combined reaction scheme for the synthesis of ammonia on the metallic surface, in accordance with previous literature works [170,171]. However, given the high flow of atoms to the wall characteristic of the low pressure plasmas in this work, it is worth investigating whether a scheme based purely on ER reactions could account for the experimental data. To this end, additional simulations with

the model have been performed. The results for the 0.8 Pa discharge, the one with the lowest pressure and most sensitive to surface processes, are represented in Figure 5.7.

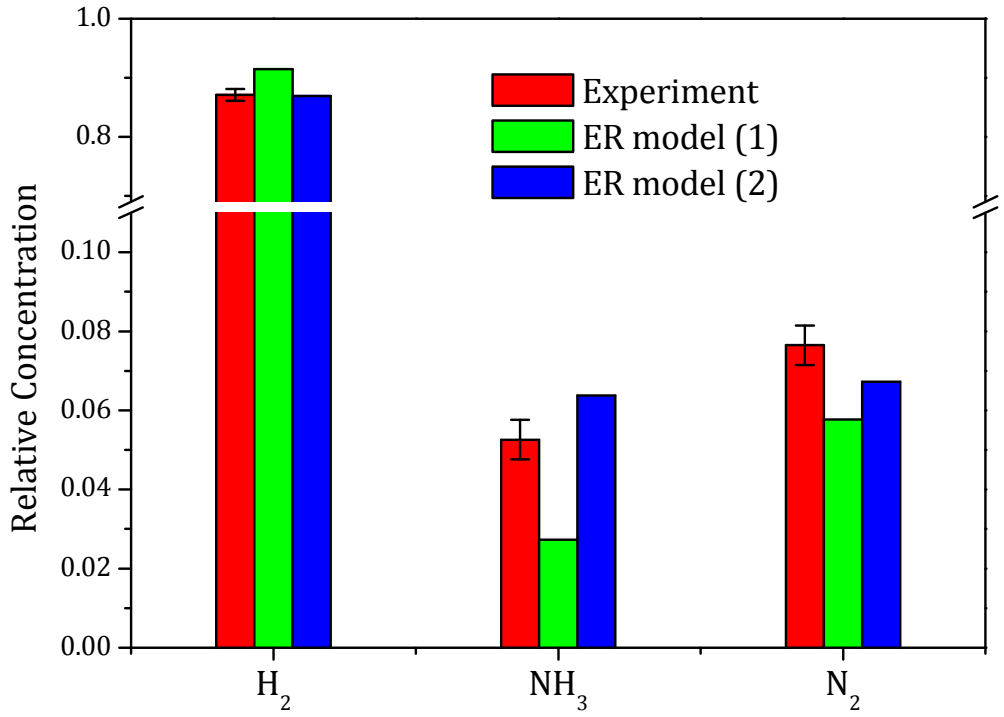

Figure 5.7. Experimental and calculated neutral species (only stable molecules are shown) by employing exclusively an Eley-Rideal model for surface reactivity (i.e. excluding LH reactions W_{11} and W_{15}) with the same γ_{ER} coefficients of the complete model (1), and with a ten-fold increase in the value of γ_{ER} for nitrogen recombination and a five-fold increase in the γ_{ER} values for all reactions involving NH_x species (2). See text for further details.

A direct elimination of the two LH processes included in the model (reactions W_{11} and W_{15}) without changing the γ_{ER} coefficients leads to a low NH_3 production and a distortion in the predicted concentrations of H_2 and N_2, which are overestimated and underestimated respectively (green bars). The agreement with the experimental results can be recovered by modifying the γ_{ER} coefficients, as shown by the blue bars in the figure, but they must be raised significantly, with a ten-fold increase in the value of γ_{ER} for nitrogen recombination and a five-fold increase in the γ_{ER} values for all reactions involving NH_x species. These values are deemed unrealistically high and are not suitable for the higher pressures. The present results support thus the prevalent view that LH reactions are also of relevance for the heterogeneous synthesis of ammonia in this type of plasmas.

The model analysis of the plasma kinetics described thus far outlines the basic processes responsible for the observed composition of neutral species and underlines the strong interconnection between gas-phase and surface chemistry and the crucial influence of electron temperature. Specifically, the production of NH_3 has been found to depend very sensitively on the delicate balance between formation and destruction of the NH_x intermediates implied. The model provides in principle a good global picture of the steady state plasma chemistry, but it also has obvious limitations, since it relies on a series of assumptions about the number of surface sites or surface reaction parameters. In the absence of in situ surface characterization, which is beyond the capabilities of the experimental setup, the predictions about coverage by the distinct species cannot be directly verified. Apart from wall neutralization, the model neglects ionic interactions with the surface and it does not consider ionic effects on the surface chemistry or a possible surface modification by electron bombardment. The reproducibility of the experiments suggests, however, that the surface is not appreciably modified by the studied discharges.

5.2.2 Positive ions

Figure 5.8 shows the measured ion distributions at 0.8, 2 and 8 Pa along with the corresponding model simulations. The global evolution with pressure is satisfactorily reproduced by the model. As found previously in plasmas of other gas mixtures [190], the overall ion results can be explained mainly by the decrease of the electron temperature T_e at higher pressures. NH_4^+ together with H_3^+ and N_2H^+ are formed exclusively by ion-molecule gas phase reactions. In contrast, the rest of the ions can also be generated in significant amounts by direct ionization, and that is the only production mechanism in the case of H_2^+ and N_2^+. This channel tends to be preferential for high T_e, since production by some of the ion-molecule reactions T_1–T_{25} is often compensated by destruction via other reactions in the group.

The rate coefficients of the most relevant ionization reactions (I_3, I_6, I_{11} and I_{12}) as a function of the electron temperature T_e are displayed in Figure 5.9, together with some rate coefficients for ion-molecule processes. At 8 Pa, T_e is slightly lower than 3 eV and the rate coefficients for electron impact ionization are smaller than those for the ion-molecule reactions. Under these circumstances, the ion distributions are determined to a large extent by ion-molecule chemistry, which leads preferentially to NH_4^+ as soon as NH_3 is present in appreciable concentrations, since the ammonium ion does not have destruction channels in the gas phase and is essentially lost through wall neutralization. However, at 0.8 Pa, the electron temperature reaches 4 eV and the rate coefficients for direct ionization, notably those for NH_x species, approach those for ion-molecule reactions.

Consequently both types of processes compete and a more uniform distribution of ionic concentrations is observed.

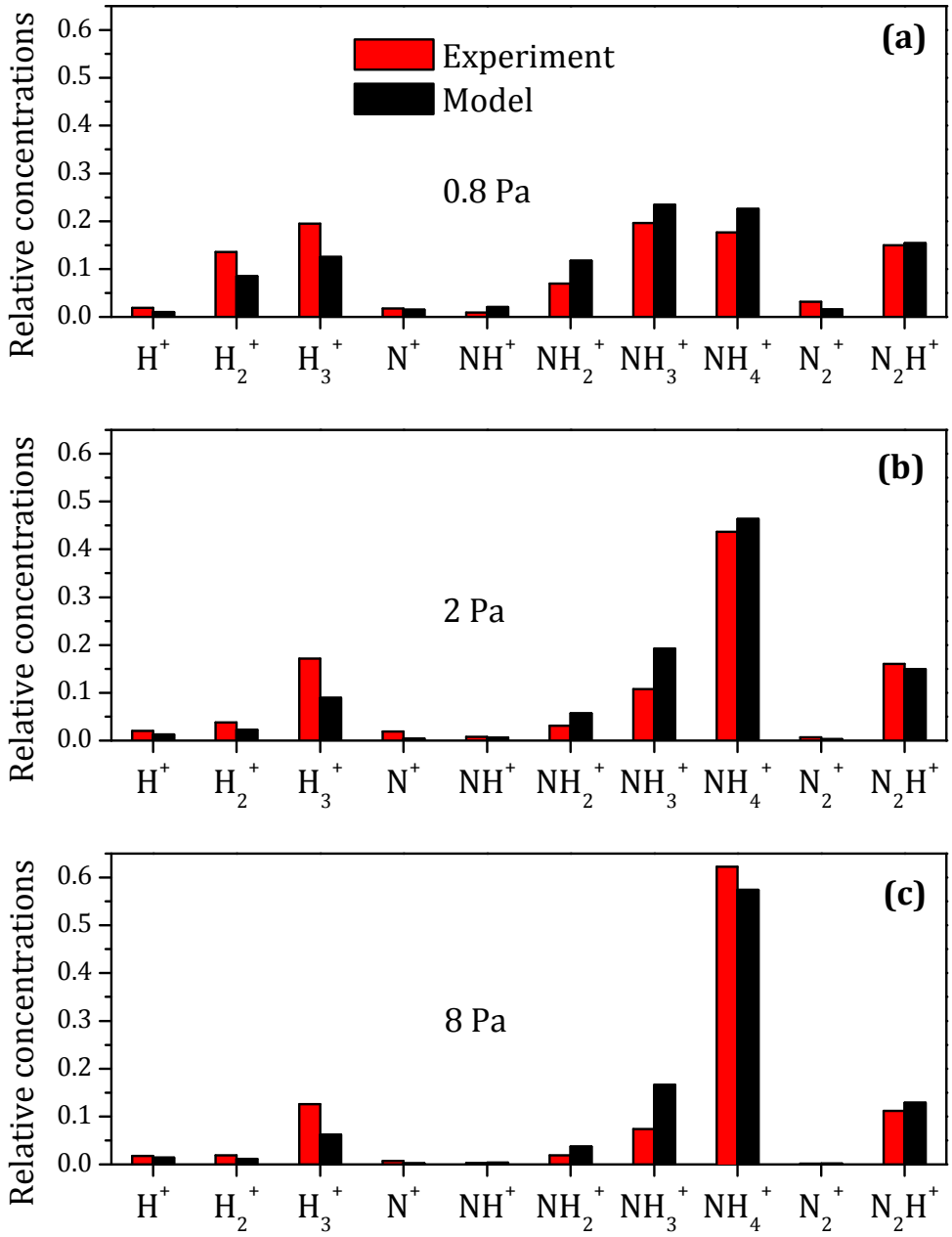

Figure 5.8. Experimental (red bars) and calculated (black bars) ion distributions for H_2 + N_2 plasmas at (a) 0.8 Pa, (b) 2 Pa and (c) 8 Pa.

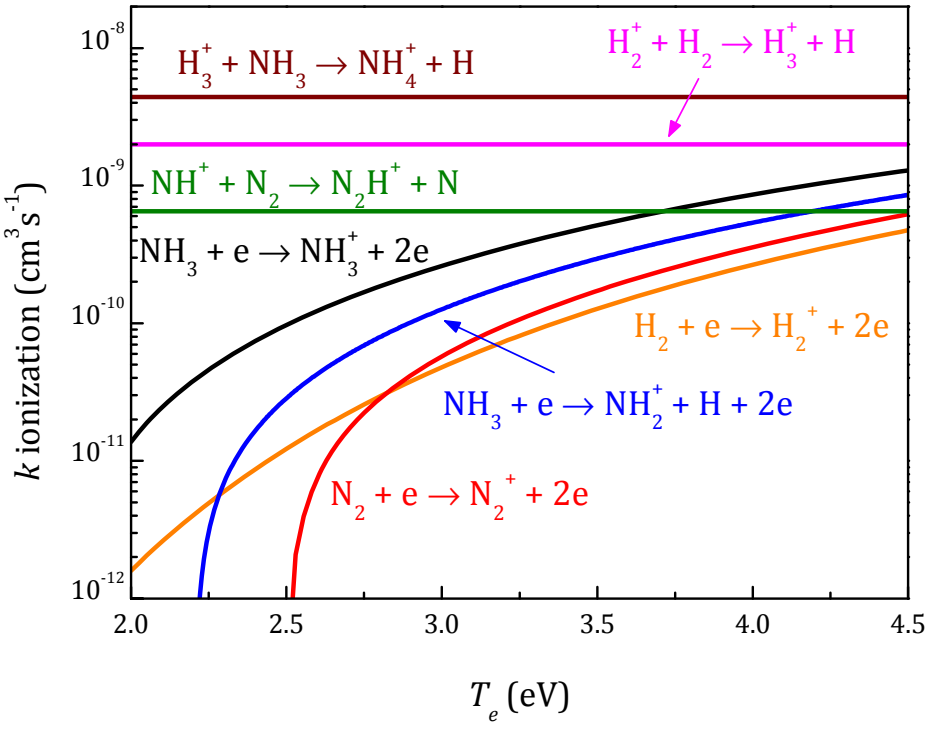

Figure 5.9. Ionization rate coefficients of H_2, N_2 and NH_3 as a function of the electron temperature. Rate coefficients for some ion-molecule reactions are shown for comparison.

The key role played by electron temperature in the ion distribution is further illustrated in Figure 5.10, which shows the calculated evolution of molecular ions with T_e in the 2 Pa discharge. For this simulation, plasma volume and electron density are kept constant. For the lowest electron temperature, the rates of ion production by electron impact are low and, as just mentioned, the generated ions are preferentially transformed into NH_4^+ through the chemical network listed in Table 3.6 (reactions T_1–T_{25}). With increasing T_e the concentration of NH_4^+ decreases sharply and those of the other ions increase, giving rise to more uniform distributions. Between $T_e \sim 3.5$ and 5 eV the major ion is NH_3^+, with a significant contribution from direct ionization. Beyond 5 eV, the H_2^+ ion, formed exclusively in the electron impact ionization of H_2, becomes dominant. Between 2 and 3 eV, the maximum in the concentration of NH_3 as a function of T_e commented on above is clearly imprinted in the curves of the various ions implied in NH_3 chemistry. Reactions T_8, T_{22} and T_{25} lead to a relative growth of NH_4^+ and to a decrease of H_3^+, NH_3^+ and N_2H^+ in clear correspondence with the NH_3 maximum shown in Figure 5.5 and Figure 5.6.

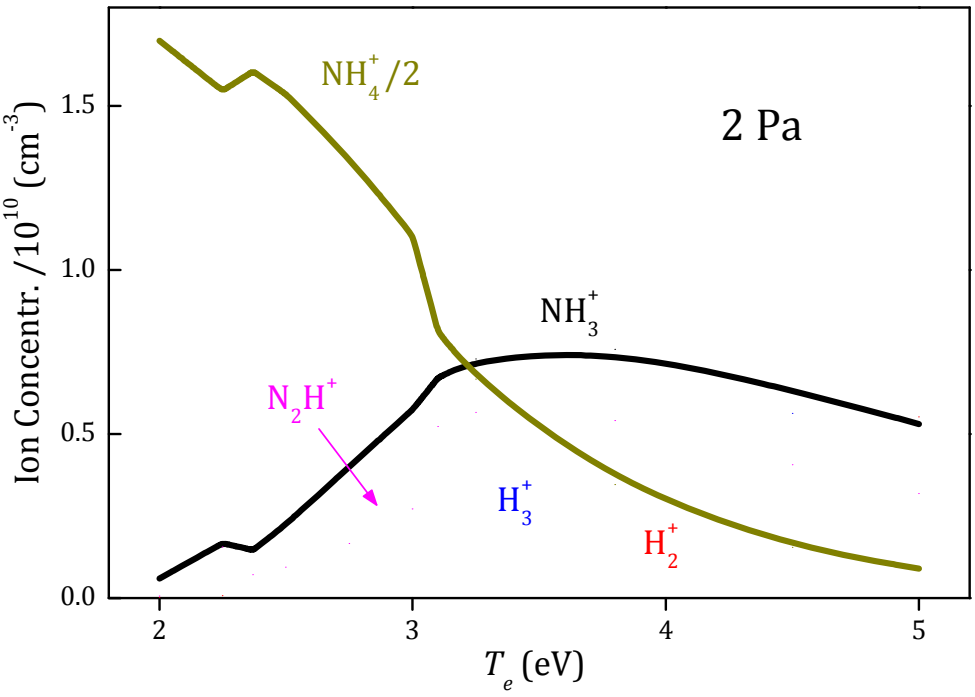

Figure 5.10. Dependence of the ion distribution on the electron temperature for the 2 Pa discharge. Note that the NH_4^+ concentrations are divided by a factor of two.

Although the model predicts well the global relative experimental ionic concentrations at a given pressure and their behavior as the pressure is modified, there are some discrepancies between the experimental concentrations of some ions and the calculated ones. NH_2^+ and NH_3^+ are overestimated by the model and H_2^+ and H_3^+ are underestimated. This happens for all the pressures studied, but it is more evident at the higher ones. The reasons for these discrepancies are not clear, especially considering that ionic chemistry is strictly restricted to the gas phase and is not plagued by the uncertainties commented on above for surface reactivity. Specifically, consistent values for the relevant electron impact ionization cross sections are available and the rate coefficients for the main gas phase sinks and sources of the various ions seem well established in the literature (see bibliographic sources in Table 3.6 and the references cited in them). Sheath collisions, leading to additional reactions or charge transfer, not considered in the model, could contribute to explain the differences between the experimental data and the model results, but they are very difficult to evaluate due to the scarcity of data on cross sections for molecular ions over the required energy range (up to 300–400 eV). The comparatively low pressure of the experiments and the analysis of the ion energy distributions reaching the cathode [41] suggest that the measurements should

not be significantly perturbed by collisions in the plasma sheath, but some distortion of the measurements cannot be entirely ruled out (see references [63,190] for more detailed comments on possible sheath effects). The assumption of a Maxwell distribution of electron energies and the neglect of internally excited species in the model calculations may also contribute to the observed discrepancies between measurements and simulations.

It is worth noting that the efficient transformation of N_2H^+ into NH_4^+ in the presence of NH_3 reflected in the results of this work can have implications for astrophysics, mainly in protostellar regions, where temperatures can be high enough to evaporate NH_3 from the dust grains. The evaporated NH_3 would then deplete N_2H^+ directly, through reaction T_{25}, and indirectly by destroying its precursors H_2^+ and H_3^+ through reactions T_4 and T_8. Under adequate circumstances, this NH_3 chemistry could modify the balance between N_2H^+ formation through proton transfer from H_3^+ to N_2 (T_9) and the destruction mechanism of dissociative electron recombination (N_{12}) assumed in estimates of molecular N_2 concentrations [189].

5.3 Summary and conclusions

$H_2 + N_2$ plasmas with a low ($\sim$ 10 %) content of N_2 in the precursor gas mixture generated in a hollow cathode DC reactor have been characterized experimentally using mass spectrometry for the measurement of neutral and ion concentrations, and a double Langmuir probe for the estimation of electron temperatures and densities. Apart from the precursors, ammonia is detected in substantial concentrations, comparable to that of N_2 at the lowest pressure. A simple zero order kinetic model, which couples gas-phase and heterogeneous chemistry, reproduces the global composition of the plasmas over the whole range of pressure experimentally studied. A detailed analysis based on the results of the model has allowed for the identification of the main processes determining the observed neutral and ion distributions and their evolution with discharge pressure.

Ammonia is formed at the surface of the metallic reactor walls by the successive hydrogenation of adsorbed atomic nitrogen and nitrogen containing radicals. Both Eley-Rideal and Langmuir-Hinshelwood mechanisms are necessary to account for the measured distributions of neutrals. At the lowest pressure, the gas phase dissociation of N_2, which is determined mainly by the electron temperature, provides an adequate flux of N atoms to the walls to favor ammonia production. A feedback mechanism allows the enrichment of the surface in atomic N which, at the same time, reduces drastically H_2 formation at the surface via an Eley-Rideal mechanism and guarantees an efficient NH_3

generation. As a result, the concentration of NH_3 approaches that of N_2. With growing pressure, the plasma conditions provide a relatively high H atomic content in the gas-phase and lead to a preferentially H-covered surface, which forms not only ammonia but also molecular H_2 (and to lesser extent N_2). As a consequence, the presence of NH_3 in the relative concentrations of neutral species decreases.

The positive ion distributions in the discharge are largely influenced by variations in the electron temperature, which controls the balance between ionization processes and ion-molecule reactions. At lower pressures and higher electron temperatures, both kinds of processes have similar relevance. The resulting ion distribution is relatively uniform, with similar concentrations of several ions. However, at higher pressures and lower electron temperatures, ion-molecule processes control the chemistry and the protonation reactions result ultimately in a distribution of ionic species with a marked NH_4^+ predominance. The strong prevalence of NH_4^+ in the distribution is a direct result of the ion molecule chemistry of NH_3, leading to the generation of ammonium ions at the expense of H_3^+ and N_2H^+. This intertwined reactivity of the three protonated ions should be considered in the estimations of molecular N_2 densities in astrochemistry, which are mostly based on N_2H^+ measurements, if ammonia is present in appreciable amounts in the gas phase.

Chapter 6.

H_2 + O_2 plasmas

Low pressure plasmas in electrical discharges with H_2 and O_2 are of interest in a variety of fields. In astrochemistry, the formation of H_2O and H_3O^+ is of great relevance as they have been detected in interstellar environments [30-32,191]. Ions containing oxygen and hydrogen are formed in interstellar clouds [192], and they are assumed to play an important role in gas phase chemical routes leading to the production of H_2O. The hydronium ion, H_3O^+, has been observed in molecular clouds since the nineties [193]. The recent Herschel mission has led to the detection of OH^+ [194] and H_2O^+ [195] in the diffuse interstellar medium and their role as markers of regions with a small fraction of H_2 has been highlighted [196]. The HO_2^+ ion, however, remains unobserved to date. It has been repeatedly considered as a possible tracer for molecular oxygen [197-199] in a similar way as N_2H^+ is for N_2, but the available thermodynamic and kinetic data suggest that the concentration of this ion in the ISM should be too small to be detectable [198]. In fusion research, discharge cleaning is used to eliminate the residual molecules in a vacuum vessel, of which oxygen and water are major components [200,201], and oxygen-containing cold plasmas have been proposed for the removal of co-deposits at the reactor walls [202,203]. Hydrogen and oxygen plasmas are also widely used in surface treatments, like chemical modification [204-206], decontamination [207] or functionalization of carbon nanotubes [208].

Previous studies on this kind of plasmas have been carried out under a variety of conditions and with very different objectives. Atmospheric pressure discharges have been used in experimental and theoretical studies of H_2 + O_2 ignition [106], in the simulation of gas heating processes in H_2 + O_2 streamers [209], or in the modeling of production mechanisms of different neutral species [210,211]. An extensive global model for mixtures of He with small fractions (< 1 %) of H_2O has been elaborated by Liu *et al.* [212], and the

formation of OH radicals in plasma assisted combustion of H_2/air mixtures has been studied experimentally and theoretically by Yin *et al.* [213]. Low pressure plasmas of H_2 + O_2, mostly in the mbar range, have been employed by various groups. They have been used in the infrared spectroscopy analysis of the spectrum of the H_3O^+ ion [26]. Nevertheless, kinetic studies of these plasmas are limited to the analysis of the neutral species, such as the determination of oxygen atom concentrations in microwave post discharges of He-H_2-O_2 mixtures using NO tritration [214], the modeling of neutral species in the afterglow of a H_2 + O_2 discharge [215], or the experimental study of the variation of the $O_2(a^1\Delta_g)$ concentration with the introduction of small amounts of H_2 in an Ar + O_2 microwave discharge [216].

In this work, a study of the chemistry of neutral and ionic species in H_2/O_2 plasmas is presented, based on the experimental diagnostics and kinetic modeling of hollow cathode discharges at a pressure of 8 Pa and mixture proportions ranging from pure H_2 to pure O_2. For the pressure value selected, which lies toward the high pressure limit of the stable operating range of the discharge (1–10 Pa), the ion distributions in the plasma are largely determined by ion-molecule chemistry, which is the goal of the present study. For the lowest operating pressures, displaying higher electron temperatures, the ion distributions tend to be dominated by the products of direct electron impact ionization [190]. Langmuir probes provide values for the electron temperatures and densities, and neutral and positive ion concentrations are determined by mass spectrometry. The main surface and gas processes are identified by comparison of experimental data and model predictions, and their relative relevance under the different discharge conditions is analysed.

6.1 Experimental results

Discharges of H_2 + O_2 have been performed at a fixed pressure of 8 Pa for the whole range of mixtures, from pure H_2 plasma to pure O_2 plasma. Electron temperatures and densities have been measured for these different conditions, along with the concentrations of the neutral stable species (H_2, O_2, H_2O) and the positive ions present in these discharges.

6.1.1 Electron temperatures and densities

Values of the electron temperature and electron density have been obtained from the measurements with the double Langmuir probe for the whole range of mixtures studied. The results are presented in Figure 6.1.

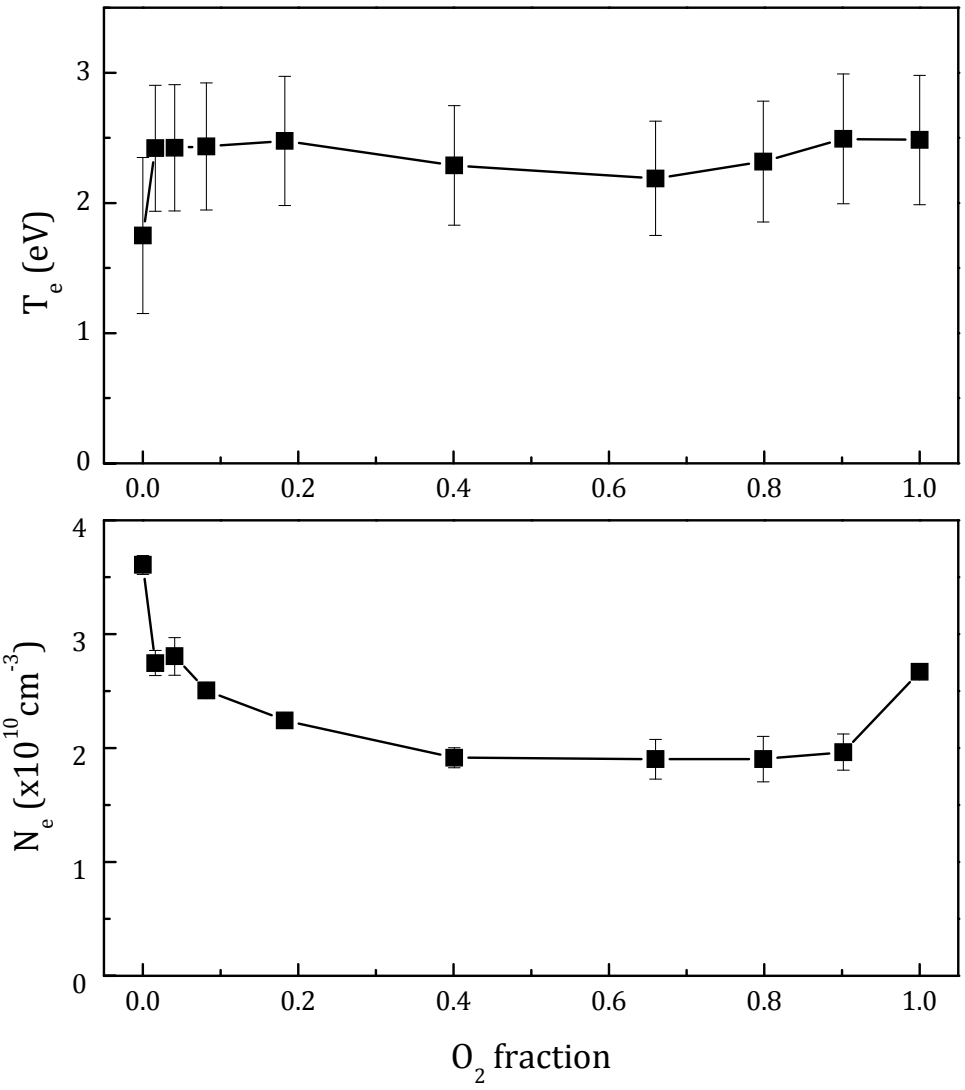

Figure 6.1. Electron temperatures (upper panel) and densities (lower panel) measured with the Langmuir probe for the different $H_2 + O_2$ mixtures at 8 Pa. The values used in the model are the same as the experimental ones except for the pure H_2 discharge, where an electron temperature of 2.4 eV is employed (see section 6.2.2 for more details). Lines are only a guide to the eye.

The electron temperatures are stable through the whole range of mixtures investigated, with a mean value of 2.4 eV, except for the pure H_2 plasma, where a value of 1.7 eV is obtained. The pure H_2 plasma is also exceptional regarding electron densities, with a higher value (3.6×10^{10} cm^{-3}) than the rest of the mixtures, which stay between 2×10^{10} and 3×10^{10} cm^{-3}.

6.1.2 Neutral concentrations

Neutral stable species were monitored using the PRISMA quadrupole mass spectrometer. The time evolution for the formation of water molecules and the attainment of the steady state was observed through mass 17, which corresponds to the OH fragment. The values of the steady state concentrations for H_2, O_2 and H_2O are displayed in Figure 6.2.

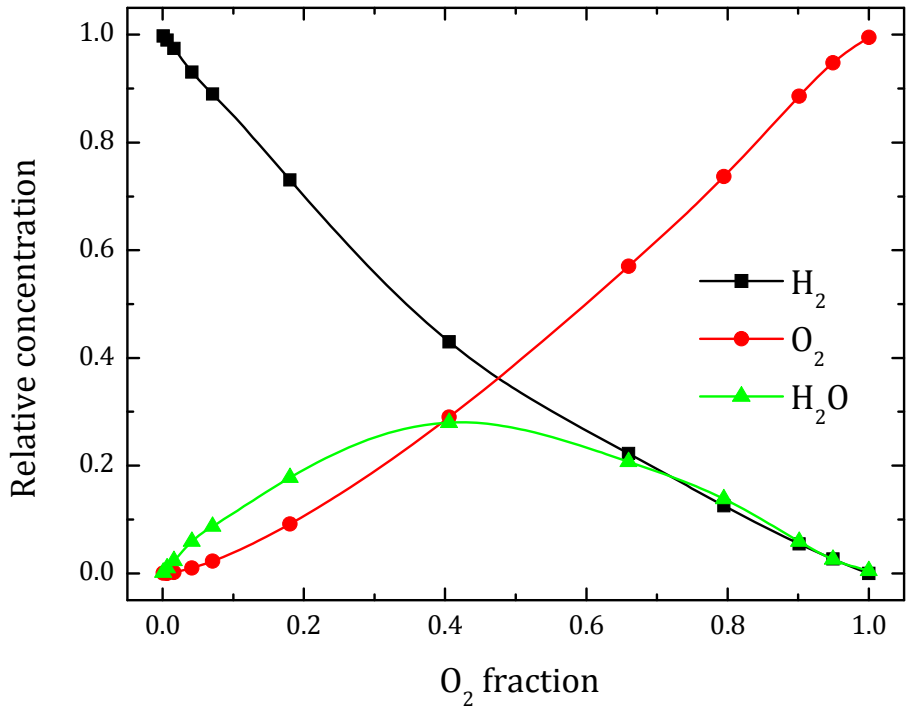

Figure 6.2. Experimental relative concentrations of the neutral stable species in the H_2 + O_2 discharge. Lines are only a guide to the eye.

Water is produced in the discharge in appreciable amounts, reaching a maximum of ~ 30 % of the total neutral concentration for a mixture with ~ 40 % O_2, close to what would be expected from a stoichiometric point of view, which would correspond to maximum water formation for a fraction of oxygen of 33 %. The oxygen precursor is depleted at high H_2 fractions, as it is mostly dissociated and then recombined at the wall to form H_2O. The H_2 precursor is also depleted at high oxygen fractions, but in a smaller proportion. Other neutral stable species, such as O_3, were not detected in the discharges.

6.1.3 Ion concentrations

Relative concentrations for the positive ions present in the plasma have been determined through PPM measurements. The experimental results for the different mixtures studied are shown in a logarithmic plot in Figure 6.3.

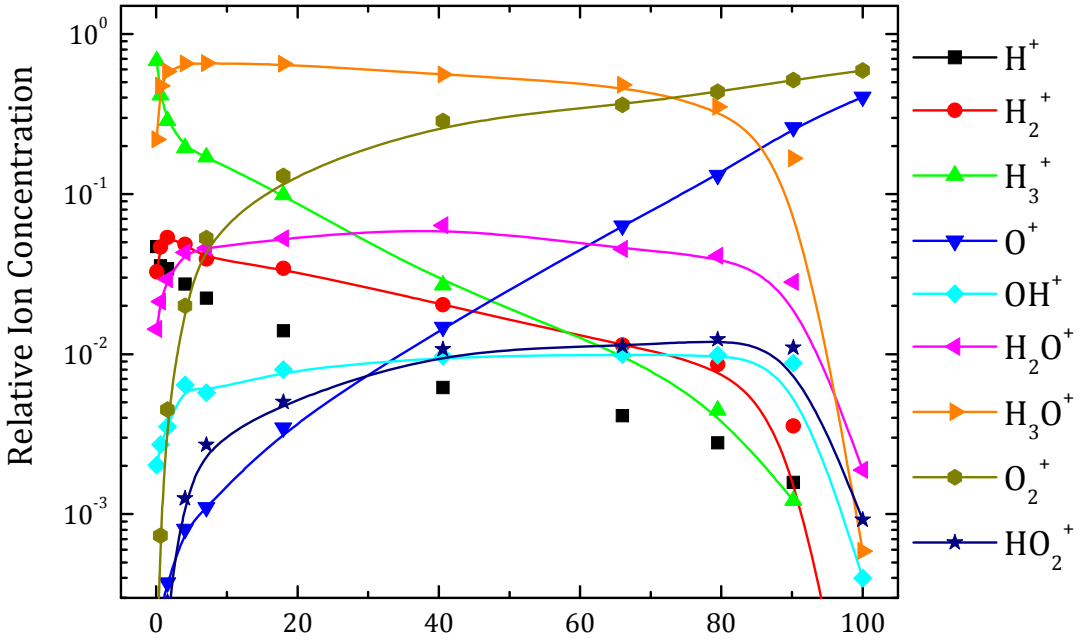

Figure 6.3. Relative concentrations for the positive ions in the discharge obtained from the PPM measurements. Lines are only a guide to the eye.

H_3^+ ions are only dominant for mixtures with nearly no oxygen. When the amount of oxygen is increased, water is formed and as a result H_3O^+ quickly becomes the major ion, maintaining a stable concentration (~ 50–60 %) for a wide range of mixture proportions. At the same time, H_3^+ concentration decreases, and at ~ 20 % O_2, O_2^+ surpasses H_3^+ as the second major ion. O_2^+ concentration keeps growing towards higher O_2 concentrations, and at ~ 70 % O_2 it becomes the dominant ion due to the decrease in neutral H_2O in the discharge. Between ~ 90–100 % O_2, hydrogen-containing ions disappear abruptly from the plasma, as could be expected, leaving only O_2^+ and O^+ in a 2:1 ratio as the relevant ions of the discharge.

H^+ and H_2^+ follow a similar behavior to H_3^+, appearing with the higher concentration in the close to pure hydrogen mixture and steadily decreasing as more oxygen is added. However, their decline is more gradual than that of H_3^+, and as a consequence H_2^+ becomes the major hydrogenic ion at ~ 60 % O_2. The mixed ions H_2O^+, OH^+ and HO_2^+ appear with relatively stable concentrations when both precursors are present in significant amounts (~ 5–90 % O_2). H_2O^+ has the largest concentration with about 5 % of the total positive charge, while OH^+ and HO_2^+ stay an order of magnitude lower, with HO_2^+ growing slightly towards higher O_2 fractions.

6.2 Model simulations and relevant processes

As in the previous works, model simulations have been performed to identify the main mechanisms behind the chemistry of the H_2 + O_2 plasmas. Details on the model can be found in section 3.4.3. References to reactions in the following text correspond to the identifiers given in Table 3.10 and Table 3.11. The results of the simulations are shown in the following sections.

6.2.1 Neutral species

Concentrations of the neutral stable species have been calculated in order to compare them with the experimental results. This is shown in Figure 6.4.

There is a generally good agreement between the simulations and the experiments. The behavior of the three molecules is well reproduced. Water has a maximum concentration of ~ 35 %, which is slightly higher than the experimental value, ~ 30 %, and both happen for the same mixture (40 % O_2). This small overestimation of the H_2O concentration occurs for mixture ratios with less than ~ 60 % O_2, and as a result the H_2 and O_2 precursors are correspondingly depleted. For O-rich mixtures, the concentration of O_2 is overestimated by the model and H_2 is underestimated. Steady state concentrations of H_2O are given by the equilibrium between the dissociation of the precursor gases and the recombination of radicals at the wall.

The model also allows the simulation of the concentration of neutral species that could not be determined experimentally, due to either their unstability or their very low abundance. These are shown in Figure 6.5.

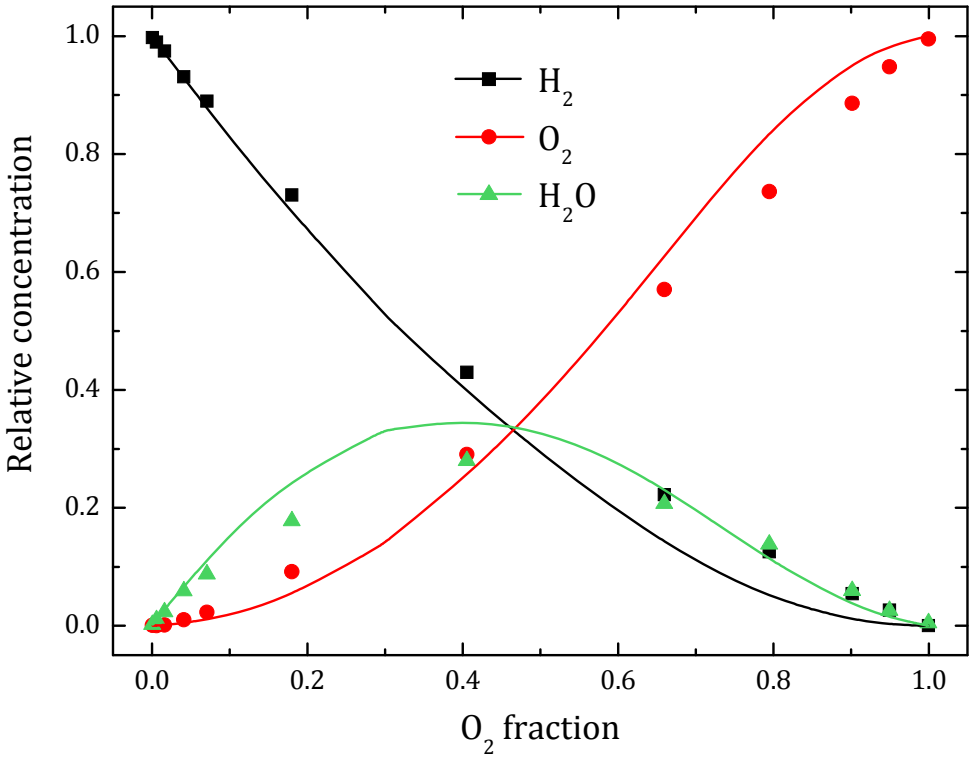

Figure 6.4. Comparison between experimental (symbols) and model (lines) results for the stable neutral species in the $H_2 + O_2$ plasma.

As could be expected, the stable species dominate the distribution, but radicals appear in significant amounts. Hydrogen atoms, produced primarily through electron impact dissociation of H_2 molecules (reaction D_1), have stable concentrations of about 5 % for the majority of the mixtures studied, only decreasing when the oxygen content in the plasma is above 90 %. Oxygen atoms in the ground state, $O(^3P)$, have comparable concentrations to those of H atoms for a wide range of mixtures, disappearing when the H_2 content is high. They reach a maximum concentration of ~ 30 % for the pure O_2 discharge, and present a steady growth with increasing O_2 fraction. The other major radical is OH, which is formed mainly from the dissociation of H_2O molecules (D_5), consequently following a similar behavior to that species. The maximum concentration of OH is ~ 10 %, and it is found for the mixture with 80 % O_2. Ozone and HO_2 are found to be very scarce in the discharge, with concentrations three or four orders of magnitude lower than the previously mentioned species. The two matastable excited species included in the model, $O_2(a^1\Delta_g)$ and $O(^1D)$, are present in very different amounts. The concentrations of $O_2(a^1\Delta_g)$ are comparatively high, typically ~ 5 % of the O_2 concentration, and as such reach almost 10 % of the total neutral concentration for the pure O_2 discharge. On the other hand, the

amounts of O(¹D) in the discharge are very low, three or four orders of magnitude below the concentration of O(³P).

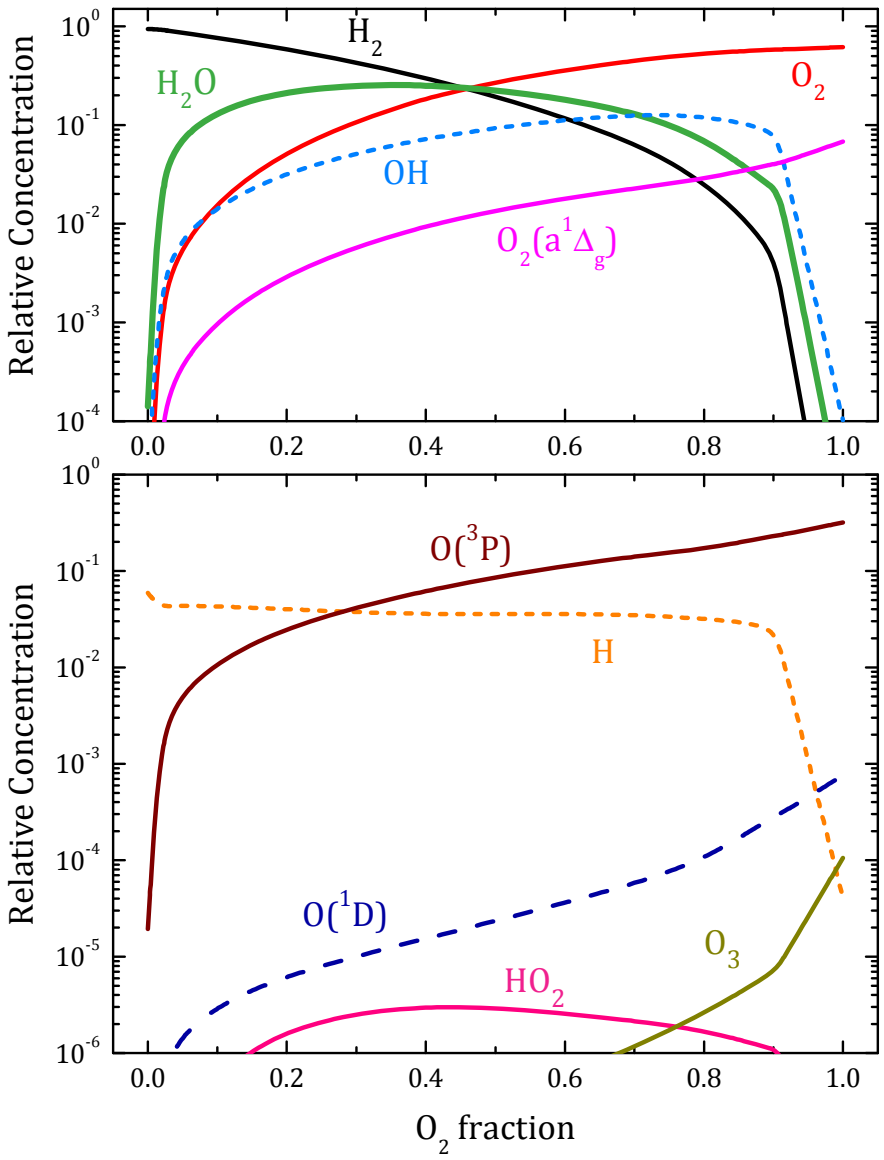

Figure 6.5. Simulated relative concentrations for all the neutral species included in the model. They are split in two panels for clarity.

The two excited species have very different effects in the chemistry of the discharge. Despite the relatively high concentrations of $O_2(a^1\Delta_g)$, the impact in the chemistry of the discharge is limited, its main role being the production of O^- ions through dissociative attachment (A_4). On the other hand, the amounts of O(¹D) in the discharge are very low, but the role in the neutral chemistry of the discharge is more relevant. The reactions of

$O(^1D)$ with H_2 and H_2O (G_{11} and G_{15}) have high rate coefficients for a homogeneous neutral process, and become a main source for OH radicals when the concentration of $O(^1D)$ is high enough (80–90 % O_2 mixtures).

6.2.2 Positive ions

The concentrations obtained from the model for the positive ions in the discharge can be compared to the experimental PPM measurements. In this case, the concentrations of all the species included in the model have been determined experimentally. The results are shown in Figure 6.6.

The global behavior of the major ions is reasonably well reproduced by the model, although some discrepancies with the experimental observations are found. At the lowest O_2 concentration, H_3^+ is the dominant ion, with an important contribution of H_3O^+ and H^+, which replicates the experimental results. However, the value for the electron temperature used for this simulation is 2.4 eV, as opposed to the 1.7 eV value measured with the Langmuir probe (see Figure 6.1). If the experimental value is used as an input for the model, the concentration of H_3O^+ is significantly overestimated. The use of a higher value for the electron temperature is supported by previous measurements in pure hydrogen plasmas at the same pressure [35,55]. The rest of the model simulations have been carried out using the experimental values for the electron temperatures and densities.

With the addition of oxygen to the mixture, H_3O^+ quickly becomes the major ion. When oxygen is only present in small amounts, the main mechanism for the formation of this ion is the proton transfer from H_3^+ to H_2O (reaction T_{12}), with a high rate coefficient warranted by the difference in proton affinity of the species involved (691.0 kJ/mol for H_2O and 422.3 kJ/mol for H_2). As the amount of precursor oxygen is increased, H_3^+ declines and other ions become important in the mixture, diversifying the production processes for H_3O^+. For intermediate mixtures, these include charge transfer reactions involving H_2O^+ (T_{21} and T_{22}) and OH^+ (T_{19}), all of which have high rate coefficients. With even higher concentrations of O_2, the concentration of hydronium decreases and O_2^+, which is mainly produced from the direct ionization of O_2 molecules (I_3), becomes the major ion. For the pure oxygen plasma, only this ion and O^+ from the dissociative ionization of O_2 remain, but the ratio between them predicted by the model (3:1) is different from the experimental one (2:1). This ratio is highly dependent on the electron temperature, so a rise in this parameter would help reproduce the experimental results.

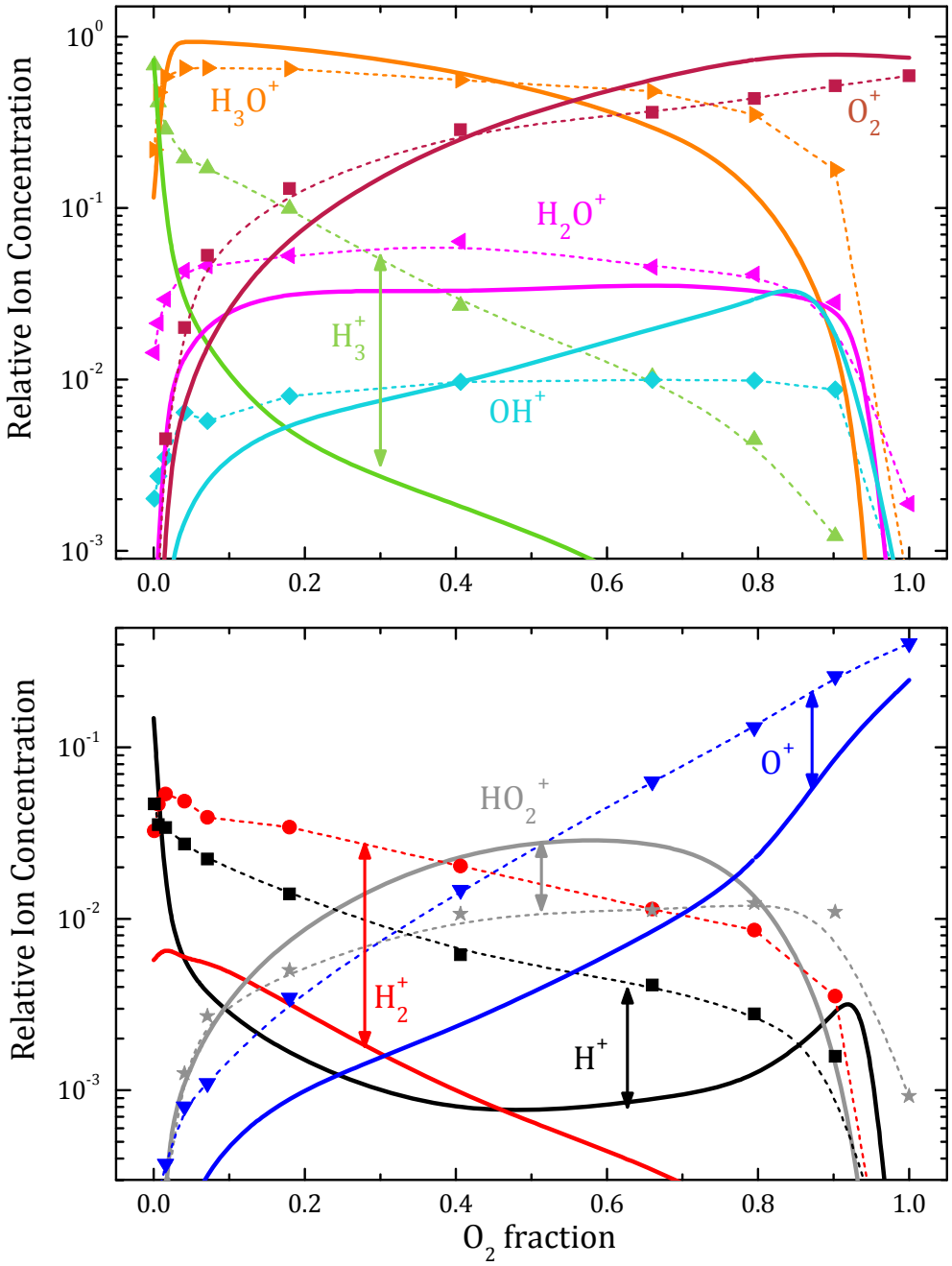

Figure 6.6. Comparison between the experimental (symbols and dashed lines) and simulated (solid lines) concentrations of the positive ions present in the discharge. Two panels with different species are used for clarity.

The three mixed ions OH^+, H_2O^+ and HO_2^+ have concentrations of the order of ~ 1–3 % for a wide range of the mixtures studied, with H_2O^+ tending to be slightly more abundant. This behavior qualitatively reproduces the experimental observations. H_2O^+ is

produced mainly through the ionization of water molecules (I_8), and then destroyed through collisions with H_2 (T_{21}) and H_2O (T_{22}), which, as mentioned before, produce H_3O^+. In the case of OH^+, it is produced mainly from the dissociative ionization of H_2O (I_9), and destroyed through collisions with all of the major molecular species in the plasma, H_2 (T_{17}), O_2 (T_{20}) and H_2O (T_{18} and T_{19}). For HO_2^+, the reaction with H_2 to form H_3^+ is nearly thermoneutral, with the forward (T_{25}) and backward (T_{13}) rate coefficients being comparable, and this equilibrium determines its concentration for H_2-rich mixtures. When oxygen is the major component of the mixture, reaction T_{24} becomes the main source of HO_2^+, while the destruction mechanism remains the same.

It is interesting to observe at this point that the relative concentrations of the H_3O^+, H_2O^+ and OH^+ ions are similar to those predicted in astrochemical models for the interior of dark clouds [196], where the chemistry leading to the formation of these ions has some similitude with that of this discharge. It starts also with the ionization of molecular hydrogen and proceeds through proton transfer reactions involving H_3^+. In diffuse clouds, where OH^+ and H_2O^+ have been detected [194,195], H_2 is scarce, and the abundant electrons neutralize H_3^+. In these regions other mechanisms starting with the ionization of atomic hydrogen become prevalent and produce an inverse ordering of the ionic relative abundances [196] ($[OH^+] > [H_2O^+] > [H_3O^+]$). The concentration of the HO_2^+ ion found in the plasmas studied here is similar to that of OH^+, which suggests that this ion might be found, as a minor species, inside dark clouds.

Purely hydrogenic ions obviously dominate the discharge for pure H_2 conditions but decrease abruptly with the addition of oxygen to the mixture, especially H_3^+, falling orders of magnitude from their initial values. This decrease is also observed in the experimental data, but with a smoother slope, with H_3^+ only going below 1 % concentration for a ~ 60 % O_2 mixture, while in the model simulations this occurs for a mere 10 % O_2. In the case of H_2^+, its concentration is underestimated by almost an order of magnitude through the whole range of mixtures, and for H^+ the behavior is only reproduced for high H_2 and high O_2 conditions.

The concentrations of these ions depend strongly on the electron temperature, as both H^+ and H_2^+ are produced by electron impact ionization of H_2 (reactions I_5 and I_6, respectively), and H_3^+ is subsequently produced from H_2^+ in a charge transfer reaction with H_2 (T_5). A higher electron temperature would enhance the production of these ions, leading to a better agreement between the experiment and the model, since all hydrogenic ions were underestimated in the simulations. However, for the majority of mixtures studied, rising the electron temperature would lead to an important increase in certain species, such as H_2O^+ and OH^+, which are already well reproduced by the model, effectively altering the behavior of the major ions in the discharge. This can be observed in Figure 6.7,

where the simulated relative concentrations of positive ions for two electron temperatures, 2 eV and 3 eV, are displayed.

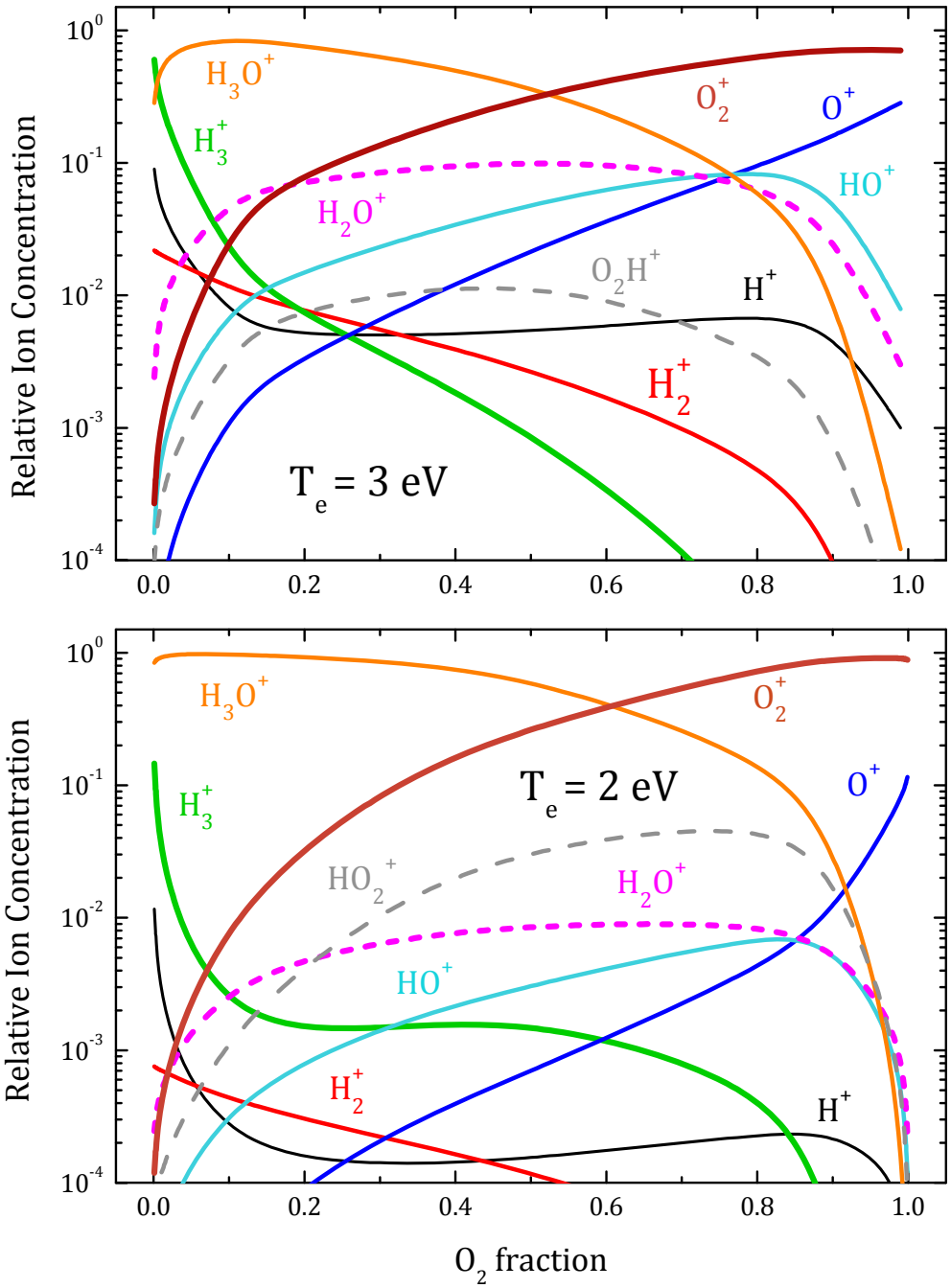

Figure 6.7. Relative concentrations of positive ions obtained from model simulations at two electron temperatures, 3 eV (upper panel) and 2 eV (lower panel).

6.2.3 Negative ions

The abundances of negative ions have not been determined experimentally, due to the limitations commented on in section 2.1.2.2. Model simulations provide the concentrations of the three negative ions considered in these discharges, H^-, OH^- and O^-. The results of the simulations for the negative charge carriers can be seen in Figure 6.8.

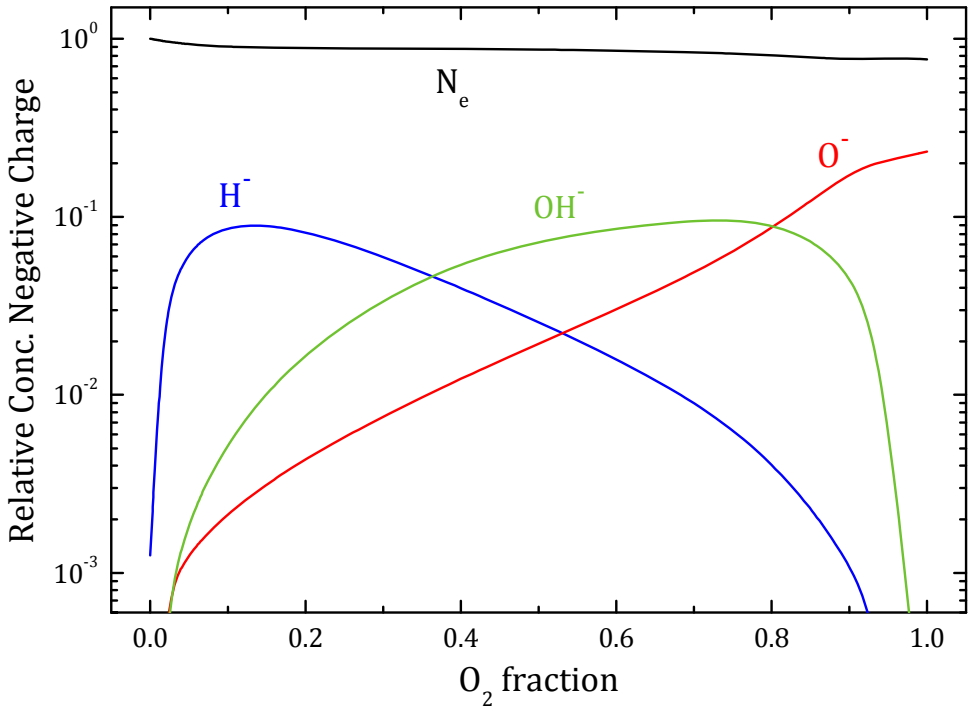

Figure 6.8. Relative concentrations for the negative charge carriers in the discharge.

Electrons are clearly the dominant species for all mixture ratios, with negative ions making up at most 25 % of the total negative charge. In the pure H_2 plasma, negative ions are hardly present, as was expected, with a relative concentration of $H^- \sim 0.1$ %. However, the addition of small amounts of O_2 to the mixture makes its concentration rise up to 10 %, due to the high cross section for the dissociative attachment of H_2O (reaction A_2), which is being formed in the discharge. As the oxygen ratio grows, H^- ions are lost due to collisional detachment with O_2 (Dt_4), whereas O^- and OH^- ions increase in concentration. O^- is produced from the dissociative attachment of water (A_5) and then transformed into OH^- through collisions with H_2 and H_2O (T_{26} and T_{27}). OH^- is the major negative ion for mixtures from 40 % to 80 % O_2. For higher oxygen concentrations, the amount of H_2 and H_2O in the discharge is not enough to maintain an efficient formation of OH^-, so it

decreases quickly. In these conditions, O^- is formed from the dissociative attachment of O_2 (reaction A_1) and $O_2(a^1\Delta_g)$ (reaction A_4).

The relevance of the negative ion processes in the chemistry of the other species in the discharge is low, as they are not involved in any main mechanism for production or destruction of positive ions or neutrals. The main gas phase process in which negative ions take part is the neutralization of positive ions. However, in the plasmas studied, ion-ion neutralization is far less important than the neutralization at the cathode walls for the destruction of positive ions. The main contribution of negative ions is in fact the reduction of the electron density, which lowers the rate of electron impact processes but, given that their concentration never exceeds 25 % of the total negative charge, this effect is not large.

6.3 $H_2 + N_2 + O_2$ discharges

The role that the proton affinities of the major species in the discharge play in the final ion distributions has already been highlighted both in the present chapter and in the previous ones. In order to emphasize this, an additional experimental study has been carried out in discharges of mixtures of $H_2 + N_2 + O_2$.

In the same way as the $H_2 + O_2$ plasmas, the experiments were performed at a total pressure of 8 Pa, to favor the ion-molecule chemistry. The mixtures employed consisted of H_2 with varying concentrations of air, from 3 % to 19 %. Electron temperatures were ~ 3 eV and electron densities ~ 3×10^{10} cm^{-3} s^{-1}.

The concentrations of the neutral stable molecules in the discharge are shown in Figure 6.9. As expected, H_2 is the dominant species for all the mixtures studied, as the precursor H_2 is always above 80 % of the composition. N_2 is the second most abundant species, with concentrations between 2 % and 13 %. H_2O and NH_3 follow, both with very similar abundances, around a factor 2 lower than that of N_2. Finally, O_2 is clearly the less abundant molecule, with a concentration more than an order of magnitude lower than N_2, despite the precursor mixture being ~ 1:4 in proportion.

This low abundance of O_2 is related to the relatively high (considering the mixture proportions) concentration of H_2O compared to NH_3. As was seen in the models of $H_2 + N_2$ and $H_2 + O_2$, NH_3 requires an extra step for its formation through heterogeneous reactions, making it a slower process than the formation of water at the reactor walls. The faster formation of H_2O leads in turn to a depletion of the O_2 precursor.

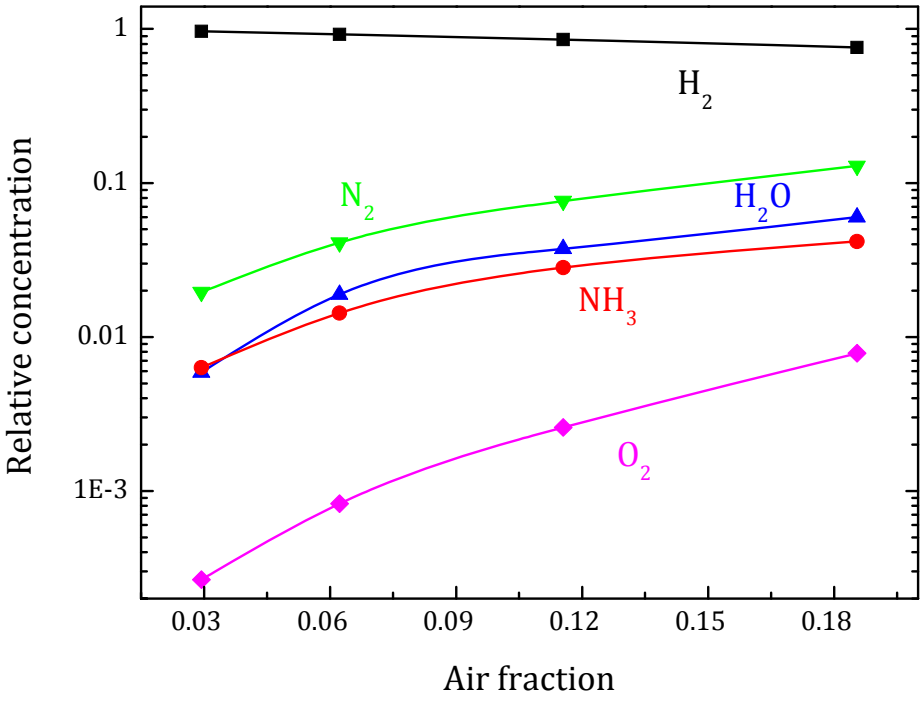

Figure 6.9. Experimental concentrations of the neutral stable species in the H_2 + air discharge.

The focus of this study, however, lies in the protonated ions. Their concentrations are shown in Figure 6.10. The distributions of protonated ions are always dominated by NH_4^+ except for the lowest air fraction, where the densities of H_3O^+ and NH_4^+ are comparable. With growing air content, the proportion of NH_4^+ increases steadily, whereas the relative densities of the other three ions, H_3O^+, H_3^+ and N_2H^+, decrease monotonically and only traces of HO_2^+ are detected. The results can be rationalized in terms of the proton affinities and collision frequencies of the various ions and molecules involved. Table 6.1 shows the proton affinities for the neutral stable molecules of the discharge.

The distributions are largely determined by the ion-molecule reactions leading to the production and destruction of the protonated ions. Most of the relevant processes have already been discussed in the present and previous chapters, but there are a couple of important reactions specific to these plasmas.

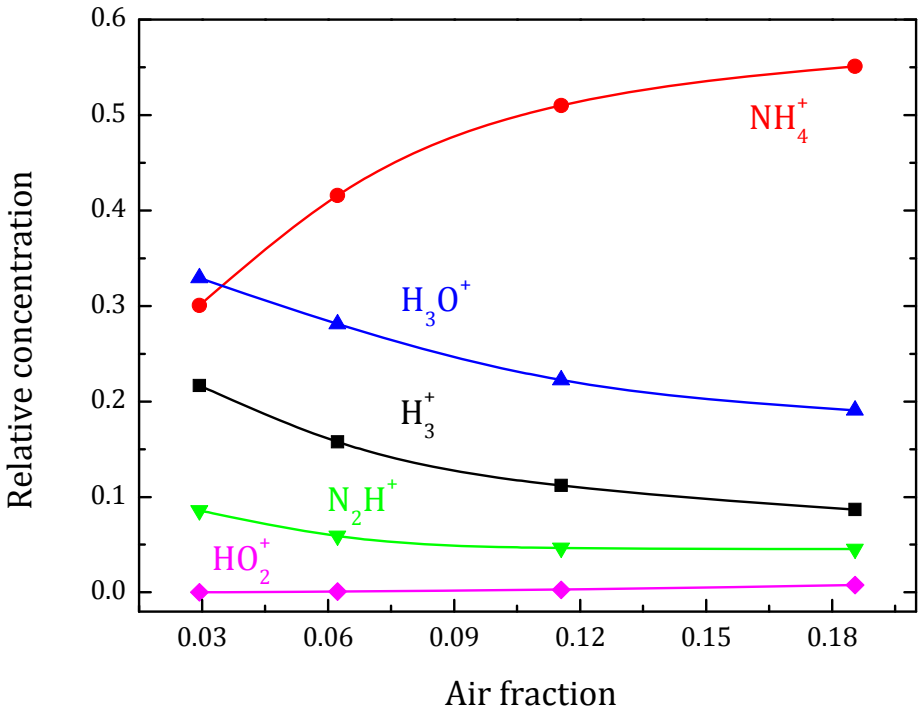

Figure 6.10. Relative concentrations of the protonated ions in the H_2 + air discharge.

In particular, the hydronium ion can be formed via reaction T_{12} (H_2 + O_2 model) but also through collisions of N_2H^+ with water:

$$N_2H^+ + H_2O \rightarrow H_3O^+ + N_2 \qquad k = 2.60 \times 10^{-9}\ \text{cm}^3\ \text{s}^{-1}$$

The ammonium ion is formed through collisions of ammonia with H_3^+, N_2H^+ (reactions T_8 and T_{25} of the H_2 + N_2 model) and H_3O^+:

$$H_3O^+ + NH_3 \rightarrow NH_4^+ + H_2O \qquad k = 2.23 \times 10^{-9}\ \text{cm}^3\ \text{s}^{-1}$$

The direction of the proton transfer in the two written reactions is determined by the ordering of the proton affinities of the participating molecules, ultimately leading to the formation of NH_4^+. This oversimplified set of reactions is sufficient to justify the observed ion distributions.

When the relative densities of the minor molecules are high enough to allow for collisions between them and positive ions to be relevant in the plasma chemistry, the rest of the protonated ions can transfer their proton to ammonia and contribute to the production of NH_4^+. On the other hand, the ammonium ion has no destruction mechanisms

other than wall neutralization in the plasmas under consideration and therefore tends to concentrate in them. The same line of reasoning applies to the rest of the protonated ions in Figure 6.10. Their relative abundances are largely determined by the number of formation and destruction pathways, which are related to their respective proton affinities, and also by the relative concentration of their neutral precursors. It can be seen that, for the larger air fractions, protonated ions are ordered according to their proton affinities, except for H_3^+ and N_2H^+, which are interchanged. In spite of the fact that the proton affinity of N_2 is higher than that of H_2, the N_2H^+ ion is efficiently destroyed in collisions with H_2O and NH_3 and the concentration of its neutral precursor, N_2, is always much lower than that of H_2.

Table 6.1. Proton affinities for the neutral stable molecules present in $H_2 + N_2 + O_2$ discharges. The values are taken from [217].

Molecule	Proton affinity (kJ mol^{-1})
NH_3	853.6
H_2O	691
N_2	493.8
H_2	422.3
O_2	421

It should be noted that, in most cases, proton transfer processes like those exemplified in the previous paragraphs occur irreversibly on every collision and thus, given sufficient time, a very small amount of a suitable precursor could lead to the predominace of a given protonated ion. In this respect, the present results support the predictions of astrochemical models [218,219] that indicate that H_3O^+ and NH_4^+ might be dominant in warm environments like hot cores, where molecules with high proton affinity like H_2O and NH_3 are evaporated from the grains. Given the very high proton affinity of NH_3 as compared with most small molecules, (see Table 6.1 and ref. [217]) the production of NH_4^+ could represent the final step in the proton transfer chain in many astronomical environments.

6.4 Summary and conclusions

A combined diagnostics and modeling of low pressure H_2 + O_2 plasmas with different mixture ratios, generated in a hollow cathode DC reactor, has been presented. The results of the model simulations have allowed the identification of the main processes determining the observed neutral and ion distributions.

Water formation is observed in the discharge for the whole range of mixtures, up to a maximum of ~ 30 % relative concentration. These results are well reproduced by the kinetic model, which predicts slightly higher concentrations (up to 35 %) of water. The concentrations of other neutrals, including radicals and excited species that could not be experimentally observed, have been also simulated with the model. Atomic oxygen and hydrogen are formed in significant amounts, with relative concentrations of the order of 10 % when the presence of their molecular precursors is significant. The OH radical, formed from the dissociation of water, shows a similar behavior over the range of mixtures studied, with a peak value of ~ 10 % of the total neutral concentration. The metastable excited species $O_2(a^1\Delta_g)$ and $O(^1D)$ are formed in different proportions in the discharge, with $O_2(a^1\Delta_g)$ reaching up to 10 % relative concentration but having a limited impact in the chemistry. In contrast, $O(^1D)$ is produced in smaller amounts (up to ~ 0.1 % of the total concentration) but has a great relevance in the chemistry due to the high cross sections for its reactions with neutrals. The other neutral species considered, O_3 and HO_2, are hardly formed in the discharge.

The experimental ion distributions are dominated by hydrogenic ions only for mixtures with nearly no oxygen. As soon as H_2O is formed in the plasma, H_3O^+ becomes the major ion, remaining as such for mixtures with 4 % < O_2 < 70 %. For higher O_2 fractions, pure oxygen ions become dominant, with O_2^+ as the major ion for these mixtures. The concentrations of the mixed minor ions H_2O^+, OH^+, HO_2^+ are stable through a wide range of intermediate H_2/O_2 ratios, only sinking for the extreme mixtures. A comparison of the relative abundances of these ions with the predictions of astrochemical models suggests that HO_2^+ might be present as a minor component in the interior of dark interstellar clouds. Model simulations reproduce the behavior of the ions reasonably well. For the pure H_2 discharge, H_3^+ is the dominant ion, and when oxygen is added to the mixture, H_3O^+ concentration grows due to proton transfer between H_3^+ and H_2O, becoming the major ion. For high O_2 ratios, direct ionization of this precursor causes O_2^+ to prevail in the plasma.

The main discrepancy between measurements and simulations is found for the pure hydrogenic ions, whose predicted decrease upon oxygen addition to the mixture is much more abrupt than experimentally observed. This is due to the low electron temperature, which causes the charge transfer processes to prevail over electron impact. When oxygen

is added to the mixture, water is formed and H_3^+ is destroyed through charge transfer to H_2O. A higher value for the electron temperature would increase the concentration of hydrogenic ions through the direct ionization of H_2 and subsequent charge transfer; however, this would lead to a great change in the concentrations of other ions. A non-maxwellian electron energy distribution function could justify a different balance of these processes, by increasing or decreasing the population of the high energy tail.

The concentrations of negative charge carriers have been simulated with the model. The distribution is dominated by electrons for all mixture ratios, with negative ion concentrations reaching up to 25 % of the total negative charge. H^- and O^- are the major negative ions for the H-rich and O-rich discharges, respectively, while OH^- prevails for the intermediate mixtures. For the pure H_2 plasma, the concentration of negative ions (H^-) is much lower than for the rest of the conditions. The relevance of negative ions to the global chemistry is limited, as their main role is just decreasing the electron density available for electron impact processes.

Plasmas of $H_2 + N_2 + O_2$ have also been studied through experimental means. Mixtures of H_2 with small amounts (3–19 %) of air have been employed as the precursor gas and mass spectrometry of neutrals and ions was used to determine the concentrations of the relevant species. Concerning the neutrals, NH_3 and H_2O appear in comparable amounts in the discharge, despite the 4:1 ratio of N_2 to O_2 in the precursor mixture, due to the fewer amount of steps required for the formation of water at the reactor walls. Protonated species dominate the positive ion distributions. In particular, NH_4^+ is the dominant species for most of the mixture ratios, with H_3O^+ being the major ion only for the lowest air concentration studied. The efficient ion-molecule chemistry of the discharge causes the relative concentrations of these ions to be closely related to their proton affinity. Due to this, only negligible concentrations of H_2O^+ are found in the plasma, and the positive charge tends to accumulate in H_3O^+ and specially NH_4^+ ions.

Chapter 7.

Concluding remarks

7.1 Summary

In this work, a study of the plasma kinetics in low pressure hollow cathode dc discharges of H_2 with Ar, N_2 and O_2 has been presented. A combination of experimental diagnostics and theoretical modeling has been employed to determine the relevant processes in the discharges.

The same experimental setup has been employed for the three different mixtures. A double Langmuir probe was used to obtain the plasma parameters (electron temperature and density), and the concentrations of the different neutral and ionic species were determined by mass spectrometry.

A zero order kinetic model was developed for each of the different mixtures. The models consist of a set of time-dependent coupled differential equations for the concentration of the different species that account for the main physico-chemical processes occurring in the plasma, both in the gas phase and at the reactor walls.

The H_2 + Ar plasma is the simplest of the ones studied, due to the comparatively small number of species present in the discharge. The neutral chemistry of the discharge does not present a great relevance, since no new species are formed in the plasma, and the only significant mechanism is the dissociation and wall recombination of H_2 molecules. Thus, the study of these mixtures is focused on the ion chemistry.

Positive ion distributions were measured at 1.5 and 8 Pa and comprise the whole range of Ar/H_2 mixture ratios. The distributions were dominated by Ar^+, ArH^+ and H_3^+ ions,

with relative concentrations depending strongly on pressure and mixture ratio. In particular, the region of dominance of ArH^+ was found to greatly vary between the two pressures, from a wide range of mixture ratios at 1.5 Pa to a narrow window close to the pure Ar plasma in the 8 Pa discharge. Two key factors drive the observed ion chemistry: the electron temperature, which depends on the pressure, and the equilibrium of the process $H_3^+ + Ar \rightleftarrows ArH^+ + H_2$, which ultimately determines the ArH^+/H_3^+ ratio. The forward reaction is endothermic for ground state reactants, and thus it is slow; however, if the internal energy of the reactants is higher than 0.55 eV, it becomes exothermic with a much higher rate coefficient. The experimental data and simulations suggest that the internal excitation of H_3^+ in the plasmas studied is sufficient to overcome the energetic barrier at the lower pressure, but is efficiently quenched at 8 Pa and the reaction becomes endothermic.

The chemistry in $H_2 + N_2$ plasmas has been analyzed in detail for both the neutral and ionic species. Mixtures of $H_2 + \sim 10\ \% N_2$ at five different pressures, from 0.8 to 8 Pa, have been studied. Ammonia was found in significant amounts in all the discharges, with concentrations comparable to those of N_2 for the lowest pressures. This NH_3 is formed at the reactor walls in a series of heterogeneous reactions involving both Langmuir-Hinshelwood and Eley-Rideal mechanisms.

Ion distributions are mainly determined by the electron temperature of the discharge, which controls the balance between direct ionization and ion-molecule reactions. At the lower pressures, with high electron temperatures, both kinds of processes have a similar relevance, leading to a balanced positive ion distribution in which several ions are found in high concentrations. Conversely, when the pressure is high, the low electron temperature causes ion-molecule reactions to prevail. In these conditions, the chain of protonation reactions leads to a predominance of the ammonium ion, due the lack of a destruction reaction for NH_4^+ in the gas phase, while being formed from collisions of other relevant protonated species (H_3^+, N_2H^+) with ammonia molecules.

The third kind of discharges studied was $H_2 + O_2$. Measurements were carried out at 8 Pa for the whole range of mixture ratios. Water was detected in substantial concentrations, comparable to those of the minor precursor in the mixture. Comparison with the kinetic model shows that H_2O is primarily produced in a series of heterogeneous Eley-Rideal reactions in the surfaces of the reactor. The concentrations of other minor and unstable neutral species (atoms, radicals and metastables) were simulated with the model.

Experimental positive ion concentrations were found to be dominated by H_3O^+ for a wide variety of intermediate mixtures, due to the proton transfer between H_3^+ and H_2O, while H_3^+ is the major ion in the discharge for H-rich mixtures. For O-rich plasmas, O_2^+, formed by the direct ionization of O_2 molecules, is the dominant ion. The mixed ions (H_2O^+,

OH^+, HO_2^+) maintain a roughly stable concentration for intermediate H_2/O_2 ratios, and they obviously disappear in the extreme mixtures. These results, along with the predictions of astrochemical models, suggest that HO_2^+ might be found in small amounts in the interior of molecular clouds.

Negative ion concentrations were simulated with the kinetic model, showing that these species concentrate up to 25 % of the total negative charge in the plasma. H^-, present in small concentrations in the pure H_2 plasma, rises sharply with the addition of O_2 to the mixture. OH^- dominates for intermediate H_2/O_2 ratios and O^- is the major negative ion in O-rich plasmas. Negative ions, however, have a very limited effect in the global chemistry of the discharge.

Experimental measurements were also performed in $H_2 + N_2 + O_2$ discharges. In particular, mixtures of H_2 with small concentrations of air were employed as precursors, with a total pressure of 8 Pa. Ammonia and water were detected in comparable concentrations, despite the differences in the abundance of the precursors N_2 and O_2, due to the lower number of reactions required for the formation of H_2O. Protonated ions were found to be the major species in the positive ion distributions, with NH_4^+ prevailing in the discharge followed by H_3O^+. In these low electron temperature plasmas, a strong correlation was found between the proton affinity of the species and their abundance in the discharge.

In all of these studies, protonated ions have been shown to play a key role in the ion chemistry of the different discharges. In the plasmas studied, a balance is established between the ions produced by direct ionization of stable molecules, a process controlled by the electron temperature of the plasma, and the protonated ions, which are usually the main products of the ion-molecule chemistry of the discharge. Due to the fact that ion-molecule reactions are generally barrierless, their relevance is roughly stable as the plasma conditions are changed, while the rate coefficients for electron impact reactions are highly dependent on the electron temperature. At low electron temperatures, ion-molecule processes are highly responsible for the chemistry of the positive ions in the plasma.

In the discharges presented in this work, carried out at pressures between 0.8 and 8 Pa, the high pressure conditions entail an ion chemistry dominated by ion-molecule reactions. In those cases, the ion chemistry in the discharge is comparable up to a certain extent to the chemistry of the interstellar medium, and particularly molecular clouds, where H_2 is abundant. Therefore, these types of plasmas can provide an adequate laboratory equivalent for the study of the chemistry in these kinds of media. The experiments and simulations carried out in this thesis highlight the relevance of

protonated ions in the discharges, analogously to the influential role of these ions in the interstellar chemistry.

7.2 Future perspectives

The experimental and theoretical work performed in hydrogen-rich hollow cathode glow discharges has shown the utility of combining zero order kinetic models with experimental diagnostics to uncover the fundamental mechanisms determining the kinetics in said plasmas. Proposals for future works, relevant in different fields such as astrophysics or fusion research, are listed below.

- An extension of the H_2 + N_2 experiments presented in this work to the whole range of mixtures, and a study of discharges of hydrogen with varying amounts of ammonia, to complement the former. Ammonia contamination on fusion reactors, due to the use of nitrogen for the cooling of the divertor, is an issue under examination in fusion research, adding significance to this investigation.

- The substitution of H_2 with D_2 in the mixtures investigated in this thesis in order to compare the resulting neutral and ion distributions, with interest both in fusion and astrophysics.

- An investigation of mixtures of H_2 + CO, since they are the two most abundant molecules in the interstellar medium. This study presents more obstacles than the other proposals, due to the inclusion of an additional atomic species, greatly increasing the complexity of the kinetics, and the possible formation of carbon deposits or carbon based nanoparticles in the discharge, producing a dusty plasma.

- The coupling of the kinetic models used in this work with a Boltzmann solver in order to simulate the electron energy distributions and better understand electron impact chemistry, and at the same time adding the possibility of comparing experimental and simulated electron temperatures and densities for the different conditions studied.

Bibliography

[1] N. Bondt, J. R. Deimann, A. P. van Trootswyk, A. Lauwerenburg, cited in A.F. Fourcroy, *Ann. Chim. (Paris, Fr.)* **21** (1797) 58.

[2] W. Crookes, *On radiant matter. A lecture delivered to the British Association for the Advancement of Science, at Sheffield, Friday, August 22, 1879.* (1879).

[3] I. Langmuir, *Proc. Natl. Acad. Sci. U.S.A.* **14** (1928) 627.

[4] U. Samm, *Contemp. Phys.* **44** (2003) 203.

[5] J. Roth et al., *J. Nucl. Mater.* **390-391** (2009) 1.

[6] D. M. Goebel, I. Katz, *Fundamentals of Electric Propulsion: Ion and Hall Thrusters*, John Wiley & Sons (2008).

[7] A. Grill, *Cold Plasma Materials Fabrication: From Fundamentals to Applications*, Wiley-IEEE Press (1993).

[8] M. A. Lieberman, A. J. Lichtenberg, *Principles of Plasma Discharges and Materials Processing*, John Wiley & Sons (1994).

[9] F. J. Gordillo-Vázquez, V. J. Herrero, I. Tanarro, *Chem. Vapor Depos.* **13** (2007) 267.

[10] N. Laidani, R. Bartali, P. Tosi, M. Anderle, *J. Phys. D-Appl. Phys.* **37** (2004) 2593.

[11] I. B. Denysenko, S. Xu, J. D. Long, P. P. Rutkevych, N. A. Azarenkov, K. Ostrikov, *J. Appl. Phys.* **95** (2004) 2713.

[12] P. J. van den Oever, J. H. van Helden, J. L. van Hemmen, R. Engeln, D. C. Schram, M. C. M. van de Sanden, W. M. M. Kessels, *J. Appl. Phys.* **100** (2006).

[13] S. Xu, S. Y. Huang, I. Levchenko, H. P. Zhou, D. Y. Wei, S. Q. Xiao, L. X. Xu, W. S. Yan, K. Ostrikov, *Advanced Energy Materials* **1** (2011) 373.

[14] A. G. Aberle, *Sol. Energy Mater. Sol. Cells* **65** (2001) 239.

[15] A. V. Melechko, R. Desikan, T. E. McKnight, K. L. Klein, P. D. Rack, *J. Phys. D-Appl. Phys.* **42** (2009).

[16] C. Volcke, R. P. Gandhiraman, V. Gubala, J. Raj, T. Cummins, G. Fonder, R. I. Nooney, Z. Mekhalif, G. Herzog, S. Daniels, D. W. M. Arrigan, A. A. Cafolla, D. E. Williams, *Biosens. Bioelectron.* **25** (2010) 1875.

[17] K. Ostrikov, E. C. Neyts, M. Meyyappan, *Adv. Phys.* **62** (2013) 113.

[18] K. Ostrikov, U. Cvelbar, A. B. Murphy, *J. Phys. D-Appl. Phys.* **44** (2011) 174001.

[19] G. Federici, C. H. Skinner, J. N. Brooks, J. P. Coad, C. Grisolia, A. A. Haasz, A. Hassanein, V. Philipps, C. S. Pitcher, J. Roth, W. R. Wampler, D. G. Whyte, *Nucl. Fusion* **41** (2001) 1967.

[20] F. L. Tabarés, D. Tafalla, I. Tanarro, V. J. Herrero, A. Islyaikin, C. Maffiotte, *Plasma Phys. Control. Fusion* **44** (2002) L37.

[21] M. Oberkofler et al., *Fusion Eng. Des.* **98-99** (2015) 1371.

[22] J. H. van Helden, W. Wagemans, G. Yagci, R. A. B. Zijlmans, D. C. Schram, R. Engeln, G. Lombardi, G. D. Stancu, J. Ropcke, *J. Appl. Phys.* **101** (2007) 043305.

[23] P. Vankan, T. Rutten, S. Mazouffre, D. C. Schram, R. Engeln, *Appl. Phys. Lett.* **81** (2002) 418.

[24] K. Sugiyama, K. Akazawa, M. Oshima, H. Miura, T. Matsuda, O. Nomura, *Plasma Chem. Plasma Process.* **6** (1986) 179.

[25] T. Amano, T. Hirao, J. Takano, *J. Mol. Spectrosc.* **234** (2005) 170.

[26] W. C. Ho, C. J. Pursell, T. Oka, *J. Mol. Spectrosc.* **149** (1991) 530.

[27] A. P. Thorne, *Spectrophysics*, Springer (1988).

[28] R. B. Green, R. A. Keller, G. G. Luther, P. K. Schenck, J. C. Travis, *Appl. Phys. Lett.* **29** (1976) 727.

[29] W. Demtröder, *Laser Spectroscopy: Basic Concepts and Instrumentation*, Springer (2003).

[30] A. G. G. M. Tielens, *Rev. Mod. Phys.* **85** (2013) 1021.

[31] E. Herbst, *Chem. Soc. Rev.* **30** (2001) 168.

[32] E. Herbst, *Philos. Trans. R. Soc. A-Math. Phys. Eng. Sci.* **358** (2000) 2523.

[33] S. N. Tripathi, M. Michael, R. G. Harrison, *Space Sci. Rev.* **137** (2008) 193.

[34] D. L. Huestis, S. W. Bougher, J. L. Fox, M. Galand, R. E. Johnson, J. I. Moses, J. C. Pickering, *Space Sci. Rev.* **139** (2008) 63.

[35] I. Mendez, F. J. Gordillo-Vázquez, V. J. Herrero, I. Tanarro, *J. Phys. Chem. A* **110** (2006) 6060.

[36] L. Schott, in *Plasma Diagnostics*, W. Lochte-Holtgreven (editor), AIP Press (1995) p. 668-731.

[37] M. Castillo, *Espectrometría y cinética de plasmas fríos de óxidos de nitrógeno y aire*, PhD thesis, Dpto. Química-Física, UCM (2004).

[38] E. O. Johnson, L. Malter, *Phys. Rev.* **80** (1950) 58.

[39] H. Amemiya, *J. Phys. D-Appl. Phys.* **23** (1990) 999.

[40] P. Pecher, *Quantitative determination of the particle fluxes emanating from methane ECR plasmas*, PhD thesis, Universität Bayreuth (1997).

[41] I. Tanarro, V. J. Herrero, *Plasma Sources Sci. Technol.* **18** (2009) 034007.

[42] J. T. Gudmundsson, I. G. Kouznetsov, K. K. Patel, M. A. Lieberman, *J. Phys. D-Appl. Phys.* **34** (2001) 1100.

[43] G. Gousset, M. Touzeau, M. Vialle, C. M. Ferreira, *Plasma Chem. Plasma Process.* **9** (1989) 189.

[44] Z. Qing, D. K. Otorbaev, G. J. H. Brussaard, M. C. M. van de Sanden, D. C. Schram, *J. Appl. Phys.* **80** (1996) 1312.

[45] G. Herzberg, *Molecular Spectra and Molecular Structure. I. Spectra of Diatomic Molecules*, Van Nostrand (1955).

[46] M. Jiménez-Redondo, E. Carrasco, V. J. Herrero, I. Tanarro, *Plasma Sources Sci. Technol.* **22** (2013) 025022.

[47] B. P. Lavrov, A. S. Melnikov, M. Kaning, J. Ropcke, *Phys. Rev. E* **59** (1999) 3526.

[48] F. C. Parra-Rojas, M. Passas, E. Carrasco, A. Luque, I. Tanarro, M. Simek, F. J. Gordillo-Vázquez, *J. Geophys. Res-Space Phys.* **118** (2013) 4649.

[49] F. A. Haas, A. Goodyear, N. S. J. Braithwaite, *Plasma Sources Sci. Technol.* **7** (1998) 471.

[50] F. J. Gordillo-Vázquez, Z. Donkó, *Plasma Sources Sci. Technol.* **18** (2009) 034021.

[51] J. B. Boffard, R. O. Jung, C. C. Lin, L. E. Aneskavich, A. E. Wendt, *Plasma Sources Sci. Technol.* **20** (2011) 055006.

[52] P. Gill, C. E. Webb, *J. Phys. D-Appl. Phys.* **10** (1977) 299.

[53] A. Bogaerts, R. Gijbels, W. J. Goedheer, *J. Appl. Phys.* **78** (1995) 2233.

[54] M. Castillo, I. Mendez, A. M. Islyaikin, V. J. Herrero, I. Tanarro, *J. Phys. Chem. A* **109** (2005) 6255.

[55] M. Jiménez-Redondo, E. Carrasco, V. J. Herrero, I. Tanarro, *Phys. Chem. Chem. Phys.* **13** (2011) 9655.

[56] I. N. Levine, *Physical chemistry*, McGraw-Hill (1978).

[57] R. D. Levine, R. B. Bernstein, *Molecular reaction dynamics and chemical reactivity*, Oxford University Press (1987).

[58] T. A. Cleland, D. W. Hess, *J. Electrochem. Soc.* **136** (1989) 3103.

[59] P. Kae-Nune, J. Perrin, J. Jolly, J. Guillon, *Surf. Sci.* **360** (1996) L495.

[60] M. A. Pick, K. Sonnenberg, *J. Nucl. Mater.* **131** (1985) 208.

[61] B. Gordiets, C. M. Ferreira, M. J. Pinheiro, A. Ricard, *Plasma Sources Sci. Technol.* **7** (1998) 379.

[62] J. V. Barth, *Surf. Sci. Rep.* **40** (2000) 75.

[63] I. Mendez, I. Tanarro, V. J. Herrero, *Phys. Chem. Chem. Phys.* **12** (2010) 4239.

[64] R. Rejoub, B. G. Lindsay, R. F. Stebbings, *Phys. Rev. A* **65** (2002) 042713.

[65] V. G. Anicich, *J. Phys. Chem. Ref. Data* **22** (1993) 1469.

[66] D. L. Albritton, *At. Data Nucl. Data Tables* **22** (1978) 1.

[67] A. T. Hjartarson, E. G. Thorsteinsson, J. T. Gudmundsson, *Plasma Sources Sci. Technol.* **19** (2010) 065008.

[68] A. Bogaerts, R. Gijbels, *Spectroc. Acta Pt. B-Atom. Spectr.* **57** (2002) 1071.

[69] Y. K. Kim, J. P. Desclaux, *Phys. Rev. A* **66** (2002) 012708.

[70] H. C. Straub, P. Renault, B. G. Lindsay, K. A. Smith, R. F. Stebbings, *Phys. Rev. A* **54** (1996) 2146.

[71] V. Tarnovsky, H. Deutsch, K. Backer, *Int. J. Mass Spectrom. Ion Process.* **167-168** (1997) 69.

[72] P. C. Cosby, *J. Chem. Phys.* **98** (1993) 9544.

[73] L. C. Owono Owono, N. Jaidane, M. G. Kwato Njock, Z. Ben Lakhdar, *J. Chem. Phys.* **126** (2007) 244302.

[74] R. Vetter, L. Zülicke, A. Koch, E. F. van Dishoeck, S. D. Peyerimhoff, *J. Chem. Phys.* **104** (1996) 5558.

[75] H. Biehl, G. Schoennenbeck, F. Stuhl, V. Staemmler, *J. Chem. Phys.* **101** (1994) 3819.

[76] H. Okabe, *Photochemistry of small molecules*, John Wiley & Sons (1978).

[77] I. A. Kossyi, A. Y. Kostinsky, A. A. Matveyev, V. P. Silakov, *Plasma Sources Sci. Technol.* **1** (1992) 207.

[78] J. B. A. Mitchell, *Phys. Rep.-Rev. Sec. Phys. Lett.* **186** (1990) 215.

[79] L. Vikor, A. Al-Khalili, H. Danared, N. Djuric, G. H. Dunn, M. Larsson, A. Le Padellec, S. Rosén, M. Af Ugglas, *Astron. Astrophys.* **344** (1999) 1027.

[80] T. Amano, *J. Chem. Phys.* **92** (1990) 6492.

[81] Y. Itikawa, *J. Phys. Chem. Ref. Data* **38** (2009) 1.

[82] V. Tarnovsky, H. Deutsch, K. Becker, *J. Chem. Phys.* **109** (1998) 932.

[83] Y. Itikawa, N. Mason, *J. Phys. Chem. Ref. Data* **34** (2005) 1.

[84] C. Lee, D. B. Graves, M. A. Lieberman, D. W. Hess, *J. Electrochem. Soc.* **141** (1994) 1546.

[85] E. F. van Dishoeck, S. R. Langhoff, A. Dalgarno, *J. Chem. Phys.* **78** (1983) 4552.

[86] R. Peverall, S. Rosen, J. R. Peterson, M. Larsson, A. Al-Khalili, L. Vikor, J. Semaniak, R. Bobbenkamp, A. Le Padellec, A. N. Maurellis, W. J. van der Zande, *J. Chem. Phys.* **114** (2001) 6679.

[87] S. Rosen, A. Derkatch, J. Semaniak, A. Neau, A. Al-Khalili, A. Le Padellec, L. Vikor, R. Thomas, H. Danared, M. af Ugglas, M. Larsson, *Faraday Discuss.* **115** (2000) 295.

[88] M. J. Jensen, R. C. Bilodeau, C. P. Safvan, K. Seiersen, L. H. Andersen, H. B. Pedersen, O. Heber, *Astrophys. J.* **543** (2000) 764.

[89] J. Woodall, M. Agúndez, A. J. Markwick-Kemper, T. J. Millar, *Astron. Astrophys.* **466** (2007) 1197.

[90] E. Neyts, M. Yan, A. Bogaerts, R. Gijbels, *J. Appl. Phys.* **93** (2003) 5025.

[91] F. J. Gordillo-Vázquez, *J. Phys. D-Appl. Phys.* **41** (2008) 234016.

[92] O. Eichwald, M. Yousfi, A. Hennad, M. D. Benabdessadok, *J. Appl. Phys.* **82** (1997) 4781.

[93] D. S. Stafford, M. J. Kushner, *J. Appl. Phys.* **96** (2004) 2451.

[94] R. Atkinson, D. L. Baulch, R. A. Cox, R. F. Hampson, J. A. Kerr, M. J. Rossi, J. Troe, *J. Phys. Chem. Ref. Data* **26** (1997) 1329.

[95] T. J. Millar, P. R. A. Farquhar, K. Willacy, *Astron. Astrophys. Suppl. Ser.* **121** (1997) 139.

[96] E. E. Ferguson, *At. Data Nucl. Data Tables* **12** (1973) 159.

[97] T. Jaffke, M. Meinke, R. Hashemi, L. G. Christophorou, E. Illenberger, *Chem. Phys. Lett.* **193** (1992) 62.

[98] H. Tawara, Y. Itikawa, H. Nishimura, M. Yoshino, *J. Phys. Chem. Ref. Data* **19** (1990) 617.

[99] R. K. Janev, W. D. Langer, J. K. Evans, D. E. Post, *Elementary Processes in Hydrogen - Helium Plasmas: Cross Sections and Reaction Rate Coefficients*, Springer (1987).

[100] T. G. Slanger, G. Black, *J. Chem. Phys.* **68** (1978) 989.

[101] D. B. Dunkin, F. C. Fehsenfeld, E. E. Ferguson, *J. Chem. Phys.* **53** (1970) 987.

[102] M. J. McEwan, L. F. Phillips, *Chemistry of the atmosphere*, Halsted Press (1975).

[103] R. Riahi, P. Teulet, Z. Ben Lakhdar, A. Gleizes, *Eur. Phys. J. D* **40** (2006) 223.

[104] S. G. Belostotsky, D. J. Economou, D. V. Lopaev, T. V. Rakhimova, *Plasma Sources Sci. Technol.* **14** (2005) 532.

[105] M. McFarland, D. L. Albritton, F. C. Fehsenfeld, E. E. Ferguson, A. L. Schmeltekopf, *J. Chem. Phys.* **59** (1973) 6629.

[106] R. S. Konstantinovskii, V. M. Shibkov, L. V. Shibkova, *Kinet. Catal.* **46** (2005) 775.

[107] C. D. Scott, S. Farhat, A. Gicquel, K. Hassouni, *J. Thermophys. Heat Transfer* **10** (1996) 426.

[108] K. Hassouni, T. A. Grotjohn, A. Gicquel, *J. Appl. Phys.* **86** (1999) 134.

[109] J. T. Gudmundsson, E. G. Thorsteinsson, *Plasma Sources Sci. Technol.* **16** (2007) 399.

[110] C. S. Corr, S. Gomez, W. G. Graham, *Plasma Sources Sci. Technol.* **21** (2012) 055024.

[111] A. Govender, D. Curulla Ferré, J. W. Niemantsverdriet, *ChemPhysChem* **13** (2012) 1583.

[112] E. Carrasco, I. Tanarro, V. J. Herrero, J. Cernicharo, *Phys. Chem. Chem. Phys.* **15** (2013) 1699.

[113] R. L. Sharpless, T. G. Slanger, *J. Chem. Phys.* **91** (1989) 7947.

[114] M. J. Barlow, B. M. Swinyard, P. J. Owen, J. Cernicharo, H. L. Gomez, R. J. Ivison, O. Krause, T. L. Lim, M. Matsuura, S. Miller, G. Olofsson, E. T. Polehampton, *Science* **342** (2013) 1343.

[115] P. Schilke et al., *Astron. Astrophys.* **566** (2014) A29.

[116] V. D. Hodoroaba, V. Hoffmann, E. B. M. Steers, K. Wetzig, *J. Anal. At. Spectrom.* **15** (2000) 1075.

[117] K. Newman, R. S. Mason, D. R. Williams, I. P. Mortimer, *J. Anal. At. Spectrom.* **19** (2004) 1192.

[118] A. Martin, A. Menendez, R. Pereiro, N. Bordel, A. Sanz-Medel, *Anal. Bioanal. Chem.* **388** (2007) 1573.

[119] S. Weyler, A. Bengtson, *J. Anal. At. Spectrom.* **25** (2010) 849.

[120] F. L. Tabares, D. Tafalla, *J. Vac. Sci. Technol. A* **14** (1996) 3087.

[121] C. V. Budtz-Jorgensen, P. Kringhoj, J. Bottiger, *Surf. Coat. Technol.* **116** (1999) 938.

[122] C. V. Budtz-Jorgensen, P. Kringhoj, J. F. Nielsen, J. Bottiger, *Surf. Coat. Technol.* **135** (2001) 299.

[123] P. Saikia, B. Kakati, B. K. Saikia, *Phys. Plasmas* **20** (2013) 103505.

[124] C. F. Yeh, T. J. Chen, C. Liu, J. T. Gudmundsson, M. A. Lieberman, *IEEE Electron Device Lett.* **20** (1999) 223.

[125] N. Fox-Lyon, G. S. Oehrlein, N. Ning, D. B. Graves, *J. Appl. Phys.* **110** (2011) 104314.

[126] K. Ostrikov, H. J. Yoon, A. E. Rider, S. V. Vladimirov, *Plasma Process. Polym.* **4** (2007) 27.

[127] R. F. G. Meulenbroeks, R. A. H. Engeln, M. N. A. Beurskens, R. M. J. Paffen, M. C. M. van de Sanden, J. A. M. van der Mullen, D. C. Schram, *Plasma Sources Sci. Technol.* **4** (1995) 74.

[128] S. B. Radovanov, J. K. Olthoff, R. J. Vanbrunt, S. Djurovic, *J. Appl. Phys.* **78** (1995) 746.

[129] R. S. Mason, P. D. Miller, I. P. Mortimer, *Phys. Rev. E* **55** (1997) 7462.

[130] J. T. Gudmundsson, *Plasma Sources Sci. Technol.* **7** (1998) 330.

[131] J. T. Gudmundsson, *Plasma Sources Sci. Technol.* **8** (1999) 58.

[132] T. G. Beuthe, J. S. Chang, *Jpn. J. Appl. Phys., Part 1* **38** (1999) 4576.

[133] A. Bogaerts, R. Gijbels, *J. Anal. At. Spectrom.* **15** (2000) 441.

[134] A. Bogaerts, *J. Anal. At. Spectrom.* **23** (2008) 1476.

[135] T. Kimura, H. Kasugai, *J. Appl. Phys.* **107** (2010) 083308.

[136] M. Sode, T. Schwarz-Selinger, W. Jacob, *J. Appl. Phys.* **113** (2013) 093304.

[137] M. Sode, T. Schwarz-Selinger, W. Jacob, *J. Appl. Phys.* **114** (2013) 063302.

[138] J. W. Brault, S. P. Davis, *Phys. Scr.* **25** (1982) 268.

[139] N. N. Haese, F. S. Pan, T. Oka, *Phys. Rev. Lett.* **50** (1983) 1575.

[140] J. W. C. Johns, *J. Mol. Spectrosc.* **106** (1984) 124.

[141] K. B. Laughlin, G. A. Blake, R. C. Cohen, R. J. Saykally, *J. Chem. Phys.* **90** (1989) 1358.

[142] J. M. Brown, D. A. Jennings, M. Vanek, L. R. Zink, K. M. Evenson, *J. Mol. Spectrosc.* **128** (1988) 587.

[143] R. R. Filgueira, C. E. Blom, *J. Mol. Spectrosc.* **127** (1988) 279.

[144] M. Cueto, J. Cernicharo, M. J. Barlow, B. M. Swinyard, V. J. Herrero, I. Tanarro, J. L. Doménech, *Astrophys. J. Lett.* **783** (2014) L5.

[145] R. D. Smith, J. H. Futrell, *Int. J. Mass Spectrom. Ion Process.* **20** (1976) 33.

[146] C. R. Blakley, M. L. Vestal, J. H. Futrell, *J. Chem. Phys.* **66** (1977) 2392.

[147] A. B. Rakshit, P. Warneck, *J. Chem. Phys.* **74** (1981) 2853.

[148] H. Villinger, J. H. Futrell, F. Howorka, N. Duric, W. Lindinger, *J. Chem. Phys.* **76** (1982) 3529.

[149] B. R. Rowe, A. Canosa, V. Lepage, *Int. J. Mass Spectrom. Ion Process.* **149** (1995) 573.

[150] M. T. Bowers, D. D. Elleman, *J. Chem. Phys.* **51** (1969) 4606.

[151] A. E. Roche, M. M. Sutton, D. K. Bohme, H. I. Schiff, *J. Chem. Phys.* **55** (1971) 5480.

[152] J. E. Pollard, L. K. Johnson, D. A. Lichtin, R. B. Cohen, *J. Chem. Phys.* **95** (1991) 4877.

[153] J. J. Leventhal, L. Friedman, *J. Chem. Phys.* **50** (1969) 2928.

[154] J. K. Kim, L. P. Theard, W. T. Huntress Jr, *Int. J. Mass Spectrom. Ion Phys.* **15** (1974) 223.

[155] C. W. Eaker, G. C. Schatz, *J. Phys. Chem.* **89** (1985) 2612.

[156] V. Kokoouline, A. Faure, J. Tennyson, C. H. Greene, *Mon. Not. R. Astron. Soc.* **405** (2010) 1195.

[157] K. M. Ervin, P. B. Armentrout, *J. Chem. Phys.* **83** (1985) 166.

[158] M. Sizun, J. B. Song, E. A. Gislason, *J. Chem. Phys.* **116** (2002) 2888.

[159] S. Chapman, *J. Chem. Phys.* **82** (1985) 4033.

[160] R. R. Filgueira, L. L. Fournier, C. E. Blom, *J. Mol. Struct.* **175** (1988) 105.

[161] D. K. Bedford, D. Smith, *Int. J. Mass Spectrom. Ion Process.* **98** (1990) 179.

[162] J. Amorim, G. Baravian, A. Ricard, *Plasma Chem. Plasma Process.* **15** (1995) 721.

[163] J. L. Jauberteau, I. Jauberteau, J. Aubreton, *J. Phys. D-Appl. Phys.* **35** (2002) 665.

[164] H. Kiyooka, O. Matsumoto, *Plasma Chem. Plasma Process.* **16** (1996) 547.

[165] A. Ricard, B. F. Gordiets, M. J. Pinheiro, C. M. Ferreira, G. Baravian, J. Amorim, S. Bockel, H. Michel, *Eur. Phys. J-Appl. Phys.* **4** (1998) 87.

[166] M. Touvelle, J. L. M. Licea, M. Venugopalan, *Plasma Chem. Plasma Process.* **7** (1987) 101.

[167] K. S. Yin, M. Venugopalan, *Plasma Chem. Plasma Process.* **3** (1983) 343.

[168] E. N. Eremin, A. N. Maltsev, V. M. Belova, *Russ. J. Phys. Chem.* **45** (1971) 635.

[169] A. Garscadden, R. Nagpal, *Plasma Sources Sci. Technol.* **4** (1995) 268.

[170] B. Gordiets, C. M. Ferreira, M. J. Pinheiro, A. Ricard, *Plasma Sources Sci. Technol.* **7** (1998) 363.

[171] R. A. B. Zijlmans, *Molecule conversion in recombining plasmas*, PhD thesis, Eindhoven University of Technology (2008).

[172] M. L. Steen, K. R. Kull, E. R. Fisher, *J. Appl. Phys.* **92** (2002) 55.

[173] T. P. Ma, *IEEE Trans. Electron Devices* **45** (1998) 680.

[174] D. T. Murley, R. A. G. Gibson, B. Dunnett, A. Goodyear, I. D. French, *J. Non-Cryst. Solids* **187** (1995) 324.

[175] D. L. Smith, A. S. Alimonda, C. C. Chen, S. E. Ready, B. Wacker, *J. Electrochem. Soc.* **137** (1990) 614.

[176] H. Umemoto, T. Morimoto, M. Yamawaki, Y. Masuda, A. Masuda, H. Matsumura, *Thin Solid Films* **430** (2003) 24.

[177] M. F. Romero, M. M. Sanz, I. Tanarro, A. Jiménez, E. Muñoz, *J. Phys. D-Appl. Phys.* **43** (2010) 495202.

[178] W. Jacob, C. Hopf, M. Meier, T. Schwarz-Selinger, in *Nuclear Fusion Research: Understanding Plasma-Surface Interactions*, R.E.H. Clark and D. Reiter (editors), Springer (2005) p. 249-287.

[179] T. Schwarz-Selinger, C. Hopf, C. Sun, W. Jacob, *J. Nucl. Mater.* **363-365** (2007) 174.

[180] I. Tanarro, V. J. Herrero, A. M. Islyaikin, I. Mendez, F. L. Tabares, D. Tafalla, *J. Phys. Chem. A* **111** (2007) 9003.

[181] F. L. Tabarés, J. A. Ferreira, A. Ramos, G. Van Rooij, J. Westerhout, R. Al, J. Rapp, A. Drenik, M. Mozetic, *Phys. Rev. Lett.* **105** (2010) 175006.

[182] A. De Castro, D. Alegre, F. L. Tabarés, *J. Nucl. Mater.* **463** (2015) 676.

[183] I. Lohmar, J. Krug, O. Biham, *Astron. Astrophys.* **504** (2009) L5.

[184] P. Hall, T. J. Millar, *Astron. Astrophys.* **517** (2010) A1.

[185] N. Watanabe, A. Kouchi, *Prog. Surf. Sci.* **83** (2008) 439.

[186] D. J. Burke, W. A. Brown, *Phys. Chem. Chem. Phys.* **12** (2010) 5947.

[187] S. Petrie, D. K. Bohme, *Mass Spectrom. Rev.* **26** (2007) 258.

[188] E. Herbst, W. Klemperer, *Astrophys. J.* **185** (1973) 505.

[189] M. Womack, L. M. Ziurys, S. Wyckoff, *Astrophys. J.* **393** (1992) 188.

[190] I. Tanarro, V. J. Herrero, *Plasma Sources Sci. Technol.* **20** (2011) 024006.

[191] D. M. Meyer, in *Molecules in Astrophysics: Probes and Processes*, E.F. van Dishoeck (editor), Springer (1997) p. 407-419.

[192] T. L. Williams, N. G. Adams, L. M. Babcock, C. R. Herd, M. Geoghegan, *Mon. Not. R. Astron. Soc.* **282** (1996) 413.

[193] A. Wootten, J. G. Mangum, B. E. Turner, M. Bogey, F. Boulanger, F. Combes, P. J. Encrenaz, M. Gerin, *Astrophys. J.* **380** (1991) L79.

[194] F. Wyrowski, K. M. Menten, R. Güsten, A. Belloche, *Astron. Astrophys.* **518** (2010) A26.

[195] V. Ossenkopf et al., *Astron. Astrophys.* **518** (2010) L111.

[196] D. Hollenbach, M. J. Kaufman, D. Neufeld, M. Wolfire, J. R. Goicoechea, *Astrophys. J.* **754** (2012) 105.

[197] E. Herbst, S. Green, P. Thaddeus, W. Klemperer, *Astrophys. J.* **215** (1977) 503.

[198] S. L. W. Weaver, D. E. Woon, B. Ruscic, B. J. McCall, *Astrophys. J.* **697** (2009) 601.

[199] L. Kluge, S. Gartner, S. Brunken, O. Asvany, D. Gerlich, S. Schlemmer, *Philos. Trans. R. Soc. A-Math. Phys. Eng. Sci.* **370** (2012) 5041.

[200] M. Mushiaki, *Fusion Eng. Des.* **47** (1999) 85.

[201] F. Waelbroeck, J. Winter, P. Wienhold, *J. Vac. Sci. Technol. A* **2** (1984) 1521.

[202] G. Counsell et al., *Plasma Phys. Control. Fusion* **48** (2006) B189.

[203] F. L. Tabarés, J. A. Ferreira, D. Tafalla, I. Tanarro, V. J. Herrero, I. Méndez, C. Gómez-Aleixandre, J. M. Albella, *J. Phys. Conf. Ser.* **100** (2008) 062025.

[204] G. Ceccone, D. Gilliland, O. Kylian, F. Rossi, *Czech. J. Phys.* **56** (2006) B672.

[205] C. Huang, C. Y. Tsai, R. S. Juang, *J. Appl. Polym. Sci.* **124** (2012) E108.

[206] V. Rybkin, E. Kuvaldina, A. Grinevich, A. Choukourov, H. Iwai, H. Biederman, *Plasma Process. Polym.* **5** (2008) 778.

[207] F. Fumagalli, O. Kylian, L. Amato, J. Hanus, F. Rossi, *J. Phys. D-Appl. Phys.* **45** (2012) 135203.

[208] T. Thandavan, C. Wong, S. Gani, R. Nor, *Appl. Nanosci.* **2** (2012) 47.

[209] D. Breden, L. L. Raja, *IEEE Trans. Plasma Sci.* **39** (2011) 2250.

[210] R. Peyrous, P. Pignolet, B. Held, *J. Phys. D-Appl. Phys.* **22** (1989) 1658.

[211] C. A. Vasko, D. X. Liu, E. M. van Veldhuizen, F. Iza, P. J. Bruggeman, *Plasma Chem. Plasma Process.* **34** (2014) 1081.

[212] D. X. Liu, P. Bruggeman, F. Iza, M. Z. Rong, M. G. Kong, *Plasma Sources Sci. Technol.* **19** (2010) 22.

[213] Z. Yin, I. V. Adamovich, W. R. Lempert, *Proc. Combust. Inst.* **34** (2013) 3249.

[214] T. Czerwiec, J. Gavillet, T. Belmonte, H. Michel, A. Ricard, *J. Phys. III* **6** (1996) 1205.

[215] A. V. Levanov, E. E. Antipenko, V. V. Lunin, *Moscow Univ. Chem. Bull.* **65** (2010) 341.

[216] K. Y. Du, O. Krogh, D. W. Setser, *Int. J. Chem. Kinet.* **38** (2006) 12.

[217] E. P. L. Hunter, S. G. Lias, *J. Phys. Chem. Ref. Data* **27** (1998) 413.

[218] N. Harada, E. Herbst, V. Wakelam, *Astrophys. J.* **721** (2010) 1570.

[219] S. D. Rodgers, S. B. Charnley, *Astrophys. J.* **585** (2003) 355.

[220] C. W. Gear, *Numerical initial value problems in ordinary differential equations*, Prentice Hall (1971).

Publications

Publications related to this thesis

M. Jiménez-Redondo, E. Carrasco, V. J. Herrero, I. Tanarro, "Isotopic exchange processes in cold plasmas of H_2/D_2 mixtures", *Phys. Chem. Chem. Phys.* **13** (2011) 9655.

E. Carrasco, M. Jiménez-Redondo, I. Tanarro, V. J. Herrero, "Neutral and ion chemistry in low pressure dc plasmas of H_2/N_2 mixtures: routes for the efficient production of NH_3 and NH_4^+", *Phys. Chem. Chem. Phys.* **13** (2011) 19561.

E. Carrasco, M. Jiménez-Redondo, I. Tanarro, V. J. Herrero, "Chemistry in low-pressure cold plasmas: ions of astrophysical interest", *Plasma Phys. Control. Fusion* **54** (2012) 124019.

M. Jiménez-Redondo, E. Carrasco, V. J. Herrero, I. Tanarro, "Energy distributions of neutrals and charged species in hollow cathode H_2 discharges: A study of fast H atoms", *Plasma Sources Sci. Technol.* **22** (2013) 025022.

M. Jiménez-Redondo, M. Cueto, J. L. Doménech, I. Tanarro, V. J. Herrero, "Ion kinetics in Ar/H_2 cold plasmas: the relevance of ArH^+", *RSC Adv.* **4** (2014) 62030.

M. Jiménez-Redondo, E. Carrasco, V. J. Herrero, I. Tanarro, "Chemistry in glow discharges of H_2/O_2 mixtures: Diagnostics and modelling", *Plasma Sources Sci. Technol.* **24** (2015) 015029.

Other publications

I. Tanarro, V. J. Herrero, E. Carrasco, M. Jiménez-Redondo, "Cold plasma chemistry and diagnostics", *Vacuum* **85** (2011) 1120.

B. Maté, I. Tanarro, M. A. Moreno, M. Jiménez-Redondo, R. Escribano, V. J. Herrero, "Stability of carbonaceous dust analogues and glycine under UV irradiation and electron bombardment", *Faraday Discuss.* **168** (2014) 267.

Appendices

A.1. Langmuir probe analyzer

In this section, the MATLAB program used to analyze the measurements of the double Langmuir probe is described. As mentioned in section 2.1.1, the objective of this program is to calculate the values of N_e ($\approx N_c$) and T_e in the plasma analyzing the data acquired with the oscilloscope. The following is a scheme of the different tasks performed by the program:

- Convert voltage values from the oscilloscope to the values of voltage and current measured by the probe.
- Average the different characteristics measured to obtain a single curve to analyze, and smooth it.
- Cut the extremes of the curve to perform the analysis between an established range of voltages (usually –35 to +35 V).
- Differentiate, smooth, and fit the resulting curve to a Gaussian in order to obtain the position of the maximum, as shown in Figure 7.1. This is done to correct the position of the characteristic to make it as symmetrical as possible with respect to the origin.
- A small amount of points close to the origin is taken to obtain the slope with a linear fit, shown in Figure 7.2.
- Some points from the extreme of the curve (ion saturation region) are used for a linear fit to find points F and G by extrapolation. Two different linear fits are performed for each branch of the curve, and two different separation points F are selected, so a total of eight values for the G point current (and thus T_e) are obtained.

- The two points in the extreme of the curve and two other points close to each of them are used to obtain V_{sat} and I_{sat}, obtaining four different values for N_e.

- Finally, average values of T_e and N_e and their standard deviations are shown as output.

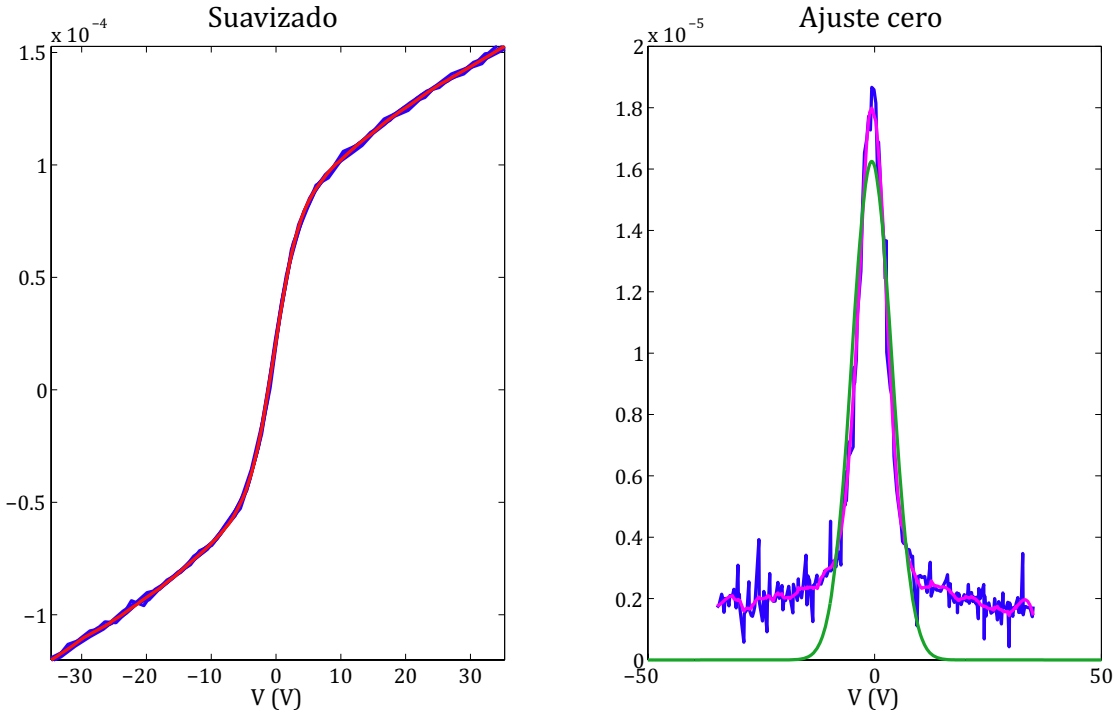

Figure 7.1. Smoothed characteristic (left panel) and Gaussian fit for its derivative (right panel).

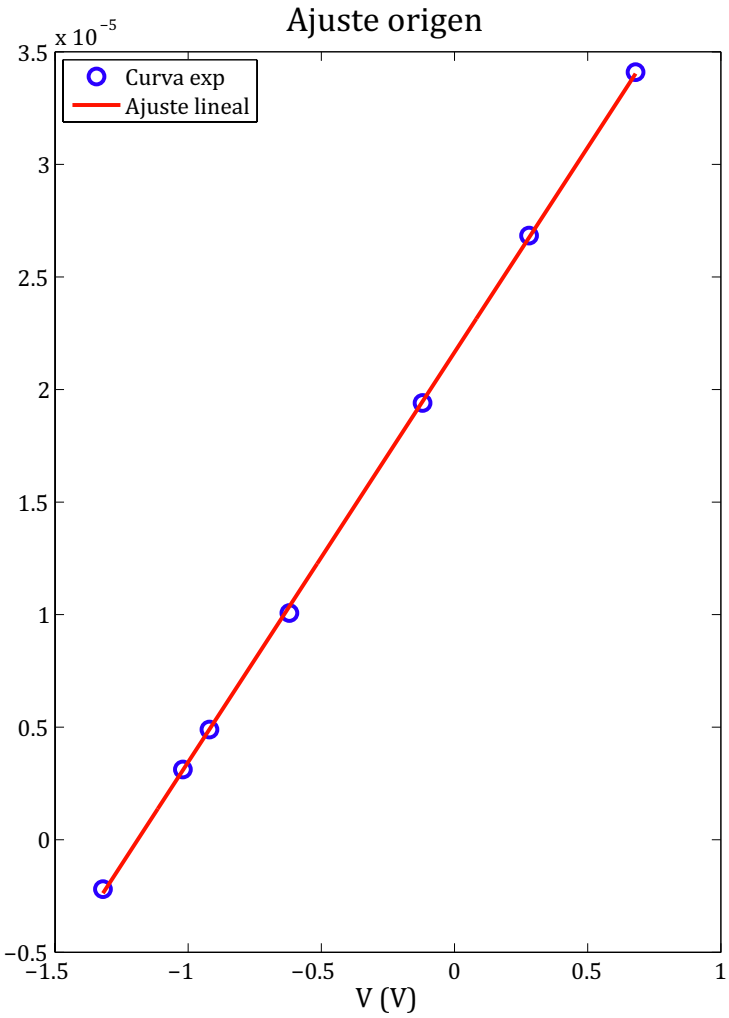

Figure 7.2. Linear fit to obtain the equivalent resistance.

The program is composed of three functions. Function sondadoble is the main program, and it performs the average and smoothing of the characteristic. The subroutine analisisdoble is called to analyze the curve, and values for T_e and N_e are outputted. The following is the code for the sondadoble function.

```
function
[Te,Ne,Te_prom,Ne_prom]=sondadoble(VmaxA,VmaxB,fichero,MpromI,puntos_suav)

% SONDADOBLE Cálculo de Te y Ne en sondas dobles.
%
% [Te,Ne,Te_prom,Ne_prom]=sondadoble(VmaxA,VmaxB,fichero,MpromI,puntos_suav)
%
% Función para calcular Te y Ne a partir de un fichero de sondas
% introducido en forma de string, poniéndole apóstrofes antes y después:
% [Te,Ne,Te_prom,Ne_prom]=sondadoble(100,10,'13013110.asd',8.4,25)
%
% El programa consta de tres funciones: sondadoble.m, analisisdoble.m y
% puntosF.m, siendo necesario que las tres estén en el directorio de
% trabajo de Matlab para funcionar correctamente. Tanto analisisdoble.m
% como puntosF.m son funciones auxiliares, por lo que la única que hay que
% ejecutar es ésta.
%
% Al ejecutarlo hay que cambiar para cada fichero:
% - La variable fichero.
% - La masa promedio MpromI de los iones para las condiciones de medida.
% - El número de puntos para el suavizado. En general para un fichero de 1k
% datos 25 es un buen valor, pero si hay problemas en el suavizado de la
% curva se puede modificar.
%
% En general dentro del análisis de una misma serie de medidas no va a ser
% necesario cambiar VmaxA y VmaxB, que son las ganancias de los canales
% leídas directamente del amplificador (1,10,100,1000). Sin embargo hay que
% tener cuidado y utilizar las correctas.
%
% El área de la sonda está definida dentro del programa, por lo que si se
% cambia la sonda hay que modificarlo.
%
% Los diferentes barridos obtenidos experimentalmente se promedian y
% suavizan y se analiza esta única curva.
%
% El programa genera gráficas con los distintos ajustes realizados que
% permiten ver si alguna parte del análisis no es correcta:
%
% Figura 1:
%   - Curva suavizada frente a datos experimentales.
%   - Primera derivada de la curva suavizada junto con los diferentes
%   ajustes para determinar la posición del cero.
```

```
%
% Figura 2:
%   - Ajuste de la pendiente en el origen.
%   - Análisis de la curva con las diferentes asíntotas y puntos usados
%   para el cálculo.
%
%
% El programa da como salida los diferentes valores de Te y Ne calculados
% en los vectores Te y Ne. Por otra parte, las variables Te_prom y Ne_prom
% contienen los valores promedio y desviación típica de los vectores
% anteriores.


datos = dlmread(fichero,',',15,0);

Lfil = 7.0; % Longitud del filamento en mm
rfil = 0.065; % Radio del filamento en mm
A = 2*pi*rfil*Lfil/100; % Área de la sonda en cm2
R = 1000; % Resistencia
limVinf = -35;
limVsup = 35; % Rango de voltajes usado en el análisis (en V)



ganA = 10/VmaxA;
ganB = 10/VmaxB;
Vs = datos(:,1)/ganA;
Is = datos(:,2)/(ganB*R);

% Vs e Is son vectores con todos los datos de la sonda en A y V
% respectivamente



        [Vord,ord] = sort(Vs);
        Iord = Is(ord);

        Vprom = zeros(2,1);
        Iprom = zeros (2,1);

        k1 = 1;
        k2 = 1;
        while k1<length(Vord)
            if Vord(k1+1)~=Vord(k1)
                Vprom(k2) = Vord(k1);
                Iprom(k2) = Iord(k1);
```

```
                k1 = k1+1;
                k2 = k2+1;
            else
                Vprom(k2) = Vord(k1);
                count = 1;
                Iaux = Iord(k1);
                while Vord(k1+1)==Vord(k1)
                    Iaux = Iaux + Iord(k1+1);
                    count = count+1;
                    k1 = k1+1;
                    if k1 == length(Vord)
                        break
                    end
                end
                Iprom(k2) = Iaux/count;
                k1 = k1+1;
                k2 = k2+1;
            end
        end


        Vsuav = Vprom;
        Isuav = smooth(Vsuav,Iprom,puntos_suav,'sgolay',3);

        % Todo el código anterior tiene como objetivo promediar y suavizar
        % los diferentes barridos para obtener una única curva para el
        % análisis

ii = 1;
while Vsuav(ii)<limVinf
    ii = ii+1;
end
ind_inf = ii;

while Vsuav(ii)<limVsup
    ii = ii+1;
end
ind_sup = ii;

V = Vsuav(ind_inf:ind_sup);
I = Isuav(ind_inf:ind_sup);

% V e I contienen la curva suavizada restringida al rango de voltajes
% definido anteriormente para el análisis

tam_suav = length(V);
```

```
figure
subplot(1,2,1)

plot(Vs,Is,V,I,'r','LineWidth',2);
axis([V(1) V(tam_suav) I(1) I(tam_suav)]);

% Representación de la curva suavizada y los datos originales



[Ic,Te_j,Ne_j] = analisisdoble(V,I,MpromI,A);
Te=Te_j;
Ne=Ne_j;

% Llamada a la función analisisdoble para analizar la curva suavizada

Te_prom = zeros(2,1);
Ne_prom = zeros(2,1);

Te_prom(1) = mean(Te);
Te_prom(2) = std(Te);

Ne_prom(1) = mean(Ne);
Ne_prom(2) = std(Ne);

% Variables de salida del programa
```

The function analisisdoble called in this program performs the analysis of the characteristic. It corrects the position of the zero of the curve and calculates the slope in that point, and performs the linear extrapolations necessary to obtain points E, F and G through the subroutine puntosF, calculating then the values for T_e. Values for the saturation voltage and current are obtained and used to obtain N_e.

```
function [Ic,Te,Ne]=analisisdoble(V,I,MpI,A)

% Función auxiliar. Análisis de un barrido de voltajes de la sonda.


% ========= (1) Cálculo de la posición del cero en voltaje ================

tam_der =length(V)-1;
der = diff(I)./diff(V);
Vder=V(1:tam_der);
% Cálculo de la derivada de la curva


dsuav = smooth(Vder,der,20,'sgolay',3);
% Suavizado de la derivada


gaussfit = fit(Vder,dsuav,'gauss1');
coef=coeffvalues(gaussfit);
% Ajuste gaussiano de la derivada


V_00 = coef(2); % Valor del voltaje "0"

q=1;
while V(q)<V_00
    q=q+1;
end
v0=q;
% Se halla el valor de la curva de la sonda inmediatamente anterior al
% voltaje V_00



subplot(1,2,2)
plot(Vder,der);
```

```
hold on
plot(Vder,dsuav,'m');
plot(gaussfit);
hold off
% Representación de la derivada, su suavizado y el ajuste gaussiano




% ================= (2) Pendiente en el origen ============================

V_0 = V(v0);
I_0 = I(v0);

Tam = length(V);

N = 2*floor(length(V)/50);
% N° de puntos para el ajuste de la pendiente en el 0 (debe ser par). El
% valor de 50 incluido en la fórmula funciona bien habitualmente pero se
% puede modificar si es necesario.

m=1;

for n=[v0-N/2:v0+N/2]
    Vreg(m,1) = V(n);
    Ireg(m,1) = I(n);
    m=m+1;
end
% Extracción de los puntos alrededor del 0 para el ajuste de la pendiente



fit_origen = fit(Vreg,Ireg,'poly1');
coefs_origen = coeffvalues(fit_origen);
pend_origen = coefs_origen(1);
ord_origen = coefs_origen(2);
% Cálculo de la pendiente en el origen



figure
subplot(1,2,1)
plot(fit_origen,Vreg,Ireg,'o');
title('Ajuste origen','FontSize',12)
xlabel('V (V)')
ylabel('I (A)')
legend('Curva exp','Ajuste lineal','Location','NorthWest')
% Representación del ajuste
```

```
% =============== (3) Asíntotas y puntos F y G ============================

Vc=V-V_0;
Ic=I-I_0;
% Corrección de la posición del 0 en intensidades y voltajes


Nasint = floor(Tam/6);
Nasint2 = floor(Tam/10);
% Número de datos utilizados para calcular cada una de las dos asíntotas de
% cada rama. Los valores de 6 y 10 que aparecen en la fórmula se pueden
% cambiar si hay problemas en el cálculo.


Vasint1_1 = Vc(1:Nasint);
Iasint1_1 = Ic(1:Nasint);
% Extracción de los puntos para el ajuste de la asíntota


asint1_1 = fit(Vasint1_1,Iasint1_1,'poly1');
coefs_asint1_1 = coeffvalues(asint1_1);
pend_asint1_1 = coefs_asint1_1(1);
ord_asint1_1 = coefs_asint1_1(2);
% Ajuste de la asíntota. El proceso se repite para el resto de asíntotas.


Vasint1_2 = Vc(Nasint2:Nasint2+Nasint);
Iasint1_2 = Ic(Nasint2:Nasint2+Nasint);

asint1_2 = fit(Vasint1_2,Iasint1_2,'poly1');
coefs_asint1_2 = coeffvalues(asint1_2);
pend_asint1_2 = coefs_asint1_2(1);
ord_asint1_2 = coefs_asint1_2(2);



Vasint2_1 = Vc(Tam-Nasint:Tam);
Iasint2_1 = Ic(Tam-Nasint:Tam);

asint2_1 = fit(Vasint2_1,Iasint2_1,'poly1');
```

```
coefs_asint2_1 = coeffvalues(asint2_1);
pend_asint2_1 = coefs_asint2_1(1);
ord_asint2_1 = coefs_asint2_1(2);




Vasint2_2 = Vc(Tam-Nasint-Nasint2:Tam-Nasint2);
Iasint2_2 = Ic(Tam-Nasint-Nasint2:Tam-Nasint2);

asint2_2 = fit(Vasint2_2,Iasint2_2,'poly1');
coefs_asint2_2 = coeffvalues(asint2_2);
pend_asint2_2 = coefs_asint2_2(1);
ord_asint2_2 = coefs_asint2_2(2);




subplot(1,2,2)
plot(asint1_1,'r',Vc,Ic,'b');
title('Ajuste asíntotas','FontSize',12)
grid on
hold on
as1_2 = feval(asint1_2,Vc);
as2_1 = feval(asint2_1,Vc);
as2_2 = feval(asint2_2,Vc);
plot(Vc,as1_2,'g');
plot(Vc,as2_1,'c');
plot(Vc,as2_2,'k');
% Representación de la curva con las asíntotas


% Puntos "F"

desv = 0.02;
[VF(1,1),F(1,1),VF(2,1),F(2,1)]                                          =
puntosF(asint1_1,asint2_1,Vc,Ic,Tam,desv,Nasint2);
[VF(3,1),F(3,1),VF(4,1),F(4,1)]                                          =
puntosF(asint1_2,asint2_2,Vc,Ic,Tam,desv,Nasint2);

desv = 0.05;
[VF(5,1),F(5,1),VF(6,1),F(6,1)]                                          =
puntosF(asint1_1,asint2_1,Vc,Ic,Tam,desv,Nasint2);
[VF(7,1),F(7,1),VF(8,1),F(8,1)]                                          =
puntosF(asint1_2,asint2_2,Vc,Ic,Tam,desv,Nasint2);
% Llamada a la función puntosF para calcular los puntos F en los que la
% asíntota se separa de la curva. El criterio de separación viene dado por
```

```
% el valor de desv, usándose dos diferentes para cada asíntota.



% Puntos "G"

VG(1,1) = VF(1)/5;
G(1,1) = asint1_1(0)+(F(1)-asint1_1(0))/5;
VG(2,1) = VF(2)/5;
G(2,1) = asint2_1(0)+(F(2)-asint2_1(0))/5;
G(3) = asint1_2(0)+(F(3)-asint1_2(0))/5;
VG(3) = VF(3)/5;
G(4) = asint2_2(0)+(F(4)-asint2_2(0))/5;
VG(4) = VF(4)/5;

VG(5) = VF(5)/5;
G(5) = asint1_1(0)+(F(5)-asint1_1(0))/5;
VG(6) = VF(6)/5;
G(6) = asint2_1(0)+(F(6)-asint2_1(0))/5;
G(7) = asint1_2(0)+(F(7)-asint1_2(0))/5;
VG(7) = VF(7)/5;
G(8) = asint2_2(0)+(F(8)-asint2_2(0))/5;
VG(8) = VF(8)/5;
% Cálculo de la intensidad en los puntos G (situados a 1/5 de la distancia
% entre la ordenada en el origen de la asíntota y el punto F). El vector G
% contiene las intensidades de los diferentes puntos.



Vfit_or = linspace(VG(1),VG(2),10);
fit_or = pend_origen*Vfit_or;
plot(VF,F,'ko')
plot(VG,G,'k+')
plot(Vfit_or,fit_or,'m')
xlabel('V (V)')
ylabel('I (A)')
legend('Curva    exp','Asíntota    1','Asíntota    2','Asíntota    3','Asíntota
4','F','G','Ajuste origen','Location','NorthWest')
hold off
% Se añaden a la gráfica de las asíntotas las representaciones de la
% pendiente en el origen y los puntos F y G



% ==================== (4) Cálculo de Te y Ne ============================
```

```
% Cálculo de Te

Te = abs(G/(2*pend_origen));
% Valores de la temperatura electrónica a partir de la intensidad en G y la
% pendiente en el origen




% Cálculo de Ne

P = 1;
Ne(1,1) = abs(1.81E13*sqrt(MpI)*Ic(P)/(sqrt(abs(V(P)))*A));

P = floor(Tam/10);
Ne(2,1) = abs(1.81E13*sqrt(MpI)*Ic(P)/(sqrt(abs(V(P)))*A));

P = floor(9*Tam/10);
Ne(3) = abs(1.81E13*sqrt(MpI)*Ic(P)/(sqrt(abs(V(P)))*A));

P = Tam;
Ne(4) = abs(1.81E13*sqrt(MpI)*Ic(P)/(sqrt(abs(V(P)))*A));

% Para el cálculo de Ne se usan los puntos extremos de la curva analizada y
% los situados a 1/10 del total de puntos de los extremos. El valor de 1/10
% se puede revisar, si bien la densidad electrónica no suele variar
% demasiado con el punto utilizado para el cálculo
```

Function puntosF is a small subroutine that, given the extrapolation of the ion saturation region, obtains the point F of separation from the characteristic.

```
function [VF1,IF1,VF2,IF2] = puntosF(asint1,asint2,V,Ic,Tam,desv,Nasint2)

% Función auxiliar. Obtención de los puntos F de la gráfica.

% Los puntos F se calculan buscando en la curva el primer punto que se
% desvíe en intensidades de la asíntota en la cantidad marcada por desv
% (2% ó 5%)

Ic = smooth(V,Ic,15,'sgolay');
% Para este cálculo se vuelve a suavizar la curva ya que cualquier punto
% que se desvíe de la misma puede afectar mucho a los resultados



l = Nasint2;
% Para empezar a buscar se parte del último punto usado para el cálculo de
% la asíntota

while abs((asint1(V(l))-Ic(l))/Ic(l))<desv
l = l+1;
end

VF1 = V(l);
IF1 = asint1(VF1);
% Se comprueba el criterio hasta que se cumple y se establece ese punto
% como F




l = Tam-Nasint2;

while abs((asint2(V(l))-Ic(l))/Ic(l))<desv
l = l-1;
end

VF2 = V(l);
IF2 = asint2(VF2);
end
% Se repite el mismo proceso para la asíntota de la otra rama
```

A.2. Kinetic models

The models used for the simulation of the discharges have been built using the FACSIMILE software, which implements the Gear method [220] to solve coupled differential equations. Each kinetic model consists of various different parts:

- Specification of parameters to be changed by the user depending on the conditions to be simulated. These include the electron temperature and density, pressure, and precursor fractions.
- Declaration of constant parameters, such as physical constants or rate coefficients.
- Calculation of some of the parameters appearing in the differential equations, which depend on the previously declared constants or the concentrations of the different species. For example, the calculation of rate coefficients that depend on the electron temperature, or the flow of the species out of the reactor.
- Formulation of the differential equations using the previously declared parameters and variables.

The models used for the three different mixtures studied in this work are shown below.

A.2.1 H_2 + Ar

```
*=======================================================;
* Modelo H2 + Ar;
* % VARIABLE electrones de alta E Energías promedio    ;
* Tvib(H2) = 3000 K                                     ;
* Tgas = 300 K                                          ;
* Formación del H en el volumen del plasma              ;
* Pérdida de H por flujo                                ;
* Gamma = 0.03                                          ;
* Preparado para modulación, cambiando t integración   ;
* Th = proporción de electrones de alta energía        ;
* proAr = Ar/(Ar+H2)inicial
*=======================================================;
```

```
EXECUTE OPEN 8 "Plasmas\Fcsm\Ar+H2\ArH2.out";
EXECUTE OPEN 9 "Plasmas\Fcsm\Ar+H2\par.out";

PARAMETER
pres 0.015
proAr 0.8
e 5.45E+10
T 2.70
Th 0.0003
;
PARAMETER
a1      6.5023E-9    b1       0.48931    c1      -12.89365
a2      2.9962E-8    b2       0.44456    c2      -37.72836
a3      1.0702E-7    b3       0.04876    c3       -9.69028
a4      2.1202E-9    b4       0.31394    c4      -23.29885
a7      3.1228E-8    b7       0.17156    c7      -20.07734
a8      4.8462E-7    b8      -0.04975    c8      -19.16565
a13     1.7527E-7    b13     -1.23668    c13     -12.59243
a18     2.5300E-8    b18      0.50000    c18     -16.30000
a19     2.5800E-9    b19      0.50000    c19     -47.00000
a20     1.9000E-8    b20      0.50000    c20     -27.67000
a28     9.9e-10      b28      -0.08      c28     -11.72
k5      6.4E-10
k6      1.189E-22
k11     2E-9
k25     1.78E-11
k23     2.1E-9
k24     1e-11
k26     8.72E-10
k27     6.3E-10
k29     7e-11
k30     0
;

PARAMETER
k1 k2 k3 k4
k7 k8 k13
k10 k12
k18 k19 k20
Vol
Are Gamma pres
Rad vth Dh Tdif
Twall Ttotal kk
n iH2 iH3
e0 Ne A
VP VR VPR
tR Cin
Fe Fs FsH FsH2 FsAr
;
```

```
VARIABLE HC;
VARIABLE H2C;
VARIABLE H3C;
VARIABLE H;
VARIABLE H2;
VARIABLE Ar;
VARIABLE ArC;
VARIABLE Ar2C;
VARIABLE ArHC;
VARIABLE ArM;


COMPILE INSTANT;

Cin = pres*2.435E16;
CinH2 = (1-proAr)*Cin;
CinAr = proAr*Cin;
**;


COMPILE GENERAL;
Ne = e0*e;
k1 = (1-Th)*k1a + Th*k1b;
k1a = a1*T@b1*exp(c1/T);
k1b = 4.2E-8;
k2 = (1-Th)*k2a + Th*k2b;
k2a = a2*T@b2*exp(c2/T);
k2b = 4.5E-9;
k3 = a3*T@b3*exp(c3/T);
k4 = a4*T@b4*exp(c4/T);
k7a = a7*T@b7*exp(c7/T);
k7b = 5E-8;
k7 = (1-Th)*k7a + Th*k7b;
k8 = a8*T@b8*exp(c8/T);
*k10 = 7.51371E-9 - (1.11516E-9)*T +
(1.03156E-10)*T@2 - (4.14905E-12)*T@3
+ (5.85916E-14)*T@4;
k10=0;
*k12 = 8.39247E-9 + (3.01631E-9)*T -
(3.80439E-10)*T@2 +(1.31108E-11)*T@3 +
(2.41631E-13)*T@4 - (2.29832E-14)*T@5
+ (3.5472E-16)*T@6;
k12=0;
k13a = a13*T@b13*exp(c13/T);
k13b = 1E-8;
k13 = (1-Th)*k13a+ Th*k13b;
k18a = a18*T@b18*exp(c18/T);
k18b = 1.6E-7;
k18 = (1-Th)*k18a + Th*k18b;
```

```
k19a = a19*T@b19*exp(c19/T);
k19b = 1.1E-8;
k19 = (1-Th)*k19a + Th*k19b;
k20a = a20*T@b20*exp(c20/T);
k20b = 6.5E-8;
k20 = (1-Th)*k20a + Th*k20b;
k28 = a28*T@b28*exp(c28/T);
*k28=0;
Vol = 2670;
Are = 1225;
Gamma = 0.03;
GammaAr = 1;
Rad = 5;
A = Rad/2.405;
vth = 1.75E+5;
vtAr = 4e4;
Dh = 1196/(pres*0.76);
DAr = 800/pres;
Tdif = (A@2)/Dh;
TdifAr = (A@2)/DAr;
Twall = (4*Vol)/(Are*Gamma*vth);
TwallAr = (4*Vol)/(Are*GammaAr*vtAr);
Ttotal = Tdif + Twall;
TtotalAr = TdifAr + TwallAr;
kk = 1/Ttotal;
kk2 = 1/TtotalAr;
VP = 2670;
VR = 4698;
VPR = 0.56;
tR = 1;
Fe = Cin*VR/tR;
FeH2=CinH2*VR/tR;
FeAr=CinAr*VR/tR;
Fs = (H2*VR + H*VR + Ar*VR)/tR;
FsH = H*VR/tR;
FsH2 = H2*VR/tR;
FsAr = Ar*VR/tR;
n = H*kk;
R = 1;
NG = -k10*H2C-k12*H3C;
I = Ne*(k1*H+k2*H2+k7*H2+k4*H2C+k18*Ar+k19*Ar
+NG)/(HC + (H2C/(2@0.5)) + (H3C/(3@0.5))
+ (ArC/(40@0.5)) + (Ar2C/(20@0.5))
+ (ArHC/(41@0.5)));

kWHC = R*I;
kWH2C = R*I/(2@0.5);
kWH3C = R*I/(3@0.5);
kWArC = R*I/(40@0.5);
kWAr2C = R*I/(20@0.5);
```

```
kWArHC = R*I/(41@0.5);


PH=H/H2;
PHC = HC/Ne;
PH2C = H2C/Ne;
PH3C = H3C/Ne;
PAr2C = Ar2C/Ne;
PArC = ArC/Ne;
PARHC = ArHC/Ne;

eNeu = HC+H2C+H3C+ArC+Ar2C+ArHC-Ne;

par1 =- k18*Ar*Ne*VPR;
par2 = R*ArC*0.1581*Ne*I*VPR;
par3 = k25*ArC*H2*VPR;
par4 = - k19*Ar*Ne*VPR;
par5 =  R*Ar2C*0.2236068*Ne*I*VPR;
par6 = - k23*H2C*Ar*VPR;
par7 = - k24*H3C*Ar*VPR;
par8 =  k27*ArHC*H2*VPR;
par9 = R*ArHC*0.15617*Ne*I*VPR;
par0 = FeAr/VR;
par00 = - FsAr/VR;
par10 = par0+ par00 +par1 +par2+ par3
 +par4+ par5 +par6 +par7+ par8 +par9;
par11=k1*H*Ne;
par12= k2*H2*Ne;
par13= k3*H2C*Ne;
par14= 2*k4*H2C*Ne ;
par15= k5*H2C*H;
par16= - k6*H2*HC;
par17= - R*HC*Ne*I;
par18= (HC + (H2C/(2@0.5)) + (H3C/(3@0.5))
+ (ArC/(40@0.5)) + (Ar2C/(20@0.5))
+ (ArHC/(41@0.5)));
par19 = (HC+H2C*0.7071068+H3C*0.5773503
+ArC*0.1581139
+Ar2C*0.2236068+ArHC*0.1561738);

par20= k19*Ar;
par21=k27*ArHC*H2-k24*H3C*Ar-kWH3C*H3C;
par22=k19*Ar*Ne;
par23=k20*ArC*Ne;
par24=- kWAr2C;

**;

COMPILE INITIAL;
e0 = 1;
```

```
HC = 0;
H2C = (1-proAr)*e;
H3C = 0;
H = 0;
H2 = CinH2;
Ar = CinAr;
ArC = proAr*e;
Ar2C = 0;
ArHC = 0;
ArM = 0;

**;
COMPILE OFF;
e0 = 0;
**;



COMPILE EQUATIONS ;

'HC = k1*H*Ne + k2*H2*Ne + k3*H2C*Ne + 2*k4*H2C*Ne
+ k5*H2C*H - k6*H2*HC - kWHC*HC;

'H = -FsH/VP + 2*Ne*H2*k13 - H*(kk)
- k1*H*Ne + k2*H2*Ne + k3*H2C*Ne
- k5*H2C*H + k6*H2*HC + k8*H3C*Ne
+ 2*k10*H2C*Ne + k11*H2C*H2
+ 0.5*k12*H3C*Ne + 3*0.5*k12*H3C*Ne
+ k23*H2C*Ar + k26*ArC*H2 + kWArHC*ArHC
+ kWHC*HC
+ kWH3C*H3C + 2*k29*ArM*H2;

'H2C = k7*H2*Ne - k3*H2C*Ne + k6*H2*HC-k4*H2C*Ne
- k5*H2C*H + k6*H2*HC + k8*H3C*Ne - k10*H2C*Ne
- k11*H2C*H2 + k25*ArC*H2 - kWH2C*H2C
- k23*H2C*Ar;

'H3C = -k8*H3C*Ne+k11*H2C*H2-0.5*k12*H3C*Ne-
0.5*k12*H3C*Ne - k24*H3C*Ar + k27*ArHC*H2
- kWH3C*H3C;

'H2 = FeH2/VR - FsH2/VR - k13*H2*Ne*VPR
+ 0.5*H*(kk)*VPR - k7*H2*Ne*VPR - k2*H2*Ne*VPR
+ k5*H2C*H*VPR - k6*H2*HC*VPR- k11*H2C*H2*VPR
+ 0.5*k12*H3C*Ne*VPR - k25*ArC*H2*VPR
+ k24*H3C*Ar*VPR - k26*ArC*H2*VPR - k27*ArHC*H2*VPR
+ kWH3C*H3C*VPR
+ kWH2C*H2C*VPR - k29*ArM*H2*VPR;

'Ar = FeAr/VR - FsAr/VR - k18*Ar*Ne*VPR
```

```
+ kWArC*ArC*VPR
+ k25*ArC*H2*VPR - k19*Ar*Ne*VPR
 + kWAr2C*Ar2C*VPR
- k23*H2C*Ar*VPR - k24*H3C*Ar*VPR + k27*ArHC*H2*VPR
+ kWArHC*ArHC*VPR - k28*Ar*Ne*VPR + k29*ArM*H2*VPR
+ 2*k30*ArM*ArM*VPR + kk2*ArM*VPR;

'ArC = k18*Ar*Ne - kWArC*ArC - k25*ArC*H2
- k20*ArC*Ne - k26*ArC*H2;

'Ar2C = k19*Ar*Ne + k20*ArC*Ne - kWAr2C*Ar2C;

'ArHC = k23*H2C*Ar + k24*H3C*Ar + k26*ArC*H2
- k27*ArHC*H2 - kWArHC*ArHC;

'ArM = k28*Ar*Ne - k29*ArM*H2 - 2*k30*ArM*ArM - kk2*ArM;

**;



SETPSTREAM 1 8 16;
TIME   H H2 Ar ArM PH;
**;

SETPSTREAM 2 9 16;
TIME  PHC PH2C PH3C PArC PAr2C PArHC;
**;


COMPILE OUT ;
PSTREAM 1 ;
PSTREAM 2 ;

**;

WHENEVER
*TIME = 1 CALL OFF RESTART;
*TIME = 2 CALL INITIAL RESTART;
*TIME = 3 CALL OFF RESTART;
TIME = 10000 * (+0.01) 0  %
CALL OUT;
**;

BEGIN;
STOP;
```

A.2.2 $H_2 + N_2$

```
*=======================================================;
* H2-N2_10062011.fac Modelo amoniaco CON superficie (w1-w21);
* Se incluye w21, reacción L-H para formación NHS;
* En esta variante de programa w21 =0;
* Incluida reacción w22 con NH + H(s) para formar NHS;
* Con neutralización en pared (k1-k10) y en fase gas (n1-n12);
* Fase gas r.ionización (i1-i15), disociación (d1-d7);
* Transferencia de carga (t1-t25);
* R (neutralización de iones en pared dando gas neutro)= 1    ;
* 1 mbar a 298 K equivale a 2.435E16 molecs/cm3;
* Tvib(H2) = 3000 K                                          ;
* Tgas = 300 K                                               ;
* DATOS EXPERIMENTALES A DISTINTAS PRESIONES;


* (pres(mbar), Te (eV), Ne (cm-3));

*      Pres    0.08  T  3.0       Ne   3.0e10  tr     0.65;
*      Pres    0.04  T  3.0       Ne   3.7e10  tr     0.6;
*      Pres    0.02  T  3.2       Ne   3.8e10  tr     0.5;
*      Pres    0.01  T  3.5       Ne   3.2e10  tr     0.5 ;
*      Pres    0.008 T  4.1       Ne   2.3e10  tr     0.45;

*=======================================================;
*Conviene cambiar el nombre del fichero de salida cada vez;

EXECUTE OPEN 8 "Plasmas\Fcsm\N\H2-N2_neu.out";
EXECUTE OPEN 7 "Plasmas\Fcsm\N\H2-N2_ion.out";
EXECUTE OPEN 10 "Plasmas\Fcsm\N\H2-N2_mi.out";
EXECUTE OPEN 11 "Plasmas\Fcsm\N\H2-N2_at.out";
EXECUTE OPEN 12 "Plasmas\Fcsm\N\H2-N2_cn.out";
EXECUTE OPEN 14 "Plasmas\Fcsm\N\H2-N2_pr.out";
EXECUTE OPEN 16 "Plasmas\Fcsm\N\H2-N2_nor.out";
EXECUTE OPEN 18 "Plasmas\Fcsm\N\H2-N2_rad.out";
EXECUTE OPEN 2 "Plasmas\Fcsm\N\H2-N2_mol.out";
EXECUTE OPEN 21 "Plasmas\Fcsm\N\H2-N2_amo.out";

*Parámetros a cambiar cada vez ;

PARAMETER

       Pres    0.08  T  2.0 Ne  3.3e10
       PropH2ini 0.10      PropN2ini 0.90 ;

*Valores para los coeficientes cinéticos;

PARAMETER
```

```
ad1     1.7527E-7    bd1      -1.23668   cd1     -12.59243
ad2     1.2E-8       bd2      0.5        cd2      -13.3
ad3     5.0E-8               bd3   0.5           cd3   -8.6
ad4     5.0E-8               bd4   0.5           cd4   -7.6
ad5       5.0E-8             bd5   0.5           cd5   -7.6
ad6       5.0E-8             bd6   0.5           cd6   -4.4
ad7       5.0E-8             bd7   0.5           cd7   -5.5
ai1       1.3E-8       bi1      0.5        ci1      -14.5
ai2     6.1E-9       bi2      0.5        ci2      -30.0
ai3     1.67E-8      bi3      0.5        ci3      -17.16
ai4     6.5023E-9    bi4      0.48931    ci4      -12.89365
ai5     2.9962E-8    bi5      0.44456    ci5      -37.72836
ai6     3.1228E-8    bi6      0.17156    ci6     -20.07734
ai10    1.43E-8       bi10  0.5          ci10   -14.5
ai11      5.05E-9     bi11  0.5     ci11  -16.5
ai12      1.33E-8     bi12  0.5           ci12  -11.8
ai13      1.18E-8     bi13  0.5           ci13  -17.3
ai14      1.12E-8     bi14  0.5           ci14  -11.0
ai15      1.15E-8     bi15  0.5           ci15  -17.6
an4     2.8E-7       bn4      0.026
an5       4.30E-8    cn5          0.5
an6       1.02E-7    cn6          0.4
an7       1.98E-7    cn7          0.4
an8       1.55E-7    cn8          0.5
an9       1.55E-7    cn9          0.5
an10      8.015E-7   cn10   0.605
an11    1.226E-7     cn11         0.605
an12      7.1E-7           cn12   0.72
t2      6.4E-10      t3      2.0E-9        t8       5.0E-10
t12     1.85E-10     t24     2.6E-10             t16     6.5E-10
t21     2.0E-9       t7      1.86E-9             t5      2.00E-9
t13       1.05E-9            t25     3.9E-10             t17     1.95E-10
t23     2.3E-9       t6      4.4E-9       t15     6.0E-10
t19     1.15E-9              t20     2.1E-9       t1      5.2E-9
t4      5.7E-9       t9      4.7E-10             t10     1.67E-9
t11       2.12E-10   t14     1.8E-9       t18     1.15E-9
t22     1.95E-9      ;

* Definición de parámetros;
* i1-i15: coef. cinéticos r. ionización ai(1-15),bi(1-15),ci(1-15);
* d1-d7: coef. cinéticos r. disociación ad(1-7),bd(1-7),cd(1-7);
* n1-n12 coef. cinéticos r. neutralización en volumen;
* t1 a t25: coeficientes cinéticos de r. transferencia de carga;
* k1-k10: coef. cinéticos r. neutralización en pared;
* w1-w19: coef. cinéticos r. heterogéneas en pared;
* Volúmenes: VR, VP, y Area: Are;
* VR= volumen del reactor;
* Are= Area del reactor;
* vtN = velocidad del N = 6.74E4 cms-1 (vtNH, velocidad NH);
```

```
* DH coeficiente difusión H, DNH coeficiente difusión NH, etc.;
* TdifH=A@2/DH tiempo de difusión;
* A=Rad/2.405 (Chantry);
* Rad = radio del reactor= 5 cm;
* Twall1 = (4*VRS*(1-0.5*Gamma1))/(Gamma1*vtH);
* Cambia el número y expresión de Twall según neutro que difunde;
* Ttotal1 = Twall1 + TdifH;
* Ne: densidad de electrones, variable con el tiempo si se modula la descarga;
* e0: parámetro para modular temporalmente la descarga;
* VP: volumen del plasma;
* VPC: relación del volumen del plasma al del reactor;
* tR: tiempo de residencia;
* Cin: concentración inicial (=pres*2.435E16);
* Fe, Fs: flujos de entrada y salida totales;
* FeH2, FeN2: flujos de entrada de H2 y N2;
* FsN, FsN2: flujos de salida de N y N2 (resto igual);

PARAMETER

d1 d2 d3 d4 d5 d6 d7 i1  i2  i3  i4  i5  i6 w17 w18 w19 w20
i10 i11 i12 i13 i14 i15 n1  parn2  n3  n4  n5  n6 n7
n8  n9  n10 n11 n12 k1  k2  k3  k4 k5 k6  k7  k8  k9  k10
w1  w2  w3  w4  w5  w6  w7  w8  w9  w10 w11 w12 w13 w14 w15 w16
VP VR VRS A Rad Are Ne e0 tR R vtH vtN vtH2 vtN2 vtNH vtNH2 ST SF kB
Fe FeH2 FeN2 Fs FsN FsN2 FsH FsH2 FsNH FsNH2 FsNH3
Cin CinH2 CinN2
thetaHS thetaNS thetaNHS thetaNH2S
DH DN DN2 DH2 DNH DNH2 TdifH TdifN TdifN2 TdifNH TdifNH2 TdifH2
Gamma1 Gamma3 Gamma5 Gamma7 Gamma9
Gamma10 Gamma13 Gamma15 Gamma16 Gamma17 Gamma18 Gamma20
nudesH nudifH nudesN nudifN nudesNH2 nudesNH
EdesH EdifN EdesN EdifH EdesNH2 EdesNH
Twall1 Twall3 Twall5 Twall7 Twall9
Twall10 Twall13 Twall15 Twall16 Twall17 Twall18 Twall20
Ttotal1 Ttotal3 Ttotal5 Ttotal7
Ttotal9 Ttotal10 Ttotal13 Ttotal15 Ttotal16
Ttotal17 Ttotal18 Ttotal20
CTiones mc1 mc2 mc3 mc14 mc15
mc16 mc17 mc18 mc28 mc29
CPie CNie DenMI T_HC T_H2C T_H3C T_NC T_NHC T_NH2C
T_NH3C T_NH4C T_N2C T_N2HC
PieNC PieN PieN2 PieNH PieNH2 PieNH3
PieN2C PieHC PieH PieH2C PieH2 PieNHC
PieNH2C PieNH3C DieN DieN2 DieN2C DieH
DieH2 DieH2C DieH3C DieNH DieNH2 DieNH3
DieNHC DieNH2C DieNH3C DieNH4C DieN2HC
PtH3C PtH PtNH4C PtHC PtH2 PtNH3C PtN2HC
PtNHC PtNH2C PtNH PtN PtNH2 PtN2
DtHC DtNH3 DtH2C DtH DtH2 DtH3C DtN2 DtNC DtN
DtNHC DtNH2C DtNH3C DtN2C DtN2HC PrH PrN PrH2 PrN2
```

```
PrNH PrNH2 PrNH3 NeuHC NeuH2C NeuH3C NeuNC NeuN2C
NeuNHC NeuNH2C NeuNH3C NeuNH4C NeuN2HC
PwHS PwH PwH2 PwNS PwN PwN2 PwNHS PwNH2S
PwNH2 PwNH3 DwH DwHS DwN DwNS DwNHS DwNH2S DwNH2 DwH2 VPC
PwNH DwNH atH atN
atSTotal atGTotal Iontotal
CTNeutros cH cH2 cN cN2 cNH cNH2 cNH3 Suma
PropH2 PropN2 PropNH3
Eaw4 Eaw8 Eaw11 Eaw14 Eaw21 w21
InFNat OutFNat InFHat OutFHat
FH FN FNH FNH2 Natout Hatout DifNH3
H2norm N2norm NH3norm fradicales
FormNH3 DesNH3 FoutNH3 atHini atNini atNsurf
HSvol NSvol NHSvol NH2Svol Sumafgas FinN2 FoutN2
atHradi atNradi atHmol atNmol atHion atNion atNsurf atHsurf
FormH2 FormN2 DesH2 DesN2 FinH2 FoutH2 Prow9NHS Prow20NHS
Prow13NH3 Prow14NH3 Prow15NH3 Prow16NH3
;


VARIABLE

       H2
       H
       HC
       H2C
       H3C
       HS
       N2
       N
       NC
       N2C
       NS
       NH
       NHC
       NH2
       NH2C
       NH3
       NH3C
       NH4C
       N2HC
       NHS
       NH2S
       ;

*Se usa COMPILE INITIAL tras GENERAL;
*para inicializar las variables a posteriori;
*y antes de GENERAL se usa COMPILE INSTANT;

COMPILE INSTANT;
```

```
Cin = pres*2.435E16;
CinH2 = propH2ini*Cin;
CinN2 = propN2ini*Cin;

**;

COMPILE GENERAL;

Rad = 5.0;
VP = 1709.;
VR = 4698.;
Are = 2494.;
tR = 0.61;
VPC = VP/VR;
VRS = VR/Are;
ST = 1.0E15;
SF = ST-NS-HS-NHS-NH2S;
*Constantes reacciones impacto electrónico;
d1 = ad1*T@bd1*exp(cd1/T);
d2 = ad2*T@bd2*exp(cd2/T);
d3 = ad3*T@bd3*exp(cd3/T);
d4 = ad4*T@bd4*exp(cd4/T);
d5 = ad5*T@bd5*exp(cd5/T);
*d6 = 0.;
d6 = ad6*T@bd6*exp(cd6/T);
d7 = ad7*T@bd7*exp(cd7/T);
*d7 = 0.;
*i1 = ai1*T@bi1*exp(ci1/T);
i1 = (1.25819E-10)*T - (1.71845E-10)*T@2 + (6.50747E-11)*T@3
- (5.74619E-12)*T@4 + (1.70511E-13)*T@5;
*i2 = ai2*T@bi2*exp(ci2/T);
i2 = -(5.67682E-12)*T + (8.57259E-12)*T@2 - (4.10542E-12)*T@3
+ (7.25965E-13)*T@4 - (3.09145E-14)*T@5;
*i3 = ai3*T@bi3*exp(ci3/T);
i3 = (1.01256E-10)*T - (1.12935E-10)*T@2 + (3.13929E-11)*T@3
- (7.51876E-13)*T@4 - (5.1428E-14)*T@5;
i4 =  ai4*T@bi4*exp(ci4/T);
i5 =  ai5*T@bi5*exp(ci5/T);
i6 = ai6*T@bi6*exp(ci6/T);
i10 = (1.37539E-10)*T - (1.85423E-10)*T@2 + (6.64995E-11)*T@3
- (4.36204E-12)*T@4 + (3.01658E-14)*T@5;
*i10 = ai10*T@bi10*exp(ci10/T);
i11 = (5.66045E-11)*T - (6.90587E-11)*T@2 + (2.33164E-11)*T@3
- (1.96203E-12)*T@4 + (4.96141E-14)*T@5;
*i11 = ai11*T@bi11*exp(ci11/T);
i12 = (1.76195E-10)*T - (2.7011E-10)*T@2 + (1.17338E-10)*T@3
- (1.23559E-11)*T@4 + (4.22944E-13)*T@5;
*i12 = ai12*T@bi12*exp(ci12/T);
i13 = (1.07819E-10)*T - (1.28046E-10)*T@2 + (4.10674E-11)*T@3
```

```
- (2.91042E-12)*T@4 + (5.15275E-14)*T@5;
*i13 = ai13*T@bi13*exp(ci13/T);
i14 = (1.5257E-10)*T - (2.24489E-10)*T@2 + (9.37232E-11)*T@3
- (9.7924E-12)*T@4 + (3.33299E-13)*T@5;
*i14 = ai14*T@bi14*exp(ci14/T);
i15 = (1.57401E-10)*T - (2.01591E-10)*T@2 + (7.22108E-11)*T@3
- (6.685E-12)*T@4 + (1.97299E-13)*T@5;
*i15 = ai15*T@bi15*exp(ci15/T);
n1 = 7.51371E-9 - (1.11516E-9)*T + (1.03156E-10)*T@2
-(4.14905E-12)*T@3 + (5.85916E-14)*T@4;
parn2 = 0.5*(8.39247E-9 + (3.01631E-9)*T - (3.80439E-10)*T@2
+ (1.31108E-11)*T@3 + (2.41631E-13)*T@4
- (2.29832E-14)*T@5 + (3.5472E-16)*T@6);
n3 = 0.5*(8.39247E-9 + (3.01631E-9)*T - (3.80439E-10)*T@2
+ (1.31108E-11)*T@3 + (2.41631E-13)*T@4
- (2.29832E-14)*T@5 + (3.5472E-16)*T@6);
n4 = an4*(bn4/T)@0.5;
n5 = an5*(0.026/T)@cn5;
n6 = an6*(0.026/T)@cn6;
n7 = an7*(0.026/T)@cn7;
n8 = an8*(0.026/T)@cn8;
n9 = an9*(0.026/T)@cn9;
n10 = an10*(0.026/T)@cn10;
n11 = an11*(0.026/T)@cn11;
n12 = an12*(0.026/T)@cn12;
*Concentraciones especies moleculares neutras relativas;
atH = (2*H2+H+NH+2*NH2+3*NH3)*VR + ((HC+2*H2C+3*H3C+NHC
+2*NH2C+3*NH3C+4*NH4C+N2HC)*VP) + ((HS+NHS+2*NH2S)*Are);
atN = (2*N2+N+NH+NH2+NH3)*VR + ((NC+2*N2C+2*N2HC
+NHC+NH2C+NH3C+NH4C)*VP) + ((NS+NHS+NH2S)*Are);
atSTotal = ((NS+NHS+NH2S)*Are) + ((HS+NHS+2*NH2S)*Are);
atGTotal = (2*H2+H+NH+2*NH2+3*NH3)*VR + (2*N2+N+NH+NH2+NH3)*VR;
*Atomos H y N iniciales;
atHini= 2*CinH2*VR;
atNini= 2*CinN2*VR;
*Atomos H y N en forma de radicales;
atHradi=(H+NH+2*NH2)*VR;
atNradi=(N+NH+NH2)*VR;
*Atomos H y N en forma de especies moleculares;
atHmol = (2*H2+3*NH3)*VR;
atNmol = (2*N2 + NH3)*VR;
*Atomos H y N en forma ionica;
atHion = ((HC+2*H2C+3*H3C+NHC+2*NH2C+3*NH3C+4*NH4C+N2HC)*VP);
atNion = ((NC+2*N2C+2*N2HC+NHC+NH2C+NH3C+NH4C)*VP);
*Atomos H y N en superficie;
atHsur = ((HS+NHS+2*NH2S)*Are);
atNsur = ((NS+NHS+NH2S)*Are);
*Atomos H y N salientes;
Natout = (2*N2+N+NH+NH2+NH3)*VR;
Hatout = (2*H2+H+NH+2*NH2+3*NH3)*VR;
```

```
*Coberturas superficiales de especies atómicas y radicales;
thetaHS=HS/ST;
thetaNS=NS/ST;
thetaNHS=NHS/ST;
thetaNH2S=NH2S/ST;
*Concentraciones superficiales expresadas en cm-3;
HSvol=HS*(1/VRS);
NSvol=NS*(1/VRS);
NHSvol=NHS*(1/VRS);
NH2Svol=NH2S*(1/VRS);
*Concentraciones iónicas relativas;
CTiones=HC+H2C+H3C+NC+N2C+NHC+NH2C+NH3C+NH4C+N2HC;
Iontotal = CTiones*VP;
mc1=HC/CTiones;
mc2=H2C/CTiones;
mc3=H3C/CTiones;
mc14=NC/CTiones;
mc15=NHC/CTiones;
mc16=NH2C/CTiones;
mc17=NH3C/CTiones;
mc18=NH4C/CTiones;
mc28=N2C/CTiones;
mc29=N2HC/CTiones;
*Concentraciones de neutros relativas;
CTNeutros=H+H2+N+N2+NH+NH2+NH3;
cH2=H2/CTNeutros;
cN2=N2/CTNeutros;
cN=N/CTNeutros;
cH=H/CTNeutros;
cNH3=NH3/CTNeutros;
cNH=NH/CTNeutros;
cNH2=NH2/CTNeutros;
propH2=H2/(H2+N2+NH3);
propN2=N2/(H2+N2+NH3);
propNH3=NH3/(H2+N2+NH3);
Sumafgas=H2+N2+NH3;
fradicales=CTNeutros/Sumafgas;
H2norm=propH2*Cin;
N2norm=propN2*Cin;
NH3norm=propNH3*Cin;
*Términos reacciones heterogéneas;
*Difusión neutros a la pared y recombinación;
*Se incluyen radicales (NH y NH2) y especies atómicas (N y H);
*Velocidades medias especies neutras;
vtH = 2.52E+5;
vtH2 = 1.78E+5;
vtN = 6.74E+4;
vtNH = 6.5E+4;
vtNH2 = 6.3E+4;
*Coeficientes de difusión;
```

```
DH = 3319.61/pres;
DN = 1985.7/pres;
DNH = 756.66/pres;
DNH2 = 646.17/pres;
A = Rad/2.405;
*Tiempos de difusión;
*Se considera difusión radial;
TdifH = (A@2)/DH;
TdifN = (A@2)/DN;
TdifNH = (A@2)/DNH;
TdifNH2 = (A@2)/DNH2;
*Coeficientes de adsorción y recombinación;
Gamma1 = 1.0;
Gamma3 = 0.0015;
Gamma5 = 1.0;
Gamma7 = 0.006;
Gamma9 = 0.01;
Gamma10 = 0.008;
Gamma13 = 0.008;
Gamma15 = 0.01;
Gamma16 = 0.0008;
Gamma17 = 1.0;
Gamma18 = 1.0;
Gamma20 = 0.008;
Gamma22 = 0.01;
*Prefactores (ley tipo Arrhenius);
nudesH = 1.0E13;
nudifH = 1.0E13;
nudesN = 1.0E13;
nudifN = 1.0E13;
nudesNH2 = 1.0E12;
nudesNH = 1.0E12;
*Energías de desorción y difusión;
EdesH = 2.0;
EdifH = 0.2;
EdesN = 3.0;
EdifN = 0.65;
EdesNH2 = 4.0;
EdesNH = 4.0;
Eaw4 = 0.5;
Eaw8 = 0.5;
Eaw11 = 0.3;
Eaw14 = 0.2;
Eaw21 = 0.4;
*Constante de Boltzmann kB en eV*K-1;
kB= 8.6173E-5;
*Tiempos interaccion pared;
Twall1 = (4*VRS*(1-0.5*Gamma1))/(Gamma1*vtH);
Twall3 = (4*VRS*(1-0.5*Gamma3))/(Gamma3*vtH);
Twall5 = (4*VRS*(1-0.5*Gamma5))/(Gamma5*vtN);
```

```
Twall7 = (4*VRS*(1-0.5*Gamma7))/(Gamma7*vtN);
Twall9 = (4*VRS*(1-0.5*Gamma9))/(Gamma9*vtN);
Twall10 = (4*VRS*(1-0.5*Gamma10))/(Gamma10*vtH);
Twall13 = (4*VRS*(1-0.5*Gamma13))/(Gamma13*vtH);
Twall15 = (4*VRS*(1-0.5*Gamma15))/(Gamma15*vtNH2);
Twall16 = (4*VRS)/(Gamma16*vtH2);
Twall17 = (4*VRS*(1-0.5*Gamma17))/(Gamma17*vtNH);
Twall18 = (4*VRS*(1-0.5*Gamma18))/(Gamma18*vtNH2);
Twall20 = (4*VRS*(1-0.5*Gamma20))/(Gamma20*vtH);
Twall22 = (4*VRS*(1-0.5*Gamma22))/(Gamma22*vtNH);
Ttotal1 = TdifH + Twall1;
Ttotal3 = TdifH + Twall3;
Ttotal5 = TdifN + Twall5;
Ttotal7 = TdifN + Twall7;
Ttotal9 = TdifN + Twall9;
Ttotal10 = TdifH + Twall10;
Ttotal13 = TdifH + Twall13;
Ttotal15 = TdifNH2 + Twall15;
Ttotal16 = Twall16;
Ttotal17 = TdifNH + Twall17;
Ttotal18 = TdifNH2 + Twall18;
Ttotal20 = TdifH + Twall20;
Ttotal22 = TdifNH + Twall22;
*Coeficientes cinéticos r. pared;
*w1 = 0.;
w1 = VRS/(Ttotal1*ST);
w2 = 0.;
*w2 = nudesH*exp(-EdesH/(kB*300.));
*w3 = 0.;
w3 = 1/(Ttotal3*ST);
w4 = 0.;
*w4 = (nudifH*exp((-EdifH -Eaw4)/(kB*300.)))/(4*ST);
*w5 = 0.;
w5 = VRS/(Ttotal5*ST);
w6 = 0.;
*w6 = nudesN*exp(-EdesN/(kB*300.));
*w7 = 0.;
w7 = 1/(Ttotal7*ST);
w8 = 0.;
*w8 = (nudifN*exp((-EdifN -Eaw8)/(kB*300.)))/(4*ST);
*w9 = 0.;
w9 = VRS/(Ttotal9*ST);
*w10 = 0.;
w10 = VRS/(Ttotal10*ST);
*w11 = 0.;
w11 = (nudifH*exp((-EdifH -Eaw11)/(kB*300.)))/(4*ST);
*w12 = nudesNH2*exp(-EdesNH2/(kB*300.));
w12 = 0.;
w13 = 1/(Ttotal13*ST);
*w13 = 0.;
```

```
*w14 = 0.;
w14 = (nudifH*exp((-EdifH -Eaw14)/(kB*300.)))/(4*ST);
*w15 = 0.;
w15 = 1/(Ttotal15*ST);
*w16 = 0.;
w16 = 1/(Ttotal16*ST);
w17 = VRS/(Ttotal17*ST);
w18 = VRS/(Ttotal18*ST);
*w19 = nudesNH*exp(-EdesNH/(kB*300.));
w19 = 0.;
w20 = VRS/(Ttotal20*ST);
*w20 = 0.;
*w21 = (nudifH*exp(-EdifH/(kB*300.))*exp(-Eaw21/(kB*300.)))/(4*ST);
w21 = 0.;
w22 = VRS/(Ttotal22*ST);
*Neutralización de iones en el cátodo;
CPie = Ne*(i1*N + i2*N2 + i3*N2 + i4*H
 + i5*H2 + i6*H2 + i10*NH + i11*NH
 + i12*NH2 + i13*NH2 + i14*NH3 + i15*NH3);
CNie = Ne*(n1*H2C + parn2*H3C + n3*H3C + n4*N2C
 + n5*NHC + n6*NH2C + n7*NH2C + n8*NH3C + n9*NH3C
 + n10*NH4C + n11*NH4C + n12*N2HC);
DenMI = HC + (H2C/(2@0.5)) + (H3C/(3@0.5))
 + (NC/(14@0.5)) + (NHC/(15@0.5)) + (NH2C/(16@0.5))
 + (NH3C/(17@0.5)) + (NH4C/(18@0.5)) + (N2C/(28@0.5))
 + (N2HC/(29@0.5));
T_HC = (CPie - CNie)/DenMI;
T_H2C = (CPie - CNie)/((2@0.5)*DenMI);
T_H3C = (CPie - CNie)/((3@0.5)*DenMI);
T_NHC = (CPie - CNie)/((15@0.5)*DenMI);
T_NH2C = (CPie - CNie)/((16@0.5)*DenMI);
T_NH3C = (CPie - CNie)/((17@0.5)*DenMI);
T_NH4C = (CPie - CNie)/((18@0.5)*DenMI);
T_NC = (CPie - CNie)/((14@0.5)*DenMI);
T_N2C = (CPie - CNie)/((28@0.5)*DenMI);
T_N2HC = (CPie - CNie)/((29@0.5)*DenMI);
R = 1;
k1 = R*T_HC;
k2 = R*T_H2C;
k3 = R*T_H3C;
k4 = R*T_NC;
k5 = R*T_N2C;
k6 = R*T_NHC;
k7 = R*T_NH2C;
k8 = R*T_NH3C;
k9 = R*T_NH4C;
k10 = R*T_N2HC;
*Terminos de formacion por impacto electronico;
*Incluye ionizacion, disociacion y neutralizacion;
*Notacion:PieNC es produccion por i.e. de N+, ...;
```

```
PieHC = i4*H*Ne + i5*H2*Ne;
PieH = i5*H2*Ne + 2*d1*H2*Ne + 2*n1*H2C*Ne + 3*parn2*H3C*Ne
+ n3*H3C*Ne + i11*NH*Ne + i13*NH2*Ne + i15*NH3*Ne
+ d3*NH*Ne + d5*NH2*Ne + d6*NH3*Ne
+ n5*NHC*Ne + n6*NH2C*Ne + 2*n7*NH2C*Ne + 2*n8*NH3C*Ne
+ n9*NH3C*Ne + n10*NH4C*Ne + 2*n11*NH4C*Ne + n12*N2HC*Ne;
PieH2C = i6*H2*Ne;
PieH2 = n3*H3C*Ne + d7*NH3*Ne + d4*NH2*Ne;
PieNC = i1*N*Ne + i2*N2*Ne + i11*NH*Ne;
PieN = i2*N2*Ne + 2*d2*N2*Ne + 2*n4*N2C*Ne
 + d3*NH*Ne + d4*NH2*Ne + n5*NHC*Ne + n7*NH2C*Ne;
PieNH = d5*NH2*Ne + d7*NH3*Ne + n6*NH2C*Ne + n8*NH3C*Ne;
PieNH2 =  d6*NH3*Ne + n9*NH3C*Ne + n11*NH4C*Ne;
PieN2C = i3*N2*Ne;
PieNHC = i10*NH*Ne + i13*NH2*Ne;
PieNH2C = i12*NH2*Ne + i15*NH3*Ne;
PieNH3C = i14*NH3*Ne;
PieNH3 = n10*NH4C*Ne;
PieN2 = n12*N2HC*Ne;
*Terminos de destrucción por impacto electronico;
*Notacion:DieN es destruccion por i.e. de N, ...;
DieH = -i4*H*Ne;
DieH2 = -i5*H2*Ne - i6*H2*Ne -d1*H2*Ne;
DieH2C =  - n1*H2C*Ne;
DieH3C =  - parn2*H3C*Ne -n3*H3C*Ne;
DieN = -i1*N*Ne;
DieN2 = -i2*N2*Ne -i3*N2*Ne -d2*N2*Ne;
DieN2C = -n4*N2C*Ne;
DieNH = -i10*NH*Ne -i11*NH*Ne -d3*NH*Ne;
DieNH2 = -i12*NH2*Ne -i13*NH2*Ne -d4*NH2*Ne -d5*NH2*Ne;
DieNH3 = -i14*NH3*Ne -i15*NH3*Ne -d6*NH3*Ne -d7*NH3*Ne;
DieNHC = -n5*NHC*Ne;
DieNH2C = -n6*NH2C*Ne -n7*NH2C*Ne;
DieNH3C = -n8*NH3C*Ne -n9*NH3C*Ne;
DieNH4C = -n10*NH4C*Ne -n11*NH4C*Ne;
DieN2HC = -n12*N2HC*Ne;
*Terminos de formación por reacciones homogéneas;
*con transferencia de carga ión-neutro;
*Notación:PtH3C es producción de H3+, ...;
PtH3C = t3*H2C*H2 + t12*NHC*H2;
PtHC = t2*H2C*H;
PtN2 = t22*N2C*NH3 + t23*N2HC*NH3;
PtNH2C = t9*NC*NH3 + t13*NHC*H2 + t25*H3C*N;
PtN2HC = t5*H2C*N2 + t7*H3C*N2 + t11*NC*NH3
+ t16*NHC*N2 + t21*N2C*H2;
PtNHC = t8*NC*H2 + t24*H3C*N;
PtNH = t9*NC*NH3 + t14*NHC*NH3 + t19*NH2C*NH3;
PtNH2 = t18*NH2C*NH3 + t20*NH3C*NH3;
PtNH3C = t1*NH3*HC + t4*H2C*NH3 + t10*NC*NH3 + t14*NHC*NH3
+ t17*NH2C*H2 + t18*NH2C*NH3 + t22*N2C*NH3;
```

```
PtNH4C = t6*H3C*NH3 + t15*NHC*NH3 + t19*NH2C*NH3
+ t20*NH3C*NH3 + t23*N2HC*NH3;
PtH = t1*HC*NH3 + t3*H2C*H2 + t5*H2C*N2
+ t8*NC*H2 + t13*NHC*H2 + t17*NH2C*H2 + t21*N2C*H2
+ t25*H3C*N;
PtH2 = t2*H2C*H + t4*H2C*NH3 + t6*H3C*NH3
+ t7*H3C*N2 + t11*NC*NH3 + t24*H3C*N;
PtN = t10*NC*NH3 + t12*NHC*H2
+ t15*NHC*NH3 + t16*NHC*N2;
*Terminos de destrucción por reacciones homogéneas;
*con transferencia de carga;
*Notacion:DtH3C es destruccion reac. homogenea de H3+, ...;
DtH = -t2*H2C*H;
DtH2 = -t3*H2C*H2 -t8*NC*H2 -t12*NHC*H2
- t13*NHC*H2 -t17*NH2C*H2 -t21*N2C*H2;
DtHC = -t1*HC*NH3;
DtH2C = -t2*H2C*H - t3*H2C*H2 - t4*H2C*NH3
-t5*H2C*N2;
DtH3C = -t6*H3C*NH3 -t7*H3C*N2 -t24*H3C*N -t25*H3C*N;
DtNC = -t8*NC*H2 - t9*NC*NH3 - t10*NC*NH3 - t11*NC*NH3;
DtNHC = -t12*NHC*H2 - t13*NHC*H2 - t14*NHC*NH3
-t15*NHC*NH3 - t16*NHC*N2;
DtNH2C = -t17*NH2C*H2 - t18*NH2C*NH3 -t19*NH2C*NH3;
DtNH3C = -t20*NH3C*NH3;
DtN2 = -t5*H2C*N2 -t7*H3C*N2 -t16*NHC*N2;
DtN2C = -t21*N2C*H2 - t22*N2C*NH3;
DtN2HC = -t23*N2HC*NH3;
DtNH3 = -t1*NH3*HC -t4*H2C*NH3 -t6*H3C*NH3
- t9*NC*NH3 - t10*NC*NH3 - t11*NC*NH3
- t14*NHC*NH3 - t15*NHC*NH3 -t18*NH2C*NH3
- t19*NH2C*NH3 - t20*NH3C*NH3 - t22*N2C*NH3
-t23*N2HC*NH3;
DtN = -t24*H3C*N -t25*H3C*N;
*Producción especies neutras por neutralización;
*en la pared;
PrH = k1*HC + k3*H3C + k9*NH4C + k10*N2HC;
PrH2 = k2*H2C + k3*H3C;
PrN = k4*NC;
PrN2 = k5*N2C + k10*N2HC;
PrNH = k6*NHC;
PrNH2 = k7*NH2C;
PrNH3 = k8*NH3C + k9*NH4C;
*Destrucción de iones por neutralización en la pared;
NeuHC = -k1*HC;
NeuH2C = -k2*H2C;
NeuH3C = -k3*H3C;
NeuNC = -k4*NC;
NeuN2C = -k5*N2C;
NeuNHC = -k6*NHC;
NeuNH2C = -k7*NH2C;
```

```
NeuNH3C = -k8*NH3C;
NeuNH4C = -k9*NH4C;
NeuN2HC = -k10*N2HC;
*Términos reacciones heterogéneas en pared;
*Producción de especies por r. heterog.;
*Los términos de superficie en molec.cm-2;
PwHS = w1*H*SF;
PwH = w2*HS*(1/VRS);
PwH2 = w3*HS*H + w4*HS*HS*(1/VRS);
PwNS = w5*N*SF;
PwN = w6*NS*(1/VRS);
PwN2 = w7*N*NS + w8*NS*NS*(1/VRS);
PwNHS = w9*HS*N + w17*NH*SF + w20*NS*H + w21*HS*NS;
PwNH2S = w10*NHS*H + w11*NHS*HS + w18*NH2*SF + w22*NH*HS;
PwNH2 = w12*NH2S*(1/VRS);
PwNH3 = w13*NH2S*H + w14*NH2S*HS*(1/VRS)
+ w15*NH2*HS + w16*NHS*H2;
PwNH = w19*NHS*(1/VRS);
*Destrucción de especies por r. heterog.;
DwH = -w1*H*SF*(1/VRS) -w3*H*HS  -w10*NHS*H*(1/VRS)
-w13*NH2S*H -w20*H*NS*(1/VRS);
DwHS = -w2*HS -w3*HS*H*VRS -2*w4*HS*HS -w9*HS*N
 -w11*NHS*HS -w14*NH2S*HS -w15*NH2*HS*VRS
-w21*NS*HS -w22*NH*HS;
DwN = -w5*N*SF*(1/VRS) -w7*NS*N -w9*HS*N*(1/VRS);
DwNS = -w6*NS -w7*NS*N*VRS -2*w8*NS*NS -w20*NS*H -w21*NS*HS;
DwNHS = -w10*NHS*H -w11*NHS*HS
-w16*NHS*H2*VRS -w19*NHS;
DwNH2S = -w12*NH2S -w13*NH2S*H*VRS -w14*NH2S*HS;
DwNH2 = -w15*NH2*HS -w18*NH2*SF*(1/VRS);
DwH2 = -w16*NHS*H2;
DwNH = -w17*NH*SF*(1/VRS)-w22*NH*HS*(1/VRS);
*Flujos definidos según programa I. Méndez;
*Volumen del reactor para H y N también;
FeH2 = CinH2*VR/tR;
FeN2 = CinN2*VR/tR;
Fe = FeH2 + FeN2;
FsN = N*VR/tR;
FsN2 = N2*VR/tR;
FsH = H*VR/tR;
FsH2 = H2*VR/tR;
FsNH = NH*VR/tR;
FsNH2 = NH2*VR/tR;
FsNH3 = NH3*VR/tR;
Fs = FsN + FsN2 + FsH + FsH2 + FsNH + FsNH2 + FsNH3;
*FeH2 = 0.;
*FeN2 = 0.;
*FsN = 0.;
*FsN2 = 0.;
*FsNH = 0.;
```

```
*FsNH2 = 0.;
*FsNH3 = 0.;
*FsH = 0.;
*FsH2 = 0.;
*Flujos atómicos de entrada y salida;
InFHat = 2*CinH2*VR/tR;
OutFHat = (2*H2+H+NH+2*NH2+3*NH3)*VR/tR;
InFNat = 2*CinN2*VR/tR;
OutFNat = (2*N2+N+NH+NH2+NH3)*VR/tR;
*Formación y destrucción de amoniaco;
FormNH3 = (PieNH3 + PrNH3)*VPC;
DesNH3 = -(DtNH3 + DieNH3)*VPC;
FoutNH3 = NH3/tR;
DifNH3 = FormNH3 + PwNH3 - DesNH3;
*Formación y destrucción de H2;
FormH2 = (PieH2 + PrH2 + PtH2)*VPC;
DesH2 = -(DieH2 + DtH2)*VPC;
FinH2 = CinH2/tR;
FoutH2 = H2/tR;
*Formación y destrucción de N2;
FormN2 = (PieN2 + PrN2 + PtN2)*VPC;
DesN2 = -(DieN2 + DtN2)*VPC;
FinN2 = CinN2/tR;
FoutN2 = N2/tR;
*Produccion NHS via w20 y w9;
Prow9NHS = w9*HS*N;
Prow20NHS = w20*NS*H;
*Produccion NH3 via w13 a w16;
Prow13NH3 = w13*NH2S*H;
Prow14NH3 = w14*NH2S*HS*(1/VRS);
Prow15NH3 = w15*NH2*HS;
Prow16NH3 = w16*NHS*H2;
*Flujos átomos y radicales (cm-2*s-1) hacia la superficie aprox.;
FH = H*vtH/4;
FN = N*vtN/4;
FNH = NH*vtNH/4;
FNH2 = NH2*vtNH2/4;

**;

COMPILE INITIAL;

       H2 = CinH2;
       H = 0;
       HC = 0;
       H2C = PropH2ini*Ne;
       H3C    = 0;
       HS = 0;
       N2 = CinN2;
       N = 0;
```

```
       NC = 0;
       N2C = PropN2ini*Ne;
       NS = 0;
       NH = 0;
       NHC    = 0;
       NH2    = 0;
       NH2C   = 0;
       NH3    = 0;
       NH3C = 0;
       NH4C = 0;
       N2HC   = 0;
       NHS = 0;
       NH2S = 0;

**;

COMPILE EQUATIONS ;
*Ecuaciones diferenciales;
*Notación 'N2 significa derivada primer orden respecto al tiempo;

'H2 = FeH2/VR -FsH2/VR + (PieH2 + DieH2 + PrH2 + PtH2
 + DtH2)*VPC + PwH2 + DwH2;
'H = -FsH/VR + (PieH + DieH + PtH + DtH + PrH)*VPC + PwH + DwH;
'HC = PieHC + PtHC + DtHC + NeuHC;
'H2C = PieH2C + DieH2C + DtH2C + NeuH2C;
'H3C = DieH3C + PtH3C + DtH3C + NeuH3C;
'HS = PwHS + DwHS;
'N2 = FeN2/VR -FsN2/VR + (PieN2 + DieN2 + PrN2 + PtN2
 + DtN2)*VPC + PwN2;
'N = -FsN/VR + (PieN + DieN + PrN + PtN + DtN)*VPC + PwN + DwN;
'NC = PieNC + DtNC + NeuNC;
'N2C = PieN2C + DieN2C + DtN2C + NeuN2C;
'NS = PwNS + DwNS;
'NH = -FsNH/VR + (PieNH + DieNH + PrNH + PtNH)*VPC + PwNH + DwNH;
'NH2 = -FsNH2/VR + (PieNH2 + DieNH2 + PtNH2 + PrNH2)*VPC
 + PwNH2 + DwNH2;
'NH3 = -FsNH3/VR + (PieNH3 + DieNH3 + DtNH3 + PrNH3)*VPC + PwNH3;
'NHC = PieNHC + DieNHC + PtNHC + DtNHC + NeuNHC;
'NH2C = PieNH2C + DieNH2C + PtNH2C + DtNH2C + NeuNH2C;
'NH3C = PieNH3C + DieNH3C + PtNH3C + DtNH3C + NeuNH3C;
'NH4C = PtNH4C + DieNH4C + NeuNH4C;
'N2HC = PtN2HC + DieN2HC + DtN2HC + NeuN2HC;
'NHS = PwNHS + DwNHS;
'NH2S = PwNH2S + DwNH2S;
**;

SETPSTREAM 1 8 ;
TIME   H H2 N N2 NH NH2 NH3 NH4C Prow20NHS;
**;
SETPSTREAM 3 7 ;
```

```
TIME   HC H2C H3C NC N2C NHC NH2C NH3C N2HC;
**;
SETPSTREAM 4 10 ;
TIME   mc1 mc2 mc3 mc14 mc16 mc17 mc18 mc28 mc29;
**;
SETPSTREAM 9 11 ;
TIME  HSvol NSvol NHSvol NH2Svol Iontotal mc15 OutFHat OutFNat;
**;
SETPSTREAM 13 12 ;
TIME  cH cH2 cN cNH cNH2 cNH3 cN2 FinN2 FoutN2;
**;
SETPSTREAM 15 14 ;
TIME NHS NH2S HS NS propH2 propN2 propNH3 DifNH3 PwNH3;
**;
SETPSTREAM 17 16 ;
TIME H2norm N2norm NH3norm mc15 atH atN FormNH3     DesNH3 FoutNH3;
**;
SETPSTREAM 19 18 ;
TIME atHradi atNradi atHmol atNmol atHion atNion atNsur atHsur;
**;
SETPSTREAM 20 2 ;
TIME FormH2 DesH2 DwH2 PwH2 FinH2 FoutH2 FormN2 DesN2 PwN2;
**;
SETPSTREAM 5 21 ;
* TIME Prow13NH3 Prow14NH3 Prow15NH3 Prow16NH3 PieN PieH;
TIME PieN2C DieN2C DtN2C NeuN2C i3 N2 Ne;

**;

COMPILE OUT;
PSTREAM 1 ;
PSTREAM 3 ;
PSTREAM 4 ;
PSTREAM 9 ;
PSTREAM 13 ;
PSTREAM 15 ;
PSTREAM 17 ;
PSTREAM 19 ;
PSTREAM 20 ;
PSTREAM 5 ;
**;

WHENEVER
TIME = 100000 * (+0.000001) 0  %
CALL OUT;
**;

BEGIN;
STOP;
```

A.2.3 $H_2 + O_2$

```
*=======================================================;
* H2-O2_12082301.fac Modelo H2O CON superficie;
* Reacciones L-H con w21 y w14 igual a cero;
* El H2O tras formarse pasa a fase gas (se omite desorción);
* No se considera la adsorción de H2O en superficie;
* Con neutralización en pared (k1-k9) y en fase gas (n1-n15);
* Fase gas r.ionización (i1-i11), disociación (d1-d6);
* Transferencia de carga (t1-t25);
* R (neutralización de iones en pared dando gas neutro)= 1    ;
* Tvib(H2) = 3000 K                                          ;
* Tgas = 300 K                                               ;
*=======================================================;

EXECUTE OPEN 8 "Plasmas\Fcsm\O\H2-O2_neu1.out";
EXECUTE OPEN 7 "Plasmas\Fcsm\O\H2-O2_ion1.out";
EXECUTE OPEN 10 "Plasmas\Fcsm\O\H2-O2_mi1.out";
EXECUTE OPEN 11 "Plasmas\Fcsm\O\H2-O2_at1.out";
EXECUTE OPEN 12 "Plasmas\Fcsm\O\H2-O2_cn1.out";
EXECUTE OPEN 14 "Plasmas\Fcsm\O\H2-O2_pr1.out";
EXECUTE OPEN 16 "Plasmas\Fcsm\O\H2-O2_nor1.out";
EXECUTE OPEN 18 "Plasmas\Fcsm\O\H2-O2_rad1.out";
EXECUTE OPEN 2 "Plasmas\Fcsm\O\H2-O2_mol1.out";
EXECUTE OPEN 21 "Plasmas\Fcsm\O\H2-O2_amo1.out";
EXECUTE OPEN 22 "Plasmas\Fcsm\O\H2-O2_ohs1.out";

*Parámetros a cambiar cada vez ;

PARAMETER

      Pres    0.08    T  4.5       NeTot 2.2e10
      PropO2ini 0.2;

*Valores para los coeficientes cinéticos;


PARAMETER

Tg     300
Cov_OH 1


ad1      1.7527E-7     bd1       -1.23668    cd1      -12.59243
ad2      4.2E-9                                cd2      -5.56
ad3      5.0E-8                                         cd3   -8.40

ad4      2.08E-7        bd4   -0.76     cd4   -6.9
ad5        3.04E-9      bd5   0.5               cd5   -7.0
```

```
ad6       2.0E-9             bd6   0.5            cd6   -7.0
ad7       4.0e-8             bd7   0              cd7   -8.4

ai1       1.03E-8     bi1   0.5            ci1   -14.3
ai2       4.84E-9     bi2   0.5            ci2   -22.5
ai3       7.07E-9     bi3   0.5            ci3   -13.1
ai4     6.5023E-9    bi4      0.48931    ci4      -12.89365
ai5     2.9962E-8    bi5      0.44456    ci5      -37.72836
ai6     3.1228E-8    bi6      0.17156    ci6      -20.07734
ai7       1.48E-8     bi7   0.5            ci7   -12.6
ai8       9.87E-9     bi8   0.5            ci8   -13.3
ai9       2.88E-9     bi9   0.5            ci9         -17.7
ai10    1.77E-9       bi10     0.5         ci10     -20.0
ai11      3.03E-10    bi11  0.5            ci11        -23.5
ai12    9e-10         bi12  2.0            ci12        -12.6

an4     4.9E-8     cn4       0.7
an5       1.06E-7   cn5          0.7
an6       7.56E-8   cn6          0.7
an7       3.75E-8   cn7          0.5
an8       8.6E-8          cn8          0.5
an9       3.9E-8          cn9          0.5
an10      3.05E-7   cn10   0.5
an11    2.85E-7     cn11         0.5
an12      5.6E-9          cn12   0.5
an13      6.02E-8   cn13         0.5
an14    1.08E-7     cn14         0.5
an15      3.0E-7          cn15         0.5

t1     3.75E-10     t2     8.20E-9      t3     1.17E-9
t4     6.40E-10     t5     2.00E-9      t6     3.87E-9
t7     3.43E-9      t8     7.83E-10     t9     1.92E-10
t10    8.40E-10     t11    3.60E-10     t12    5.3E-9
t13    6.70E-10     t14    6.40E-10     t15    1.62E-9
t16    2.60E-9      t17    9.70E-10     t18    1.59E-9
t19    1.30E-9      t20    3.80E-10     t21    7.60E-10
t22    1.85E-9      t23    3.3E-10      t24  4.00E-11
t25    3.30E-10     t26    1.6E-10      t27    3e-11
t28    1.4e-9


aa1    1.07E-9      ba1    -1.391 ca1    -6.26
aa2    3.54e-9      ba2    -1.5   ca2    -6.66
aa3    5.6e-13      ba3    0.5    ca3    -5.5
aa4    2.28e-10     ba4    0      ca4    -2.29

adt1   2.32e-8      bdt1   2      cdt1   -0.13
dt2    1.3e-9
dt3    1e-9
dt4    1.2e-9
```

```
dt5    1.8e-9
dt6    2e-10
dt7    3e-10
adt8   9.67e-6      bdt8   -1.9         cdt8   -12.1

adx1   4.2e-9 bdx1   0      cdx1   -4.6
adx2   5.6e-9 bdx2   0      cdx2   -2.2

hn1           7.51e-13
ahn2          9.18e-11      bhn2          0      chn2          -971.9
ahn3          4.8e-16       bhn3          1.55          chn3          80.58
ahn4          1.1e-12       bhn4          0.56          chn4          -346
ahn5          2.35e-10      bhn5          0             chn5          -373.7
ahn6          2.9e-11       bhn6          0             chn6          200
hn7           1.66e-11
hn8           2.71e-11
hn9           1.2e-10
hn10          1.2e-10
hn11          1.1e-10
ahn12  4.8e-12       bhn12  0             chn12  67
ahn13  1.6e-12       bhn13  0             chn13  67
ahn14  6e-11  bhn14   -0.186 chn14  -154
ahn15  1.62e-10      bhn15  0             chn15  64.95
hn16          1.2e-11

ax1    1.7e-9 bx1    0      cx1    -3.1
ax2    4.5e-9 bx2    0      cx2    -2.29

       ;

* Definición de parámetros;
* i1-i11: coef. cinéticos r. ionización ai(1-11),bi(1-11),ci(1-11);
* d1-d6: coef. cinéticos r. disociación ad(1-6),bd(1-6),cd(1-6);
* Omitida reaccion d3 (por ser especies excitada);
* n1-n15: coef. cinéticos r. neutralización en volumen;
* Omitidas reacciones n5 y n6 (por ser especies excitadas);
* t1 a t25: coeficientes cinéticos de r. transferencia de carga;
* k1-k9: coef. cinéticos r. neutralización en pared;
* w1-w21: coef. cinéticos r. heterogéneas en pared;
* Volúmenes: VR, VP, y Area: Are;
* VR= volumen del reactor;
* Are= Area del reactor;
* vtO = velocidad del O = 6.74E4 cms-1 (vtOH, velocidad OH);
* DH coeficiente difusión H, DOH coeficiente difusión OH, etc.;
* TdifH=A@2/DH tiempo de difusión;
* A=Rad/2.405 (Chantry);
* Rad = radio del reactor= 5 cm;
* Twall1 = (4*VRS*(1-0.5*Gamma1))/(Gamma1*vtH);
* Cambia el número y expresión de Twall según neutro que difunde;
* Ttotal1 = Twall1 + TdifH;
```

```
* Ne: densidad de electrones, variable
* con el tiempo si se modula la descarga;
* e0: parámetro para modular temporalmente la descarga;
* VP: volumen del plasma;
* VPC: relación del volumen del plasma al del reactor;
* tR: tiempo de residencia;
* Cin: concentración inicial (=pres*2.435E16);
* Fe, Fs: flujos de entrada y salida totales;
* FeH2, FeO2: flujos de entrada de H2 y O2;
* FsO, FsO2: flujos de salida de O y O2 (resto igual);

PARAMETER

d1 d2 d3 d4 d5 d6 i1  i2  i3  i4  i5  i6 i7 i9 i11
w17 w19 w20 nudesO3P nudifO3P EdesO3P EdifO3P
i10 i13 i8 i15 n1  parn2  n3  n4  n5  n6 n7
n8  n9  n10 n11 n12 n13 n14 k1  k2  k3  k4 k5 k6  k7  k8  k9
w1  w2  w3  w4  w5  w6  w7  w8  w9 w13 w14 w15 w16 w21
VP VR VRS A Rad Are Ne e0 tR R vtH vtO3P vtH2 vtO2 vtOH ST SF kB
Fe FeH2 FeO2 Fs FsO FsO2 FsH FsH2 FsOH FsH2O
Cin CinH2 CinO2 vtO1D
thetaHS thetaOS thetaOHS
DH DO3P DO2 DH2 DOH DO1D TdifH TdifO3P TdifO2 TdifOH TdifO1D
Gamma1 Gamma3 Gamma5 Gamma7 Gamma9
Gamma13 Gamma15 Gamma16 Gamma17 Gamma18 Gamma20
nudesH nudifH nudesO nudifO nudesOH
EdesH EdifO EdesO EdifH EdesOH
Twall1 Twall3 Twall5 Twall7 Twall9
Twall13 Twall15 Twall16 Twall17 Twall20
Ttotal1 Ttotal3 Ttotal5 Ttotal7
Ttotal9 Ttotal13 Ttotal15 Ttotal16
Ttotal17 Ttotal20
CTiones mc1 mc2 mc3 mc16
mc17 mc18 mc19 mc32 mc33
CPie CNie DenMI T_HC T_H2C T_H3C T_OC T_OHC T_HO2C
T_H2OC T_H3OC T_O2C DieO2C
PieHC PieH PieH2C PieH2 PieOC PieO2C PieOHC
PieO3P PieOH PieH2OC DieH
PieO2 DieH2 DieH2C DieH3C DieO2 DieOH DieO3P
PtH3C PtH PtHC PtH2 PtH3OC PtHO2C PtOC
PtOHC PtH2OC PtOH PtO3P PtH2O PtO2 DieOHC
DieH2O DieH2OC DieH3OC DieHO2C PtO2C DtHO2C
DtHC DtH2O DtH2C DtH DtH2 DtH3C DtO2 DtOC DtO3P
DtOHC DtH2OC DtO2C DtH2OC PrH PrO3P PrH2 PrO2
PrOH PrH2O NeuHC NeuH2C NeuH3C NeuOC NeuO2C
NeuOHC NeuH2OC NeuH3OC NeuHO2C
PwHS PwH PwH2 PwOS PwO3P PwO2 PwOHS PwOH
PwH2O DwH DwHS DwO3P DwOS DwOHS DwOH DwH2 VPC
atH atO atSTotal atGTotal Iontotal
CTNeutros cH cH2 cO1D cO3P cO2 cOH cH2O Suma
```

```
PropH2 PropO2 PropH2O FsO3P FO3P
Eaw4 Eaw8 Eaw14 Eaw21
InFOat OutFOat InFHat OutFHat
FH FO FOH FH2O Oatout Hatout DifH2O
H2norm O2norm H2Onorm fradicales
FormH2O DesH2O FoutH2O atHini atOini atOsurf
HSvol OSvol OHSvol H2OSvol Sumafgas FinO2 FoutO2
atHradi atOradi atHmol atOmol atHion atOion atOsurf atHsurf
FormH2 FormO2 DesH2 DesO2 FinH2 FoutH2 Prow9OHS Prow20OHS
Prow13H2O Prow14H2O Prow15H2O Prow16H2O atHsur atOsur
Prow17OHS
;


VARIABLE

       H2
       H
       HC
       H2C
       H3C
       HS
       O2
       O3P
       OC
       O2C
       OS
       OH
       OHC
       H2O
       H2OC
       H3OC
       HO2C
       OHS
       OA
       O1D
       O2a
       HO2
       HA
       OHA
       O3
       ;

*Según programa Miguel se usa COMPILE INITIAL tras GENERAL;
*para inicializar las variables a posteriori;
*y antes de GENERAL se usa COMPILE INSTANT;

COMPILE INSTANT;

PropH2ini = 1 - PropO2ini;
```

```
Cin = pres*2.435E16;
CinH2 = propH2ini*Cin;
CinO2 = propO2ini*Cin;

i3 = ai3*T@bi3*exp(ci3/T);
i6 = ai6*T@bi6*exp(ci6/T);
a1 = aa1*T@ba1*exp(ca1/T);

ionO2 = propO2ini*i3/(propO2ini*i3 + propH2ini*i6);
ionH2 = propH2ini*i6/(propO2ini*i3 + propH2ini*i6);
ionOA = propO2ini*a1/(propO2ini*i3 + propH2ini*i6);

**;

COMPILE GENERAL;

Ne = NeTot-OA-HA-OHA;

Rad = 5.0;
VP = 1709.;
VR = 4698.;
Are = 2494.;
tR = 0.61;
VPC = VP/VR;
VRS = VR/Are;
ST = 1.0E15;
SF = ST-OS-HS-Cov_OH*OHS;
*Constantes reacciones impacto electrónico;
d1 = ad1*T@bd1*exp(cd1/T);
d2 = ad2*exp(cd2/T);
*d2 = 3.49e-8*exp(-5.92/T);
d3 = ad3*exp(cd3/T);
d4 = ad4*T@bd4*exp(cd4/T);
*d5 = ad5*T@bd5*exp(cd5/T);
*d4 = -(2.82402E-11)*T + (3.38111E-11)*T@2 - (7.01504E-12)*T@3
 + (6.09826E-13)*T@4 - (1.96671E-14)*T@5;
d5 = (1.67959E-10)*T - (1.22568E-11)*T@2 + (2.19508E-11)*T@3
 - (3.01892E-12)*T@4 + (1.2549E-13)*T@5;
*d6 = 0.;
d6 = ad6*T@bd6*exp(cd6/T);
d7 = ad7*T@bd7*exp(cd7/T);
*i1 = 0.;
*i2 = 0.;
*i3 = 0.;
*i4 = 0.;
*i5 = 0.;
*i6 = 0.;
*i7 = 0.;
*i8 = 0.;
*i9 = 0.;
```

```
*i10 = 0.;
*i11 = 0.;
i1 = ai1*T@bi1*exp(ci1/T);
*i1 = (9.55301E-11)*T - (1.21783E-10)*T@2 + (4.22787E-11)*T@3;
* - (3.18022E-12)*T@4 + (7.4575E-14)*T@5;
i2 = ai2*T@bi2*exp(ci2/T);
*i2 = (1.09055E-12)*T + (2.16443E-12)*T@2 - (2.87794E-12)*T@3;
* + (8.29676E-13)*T@4 - (4.18881E-14)*T@5;
i3 = ai3*T@bi3*exp(ci3/T);
*i3 = (7.49524E-11)*T - (9.83735E-11)*T@2 + (3.51283E-11)*T@3;
* - (2.51068E-13)*T@4 - (5.57533E-14)*T@5;
i4 =  ai4*T@bi4*exp(ci4/T);
i5 =  ai5*T@bi5*exp(ci5/T);
i6 = ai6*T@bi6*exp(ci6/T);
i7 = ai7*T@bi7*exp(ci7/T);
*i7 = (2.78054E-10)*T - (4.16184E-10)*T@2 + (1.74364E-10)*T@3;
* - (1.85461E-11)*T@4 + (6.57459E-13)*T@5;
*i8 = (1.24741E-10)*T - (1.72063E-10)*T@2 + (6.61195E-11)*T@3;
* - (6.12998E-12)*T@4 + (1.91436E-13)*T@5;
i8 = ai8*T@bi8*exp(ci8/T);
*i9 = (1.32325E-10)*T - (1.33844E-11)*T@2 + (2.88652E-12)*T@3;
* + (1.8195E-13)*T@4 - (2.06371E-14)*T@5;
i9 = ai9*T@bi9*exp(ci9/T);
*i10 = (1.15731E-12)*T - (1.85202-13)*T@2 - (7.09024E-13)*T@3;
* + (2.72931E-13)*T@4 - (1.42354E-14)*T@5;
i10 = ai10*T@bi10*exp(ci10/T);
*i11 = -(6.88544E-10)*T - (1.28431E-13)*T@2 + (3.73201E-13)*T@3;
* - (2.28823E-13)*T@4 - (2.06934E-15)*T@5;
i11 = ai11*T@bi11*exp(ci11/T);
i12 = ai12*T@bi12*exp(ci12/T);

a1 = aa1*T@ba1*exp(ca1/T);
*a1 = 0;
*n1 = 0.;
*parn2 = 0.;
*n3 = 0.;
*n4 = 0.;
*n5 = 0.;
*n6 = 0.;
*n7 = 0.;
*n8 = 0.;
*n9 = 0.;
*n10 = 0.;
*n11 = 0.;
*n12 = 0.;
*n13 = 0.;
*n14 = 0.;
*n15 = 0.;
n1 = 7.51371E-9 - (1.11516E-9)*T + (1.03156E-10)*T@2
 -(4.14905E-12)*T@3 + (5.85916E-14)*T@4;
```

```
parn2 = 0.5*(8.39247E-9 + (3.01631E-9)*T - (3.80439E-10)*T@2
 + (1.31108E-11)*T@3 + (2.41631E-13)*T@4
 - (2.29832E-14)*T@5 + (3.5472E-16)*T@6);
n3 = 0.5*(8.39247E-9 + (3.01631E-9)*T - (3.80439E-10)*T@2
 + (1.31108E-11)*T@3 + (2.41631E-13)*T@4
 - (2.29832E-14)*T@5 + (3.5472E-16)*T@6);
n4 = an4*(0.026/T)@cn4;
n5 = an5*(0.026/T)@cn5;
n6 = an6*(0.026/T)@cn6;
n7 = an7*(0.026/T)@cn7;
n8 = an8*(0.026/T)@cn8;
n9 = an9*(0.026/T)@cn9;
n10 = an10*(0.026/T)@cn10;
n11 = an11*(0.026/T)@cn11;
n12 = an12*(0.026/T)@cn12;
n13 = an13*(0.026/T)@cn13;
n14 = an14*(0.026/T)@cn14;
n15 = an15*(0.026/T)@cn15;
n16 = 2e-7;
n17 = 2e-7;
n18 = 2e-7;
n19 = 2e-7;
n20 = 2e-7;
n21 = 2e-7;
n22 = 2e-7;
n23 = 2e-7;
n24 = 2e-7;
n25 = 2e-7;
n26 = 2e-7;
n27 = 1e-7;
n28 = 2e-7;
n29 = 2e-7;
n30 = 2e-7;
n31 = 2e-7;
n32 = 4e-7;


a2 = aa2*T@ba2*exp(ca2/T);
a3 = aa3*T@ba3*exp(ca3/T);
a4 = aa4*T@ba4*exp(ca4/T);

dt1 = adt1*T@bdt1*exp(cdt1/T);
dt8 = adt8*T@bdt8*exp(cdt8/T);

dx1 = adx1*T@bdx1*exp(cdx1/T);
dx2 = adx2*T@bdx2*exp(cdx2/T);

hn2 = ahn2*Tg@bhn2*exp(chn2/Tg);
hn3 = ahn3*Tg@bhn3*exp(chn3/Tg);
hn4 = ahn4*Tg@bhn4*exp(chn4/Tg);
```

```
hn5 = ahn5*Tg@bhn5*exp(chn5/Tg);
hn6 = ahn6*Tg@bhn6*exp(chn6/Tg);
hn12 = ahn12*Tg@bhn12*exp(chn12/Tg);
hn13 = ahn13*Tg@bhn13*exp(chn13/Tg);
hn14 = ahn14*Tg@bhn14*exp(chn14/Tg);
hn15 = ahn15*Tg@bhn15*exp(chn15/Tg);

x1 = ax1*T@bx1*exp(cx1/T);
x2 = ax2*T@bx2*exp(cx2/T);


*n16 = 0;
*Concentraciones especies moleculares neutras relativas;
atH = (2*H2+H+OH+2*H2O)*VR + ((HC+2*H2C+3*H3C+OHC
+2*H2OC+3*H3OC+HO2C)*VP) + ((HS+OHS)*Are);
atO = (2*O2+O3P+OH+H2O)*VR + ((OC+2*O2C
+OHC+H2OC+H3OC+2*HO2C)*VP) + ((OS+OHS)*Are);
atSTotal = ((OS+OHS)*Are) + ((HS+OHS)*Are);
atGTotal = (2*H2+H+OH+2*H2O)*VR + (2*O2+O3P+OH+H2O)*VR;
*Atomos H y O iniciales;
atHini= 2*CinH2*VR;
atOini= 2*CinO2*VR;
*Atomos H y O en forma de radicales;
atHradi=(H+OH)*VR;
atOradi=(O3P+OH)*VR;
*Atomos H y O en forma de especies moleculares;
atHmol = (2*H2+2*H2O)*VR;
atOmol = (2*O2+H2O)*VR;
*Atomos H y O en forma ionica;
atHion = ((HC+2*H2C+3*H3C+OHC+2*H2OC+3*H3OC+HO2C)*VP);
atOion = ((OC+2*O2C+OHC+H2OC+H3OC+2*HO2C)*VP);
*Atomos H y O en superficie;
atHsur = ((HS+OHS)*Are);
atOsur = ((OS+OHS)*Are);
*Atomos H y O salientes;
Oatout = (2*O2+O3P+OH+H2O)*VR;
Hatout = (2*H2+H+OH+2*H2O)*VR;
*Atomos H y O en fase gas;
atHgas = (2*H2+H+OH+2*H2O+HO2)*VR;
atOgas = (2*O2+OH+H2O+2*HO2+3*O3+O3P+O1D+2*O2a)*VR;
*Coberturas superficiales de especies atómicas y radicales;
thetaHS=HS/ST;
thetaOS=OS/ST;
thetaOHS=OHS/ST;
*Concentraciones superficiales expresadas en cm-3;
HSvol=HS*(1/VRS);
OSvol=OS*(1/VRS);
OHSvol=OHS*(1/VRS);
*Concentraciones iónicas relativas;
CTiones=HC+H2C+H3C+OC+O2C+OHC+H2OC+H3OC+HO2C;
```

```
Iontotal = CTiones*VP;
mc1=HC/CTiones;
mc2=H2C/CTiones;
mc3=H3C/CTiones;
mc16=OC/CTiones;
mc17=OHC/CTiones;
mc18=H2OC/CTiones;
mc19=H3OC/CTiones;
mc32=O2C/CTiones;
mc33=HO2C/CTiones;
*Concentraciones de neutros relativas;
CTNeutros=H+H2+O3P+O2+OH+H2O+O1D+O2a+O3+HO2;
cH2=H2/CTNeutros;
cO2=O2/CTNeutros;
cO3P=O3P/CTNeutros;
cO1D=O1D/CTNeutros;
cH=H/CTNeutros;
cOH=OH/CTNeutros;
cH2O=H2O/CTNeutros;
cO2a=O2a/CTNeutros;
cO3=O3/CTNeutros;
cHO2=HO2/CTNeutros;
propH2=H2/(H2+O2+H2O);
propO2=O2/(H2+O2+H2O);
propH2O=H2O/(H2+O2+H2O);
Sumafgas=O2+H2+H2O;
fradicales=CTNeutros/Sumafgas;
H2norm=propH2*Cin;
O2norm=propO2*Cin;
H2Onorm=propH2O*Cin;
propOA = OA/NeTot;
propHA = HA/NeTot;
propOHA = OHA/NeTot;
propNe = Ne/NeTot;
*Términos reacciones heterogéneas;
*Difusión neutros a la pared y recombinación;
*Se incluyen radicales (OH) y especies atómicas (O3P,O1D y H);
*Velocidades medias especies neutras;
vtH = 2.52E+5;
vtH2 = 1.78E+5;
vtO3P = 6.30E+4;
vtOH = 6.11E+4;
vtO2 = 4.45E+4;
vtO1D = vtO3P;
vtO2a = vtO2;
*Coeficientes de difusión;
*Salvo H, hay que cambiar resto de valores;
DH = 3319.61/pres;
DO3P = 1890.9/pres;
DOH = 751.4/pres;
```

```
DO2a = 500/pres;
A = Rad/2.405;
*Tiempos de difusión;
*Se considera difusión radial;
TdifH = (A@2)/DH;
TdifO3P = (A@2)/DO3P;
TdifOH = (A@2)/DOH;
TdifO1D = TdifO3P;
TdifO2a = (A@2)/DO2a;
*Coeficientes de adsorción y recombinación;
Gamma1 = 1.0;
Gamma3 = 0.0035;
Gamma5 = 1.0;
Gamma7 = 0.024;
Gamma9 = 0.006;
Gamma13 = 0.004;
Gamma15 = 0.005;
Gamma16 = 0.00005;
Gamma17 = 1.0;
Gamma20 = 0.002;
Gamma22 = 1;
Gamma23 = 0.007;
*Prefactores (ley tipo Arrhenius);
nudesH = 1.0E13;
nudifH = 1.0E13;
nudesO3P = 1.0E13;
nudifO3P = 1.0E13;
nudesOH = 1.0E12;
*Energías de desorción y difusión;
EdesH = 2.0;
EdifH = 0.2;
EdesO3P = 3.0;
EdifO3P = 0.65;
EdesOH = 4.0;
Eaw4 = 0.5;
Eaw8 = 0.5;
Eaw14 = 0.2;
Eaw21 = 0.4;
*Constante de Boltzmann kB en eV*K-1;
kB= 8.6173E-5;
*Tiempos interaccion pared;
Twall1 = (4*VRS*(1-0.5*Gamma1))/(Gamma1*vtH);
Twall3 = (4*VRS*(1-0.5*Gamma3))/(Gamma3*vtH);
Twall5 = (4*VRS*(1-0.5*Gamma5))/(Gamma5*vtO3P);
Twall7 = (4*VRS*(1-0.5*Gamma7))/(Gamma7*vtO3P);
Twall9 = (4*VRS*(1-0.5*Gamma9))/(Gamma9*vtO3P);
Twall13 = (4*VRS*(1-0.5*Gamma13))/(Gamma13*vtH);
Twall15 = (4*VRS*(1-0.5*Gamma15))/(Gamma15*vtOH);
Twall16 = (4*VRS)/(Gamma16*vtH2);
Twall17 = (4*VRS*(1-0.5*Gamma17))/(Gamma17*vtOH);
```

```
Twall20 = (4*VRS*(1-0.5*Gamma20))/(Gamma20*vtH);
Twall22 = (4*VRS*(1-0.5*Gamma22))/(Gamma22*vtO1D);
Twall23 = (4*VRS*(1-0.5*Gamma23))/(Gamma23*vtO2a);
Ttotal1 = TdifH + Twall1;
Ttotal3 = TdifH + Twall3;
Ttotal5 = TdifO3P + Twall5;
Ttotal7 = TdifO3P + Twall7;
Ttotal9 = TdifO3P + Twall9;
Ttotal13 = TdifH + Twall13;
Ttotal15 = TdifOH + Twall15;
Ttotal16 = Twall16;
Ttotal17 = TdifOH + Twall17;
Ttotal20 = TdifH + Twall20;
Ttotal22 = TdifO1D + Twall22;
Ttotal23 = TdifO2a + Twall23;
*Coeficientes cinéticos r. pared;
*w1 = 0.;
w1 = VRS/(Ttotal1*ST);
w2 = 0.;
*w2 = nudesH*exp(-EdesH/(kB*300.));
*w3 = 0.;
w3 = 1/(Ttotal3*ST);
w4 = 0.;
*w4 = (nudifH*exp((-EdifH -Eaw4)/(kB*300.)))/(4*ST);
*w5 = 0.;
w5 = VRS/(Ttotal5*ST);
w6 = 0.;
*w6 = nudesO3P*exp(-EdesO3P/(kB*300.));
*w7 = 0.;
w7 = 1/(Ttotal7*ST);
w8 = 0.;
*w8 = (nudifO3P*exp((-EdifO3P -Eaw8)/(kB*300.)))/(4*ST);
*w9 = 0.;
w9 = VRS/(Ttotal9*ST);
w13 = 1/(Ttotal13*ST);
*w13 = 0.;
w14 = 0.;
*w14 = (nudifH*exp((-EdifH -Eaw14)/(kB*300.)))/(4*ST);
*w15 = 0.;
w15 = 1/(Ttotal15*ST);
*w16 = 0.;
w16 = 1/(Ttotal16*ST);
w17 = VRS/(Ttotal17*ST);
*w19 = nudesOH*exp(-EdesOH/(kB*300.));
w19 = 0.;
w20 = VRS/(Ttotal20*ST);
*w20 = 0.;
*w21 = (nudifH*exp(-EdifH/(kB*300.))*exp(-Eaw21/(kB*300.)))/(4*ST);
w21 = 0.;
w22 = 1/Ttotal22;
```

```
w23 = 1/Ttotal23;
*Neutralización de iones en el cátodo;
CPie = Ne*(i1*O3P + i2*O2 + i3*O2 + i4*H
 + i5*H2 + i6*H2 + i7*OH + i8*H2O
  + i9*H2O + i10*H2O + i11*H2O +i12*O2a);
CNie = Ne*(n1*H2C + parn2*H3C + n3*H3C + n4*O2C
 + n7*OHC + n8*H2OC + n9*H2OC + n10*H2OC
 + n11*H3OC + n12*H3OC + n13*H3OC + n14*H3OC + n15*HO2C)
 + OA*(n16*HC + n17*H2C + n18*H3C + n19*OC + (n20+n26)*OHC
 + n21*H2OC + n22*H3OC + n23*O2C + n24*HO2C)
 + OHA*(n25*OC + n27*H2C + n28*H3C + n29*O2C + n30*OHC + n31*H2OC
 + n32*H3OC);
DenMI = HC + (H2C/(2@0.5)) + (H3C/(3@0.5))
 + (OC/(16@0.5)) + (OHC/(17@0.5)) + (H2OC/(18@0.5))
 + (H3OC/(19@0.5)) + (O2C/(32@0.5))
 + (HO2C/(33@0.5));
T_HC = (CPie - CNie)/DenMI;
T_H2C = (CPie - CNie)/((2@0.5)*DenMI);
T_H3C = (CPie - CNie)/((3@0.5)*DenMI);
T_OC = (CPie - CNie)/((16@0.5)*DenMI);
T_OHC = (CPie - CNie)/((17@0.5)*DenMI);
T_H2OC = (CPie - CNie)/((18@0.5)*DenMI);
T_H3OC = (CPie - CNie)/((19@0.5)*DenMI);
T_O2C = (CPie - CNie)/((32@0.5)*DenMI);
T_HO2C = (CPie - CNie)/((33@0.5)*DenMI);
R = 1;
k1 = R*T_HC;
k2 = R*T_H2C;
k3 = R*T_H3C;
k4 = R*T_OC;
k5 = R*T_O2C;
k6 = R*T_OHC;
k7 = R*T_H2OC;
k8 = R*T_H3OC;
k9 = R*T_HO2C;
*Terminos de formacion por impacto electrónico;
*Incluye ionizacion, disociacion y neutralizacion;
*Notacion:PieOC es produccion por i.e. de O+, ...;
PieHC = i4*H*Ne + i5*H2*Ne + i10*H2O*Ne;
PieH = i5*H2*Ne + i9*H2O*Ne + 2*d1*H2*Ne
+ d4*OH*Ne + d5*H2O*Ne
+ 2*n1*H2C*Ne + 3*parn2*H3C*Ne + n3*H3C*Ne
+ n7*OHC*Ne + n8*H2OC*Ne + 2*n10*H2OC*Ne
+ 2*n11*H3OC*Ne + n12*H3OC*Ne + n14*H3OC*Ne + n15*HO2C*Ne
+ a3*H2*Ne;

PieH2C = i6*H2*Ne;
PieH2 = i11*H2O*Ne + n3*H3C*Ne
+ n9*H2OC*Ne + n12*H3OC*Ne + n13*H3OC*Ne
+d6*H2O*Ne
```

```
;
PieOC = i1*O3P*Ne + i2*O2*Ne + i11*H2O*Ne;
PieO3P = i2*O2*Ne + 2*d2*O2*Ne + d4*OH*Ne
+ 2*n4*O2C*Ne + n7*OHC*Ne
+ n9*H2OC*Ne + n10*H2OC*Ne + n12*H3OC*Ne

 + a1*O2*Ne + a4*O2a*Ne + d7*O2*Ne +2*dx1*O2a*Ne;

PieOH = i10*H2O*Ne + d5*H2O*Ne
+ n8*H2OC*Ne + n11*H3OC*Ne + n13*H3OC*Ne + a2*H2O*Ne;
PieO2C = i3*O2*Ne +i12*Ne*O2a;
PieOHC = i7*OH*Ne + i9*H2O*Ne;
PieH2OC = i8*H2O*Ne;
PieO2 = n15*HO2C*Ne +dx2*O2a*Ne;
PieH2O = n14*H3OC*Ne;

PieOA = a1*O2*Ne + a4*O2a*Ne;
PieHA = a2*H2O*Ne + a3*H2*Ne;
PieO1D = d6*H2O*Ne + d7*O2*Ne +x2*O3P*Ne;
PieO2a = x1*Ne*O2;

*Terminos de destrucción por impacto electronico;
*Notacion:DieOC es destruccion por i.e. de OC, ...;
DieH = -i4*H*Ne;
DieH2 = -i5*H2*Ne - i6*H2*Ne -d1*H2*Ne - a3*H2*Ne;
DieH2C =  -n1*H2C*Ne;
DieH3C =  -parn2*H3C*Ne -n3*H3C*Ne;
DieO3P = -i1*O3P*Ne -x2*O3P*Ne;
DieO2 = -i2*O2*Ne -i3*O2*Ne -d2*O2*Ne

 -a1*O2*Ne -d7*O2*Ne -x1*Ne*O2;

DieOH = -i7*OH*Ne -d4*OH*Ne;
DieOHC = -n7*OHC*Ne;
DieO2C = -n4*O2C*Ne;
DieH2O = -i8*H2O*Ne -i9*H2O*Ne -i10*H2O*Ne
 -i11*H2O*Ne -d5*H2O*Ne -a2*H2O*Ne -d6*H2O*Ne;
DieH2OC = -n8*H2OC*Ne -n9*H2OC*Ne -n10*H2OC*Ne;
DieH3OC = -n11*H3OC*Ne -n12*H3OC*Ne -n13*H3OC*Ne -n14*H3OC*Ne;
DieHO2C = -n15*HO2C*Ne;

DieO2a = -a4*O2a*Ne -dx1*O2a*Ne -dx2*O2a*Ne -i12*Ne*O2a;

*Terminos de formación por reacciones homogéneas;
*con transferencia de carga ión-neutro;
*Notación:PtH3C es producción de H3+, ...;
PtOC = t1*HC*O3P;
PtH = t1*HC*O3P + t2*HC*H2O + t3*HC*O2 + t5*H2C*H2
+ t7*H2C*H2O + t9*H2C*O2 + t11*H3C*O3P + t15*OC*H2
+ t17*OHC*H2  + t21*H2OC*H2 + t24*O2C*H2
```

```
 + n18*H3C*OA + n20*OHC*OA + dt1*HA*Ne
 +t27*OA*H2 +n27*H2C*OHA;

PtH2OC = t2*HC*H2O + t6*H2C*H2O + t11*H3C*O3P + t16*H2O*OC
+ t17*OHC*H2 + t18*OHC*H2O;
PtO2C = t3*HC*O2 + t8*H2C*O2 + t20*OHC*O2 + t23*H2OC*O2;
PtH2 = t4*H2C*H + t6*H2C*H2O + t8*H2C*O2 + t10*H3C*O3P
+ t12*H3C*H2O + t13*H3C*O2 + dt2*HA*H +n28*H3C*OHA;
PtHC = t4*H2C*H + t14*OC*H;
PtH3C = t5*H2C*H2 + t25*HO2C*H2;
PtH3OC = t7*H2C*H2O + t12*H3C*H2O
+ t19*OHC*H2O + t21*H2OC*H2 + t22*H2OC*H2O;
PtHO2C = t9*H2C*O2 + t13*H3C*O2 + t24*O2C*H2;
PtOHC = t10*H3C*O3P + t15*OC*H2;
PtO3P = t14*OC*H + t16*H2O*OC + t19*OHC*H2O

 + n21*H2OC*OA + n23*O2C*OA;

PtOH = t18*OHC*H2O + t20*OHC*O2 + t22*H2OC*H2O

 + n22*OA*H3OC + n16*HC*OA + n24*HO2C*OA + dt3*HA*O3P
 +t28*OA*H2O +dt8*Ne*OHA +n29*O2C*OHA +2*n30*OHC*OHA
 +n31*H2OC*OHA;

PtH2O = t23*H2OC*O2

 + n22*OA*H3OC + n17*H2C*OA + n18*H3C*OA + n21*H2OC*OA
 + dt5*OHA*H +n27*H2C*OHA +n28*H3C*OHA +n31*H2OC*OHA
 +2*n32*H3OC*OHA;

PtO2 = t25*HO2C*H2

 + t26*O3P*OA +n19*OC*OA +n20*OHC*OA +n23*O2C*OA +n24*HO2C*OA
 +n29*O2C*OHA;

PtHO2 = dt4*HA*O2 +dt6*OHA*O3P +n25*OC*OHA +n26*OHC*OA;

PtO3 = dt7*OA*O2a;

PtOHA = t27*OA*H2 +t28*OA*H2O;


*Terminos de destrucción por reacciones homogéneas;
*con transferencia de carga;
*Notacion:DtH3C es destruccion reac. homogenea de H3+, ...;
DtHC = -t1*HC*O3P -t2*HC*H2O -t3*HC*O2

 -n16*HC*OA;
```

```
DtO3P = -t1*HC*O3P -t10*H3C*O3P -t11*H3C*O3P - t26*O3P*OA
-dt3*HA*O3P -dt6*OHA*O3P;
DtH2O = -t2*HC*H2O -t6*H2C*H2O -t7*H2C*H2O -t12*H3C*H2O
-t16*OC*H2O -t18*OHC*H2O -t19*OHC*H2O -t22*H2OC*H2O
-t28*OA*H2O ;
DtO2 = -t3*HC*O2 -t8*H2C*O2 -t9*H2C*O2 -t13*H3C*O2
-t20*OHC*O2 -t23*H2OC*O2 -dt4*HA*O2;
DtH2C = -t4*H2C*H -t5*H2C*H2 -t6*H2C*H2O
-t7*H2C*H2O -t8*H2C*O2 -t9*H2C*O2

 -n17*H2C*OA -n27*H2C*OHA;

DtH = -t4*H2C*H -t14*OC*H -dt2*HA*H -dt5*OHA*H;
DtH2 = -t5*H2C*H2 -t15*OC*H2 -t17*OHC*H2 -t21*H2OC*H2
-t24*O2C*H2 -t25*HO2C*H2 -t27*OA*H2;
DtH3C = -t10*H3C*O3P -t11*H3C*O3P -t12*H3C*H2O -t13*H3C*O2

 -n18*H3C*OA -n28*H3C*OHA;

DtOC = -t14*OC*H -t15*OC*H2 -t16*OC*H2O

 -n19*OC*OA -n25*OC*OHA;

DtOHC = -t17*OHC*H2 -t18*OHC*H2O -t19*OHC*H2O -t20*OHC*O2

 -n20*OHC*OA -n26*OHC*OA -n30*OHC*OHA;

DtH2OC = -t21*H2OC*H2 -t22*H2OC*H2O -t23*H2OC*O2

 -n21*H2OC*OA -n31*H2OC*OHA;

DtO2C = -t24*O2C*H2

 -n23*O2C*OA -n29*O2C*OHA;

DtHO2C = -t25*HO2C*H2

 -n24*HO2C*OA;

DtOA = -n16*HC*OA -n17*H2C*OA -n18*H3C*OA -n19*OC*OA -n20*OHC*OA
 -n21*H2OC*OA -n22*H3OC*OA -n23*O2C*OA -n24*HO2C*OA -t26*O3P*OA
-dt7*OA*O2a -n26*OHC*OA -t27*OA*H2 -t28*OA*H2O;

DtH3OC = -n22*H3OC*OA -n32*H3OC*OHA;

DtHA = -dt1*HA*Ne -dt2*HA*H -dt3*HA*O3P -dt4*HA*O2;

DtOHA = -dt5*OHA*H -dt6*OHA*O3P -n25*OC*OHA -dt8*Ne*OHA
 -n27*H2C*OHA -n28*H3C*OHA -n29*O2C*OHA -n30*OHC*OHA
 -n31*H2OC*OHA -n32*H3OC*OHA;
```

```
DtO2a = -dt7*OA*O2a;

*Reacciones homogéneas con especies excitadas o radicales;
*en fase gas;

*Producción;

PnO3P = hn1*H*O3 +hn2*H*HO2 +hn7*O2a*HO2 +2*hn10*O1D*O3
+(hn12+hn13)*O1D*O2 +hn16*O1D*H2O;
PnHO2 = hn1*H*O3;
PnH2O = hn2*H*HO2 +hn3*H*HO2 +hn16*O1D*H2O;
PnO1D = hn3*H*HO2;
PnO2 = hn4*H*HO2 +hn6*O1D*HO2 +hn7*O2a*HO2 +hn8*H*O3
+ 2*hn9*O1D*O3 +hn10*O1D*O3 +hn12*O1D*O2 +hn14*O1D*OH;
PnH2 = hn4*H*HO2;
PnOH = 2*hn5*H*HO2 +hn6*O1D*HO2 +hn7*O2a*HO2 +hn8*H*O3
+hn11*O1D*H2 +2*hn15*O1D*H2O;
PnH = hn11*O1D*H2 +hn14*O1D*OH;
PnO2a = hn13*O1D*O2;

*Destrucción;

DnH = -(hn1+hn8)*H*O3 -(hn2+hn3+hn4+hn5)*H*HO2;
DnO3 = -(hn1+hn8)*H*O3 -(hn9+hn10)*O1D*O3;
DnHO2 = -(hn2+hn3+hn4+hn5)*H*HO2 -hn6*O1D*HO2 -hn7*O2a*HO2;
DnO1D = -hn6*O1D*HO2 -(hn9+hn10)*O1D*O3 -hn11*O1D*H2
-(hn12+hn13)*O1D*O2 -hn14*O1D*OH -(hn15+hn16)*O1D*H2O;
DnO2a = -hn7*O2a*HO2;
DnH2 = -hn11*O1D*H2;
DnO2 = -(hn12+hn13)*O1D*O2;
DnOH = -hn14*O1D*OH;
DnH2O = -(hn15+hn16)*O1D*H2O;



*Producción especies neutras por neutralización;
*en la pared;
PrH = k1*HC + k3*H3C + k8*H3OC + k9*HO2C;
PrH2 = k2*H2C + k3*H3C;

PrO2 = k5*O2C + k9*HO2C;
PrOH = k6*OHC;
PrH2O = k7*H2OC + k8*H3OC;
*Destrucción de iones por neutralización en la pared;
NeuHC = -k1*HC;
NeuH2C = -k2*H2C;
NeuH3C = -k3*H3C;
NeuOC = -k4*OC;
NeuO2C = -k5*O2C;
```

```
NeuOHC = -k6*OHC;
NeuH2OC = -k7*H2OC;
NeuH3OC = -k8*H3OC;
NeuHO2C = -k9*HO2C;


*Balance de cargas negativas;
*ambip = 1 + T/0.026;
ambip = 1;
FTotC = NeuHC + NeuH2C + NeuH3C + NeuOC + NeuO2C
 + NeuOHC + NeuH2OC + NeuH3OC + NeuHO2C;
raizmOA = ((16/5.486E-4)@0.5)/ambip;
*DAn = FTotC*OA/(Ne*raizmOA + OA);
DAn = 0;

PrO3P = k4*OC - DAn;

*Faltan introducir reacciones w10 y w11;
*Deexcitación en la pared de O1D y OH(A);
*Producción de O3P en la pared;
*Destrucción de O1D en la pared;
*Términos reacciones heterogéneas en pared;
*Producción de especies por r. heterog.;
*Los términos de superficie en molec.cm-2;
PwHS = w1*H*SF;
PwH = w2*HS*(1/VRS);
PwH2 = w3*HS*H + w4*HS*HS*(1/VRS);
PwOS = w5*O3P*SF;
PwO3P = w6*OS*(1/VRS) +w22*O1D;
PwO2 = w7*O3P*OS + w8*OS*OS*(1/VRS) +w23*O2a;
PwOHS = w9*HS*O3P + w17*OH*SF + w20*OS*H + w21*HS*OS;
PwH2O = w13*OHS*H + w14*OHS*HS*(1/VRS)
+ w15*OH*HS + w16*OS*H2;
PwOH = w19*OHS*(1/VRS);
*Destrucción de especies por r. heterog.;
DwH = -w1*H*SF*(1/VRS) -w3*H*HS
-w13*OHS*H -w20*H*OS*(1/VRS);
DwHS = -w2*HS -w3*HS*H*VRS -2*w4*HS*HS -w9*HS*O3P
 -w14*OHS*HS -w15*OH*HS*VRS -w21*OS*HS;
DwO3P = -w5*O3P*SF*(1/VRS) -w7*OS*O3P -w9*HS*O3P*(1/VRS);
DwOS = -w6*OS -w7*OS*O3P*VRS -2*w8*OS*OS -w20*OS*H -w21*OS*HS
-w16*OS*H2*VRS;
DwOHS = -w14*OHS*HS -w19*OHS -w13*OHS*H*VRS;
DwH2 = -w16*OS*H2;
DwOH = -w17*OH*SF*(1/VRS)-w15*OH*HS;
DwO1D = -w22*O1D;
DwO2a = -w23*O2a;
*Flujos definidos según programa I. Méndez;
*Volumen del reactor para H, O3P y O1D también;
FeH2 = CinH2*VR/tR;
```

```
FeO2 = CinO2*VR/tR;
Fe = FeH2 + FeO2;
FsO3P = O3P*VR/tR;
FsO2 = O2*VR/tR;
FsH = H*VR/tR;
FsH2 = H2*VR/tR;
FsOH = OH*VR/tR;
FsH2O = H2O*VR/tR;
FsO1D = O1D*VR/tR;
FsHO2 = HO2*VR/tR;
FsO2a = O2a*VR/tR;
FsO3 = O3*VR/tR;
Fs = FsO3P + FsO2 + FsH + FsH2 + FsOH + FsH2O
+ FsO1D + FsHO2 + FsO2a + FsO3;
*FeH2 = 0.;
*FeO2 = 0.;
*FsO3P = 0.;
*FsOH = 0.;
*FsH2O = 0.;
*FsH = 0.;
*FsH2 = 0.;
*FsO2 = 0.;
*Flujos atómicos de entrada y salida;
InFHat = 2*CinH2*VR/tR;
OutFHat = (2*H2+H+OH+2*H2O)*VR/tR;
InFOat = 2*CinO2*VR/tR;
OutFOat = (2*O2+O3P+OH+H2O)*VR/tR;
*Formación y destrucción de H2O;
FormH2O = (PrH2O)*VPC;
DesH2O = -(DtH2O + DieH2O)*VPC;
FoutH2O = H2O/tR;
DifH2O = FormH2O + PwH2O - DesH2O;
*Formación y destrucción de H2;
FormH2 = (PieH2 + PrH2 + PtH2)*VPC;
DesH2 = -(DieH2 + DtH2)*VPC;
FinH2 = CinH2/tR;
FoutH2 = H2/tR;
*Formación y destrucción de O2;
FormO2 = (PieO2 + PrO2 + PtO2)*VPC;
DesO2 = -(DieO2 + DtO2)*VPC;
FinO2 = CinO2/tR;
FoutO2 = O2/tR;
*Produccion OHS via w20, w9 y adsorción;
Prow9OHS = w9*HS*O3P;
Prow20OHS = w20*OS*H;
Prow17OHS = w17*OH*SF;
*Produccion H2O via w13 a w16;
Prow13H2O = w13*OHS*H;
Prow14H2O = w14*OHS*HS*(1/VRS);
Prow15H2O = w15*OH*HS;
```

```
Prow16H2O = w16*OS*H2;
*Flujos átomos y radicales (cm-2*s-1) hacia la superficie aprox.;
FH = H*vtH/4;
FO3P = O3P*vtO3P/4;
FOH = OH*vtOH/4;

evoH3C = DieH3C + PtH3C + DtH3C + NeuH3C;
ConTot = H +H2 +O3P +O2 +OH +H2O +O1D +O2a +O3 +HO2;

par1=t9*H2C*O2;
par2 =t13*H3C*O2;
par3=t24*O2C*H2;




**;

COMPILE INITIAL;

       H2 = CinH2;
       H = 0;
       HC = 0;
       H2C = ionH2*NeTot;
       H3C    = 0;
       HS = 0;
       O2 = CinO2;
       O3P = 0;
       OC = 0;
       O2C = ionO2*NeTot;
       OS = 0;
       OH = 0;
       OHC    = 0;
       H2O    = 0;
       H2OC   = 0;
       H3OC   = 0;
       HO2C   = 0;
       OHS = 0;
       OA = 0;
       HA = 0;
       O1D    = 0;
       HO2    = 0;
       OHA    = 0;
       O2a    = 0;
       O3     = 0;

**;

COMPILE EQUATIONS ;
*Ecuaciones diferenciales;
```

```
*Notación 'H2 significa derivada primer orden respecto al tiempo;
*Falta introducir ecuación diferencial para OH(A) excitado;

'H2 = FeH2/VR -FsH2/VR
 + (PieH2 + DieH2 + PrH2 + PtH2 + DtH2 )*VPC
 + PwH2 + DwH2 + PnH2 + DnH2;
'H = -FsH/VR + (PieH + DieH + PtH + DtH + PrH )*VPC
 + PwH + DwH + DnH + PnH;
'HC = PieHC + PtHC + DtHC + NeuHC;
'H2C = PieH2C + DieH2C + DtH2C + NeuH2C;
'H3C = DieH3C + PtH3C + DtH3C + NeuH3C;
'HS = PwHS + DwHS;
'O2 = FeO2/VR -FsO2/VR
 + (PieO2 + DieO2 + PrO2 + PtO2 + DtO2 )*VPC
 + PwO2 + PnO2 + DnO2;
'O3P = -FsO3P/VR
 + (PieO3P + DieO3P + PrO3P + PtO3P + DtO3P )*VPC
 + PwO3P + DwO3P + PnO3P;
'OC = PieOC + PtOC + DtOC + NeuOC;
'O2C = PieO2C + DieO2C + PtO2C + DtO2C + NeuO2C;
'OS = PwOS + DwOS;
'OH = -FsOH/VR
 + (PieOH + DieOH + PrOH + PtOH )*VPC
 + PwOH + DwOH + PnOH + DnOH;
'H2O = -FsH2O/VR
 + (PieH2O + DieH2O + DtH2O + PrH2O + PtH2O)*VPC
 + PwH2O + PnH2O + DnH2O;
'OHC = PieOHC + DieOHC + PtOHC + DtOHC + NeuOHC;
'H2OC = PieH2OC + DieH2OC + PtH2OC + DtH2OC + NeuH2OC;
'H3OC = DieH3OC + PtH3OC + NeuH3OC + DtH3OC;
'HO2C = PtHO2C + DieHO2C + DtHO2C + NeuHO2C;
'OHS = PwOHS + DwOHS;
'OA = PieOA + DtOA + DAn;

'HA = PieHA + DtHA;
'O1D = -FsO1D/VR + (PieO1D)*VPC + DwO1D  + PnO1D + DnO1D;
'HO2 = -FsHO2/VR + (PtHO2)*VPC + PnHO2 + DnHO2;
'OHA = PtOHA + DtOHA;
'O2a = -FsO2a/VR +(PieO2a + DtO2a + DieO2a)*VPC
+ DwO2a + PnO2a + DnO2a;
'O3 = -FsO3/VR + (PtO3)*VPC  + DnO3;
**;


SETPSTREAM 1 8 16;
TIME   H H2 O3P O2 OH H2O O1D O2a O3 HO2 ConTot;
**;
SETPSTREAM 3 7 16;
TIME   HC H2C H3C OC O2C OHC H2OC H3OC HO2C ;
**;
```

```
SETPSTREAM 4 10 16;
TIME   mc1 mc2 mc3 mc16 mc17 mc18 mc19 mc32 mc33;
**;
SETPSTREAM 9 11 16;
TIME  HSvol OSvol OHSvol Iontotal OutFHat OutFOat InFHat InFOat;
**;
SETPSTREAM 13 12 16;
TIME   cH2 cO2 cH2O cH cO3P cOH cO1D cO2a cHO2 cO3 OHS HS OS;
**;
SETPSTREAM 15 14 16;
TIME  OHS HS OS propH2 propO2 propH2O;
**;
SETPSTREAM 17 16 16;
TIME H2norm H2Onorm atH atO FormH2O DesH2O FoutH2O;
**;
SETPSTREAM 19 18 16;
TIME atHradi atOradi atHsur atOsur infoat outfoat atHgas atOgas;
**;
SETPSTREAM 20 2 16;
TIME FormH2 DesH2 DwH2 PwH2 FinH2 FoutH2 FormO2 DesO2 PwO2;
**;
SETPSTREAM 5 21 16;
TIME Prow13H2O Prow14H2O Prow15H2O Prow16H2O PieO3P PieH;
**;
SETPSTREAM 6 22 16;
TIME propHA propOA propOHA propNe;
**;

COMPILE OUT;
PSTREAM 1 ;
PSTREAM 3 ;
PSTREAM 4 ;
PSTREAM 9 ;
PSTREAM 13 ;
PSTREAM 15 ;
PSTREAM 17 ;
PSTREAM 19 ;
PSTREAM 20 ;
PSTREAM 5 ;
PSTREAM 6 ;
**;


WHENEVER
TIME = 20000 * (+0.1) 0  %
CALL OUT;
**;

BEGIN;
STOP;
```